A Measurement of Anisotropy in the Microwave Background on 7′-22′ Scales

Thesis by

Erik M. Leitch

In partial fulfillment of the requirements

for the degree of

Doctor of Philosophy

California Institute of Technology

Pasadena, California

1998

(Submitted March 4, 1998)

'Producing a thorough analysis of the deviations from the ideal picture of a homogeneous isotropic universe is the most important task confronting modern cosmology.'

Igor Novikov, *The Structure and Evolution of the Universe*

'The data of the cosmic creation are nothing but a deafening bombardment of our intelligence with figures furnished with a comet's tail of a couple of dozen ciphers, and comporting themselves as though they still had something, anything, to do with measurement and understanding. There is in all this monstrousness nothing that could appeal to the likes of me as goodness, beauty, greatness; and I shall never understand the glory-to-God mental attitude which certain temperaments assume when they contemplate the 'works of God,' meaning by the phrase the physics of the universe. And is a construction to be hailed as the 'works of God' when one may just as reasonably say: 'Well, what then?' instead of 'Glory to the Lord'? The first rather than the second seems to me the answer to two dozen ciphers after a one or even after a seven, which really adds nothing to it; and I can see no sort of reason to fall in the dust and adore the fifth power of a million.'

Thomas Mann, *Dr. Faustus*

Acknowledgements

'For masterpieces are not single and solitary births; they are the outcome of many years of thinking in common, of thinking by the body of the people, so that the experience of the mass is behind the single voice.'

Virginia Woolf, *A Room of One's Own*

Though this work may fall short of the mark Virginia Woolf intended for Shakespeare, it is in recognition of the many people whose abilities and generosity were the foundation upon which this experiment was built that I begin these acknowledgments with her apt words.

An enormous debt of gratitude is due Russ Keeney, whose dedication to a job well done has been instruction to rival any I've had in my academic career. Without the pride and skill that Russ brings to every endeavor, this thesis would no doubt be a detection of anisotropy in the 5.5-meter backend. Mark Hodges' many enthusiasms made even the dullest receiver autopsies a pleasure, and without his particular genius for gadgetry, the Ku-Band receiver would not be the thing of beauty that it is. When the 40-meter is long forgotten, the annals of radio astronomy will surely record the crow cannon. The thoughtful presence of guru Harry Hardebeck, from whose head receivers spring fully formed, continues to inspire those of us unable to debug microwave electronics by pure thought. Over the years, his careful observations have steadily exposed to mundane explanation the anomalies which Russ' more suspicious nature routinely attributed to aliens. In addition to the triumvirs, many members of the OVRO staff have made the observatory feel like a second home.

Steve Myers was a constant source of inspiration, in spite of his sunny disposition and many cheerful words of encouragement. Tim Pearson has been a dependable source of sober advice in matters astronomical and vegetable and mineral. I cannot overstate my indebtedness to Sensei Martin Shepherd, from whom I learned everything I know about programming. Let him cringe at the thought. His uncompromising attention to detail and unflagging generosity make him a truly irreplaceable person in a sea of academic sameness. To my fellow catastrophe theorist Gautam Vasisht, thanks for the many distractions along the way, and for a mean game of pool — it wouldn't have been the same without you (my thesis would have been written much sooner). I thank my officemate Ben Oppenheimer for providing a constant backdrop of vulgarity and carcinogens against which this thesis was completed. I thank my officemates Kurt Adelberger and Brian Mason for not being like Ben.

No Odyssey would be complete without its Mentor, and in my travels through graduate school, Tony Readhead has surpassed the archetype. His humanity is proof that the scientific quest need not be a Faustian one; as a person and as a thinker I should count myself lucky to achieve half his stature.

To Rob, what more is there to say? You'd better stick around, because I know all about the affair you had with that older woman in Sunset Beach. Thanks for everything... MARIA!

Abstract

A measurement of the anisotropy of the cosmic microwave background radiation (CMBR) at 7′-22′ scales is described. Observations of 36 blank fields near the North Celestial Pole (NCP) were made at 31.7 and 14.5 GHz, using two High Electron Mobility Transistor (HEMT) amplified radiometers. These observations were conducted at the Owens Valley Radio Observatory from 1993-1996.

We detect a significant signal, with temperature spectral index consistent with emission from a combination of a steep-spectrum foreground ($\beta < -2$) and CMBR ($\beta \simeq 0$). Multi-epoch VLA observations at 8 and 15 GHz allow removal of any discrete source contamination at 14.5 and 31.7 GHz. On the basis of low-frequency maps of the NCP, we can rule out emission with $\beta < -2.2$. Although the foreground signal dominates at 14.5 GHz, the extracted CMBR component contributes nearly 90% of the variance at 31.7 GHz, yielding an *rms* fluctuation amplitude of $78^{+12.9}_{-9.1}$ μK, including calibration uncertainty and sample variance. In terms of the angular power spectrum C_ℓ averaged over a range of multipoles $\ell_e = 589^{+167}_{-228}$, we have $\delta T_{\ell_e} = \sqrt{\ell(\ell+1)C_\ell/2\pi} = 56^{+8.5}_{-6.6}$ μK.

The extracted foreground component is found to correlate significantly with *IRAS* 100 μm dust emission. Lack of Hα emission near the NCP suggests that the foreground is either high-temperature thermal bremsstrahlung ($T_e \gtrsim 10^6$ K), flat spectrum synchrotron, or an exotic component of dust emission.

Contents

List of Tables

List of Figures

Chapter 1

Introduction

It is generally believed that large-scale structures in the universe grew via gravitational instability out of tiny departures from homogeneity in the mass distribution at z_{rec}. Though the origin of these primordial perturbations remains a ripe subject for conjecture, the theory of their effect on the isotropy of the microwave background radiation (CMBR) is well developed. As such, the CMBR provides a sensitive probe of the history of structure formation in the early universe.

Since baryonic matter is decoupled from the radiation field at z_{rec}, the horizon scale at recombination separates scales of importance for micro-physical processes leading to structure formation from scales which probe only the primordial spectrum of perturbations. For $z \gg 1$, the horizon scale is given by

$$\Delta\theta_H \approx 0^\circ.87\,\Omega_0^{1/2}(z/1100)^{-1/2} \tag{1.1}$$

so that for $z_{rec} \simeq 1100$, scales $> 1^\circ$ were outside the horizon when baryonic matter recombined (White et al. 1994). Fluctuations on these scales reflect a combination of primordial temperature anisotropies and gravitational redshifts, imprinted as temperature perturbations on the CMBR photons as they climb out of potential wells on the surface of last scattering — the so-called *Sachs-Wolfe* effect (Sachs & Wolfe 1967).

On scales $< 1^\circ$, anisotropies are directly linked to causal physical processes in the early universe. Once a perturbation re-enters the horizon, it oscillates as an acoustic

wave in the baryon-photon plasma until freed of photon pressure support at z_{rec}. Since

$$\frac{\delta T}{T} = \frac{1}{4}\frac{\delta \rho_\gamma}{\rho_\gamma} = \frac{1}{3}\frac{\delta \rho}{\rho} \tag{1.2}$$

for adiabatic (energy density) perturbations, the CMBR temperature autocorrelation function follows the power spectrum of density perturbations, and therefore depends on the details of these oscillations, in particular, on Ω_0, Ω_b, and H_0 (Scott & White 1995).

Figure 1.1 illustrates some of these dependencies. Peaks at successively smaller ℓ represent extrema of the oscillations for modes which entered the horizon at successively earlier times; the first "Doppler" peak thus corresponds to the mode which experienced only 1/4 of an oscillation before the universe recombined. The epoch of recombination is relatively insensitive to the baryon-to-photon ratio, and hence to $\Omega_b h^2$, so that z_{rec} occurs within a narrow range of $z \simeq 1100$ in all cosmologies; the location of this first peak is therefore a sensitive probe of Ω_0, shifting to smaller angular scales in accordance with (1.1) as Ω_0 is lowered. Since radiation is tightly coupled to baryons via Thompson scattering, the oscillation amplitude is sensitive to the baryon number density, as illustrated in Figure 1.1. In adiabatic scenarios, odd-numbered peaks correspond to the compressional phase of the oscillation, or temperature hot spots in the CMBR. As baryons collapse toward dark matter over-densities (in the standard CDM model), they deepen the potential well seen by the radiation, enhancing the blueshift a photon experiences during infall relative to the redshift it acquires as the oscillation rebounds out of the potential. As a result, odd-numbered peaks will be enhanced relative to the even-numbered peaks, which correspond to the rarefaction phase (Hu et al. 1997).

At the smallest angular scales, oscillations are damped by a variety of processes. Prior to the epoch of matter-radiation equality, fluctuations inside the horizon are suppressed, selectively damping modes which entered the horizon at early times.

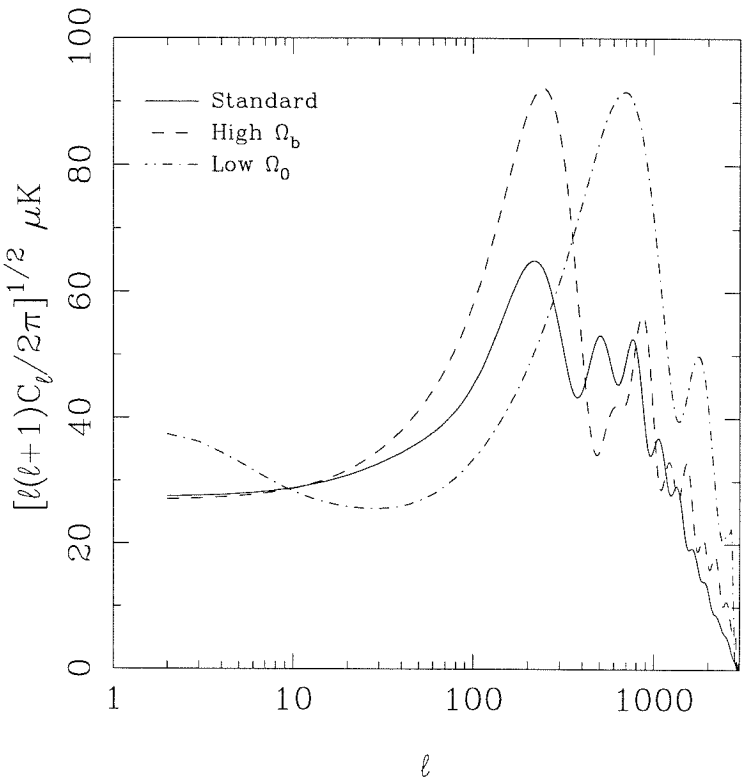

Figure 1.1 Model CMBR power spectra for adiabatic fluctuations. Multipole moment ℓ corresponds to inverse angular scale, in radians, while C_ℓ is the corresponding power. Shown are a standard CDM model (solid line) with $H_0 = 50, \Omega_0 = 1$ and $\Omega_b = 0.05$, a model with $\Omega_0 = 1, \Omega_b = 0.2$ (dashed line) and $\Omega_b = \Omega_0 = 0.2$ (dot-dashed line). The amplitude of the peaks depends on the baryon density via $\Omega_b h^2$, while the angular size of the horizon at last scattering depends on Ω_0. Models are courtesy of Seljak & Zaldarriaga (1997).

Moreover, the photons and baryons are not perfectly coupled, and photons will diffuse out of overdensities as the mean free path for a CMBR photon grows comparable to the perturbation wavelength (Silk & Wilson 1980). Near recombination, the ionization fraction x_e drops dramatically, smearing out fluctuations on ever larger scales $\lambda \propto (x_e n_b)^{-1}$. If the universe is reionized sufficiently early, i.e., $z_{reion} \gg 10$, photon diffusion can lead to erasure of all peaks in the angular power spectrum. Finally, recombination is not instantaneous, and destructive interference across the thickness of the last scattering surface leads to an exponential cutoff in the angular power

spectrum.

Thus in principle, even a null detection of the angular power spectrum can constrain the reionization history of the universe, while a detection of the classical CDM spectrum could extract some combination of the fundamental cosmological parameters, under the proviso that all of the dependencies described and others not discussed for the sake of brevity will be needed to disentangle degenerate sets of parameters. Optimistic assessments of current satellite missions designed to map the CMBR sky at high resolution indicate that by the turn of the millennium, H_0, Ω_0, Ω_b, Ω_Λ, z_{reion}, etc., will be known to an accuracy of a few percent (Scott & White 1995), but this will no doubt prove naive. Whatever the case, observations of the CMBR offer an unprecedented window on the universe in its infancy, an incandescent window through which the chaff of our theoretical preconceptions will eventually burn away.

1.1 The Ring5m Experiment: An Overview

The Ring5m experiment, described in this work, is the most recent in a series of filled-aperture, ground-based experiments at the Owens Valley Radio Observatory (OVRO) designed to detect anisotropy on arcminute scales. Previous experiments at the OVRO include the NCP experiment (Readhead et al. 1989), in which the OVRO 40-meter telescope was used to place a 95% confidence limit of $\Delta T/T < 1.7 \times 10^{-5}$ on power at $2'$ scales, and the Ring40m experiment (Myers 1990), which resulted in a detection of anisotropy of $2.3 \times 10^{-5} < \Delta T/T < 4.5 \times 10^{-5}$ (95% confidence) on similar scales, but was unable to rule out foreground contamination.

The primary instrument used in the Ring5m experiment is the OVRO 5.5-meter telescope, equipped with a dual-feed HEMT-amplified receiver, described in Chapter 2. At 31.7 GHz (Ka-Band), the feed horns produce a power pattern approximately $7'.35$ wide (fwhm). The OVRO 40-meter telescope, underilluminated to match the

7.'35 beam of the 5.5-meter, provides a second frequency channel, at 14.5 GHz (Ku-Band). Measurements of the sky temperature are obtained by a combination of rapid ("Dicke") switching between two feeds separated by $22'$ and slower azimuthal nodding of the telescopes between two symmetric offset positions, a technique known as "double switching." Dicke switching eliminates some of the atmospheric fluctuations on timescales slower than the switching rate, as both feeds see the same column of air to ~ 1 km. The second level of switching serves to remove any constant offset or linear temperature gradient, either from the ground or the sky, so that only curvature in the local temperature field contaminates the measured signal. Since the switching is azimuthal, the reference fields rotate around the main field as a source is tracked across the sky.

If a source is tracked over a wide range in zenith angle, variations in the ground temperature will produce spurious fluctuations in the measured celestial signal, as radiation from the ground leaks into sidelobes of the antenna power pattern. Lawrence et al. (1994), investigating this effect for the 5.5-meter, found that radiation from the ground scattered off the support structure for the secondary mirror could produce differential signals as large as 4 mK. Contaminating signals of this amplitude are unacceptably large, given that the experiment attempts to detect variations in the CMBR temperature field of amplitude a *few* $\times 10^{-5}$ K. Although prior to the Ring5m experiment, the 5.5-meter telescope was refitted with secondary support struts designed to reflect ground radiation onto the sky, thereby reducing the peak differential contribution by a factor of 30, the residual signal is still large enough to swamp the signal expected from CMBR anisotropy. Ground spillover and atmospheric temperatures are much stronger functions of zenith angle than of azimuth, and it is therefore particularly desirable to minimize motion of the telescope in zenith angle, requiring observations of fields near the celestial poles. Variations in the differential ground pickup can further be reduced by restricting motion of the telescope

in azimuth, requiring observations of fields near times of upper or lower culmination (transit), a strategy used with great success in both the NCP and Ring40m experiments. In the Ring5m experiment, we observe 36 fields spaced evenly in a ring around the North Celestial Pole (NCP). The fields are observed within $\pm 5^\circ$ of upper culmination only.

The spacing of fields around the ring was chosen to match the angular separation of the feed horns; since the separation between neighboring fields is approximately azimuthal near transit, the $\pm 22'$ reference beams in the double switched pattern for one field correspond to the two adjacent Ring fields, providing a number of internal consistency checks. Since the temperature *difference* between the main and reference fields is recorded, real astronomical sources will appear as a characteristic minus-plus-minus pattern in consecutive fields, allowing signals on the sky to be distinguished from sources of noise fixed to the instrument or the ground. Moreover, since the temperature difference $\Delta T_i \equiv T_i - \frac{1}{2}(T_{i-1} + T_{i+1})$ is formed for the i^{th} field, the mean of the ΔT_i around the ring should be zero. Lastly, the interlocked geometry of the ring allows, at least in theory, direct reconstruction of the field temperatures, although in practice, small errors in the field means can produce spurious large-scale temperature gradients in the inversion.

Since the measure of the CMBR power spectrum at multipole ℓ is essentially a measure of the *rms* temperature fluctuation in patches of sky of angular size $\theta \sim \ell^{-1}$, the choice to observe 36 patches represents a tradeoff between observing time and sample variance, i.e., between the accuracy with which we can measure the patch temperatures and the number of patches required to give a reasonable estimate of the variance of the underlying distribution. Once the number of patches is chosen, the requirement that the fields be interlocked fixes the declination of the ring, so that for $N = 36$, $\delta \simeq 88^\circ$. The exact locations of the fields around the ring were chosen to avoid known point sources from low-frequency surveys.

1.2 Thesis Summary

Chapter 2 details the telescopes and receivers used in the Ring5m experiment. Since the ultimate efficacy of any experiment in constraining theory rests on the experiment's internal and external calibration, much of the work of this thesis has gone into observations, instrument testing and software development for the sole purpose of reducing calibration errors to a few percent; Chapters 3 and 4 are devoted to these efforts, and can be omitted by the casual reader. Chapter 5 describes the editing and reduction of the anisotropy data; observational results are presented at the end of that chapter, along with a discussion of possible sources of systematic error, and of tests for internal consistency. The results of a VLA X-Band survey and subsequent multi-frequency monitoring of point sources for subtraction from the anisotropy data are presented in Chapter 6. Final source-subtracted anisotropy data sets are given at the end of this chapter. Chapter 7 is a discussion of the contamination of the Ring5m anisotropy data by Galactic foregrounds, and is essentially an expanded version of Leitch et al. (1997), in which an unusual component of Galactic emission discovered in this experiment is described. The thesis concludes with a discussion of the detected CMBR anisotropy.

TABLE 1.1
J2000 COORDINATES OF THE RING5M FIELDS

Field	α (2000)	δ (2000)
OV5M0024	00:24:45.10	87:55:00.96
OV5M0104	01:05:25.90	87:54:54.77
OV5M0144	01:46:04.61	87:54:46.50
OV5M0224	02:26:39.98	87:54:36.20
OV5M0304	03:07:10.92	87:54:19.70
OV5M0344	03:47:36.47	87:54:03.20
OV5M0424	04:27:55.86	87:53:42.57
OV5M0504	05:08:08.61	87:53:19.88
OV5M0544	05:48:14.34	87:52:59.25
OV5M0624	06:28:12.93	87:52:36.58
OV5M0704	07:08:04.36	87:52:13.88
OV5M0744	07:47:49.20	87:51:53.25
OV5M0824	08:27:27.84	87:51:32.62
OV5M0904	09:07:00.85	87:51:16.12
OV5M0944	09:46:29.18	87:51:01.69
OV5M1024	10:25:53.80	87:50:51.36
OV5M1104	11:05:15.67	87:50:43.13
OV5M1144	11:44:35.89	87:50:41.06
OV5M1224	12:23:55.70	87:50:41.06
OV5M1304	13:03:16.19	87:50:45.19
OV5M1344	13:42:38.47	87:50:53.43
OV5M1424	14:22:03.78	87:51:05.82
OV5M1504	15:01:33.08	87:51:20.26
OV5M1544	15:41:07.19	87:51:36.75
OV5M1624	16:20:47.07	87:51:57.38
OV5M1704	17:00:33.28	87:52:18.01
OV5M1744	17:40:26.22	87:52:40.68
OV5M1824	18:20:26.18	87:53:03.38
OV5M1904	19:00:33.44	87:53:26.08
OV5M1944	19:40:47.56	87:53:46.71
OV5M2024	20:21:08.28	87:54:07.34
OV5M2104	21:01:35.06	87:54:23.83
OV5M2144	21:42:07.05	87:54:38.27
OV5M2224	22:22:43.18	87:54:48.57
OV5M2304	23:03:22.46	87:54:56.83
OV5M2344	23:44:03.13	87:54:52.70

Chapter 2

Receiver Characteristics

2.1 5.5-Meter Telescope

An exhaustive inventory of the 5.5-meter telescope and Ka-Band receiver components has previously been given by Herbig (1994), and only the essential features are reviewed here. The 5.5-meter is a standard altitude-azimuth mount telescope, with a radiometer located at the Cassegrain focus. Besides reducing mechanical stresses on the dish, improving tracking and pointing, the Cassegrain arrangement allows considerable flexibility in the design of typically large microwave receiver packages, and provides easy access to the receiver while on the telescope. This greatly reduces down-time, as the dewar can remain at cryogenic temperatures while troubleshooting problems with room-temperature components, accessible via panels in the receiver can. At the same time, direct ground spillover is significantly reduced, since sidelobes of the feed power pattern (see §2.10) illuminate the sky rather than the ground. The backing structure is extremely rigid, so that dish deformation is negligible over the full range in zenith angle.

2.2 40-Meter Telescope

The OVRO 40-meter (130-foot) telescope is also an alt-azimuth instrument, consisting of a parabolic surface of 852 lightweight aluminum panels, precision contoured to yield an *rms* surface accuracy of 1.1 mm. The Ku-Band receiver is of the same essential design as the Ka-Band receiver but is mounted at the prime focus. Since full illumination of the 40-meter dish at 14.5 GHz yields a $\theta_{fwhm} < 2'$ beam, the feeds were designed to illuminate only an 11-meter patch on the dish surface, resulting in a beam at 14.5 GHz approximately matched to the $\theta_{fwhm} \sim 7'$ beam produced on the 5.5-meter telescope by the Ka-Band set. The significant under-illumination of the dish effectively eliminates stray radiation from the ground (see §4.4.2), as the largest sidelobes of the feed illumination pattern do not see past the edge of the dish, but are instead reflected onto the sky.

To avoid shadowing by the prime focus cage, the feed horns are displaced azimuthally by 45° from the optical axis of the primary. As a result, the angle that the feeds make with the normal to the dish surface is a strong function of position along the optical axis, and the beams steer in azimuth as the receiver package is focused at different elevations. An additional complication is that the effective beam *width* is also a strong function of focus position, and hence of zenith angle; as the telescope is focused over the full zenith angle range, the beam width can vary by as much as an arcminute (see §2.10.2). To avoid such difficulties, all observations with the Ku-Band receiver were restricted to lie within ±5° of the zenith angle of the Ring ($za \sim 50°$).

2.3 Receivers

A block diagram of the Ka-band receiver is shown in Fig 2.1. At the front of the receiver are two corrugated feed horns, offset from each other in the azimuthal direction. Each illuminates the 0.6 meter hyperbolic secondary of the 5.5-meter telescope. The small angle subtended by the secondary requires that the feeds be quite large, resulting in a beam separation of 22.′16 on the sky. The Ku-Band receiver was designed to match this separation on the 40-meter, but in practice produces a separation 3% smaller, or 21.′50 on the sky. On both telescopes, the feeds are enclosed in a Kapton window to prevent moisture from entering the receiver.

In both receivers, the RF components are maintained at 15 K via a standard two-stage Helium refrigerator. At the base of the feeds, the signal in either arm enters the 15 K dewar through a vacuum window and an IR block, then passes through a right-circular polarizer, followed by a circular-to-rectangular waveguide transition. In the Ka-Band receiver, the signal is then conducted through a ferrite switch which can be directed either to the sky or to an internal load at physical temperature $\sim$ 20 K, allowing numerous internal checks on the system's performance. Internal loads are not available in the Ku-band set. Signals from two internal noise diodes can be injected via a 30 dB coupler in front of the Dicke switch, providing stable calibration sources against which long-term system gain changes can be measured. One of these diodes (which is subsequently referred to as the *CAL diode*) is injected via an additional 20 dB coupler, providing a small-amplitude signal suitable for comparison with the small increments in total power produced by most astronomical sources. The other diode (called the *NOISE diode*) produces a significant increase in the total system power, providing a bright source suitable for measurements of the receiver temperature described in §4.2. The stability of these devices is discussed in greater detail in Chapter 4.

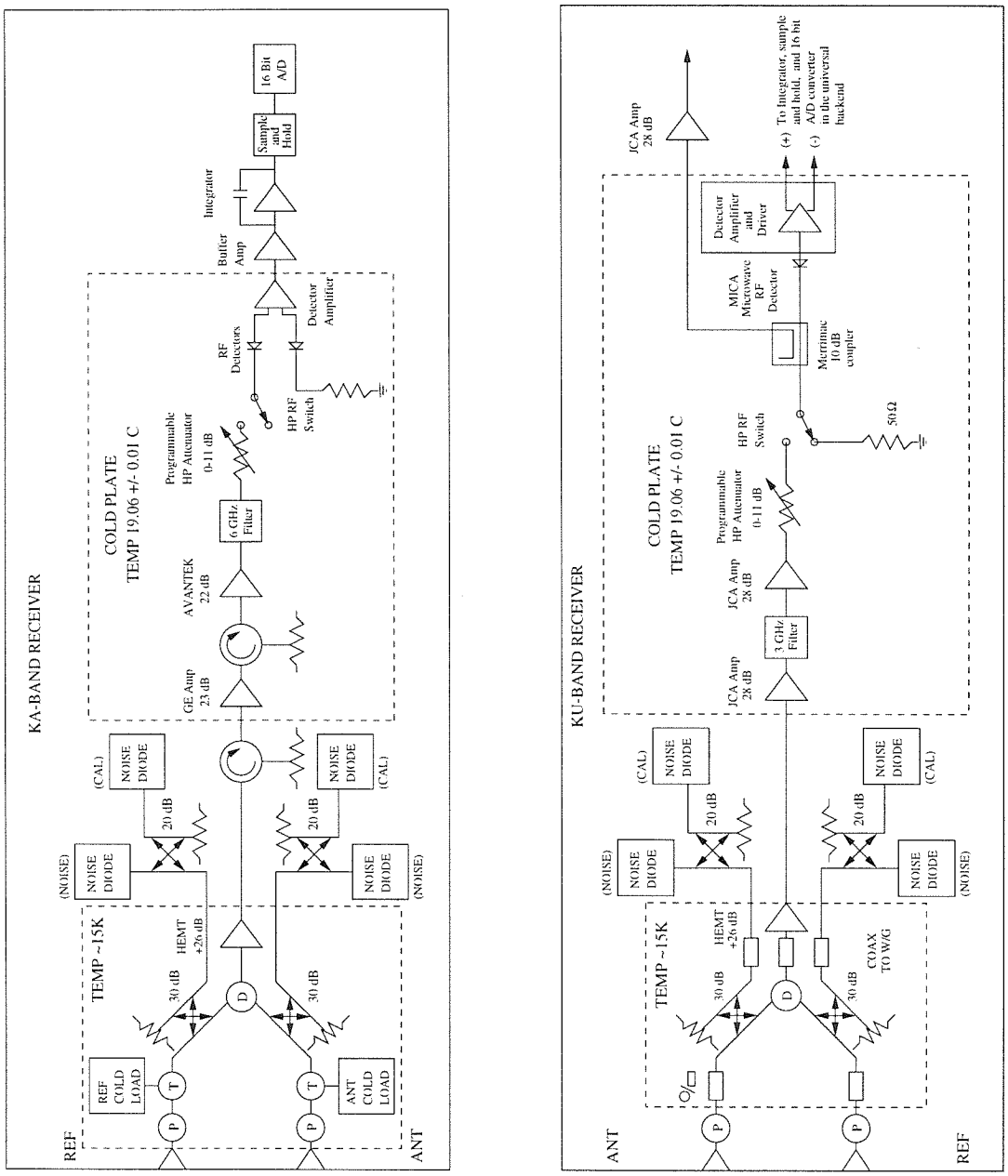

Figure 2.1 Block Diagrams for the Ka and Ku-Band receivers.

Signals from the two arms are brought together in the two input ports of the Dicke switch, a ferrite device identical to the load switches described above. During normal observing, the switch is toggled between the two ports at 500 Hz; the recorded signal is the integrated difference between successive millisecond samples from alternate ports. The entire signal path after the switch (including all signal amplification) is common to both arms, so that the rapid switching eliminates noise from system gain fluctuations on timescales slower than the switching rate.

The first-stage amplifier in both receivers is a High Electron Mobility Transistor (HEMT) (Lai et al. 1994), providing large bandwidths and low noise temperatures ($\sim$ 20 K) across the band. Because of the high gain of these devices ($\sim$ 26 dB), the HEMTs are kept at 15 K. Second and third-stage amplifiers, programmable attenuators and the detector are located outside the dewar, attached to a cold plate whose temperature is actively controlled to ± 0.1 K. The backend resides within the receiver can, and except for a 16-bit A/D converter, is fully digital.

2.4 Terminology and Basic Radiometry

Following is a review of data acquisition procedures and an explanation of terminology used in the remainder of this work. The basic function of any radiometer is to measure the total power presented at the input to the signal path. Typically, this is the input to the front of the feeds when observing the sky; with the Ka-band receiver, the load switches in front of the Dicke switch allow an alternate observing mode where the background signal is input from the internal loads. We refer to these observing modes as SKY and LOAD, respectively; e.g., LOAD CAL will refer to a CAL procedure (defined below) conducted while the load switch was pointed at the internal load. Since we also refer to the small noise diode as the CAL diode, "CAL" will sometimes refer to the procedure, and sometimes to a physical device; the distinction is readily

made from context.

On both receivers used in this experiment, the fundamental 1 millisecond interval during which the power is accumulated before being detected and digitized is hard-wired into the backend. Computer controls allow the user to specify a secondary sampling interval during which the millisecond samples are accumulated; this forms the fundamental interval for which statistics are computed and recorded. For all observations presented here, this was fixed at 1 second. For observations of duration $\Delta t > 1$s, the mean and standard error of the 1s samples are recorded.

It is worth emphasizing this last point. The estimated error reported by the computer control program is not the standard error of the millisecond samples, but that of the 1s secondary integrations which comprise any one measurement. With a 16-bit digitizer, the full detectable power range is $0 - 65,536$ digitizer units (DU), and the attenuation is adjusted to keep the background power $P_0 = P_{sky} + P_{sys}$ near half-scale. With a bandwidth of $\Delta\nu \simeq 6$ GHz (see §2.5), we expect the standard deviation of the millisecond samples to be

$$\Delta P = \frac{P_0}{\sqrt{\tau \Delta\nu}} \simeq 12 \text{ DU}, \tag{2.1}$$

which is well within the detectable power resolution, so that the variance of the 1s means recorded by the computer should be a reasonable approximation to $\sigma^2_{ms}/1000$, where σ^2_{ms} is the variance in the millisecond samples. If the power were integrated for 1 second before digitization, the standard deviation of the samples would be ~ 0.4 DU, or smaller than the digitizer resolution, so that the recorded standard error in the 1s means would be zero.

During normal observing, the Dicke switch is continuously switched at 500 Hz, so that successive millisecond samples are input to the Dicke switch from opposite arms of the receiver, referred to as the ANT and REF sides. The designation is arbitrary (although see §5.2 for a cautionary tale on arbitrariness) and is indicated on the block

diagrams for the Ka-Band and Ku-band receivers.

The essential radiometry procedures are described below. Details of these procedures are also given in Herbig (1994), but are presented here for clarity and completeness.

2.4.1 AVERAGE

A *procedure* is defined as any of a set of standard telescope operations executed as a unit for the acquisition of data. The AVERAGE is the most basic of radiometry procedures, consisting of an integration for n secondary (1s) samples of any combination of the ANT and REF total powers, plus any of 32 system monitor channels, available via a 32-channel multiplexer in the digital backend. For any of these quantities, the mean and variance of the mean are computed as

$$\overline{x} = \frac{1}{n}\sum x_i \tag{2.2}$$

$$V(\overline{x}) = \frac{1}{n(n-1)}\sum (x_i - \overline{x})^2, \tag{2.3}$$

where the sums run over the n 1s samples.

2.4.2 FLUX

The FLUX procedure is the fundamental data unit for normal observations of celestial sources and is the observation upon which this work is based. In each FLUX measurement, the telescope alternates the beams on source by slewing in azimuth an amount $\pm\Delta\phi$ equal to the separation of the feed horns, integrating for equal amounts of time in each of four successive configurations, referred to as the A, B, C and D averages, depicted in Fig. 2.2. This is the basic double switching technique used to eliminate power gradients from the atmosphere or the ground. In subsequent discussion, the fields located at the $\pm\Delta\phi$ positions will be referred to as *reference* fields.

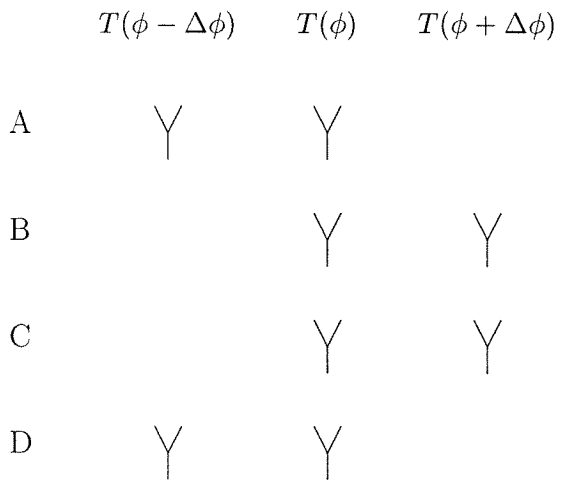

Figure 2.2 Double switching pattern in a FLUX procedure, shown here for an arbitrary temperature field on the sky. The sense of the beams is ANT left, REF right.

To avoid systematic effects associated with varying move times and settling of the telescope structure (particularly on the 40-meter telescope), an adjustable idle parameter can be set by the user, specifying a wait time before the first average, between the A and B averages, and between the C and D averages. Because the telescope does not move between the B and C averages, no time delay is inserted there.

For each set of such measurements, the quantity

$$\text{FLUX} = \frac{1}{2}(B + C - A - D) \tag{2.4}$$

is formed, along with the estimated error

$$\text{SD} = \frac{1}{2}\sqrt{V(A) + V(B) + V(C) + V(D)}, \tag{2.5}$$

where the individual mean and variance for each of the A, B, C and D averages is computed as in the AVERAGE procedure.

From Fig. 2.2, it can be seen that the Dicke switching produces

$$T_{A,D} = T(\phi - \Delta\phi) - T(\phi) \tag{2.6}$$

for the A and D averages, while for the B and C averages, we have

$$T_{B,C} = T(\phi) - T(\phi + \Delta\phi). \tag{2.7}$$

The double-switched FLUX is then given by (2.4)

$$\begin{aligned} F &= \{T(\phi) - T(\phi + \Delta\phi)\} - \{T(\phi - \Delta\phi) - T(\phi)\} && (2.8) \\ &\simeq \Delta\phi \left\{ \left.\frac{\partial T}{\partial \phi}\right|_{\phi + \frac{1}{2}\Delta\phi} - \left.\frac{\partial T}{\partial \phi}\right|_{\phi - \frac{1}{2}\Delta\phi} \right\} && (2.9) \\ &\simeq \Delta\phi^2 \left.\frac{\partial^2 T}{\partial \phi^2}\right|_{\phi}. && (2.10) \end{aligned}$$

If the source under observation is smaller than the main beam of the telescope, so that $T(\phi + \Delta\phi) = T(\phi - \Delta\phi) = 0$, it is clear from (2.8) that the recorded FLUX is just $2\Delta T(\phi)$, or twice the power difference that would be measured with a single difference observation.

2.4.3 CAL

In theory, the internal noise diodes provide stable reference sources for the removal of system gain variations from the data (see §4.2 for a discussion of their actual stability). Since the output of the diodes is injected into the signal path just behind the feeds, the signal from the diodes will contain the same gain fluctuations as the astronomical signal from the front of the feeds, provided the diodes are measured on timescales shorter than a typical gain fluctuation ($t_g \sim 1$ hr).

As with the FLUX procedure, the CAL procedure consists of four segments A, B, C and D, where now the telescope remains stationary between successive averages. The noise diode is turned off during the A and D averages, and on during the B and C averages, with idle times inserted before the first integration and between the on/off averages. The FLUX and standard error are recorded as in the FLUX procedure, but

note that now

$$\text{FLUX} = \frac{1}{2}(B + C - A - D) = T_{diode}, \tag{2.11}$$

instead of twice the power difference which results from the spatial switching performed in the FLUX procedure.

Internal loads on the Ka-Band receiver allow the noise diodes to be measured against a background signal inherently much more stable than the sky, so that accurate monitoring of the system gain can be achieved even during periods of bad weather. While this is typically pointless, as data taken during these periods will be excised in the final analysis, we nevertheless measured the diodes against the internal loads to avoid contamination during marginal weather conditions, as well as contamination due to RF interference entering the feeds.

Since the Ka-Band receiver exhibits non-linearity at the 5% level (see §2.7), some caution must be exercised when comparing LOAD CALs to SKY FLUXes, as these differential measurements are made against different total power levels. Prior to fall of 1995, the total power against the loads and against the sky were measured with separate AVERAGE procedures, reducing observing efficiency and accuracy of non-linearity corrections. To eliminate the unnecessary observing time, from fall of 1995 onward, the average total power $(P_{Ant} + P_{Ref})/2$ during each of the A, B, C and D averages was recorded as part of both the FLUX and CAL procedures. Since the A, B, C and D averages are themselves the average of $(P_{Ant} - P_{Ref})$, these can be combined to reconstruct the total power in either arm during the procedure.

2.4.4 ZERO

The ZERO procedure records the average of the total power from the ANT and REF arms with full RF attenuation inserted, so that no signal reaches the input of the detector. Thus, the ZERO FLUX is a measure of the DC offset introduced by the

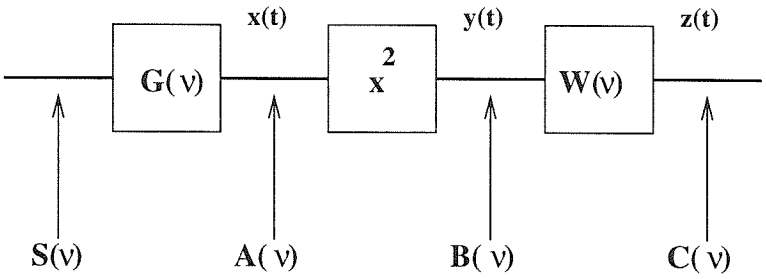

Figure 2.3 A schematic of the receiver signal path. The signal entering the bandpass filter $G(\nu)$ has spectral power density $S(\nu)$. The output signal, $x(t)$, has PSD $A(\nu)$. After the square-law detector, the signal $y(t)$ has PSD $B(\nu)$, and the output of the smoothing filter $W(\nu)$ has PSD $C(\nu)$.

detector and subsequent components. These zero levels are required for accurate non-linearity corrections, as the total power seen by components producing the non-linearity does not include this offset, although the recorded total power does.

2.5 Bandpass

A simplified receiver schematic is shown in Fig. 2.3. The signal at various stages is denoted $x(t)$, $y(t)$, and $z(t)$, with corresponding power spectral densities (PSD) $A(\nu)$, $B(\nu)$ and $C(\nu)$, after Rohlfs and Wilson (1996). The input to the square-law detector for a random noise signal is given by $x(t)$, with corresponding PSD

$$A(\nu) = kT_{sys}G(\nu), \tag{2.12}$$

where $G(\nu)$ is the filter response of the receiver and T_{sys} is the equivalent noise temperature of the radiometer from the front of the feeds to the detector, plus any signal entering the feeds. $B(\nu)$ represents the PSD of the signal $y(t)$, at the output of the square-law detector, and $C(\nu) = W(\nu)B(\nu)$ is the PSD of the signal $z(t)$ at the output of the linear smoothing filter with power transfer function $W(\nu)$.

The minimum detectable signal is the signal whose output increment is just equal

TABLE 2.1
RING5M HEMTS

Rx	HEMT	$\Delta\nu$ (GHz)	ν_{eff} (GHz)	Dates
Ka	TRW	5.76	31.6	18 Jul 93: 93/209 - 30 Mar 94: 94/089
Ka	A12	6.05	31.9	01 Apr 94: 94/091 - 07 Nov 95: 95/311
Ka	A23	6.62	31.5	07 Nov 95: 95/311 -
Ku	U62	3.00	14.5	25 Apr 94: 94/115 -

to the dispersion of z, i.e.,

$$\Delta z = \sigma_z. \tag{2.13}$$

Analysis of the power spectral density of the random noise signal $A(\nu)$ propagated through the signal path indicated in Fig. 2.3 results in (see, e.g., Rohlfs and Wilson (1996))

$$\frac{\Delta T}{T_{sys}} = \sqrt{\left(\frac{\int_{-\infty}^{\infty} W(\nu)d\nu}{W(0)}\right)\left(\frac{\int_{-\infty}^{\infty} |G(\nu)|^2 d\nu}{\left(\int_{-\infty}^{\infty} G(\nu)d\nu\right)^2}\right)}, \tag{2.14}$$

so that if we identify the two terms under the square root as $1/\tau$ and $1/\Delta\nu$, respectively, we obtain

$$\frac{\Delta T}{T_{sys}} = \frac{1}{\sqrt{\tau\Delta\nu}}. \tag{2.15}$$

This defines the equivalent rectangular bandpass $\Delta\nu$ used in computing the minimum detectable signal.

The system bandpass for each of the three Ka-Band HEMTs used in data acquisition for the Ring5m experiment is shown in Fig. 2.4. These were measured by injecting a monochromatic signal through the cross-guide coupler for the ANT noise diodes, so that the measurements represent the total system bandpass from the Dicke switch to the backend. The effective rectangular bandpass is computed by performing the integration indicated in (2.14), and ν_{eff} is computed from

$$\nu_{eff} = \frac{\int \nu G(\nu)d\nu}{\int G(\nu)d\nu}, \tag{2.16}$$

which is the appropriate center frequency for computing telescope efficiencies (see Chapter 3). Since the effective center frequencies for the three HEMTs differ by only 0.6%, we assume a constant value of 31.7 GHz over the period 1993-1996.

In the Ku-Band receiver, a single device (NRAO U62) has been used for all observations taken with the 40-meter telescope. While the Ka-Band bandpass is limited by the 20% bandwidth of the ferrite switches, the Ku-Band bandpass is truncated to 3 GHz by a $13-16$ GHz filter installed to avoid contamination from known local radio interference below 13 GHz. The system bandpass across $13-16$ GHz is extremely flat, so that $\Delta\nu = 3$ GHz and $\nu_{eff} = 14.5$ GHz are excellent approximations to the equivalent rectangular bandpass and center frequency.

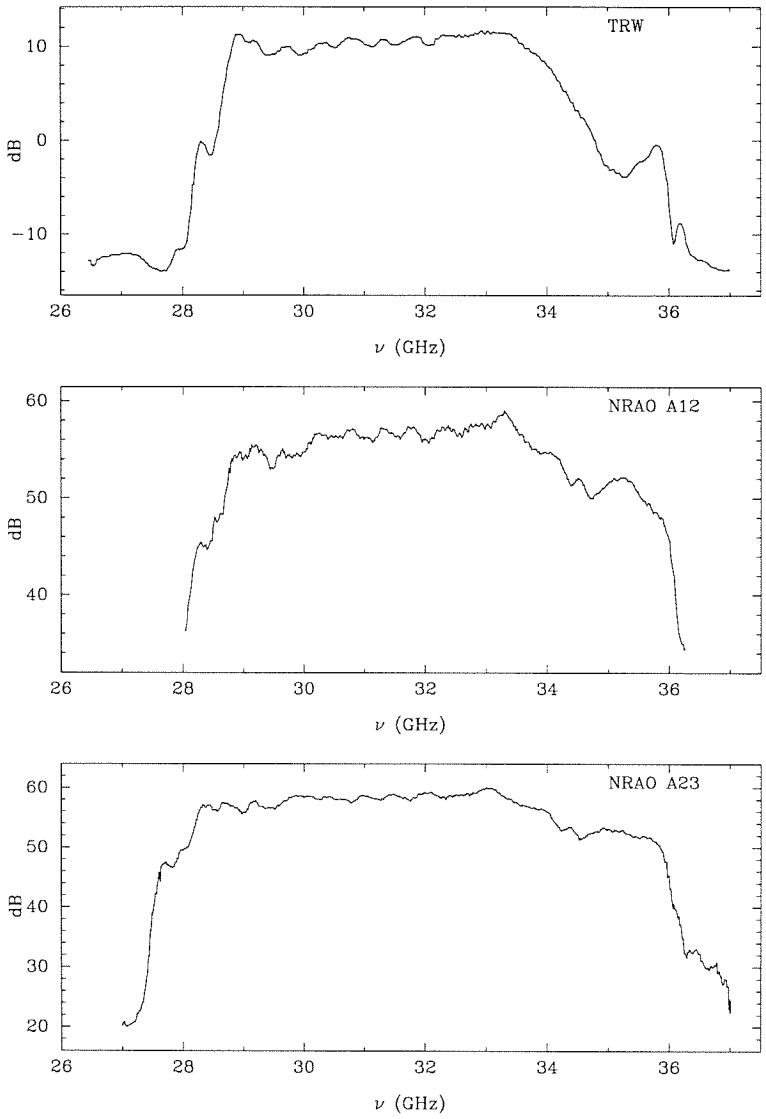

Figure 2.4 Measured system bandpass $G(\nu)$ for TRW, NRAO A12 and NRAO A23 HEMTs, including the effect of all components behind the feed horns.

2.6 Minimum Detectable Signal

For a Dicke-switched receiver, each switched measurement T_S consists of the difference between the temperatures in opposite arms of the receiver:

$$T_S = T_{Ant} - T_{Ref}, \tag{2.17}$$

with associated standard deviation

$$\begin{aligned} \sigma_S &= \sqrt{\sigma_{Ant}^2 + \sigma_{Ref}^2} \\ &\simeq \sqrt{2}\sigma_{Ant}, \end{aligned} \tag{2.18}$$

or

$$\sigma_S = \frac{\sqrt{2}T_{sys}}{\sqrt{\tau_{Ant}\Delta\nu}}, \tag{2.19}$$

from (2.15). Due to the Dicke-switching, during each integration period τ_S, only half the time is spent looking at either arm, $\tau_S = \tau_{Ant} + \tau_{Ref} = 2\tau_{Ant}$, and

$$\sigma_S = \frac{2T_{sys}}{\sqrt{\tau_S\Delta\nu}}. \tag{2.20}$$

In a standard FLUX procedure, each measurement is the difference between pairs of such switched integrations:

$$T_F = \frac{1}{2}(T_B + T_C) - \frac{1}{2}(T_A + T_D), \tag{2.21}$$

and

$$\begin{aligned} \sigma_F &= \frac{1}{2}\sqrt{\sigma_B^2 + \sigma_C^2 + \sigma_A^2 + \sigma_D^2} \\ &\simeq \sigma_A, \end{aligned} \tag{2.22}$$

or

$$\sigma_F = \frac{2T_{sys}}{\sqrt{\tau_A\Delta\nu}}, \tag{2.23}$$

where τ_A is the integration time of *one segment* of the procedure. For typical Ka-Band values $T_{sys} = 53$ K, $\Delta\nu = 6$ GHz, we obtain

$$\Delta T_{rms}^{Ka} = 1.4 \text{ mK s}^{1/2}, \tag{2.24}$$

while for Ku-Band, $T_{sys} = 63$ K, $\Delta\nu = 3$ GHz, and we find

$$\Delta T_{rms}^{Ku} = 2.3 \text{ mK s}^{1/2}. \tag{2.25}$$

These are the expected thermal standard deviations for comparison with FLUX data and are used as rejection criteria in culling data severely contaminated by atmospheric noise (see §5.3.2). Recall, however, that the FLUX procedure effectively measures twice the power increment against a source; these sensitivities therefore correspond to the *rms* in physical temperature when the full integration time for a FLUX procedure, i.e., $4\tau_A$, is used.

2.7 Nonlinearity

At the root of all radiometry is the accurate measurement of small power increments. Ideally, the power output of an amplifier or detector should be a simple linear mapping of the input power, but in practice it is found that both receivers exhibit non-linearity at the level of $5\% - 10\%$, which is to say that the measured power increment against a source in the presence of a typical background of $\sim 30,000$ DU will underestimate the power increment at the front of the feeds by $5\% - 10\%$.

2.7.1 Formalism

Absent any theoretical expectation for the form of the non-linearity, we parameterize the behavior of any device with the functional form

$$P_{out} = (1 + bP_{out})P_{in}, \tag{2.26}$$

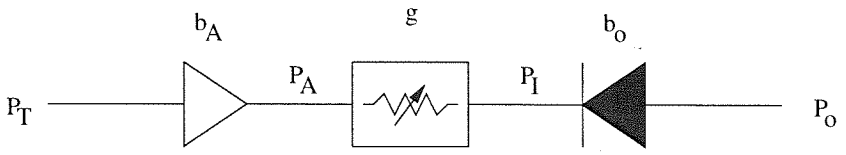

Figure 2.5 Schematic representation of the signal path. P_T is the true input power level to an amplifier, P_A is the power out of the amplifier, g is the gain introduced by the variable attenuator $g \equiv 10^{-A/10}$, where A is the attenuator setting in dB. P_o is the observed power out of the square-law detector for the input power $P_I = gP_A$.

where P_{out} is the observed power at the output of an element when P_{in} is the true input power level. A simplified receiver schematic, consisting of an amplifier, an attenuator, and a detector, is shown in Fig. 2.5. If the functional form (2.26) is assumed for the power out of an element, then

$$P_o = (1 + b_o P_o) P_I \tag{2.27}$$

$$P_I = g P_A \tag{2.28}$$

$$\Rightarrow \quad P_A = \frac{P_o}{g(1 + b_o P_o)}. \tag{2.29}$$

Since

$$P_A = (1 + b_A P_A) P_T, \tag{2.30}$$

we have

$$\begin{aligned} P_o &= (1 + b_o P_o) P_I && (2.31) \\ &= (1 + b_o P_o) g (1 + b_A P_A) P_T \\ &= (1 + b_o P_o) g \left(1 + \frac{b_A P_o}{g(1 + b_o P_o)} \right) P_T \\ &= \{ g(1 + b_o P_o) + b_A P_o \} P_T \\ &= \{ g + (g b_o + b_A) P_o \} P_T \\ &\equiv \{ g + b_{eff} P_o \} P_T \\ &\equiv \{ 1 + b_g P_o \} P'_T && (2.32) \end{aligned}$$

where we have set $P'_T \equiv gP_T$, equivalent to normalizing the model to the observed power in the absence of non-linearity. Note that model (2.32) will hold even if there is more than one amplifier before the attenuator, since for the assumed relation between P_{out} and P_{in}, a chain of amplifiers is equivalent to a single amplifier of gain $\sum g_i$.

Since CAL and FLUX procedures are differential measurements, we are interested in the *differential* nonlinearity, $\lambda(P_o) = dP_o/dP'_T$. For

$$P_o = \eta(P_o)P'_T \tag{2.33}$$

we can form the derivative

$$\begin{aligned} \frac{dP_o}{dP'_T} &= \eta + P'_T\frac{d\eta}{dP'_T} \\ &= \eta + \frac{P_o}{\eta}\frac{d\eta}{dP_o}\frac{dP_o}{dP'_T}, \end{aligned} \tag{2.34}$$

or rearranging,

$$\frac{dP_o}{dP'_T} = \frac{\eta}{1 - \frac{P_o}{\eta}\frac{d\eta}{dP_o}}. \tag{2.35}$$

With $\eta(P_o)$ defined as in (2.32), we have

$$\begin{aligned} \lambda(P_o) &= \frac{(1 + b_g P_o)}{1 - \frac{P_o b_g}{(1+b_g P_o)}} \\ &= (1 + b_g P_o)^2. \end{aligned} \tag{2.36}$$

Thus if C'_T denotes the true power increment from a CAL diode, the observed increment is given by

$$\begin{aligned} C_o &= \lambda(P_o)C'_T \\ &= (1 + b_g P_o)^2 C'_T. \end{aligned} \tag{2.37}$$

Since the internal noise diodes provide a constant power increment C'_T at the input to the signal path, a measurement of $\sqrt{C_o}$ vs. P_o suffices to determine b_g at each attenuator setting. Since from (2.32)

$$b_g = b_o + \frac{b_A}{g}, \tag{2.38}$$

a linear fit to gb_g vs. g can in principal determine b_o and b_A for our model.

2.7.2 Measurements

In practice these measurements are achieved by recording the power increment C_o against the CAL diode (the one used for gain calibration) while varying the total background power P_o by observing the sky over a range in airmass.

The calibration sessions which ultimately determine the physical temperature of the noise diodes by comparison with loads of known temperature (see §4.2) involve much higher power levels than are encountered during normal observing (the typical sky background contributes $\tau T_{atm} \simeq 14$ K to the total power, while the loads are typically $76 - 300$ K), requiring a characterization of the non-linearity over a wide range of attenuator settings.

Observations of the non-linearity of the Ka-Band receiver performed on 23-24 June 93 have previously been described by Herbig (1994), using a different parameterization of the effect. These data were reanalyzed in the context of our model, yielding the fit shown in the top panel of Fig. 2.6.

On 16-17 Oct. 97, the Ka-Band non-linearity was re-measured and was found to have changed by nearly a factor of 2. While the cause for this change has not been identified, we note that the detector biases were adjusted in early October, just prior to the measurements. Nonetheless, during 1996 the CAL diode was measured against both the internal loads and the sky, and these data (taken at 5 dB attenuation) can be used to determine which model is appropriate. By referencing nearby LOAD CALs onto the SKY CALs, for any assumed value of the nonlinearity coefficient b_g we can form the test statistic

$$\chi^2 = \frac{1}{N}\sum_i^N \left\{ \left(\frac{C'_{load}}{C'_{sky}} \right)_i - 1 \right\}^2 . \tag{2.39}$$

Minimization of this statistic shows that the 5 dB data favor a value for b_g close to

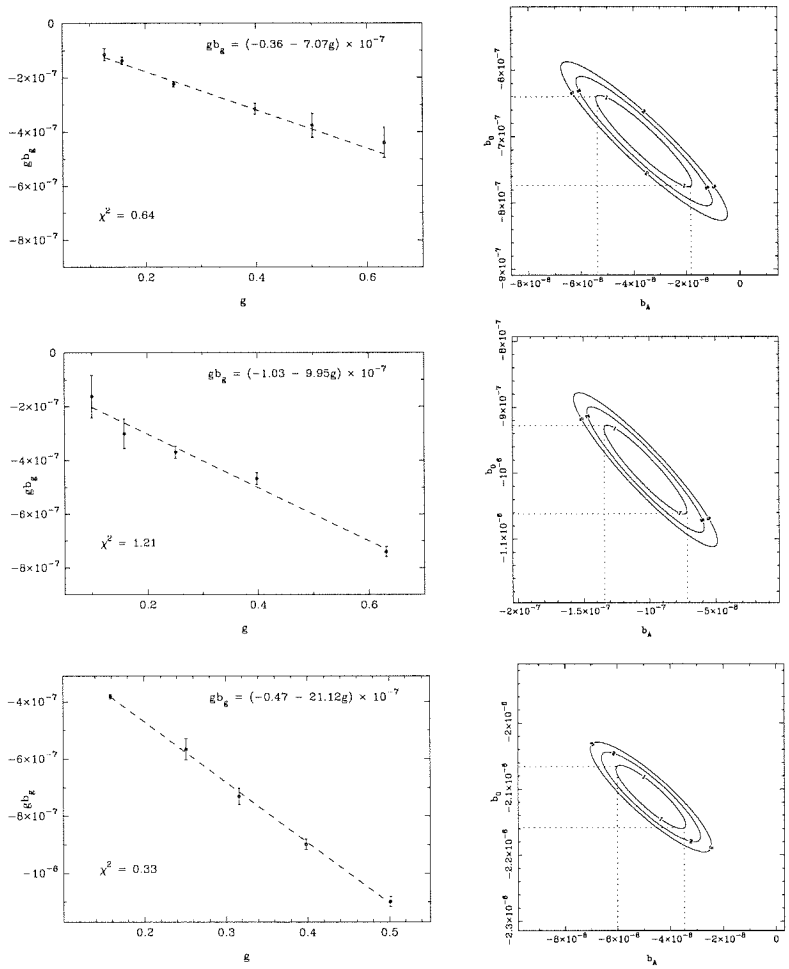

Figure 2.6 (left) Best fit to the Ka-Band nonlinearity parameter vs. gain for 1993 (top) and 1997 (middle). The fit to the Ku-Band nonlinearity is shown at bottom. (right) The corresponding $1, 2$, and 3σ confidence intervals for the fitted parameters b_A and b_0.

TABLE 2.2
NONLINEARITY FITS

Date	Rx	b_A ($\times 10^{-8}$)	b_o ($\times 10^{-7}$)	b_g(A = 5dB) ($\times 10^{-7}$)
23 Jun 93	Ka	-3.61 ± 1.77	-7.07 ± 0.67	-8.21 ± 0.87
16 Oct 97	Ka	-10.3 ± 3.2	-9.95 ± 0.67	-13.21 ± 1.21
16 Oct 97	Ku	-4.74 ± 1.26	-21.1 ± 0.5	-22.6 ± 0.6

-8.68×10^{-7}, well within the errors of the predicted value of $b_g = (-8.21 \pm 0.87) \times 10^{-7}$ for the 1993 model, and this is the model we assume holds for all of the Ring5m data.

Since under the assumptions of our model for the nonlinearity, the observed CAL FLUX is given by

$$C_o = (1 + b_g P_o)^2 C'_T, \tag{2.40}$$

where C'_T is the true CAL power, the quantity

$$\beta = \frac{\sqrt{C'_{load}/C'_{sky}} - 1}{P_{load} - \sqrt{C'_{load}/C'_{sky}} P_{sky}} \tag{2.41}$$

could have been used as an unbiased estimator of b_g at a given attenuator setting. Note, however, that since most of the time, $P_{load} \simeq P_{sky}$, when the data are least capable of discriminating between different models, one would expect the χ^2 minimization to be a more reliable indicator, as these data will contribute negligibly to the sum in (2.39), giving increasing weight to data with wider LOAD-SKY power separations, while β gives equal weight to all the data.

If both CAL and FLUX procedures are measured against the SKY, then both measurements will have the same correction term and need not be corrected if the CALs are measured at roughly the same time as the FLUXes. If CALs are instead measured against the loads and no correction for non-linearity is applied, the measured FLUX/CAL ratios are given by:

$$\frac{F_o}{C_o} = \frac{(1 + b_g P_F)^2}{(1 + b_g P_C)^2} \frac{F_T}{C_T}, \tag{2.42}$$

where P_F and P_C are the powers against which the FLUXes and CALs are measured, respectively. Since for Ka-Band, b_g is at most 10^{-6} and $P \leq 65,536$, $b_g P \leq 0.07$, and we can write

$$\frac{F_o}{C_o} \simeq (1 + 2b_g P_F)(1 - 2b_g P_C)\frac{F_T}{C_T} \tag{2.43}$$

$$\simeq \{1 + 2b_g(P_F - P_C)\}\frac{F_T}{C_T}, \tag{2.44}$$

to first order in $b_g P$. For typical FLUX powers near half scale, this error term will be of order 1%, but can be as large as 6% for $P_C \sim 30,000$ and $P_F \sim 60,000$.

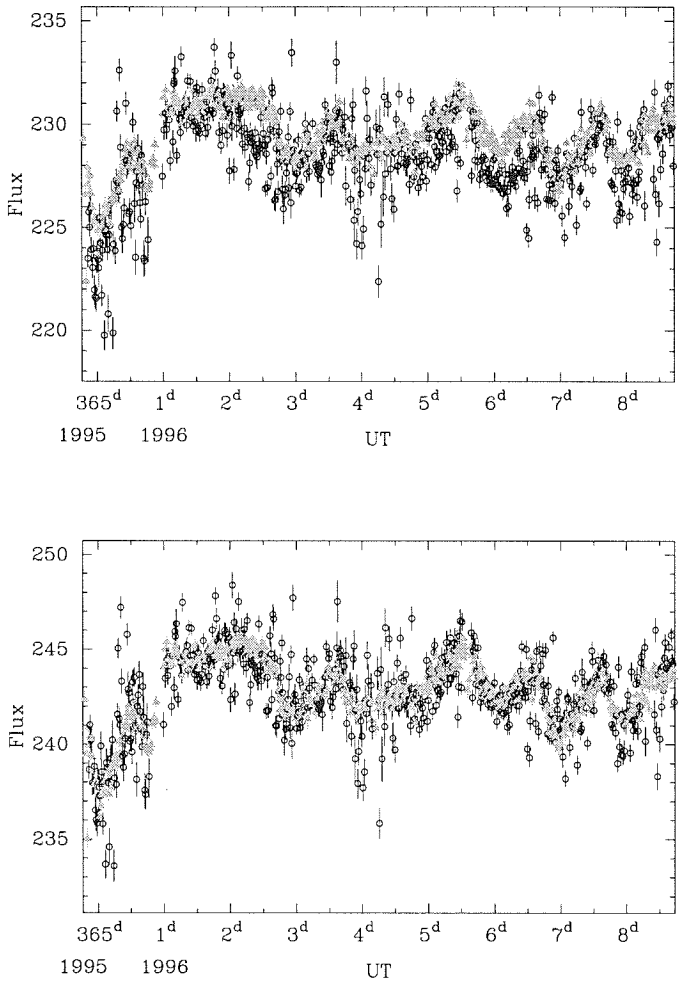

Figure 2.7 Test of the Ka-Band non-linearity correction, from the 1996 CAL flux record. CALs measured against the internal loads (filled triangles) are plotted with CALS measured against the sky (open circles) before applying the non-linearity correction (top panel) and after (bottom panel). The correction results in a ratio of LOAD CALs to SKY CALs of 99.9%, and reduces the scatter in the ratio by 5%.

2.8 Isolation

The Dicke switch is a three-port (2 input, 1 output), wide-band waveguide switch, whose direction is determined by the polarity of the magnetic field within its ferrite core. Isolation in these devices is not perfect, and a small amount of signal from one port is transmitted when the switch is directed at the other port, typically at the level of $1 - 2\%$. The directional isolations of the switch, i.e., the effective isolations with the switch in ANT or REF position, are denoted ξ_A and ξ_R, respectively, and are not in general equal. Directional isolation depends sensitively on the impedance match at the three ports, and changes to the signal chain around the switch can affect not only the level of the directional isolation but also the relative isolations against the two ports. As noted in §1.1, double-switched observations, coupled with the interlocked field geometry, should result in a zero mean for the Ring data. As discussed in §5.4.2, the mean of the Ka-Band Ring data is nevertheless found to change with time; the effect is consistent with changes in the directional isolations of the switch.

The directional isolations can be measured by observing the power increase on the active side of the switch when a sizable signal is input to the opposite port. In practice, this is accomplished by switching the load switches to observe the internal loads (on the Ku-Band receiver, this is effected by physically placing a load in front of the feeds), and measuring the power in either side when the NOISE diode is turned on in the opposite arm of the receiver. (The load switches themselves have imperfect isolation, but this does not significantly affect the measurement, as it contributes only $1 - 2\%$ of any atmospheric fluctuation to the background power.) Table 2.3 summarizes the results of three epochs of isolation measurements on the Ka-band receiver. The first of these entries is discussed in some detail by Herbig (1994). The mean of these measurements gives

$$-10 \log \xi_A = 16.86 \pm 0.33 \text{ dB}, \quad -10 \log \xi_R = 16.65 \pm 0.84 \text{ dB}. \tag{2.45}$$

TABLE 2.3
DICKE SWITCH ISOLATION MEASUREMENTS

Date	Rx	$-10\log\xi_A$	$-10\log\xi_R$
1993	Ka	16.55 ± 0.01 dB	17.71 ± 0.01 dB
94/304	Ka	16.96 ± 0.06 dB	15.82 ± 0.03 dB
95/112	Ka	17.15 ± 0.03 dB	16.63 ± 0.03 dB
94/304	Ku	14.24 ± 0.01 dB	15.35 ± 0.01 dB

When the Dicke switch was first installed in the 15 K stage of the Ku-Band set, it was found that the isolation was unacceptably low, yielding typical values for $-10\log\xi$ of $11-12$ dB. Subsequent testing of the switch revealed that its performance is significantly better at higher temperatures; since the manufacturer does not characterize these devices at cryogenic temperatures, we opted to heat the switch rather than replace it. The switch is mounted on an insulator to provide thermal isolation from the 15 K stage, attached via copper straps to the 70 K stage and resistively heated to 80 K, resulting in an improvement in isolation by a factor of two, as indicated in Table 2.3.

2.8.1 Effect of Isolation on FLUX Measurements

In a FLUX procedure, the telescope makes two sets of Dicke-switched measurements, at each of two positions separated on the sky by the beam throw $\Delta\phi$, as explained in §2.4.2. In the presence of imperfect isolation, Equation (2.6) for the A and D integrations is modified to

$$T_{A,D} = \{T(\phi - \Delta\phi) + \xi_A T(\phi)\} - \{T(\phi) + \xi_R T(\phi - \Delta\phi)\} \tag{2.46}$$

while for the B and C integrations, we have

$$T_{B,C} = \{T(\phi) + \xi_A T(\phi + \Delta\phi)\} - \{T(\phi + \Delta\phi) + \xi_R T(\phi)\}\,. \tag{2.47}$$

The result of a FLUX procedure performed at azimuth ϕ is then given by

$$\begin{aligned} F &= \{T(\phi) - T(\phi + \Delta\phi)\} - \{T(\phi - \Delta\phi) - T(\phi)\} \\ &\quad - (\xi_{\rm A}\{T(\phi) - T(\phi + \Delta\phi)\} - \xi_{\rm R}\{T(\phi - \Delta\phi) - T(\phi)\}) \\ &= \Delta\phi^2 \left.\frac{\partial^2 T}{\partial\phi^2}\right|_{\phi} - \Delta\phi \left\{ \xi_{\rm A} \left.\frac{\partial T}{\partial\phi}\right|_{\phi+\frac{1}{2}\Delta\phi} - \xi_{\rm R} \left.\frac{\partial T}{\partial\phi}\right|_{\phi-\frac{1}{2}\Delta\phi} \right\}. \end{aligned} \tag{2.48}$$

If the directional isolations are perfectly matched, i.e., $\xi_A = \xi_R = \xi$, we recover

$$F \simeq (1 - \xi)\Delta\phi^2 \left.\frac{\partial^2 T}{\partial\phi^2}\right|_{\phi}, \tag{2.49}$$

so that only curvature in the temperature from the atmosphere or ground survives the switching. If the isolations are not matched, however, not even a linear temperature gradient will be completely removed by the switching, contributing

$$\delta F \simeq \Delta\phi \frac{\partial T}{\partial\phi}(\xi_{\rm A} - \xi_{\rm R}), \tag{2.50}$$

which given the measured values of ξ_A and ξ_R, can easily be as large as ~ 0.6 mK for sky gradients as small as 0.1 K.

2.9 Pointing

Pointing on the 5.5-meter and 40-meter telescopes is governed by an analytic model in *az* and *za*. Model coefficients are determined from pointing offsets obtained by rastering across sources widely separated on the sky. In practice, sky coverage is not uniform, as few sources are bright enough at 31.7 GHz for accurate pointing, although the situation is somewhat better at 20 GHz, the frequency at which pointing offsets for the 40-meter telescope were obtained. The fit to these pointing offsets which minimizes the residual *rms* pointing error is referred to as a *pointing solution.*

The telescope pointing model consists of nine azimuthal terms and five zenith angle terms, including left-right and aft-forward tilts. It is found that the addition

of cross terms to allow for possible wobble of the telescopes does not significantly improve the fit.

Pointing solutions were obtained on three separate occasions during 1994-1996 for each telescope. On both telescopes, post-fit residual pointing errors averaged 0.′3 in both the *az* and *za* directions. These errors are taken into account when computing the contribution of point sources to the Ring fields, as errors in the pointing can significantly affect the estimated signal produced by a source in the wings of the power pattern. Incremental corrections to the pointing model can be obtained by pointing on sufficiently bright sources prior to science observations. Thus pointing errors are not important for calibrator source observations (see §3.1), since as a matter of course, these sources are pointed on before every observation. During observations of the Ring fields, however, all incremental pointing offsets are zeroed, so that the position of the telescopes is governed by the default pointing model alone. This protects against spurious pointing offsets occasionally obtained when tracking a calibrator source in bad weather or at low zenith angle.

2.10 Beam

This section describes the determination of the telescope beam pattern appropriate for switched FLUX measurements, for both receivers used in the Ring5m experiment. In general, the power pattern $P_n(\theta, \phi)$ of an antenna is simply the square of the Fourier transform of the aperture, which for a circular dish is the 2D circular analog of the *sinc* function (see Figure 2.8). Of critical importance is the *main beam*, or the beam solid angle between the first nulls of the power pattern, denoted Ω_m, as this determines the conversion of antenna temperature to Rayleigh-Jeans brightness temperature for extended sources (see §4.1). For double-switched FLUX measurements, the appropriate main beam is the average of the main beams for the ANT and REF

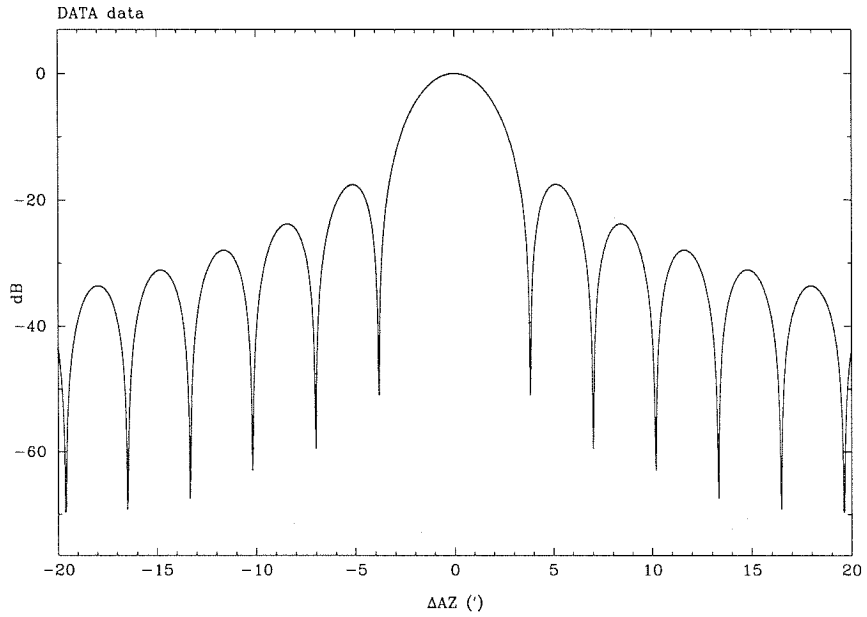

Figure 2.8 Idealized 5.5-meter beam pattern, in one dimension. The main beam solid angle Ω_m is the volume of the beam between the first nulls. First sidelobes are typically down < -20 dB from the peak.

feed horns (see Appendix A). Characterization of the detailed shape of the power pattern is important for computing the antenna temperature produced by discrete sources in the beam. The power pattern integrated over 4π steradians is referred to as the *beam solid angle*, denoted Ω_a. To ensure notational confusion, the main beam of the ANT pattern will be referred to as Ω_A, while the main beam of the average of the ANT and REF patterns will be denoted Ω_M.

2.10.1 Ka-Band Measurements

The beam is mapped on a 23×23 grid at $1\farcm2$ resolution by rastering across Jupiter and 3C 84 in azimuth for each of 23 offset positions in *za*. At the beginning and end of each scan at fixed *za*, the telescope peaks up on source, so that system gain changes can be removed from the data. Originally, the AVERAGE procedure was used (shown in Fig. 2.9), but it was found that this procedure results in significant variation among

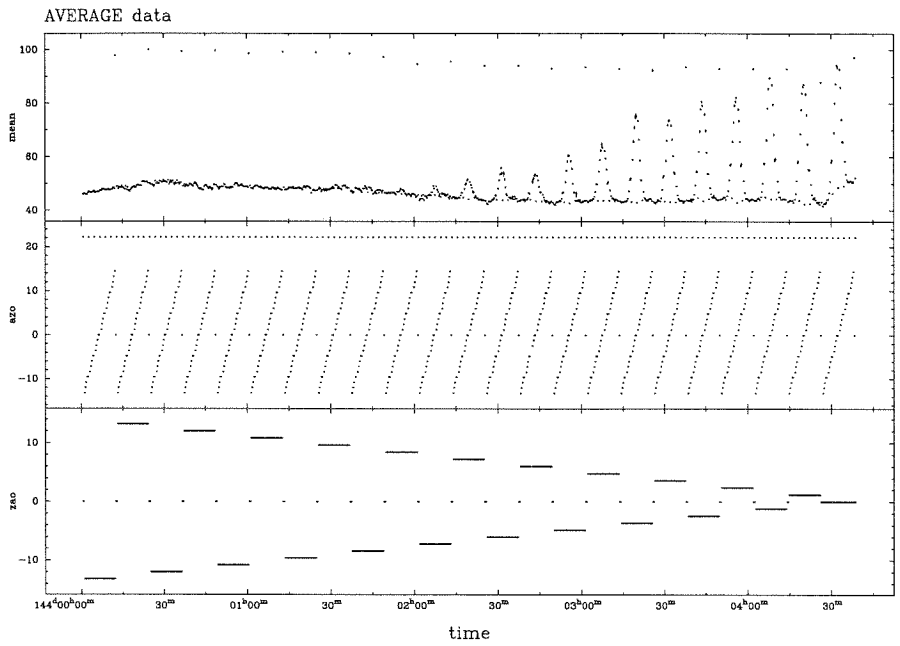

Figure 2.9 Beam map against Jupiter. The upper panel shows the switched power, the center panel the azimuthal offsets from the pointing center, and the lower panel the zenith angle offsets. After every scan, the power at $\Delta\theta = \Delta\phi = 0$ is recorded. In addition, after every few offset power measurements, a measurement is made far off source, by observing at a position offset by $+22'$ in AZ.

independent beam maps. The data presented here were measured using the FLUX procedure, which performs a second difference by switching in azimuth on the sky. An inherently more stable measurement than the AVERAGE (the FLUX procedure differences the average of two on-source and two bracketing off-source measurements), the FLUX procedure has the added advantage of automatically switching out any zero-level offsets due to slightly different gains in the feeds.

A beam map is formed by referencing the peak FLUXes onto the FLUXes at each grid point, and dividing to form the normalized beam $P_n(\theta, \phi)$. In general, due to atmospheric fluctuations on timescales longer than an individual FLUX procedure,

TABLE 2.4
KA-BAND MAIN BEAM MAP χ^2 FIT PARAMETERS

Beam	x_0	y_0	θ_{min}	θ_{maj}	ϕ	χ^2_r
Mean	0.′02	0.′15	$7.'34 \pm 0.'25$	$7.'40 \pm 0.'26$	61.°3	1.18
Ant	0.′06	0.′24	$7.'23 \pm 0.'56$	$7.'35 \pm 0.'61$	$-20.°3$	1.77
Ref	0.′00	0.′14	$7.'36 \pm 0.'50$	$7.'44 \pm 0.'42$	35.°4	2.72

Best fit values for the major axis, minor axis, and rotation angle, defined in the text. Fits were determined for the inner 2σ volume of the beam, using the gridded beam maps and the unweighted error in the mean for each grid cell.

the SD recorded with each FLUX can underestimate the true error by factors of 2-3. To improve the data quality, the 23×23 grid points in *az* and *za* are averaged over several beam maps, fitting to the mean for each grid point. Data for the Ka-Band mean beam were averaged over 7 maps of the inner 2σ region, while the outer portion of the beam was mapped 4 times.

Parameters for the fitted beam are given in Table 2.4. Beam maps are fit to an elliptical Gaussian, given by

$$P_n(x, y) = e^{-4 \ln 2 \Gamma(x,y)}, \tag{2.51}$$

where

$$\Gamma(x, y) = \frac{\{(x - x_0) \sin\phi + (y - y_0) \cos\phi\}^2}{\theta^2_{min}} + \frac{\{(x - x_0) \cos\phi - (y - y_0) \sin\phi\}^2}{\theta^2_{maj}}, \tag{2.52}$$

so that for $\phi = 0$, θ_{maj} and θ_{min} correspond to the *az* and *za* beam widths, respectively.

The main beam solid angle for the mean ANT + REF beam is then given by the integral of the fitting function, which for a Gaussian with $P_n(0, 0) = 1$ is given by

$$\iint_{4\pi} P_n(\theta, \phi) d\Omega = \frac{\pi \theta_{min} \theta_{max}}{4 \ln 2}. \tag{2.53}$$

A more accurate estimate of the beam steradians can be obtained by direct summation of the beam map, i.e., $\Omega_M = \sum_i P_n(\theta_i, \phi_i) \Delta x \Delta y$, which in the case of the Ka-Band

TABLE 2.5
SUMMARY OF KA-BAND BEAMS

	Ω_M ($\times 10^{-6}$sr)	Ω_A ($\times 10^{-6}$sr)	Ω_R ($\times 10^{-6}$sr)
Fit	5.21 ± 0.27	5.09 ± 0.58	5.25 ± 0.46
Sum	5.21 ± 0.03	5.16 ± 0.08	5.28 ± 0.06

mean beam gives

$$\Omega_M = (5.21 \pm 0.03) \times 10^{-6} \text{ sr}, \tag{2.54}$$

in good agreement with the fitted value, as shown in Table 2.5. This is the value for Ω_m used in determining telescope efficiencies in Chapter 4.

By offsetting the telescope in azimuth to bring the REF beam on source, we can obtain a map of the REF beam alone; the B and C segments of a FLUX procedure will now correspond to having the source in the REF beam, while during the A and D segments, the telescope slews to take both beams off-source, reducing the sensitivity by $\sqrt{2}$.

For the REF beam, only 2 maps of comparable quality to the mean beam maps were obtained, and χ^2 is correspondingly larger. This is attributed to underestimation of the data errors, since the mean beam is reasonably well approximated by a Gaussian, and one would expect the mean beam to be less Gaussian than either of its constituent beams. Errors on the fit in Table 2.4 are the $\Delta\chi^2 = 1$ bounds when the data errors are increased so that χ^2_r is approximately 1. The ANT beam fit parameters are derived from the difference map.

2.10.2 Ku-Band Measurements

As noted in §2.2, the Ku-Band beam width is a strong function of displacement along the optical axis of the primary. Moreover, the off-axis configuration causes the beams to move in azimuth as the receiver package is moved along the optical axis to focus

TABLE 2.6
KU-BAND MAIN BEAM MAP χ^2 FIT PARAMETERS

Beam	x_0	y_0	θ_{min}	θ_{maj}	ϕ	χ^2_r
Mean	0.′34	0.′26	$7.'17 \pm 0.'81$	$7.'80 \pm 0.'97$	26.°4	9.15
Ant	0.′32	0.′11	$6.'61 \pm 1.'19$	$7.'86 \pm 1.'27$	56.°1	5.37
Ref	0.′42	0.′39	$7.'20 \pm 1.'37$	$8.'28 \pm 1.'93$	$-2.°3$	6.34

Rough 1σ error estimates are given by the $\Delta\chi^2 = 1$ interval, when the error bars are increased so that $\chi^2_r \simeq 1$.

the telescope at different zenith angles. Because of these complications, and because the Ring5m observations take place at a fixed zenith angle, the Ku-Band receiver has been characterized only over a limited range near $za_{Ring} \simeq 50°$.

In general, there will be a unique set of focus positions vs. za for which the gain of the telescope is a maximum, and the beam width is a minimum. As the focus curve is measured by peaking up on a source at various za, this minimum-beam focus curve is in practice what is measured. To match the beam of the Ka-Band receiver on the 5.5-meter telescope, the receiver is offset by a constant amount from the minimum-beam focus position at all zenith angles, under the assumption that for constant offsets from this minimum-beam focus curve, the beam width is also constant. The minimum-beam focus curve was determined to be

$$f = 31.39 - 0.83\ za + 9.57 \times 10^{-4}\ za^2 \text{ mm}, \tag{2.55}$$

and the beam width was found to be constant to within 0.′3 over the za range $20° - 60°$. The receiver produces a minimum beam of 5.′6 (geometric mean of the az and za widths), with a dependence on focus offset from the minimum-beam focus curve of

$$\overline{\theta} = 7.50 - \cos\Delta f - 0.86\cos^2\Delta f \text{ arcmin}, \tag{2.56}$$

(with Δf in mm interpreted as degrees) so that an offset of $\Delta f = 83$ mm should approximately reproduce the Ka-Band beam width. The receiver was offset by this amount, then fine-tuned to $\Delta f = 85$ mm to give $\overline{\theta} = 7.'35$.

TABLE 2.7
SUMMARY OF KU-BAND BEAMS

	Ω_M ($\times 10^{-6}$sr)	Ω_A ($\times 10^{-6}$sr)	Ω_R ($\times 10^{-6}$sr)
Fit	5.36 ± 0.90	4.98 ± 1.20	5.72 ± 1.72
Sum	5.35 ± 0.02	4.81 ± 0.04	5.92 ± 0.03

The mean beam was mapped over several days in February of 1995 by tracking sources as they passed within $\pm 5^\circ$ of $za = 50^\circ$. By offsetting by the beam throw, the ANT beam was separately mapped, and the REF beam inferred by subtraction of the two maps. The resulting fit parameters are given in Table 2.6. The beams are (not surprisingly) non-Gaussian, as indicated by the large χ^2 of the fits. The data were, however, of good quality, and the beam volumes can be estimated directly from the maps; these are given in Table 2.7.

Post-fit residuals for both beams are plotted in Fig. 2.11. The Ka-Band fit is a reasonable approximation to the real beam, and the largest post-fit residuals are 7%, while the largest post-fit residuals for the Ku-Band beam are 11%. The largest absolute difference between the Ka and Ku-Band beams is 18%, at 1.2 resolution. On angular scales comparable to the beam width, however, the largest difference is only 3%. The fits to the beams will be used in computing the contribution of point sources to the Ring5m data. The effective power pattern for a FLUX procedure is shown in Fig. 2.10 for both the Ka-Band and Ku-Band receivers.

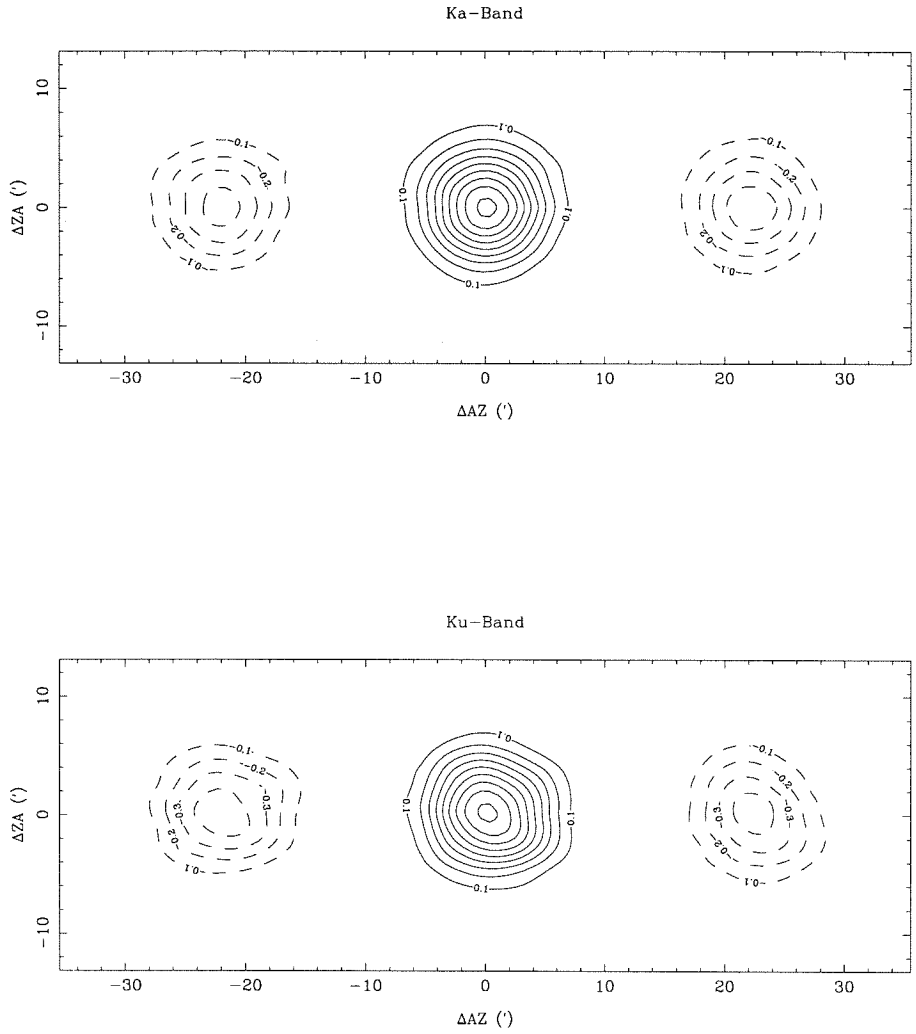

Figure 2.10 Ka and Ku-Band FLUX beam maps, 1995. Contours are from −0.5 to 1.0, in steps of 0.1, where 0.0 has been omitted.

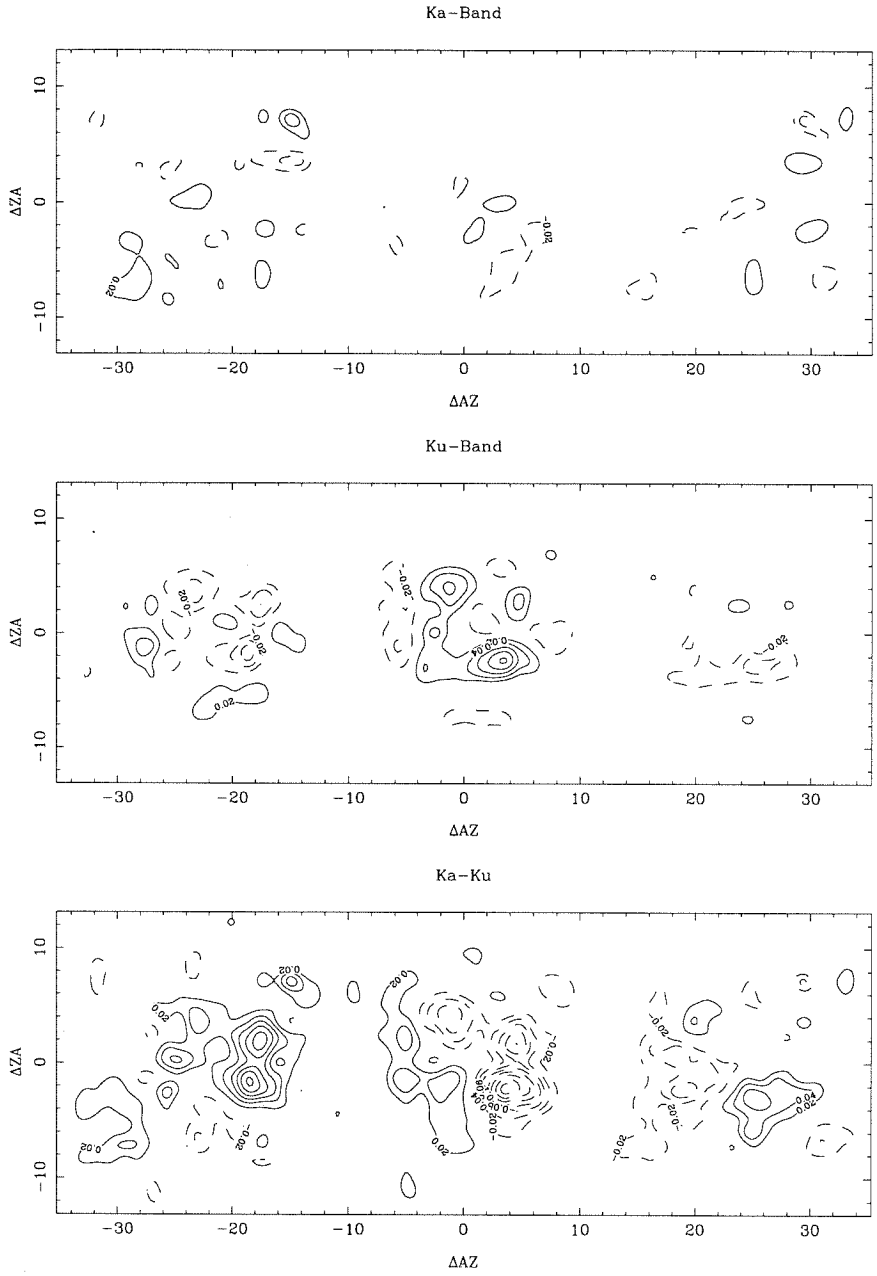

Figure 2.11 Post-fit residuals for Ka-Band (top panel) and Ku-Band (middle) FLUX beam maps, 1995. Axes are in arcminutes. Contours are in steps of 0.02. Shown at bottom is the difference map $P_n(\theta,\phi)_{Ka} - P_n(\theta,\phi)_{Ku}$.

Chapter 3

Absolute Calibration

3.1 Flux Scale

As discussed in the next chapter (§4.2), internal noise diodes are used to convert powers measured in digitizer units to antenna temperature T_A, the temperature defined by equating an observed power to kT_A, the power the telescope would receive in the Rayleigh-Jeans limit if enclosed in a blackbody cavity of physical temperature T_A. For real sources, which subtend only a fraction of the solid angle visible to the telescope, the measured antenna temperature must be converted to a physical brightness temperature, or equivalently, to flux units (Janskys), by comparison with an external reference whose flux density is known *a priori*, generally from a measurement of the received power by a simple telescope whose aperture efficiency (see §4.1) is well approximated by calculation, or whose far field is sufficiently nearby to make characterization of the actual power pattern on an antenna range feasible. Due to the difficulty of such measurements, and the steepness of most radio spectra (most radio sources are synchrotron sources, whose spectra fall with frequency as $S_\nu \propto \nu^{-0.7}$), relatively few absolute flux standards are available at microwave frequencies.

The flux density scale of both telescopes is pinned to an absolute measurement of the equivalent brightness temperature of Jupiter, which is in turn based on a fit to

the spectrum of a bright HII region DR 21 (see below). During 1996, daily calibration of the internal noise diodes on both systems was achieved by referencing to a set of secondary standards whose flux densities were determined relative to Jupiter. These measurements were made in several intensive sessions during which calibrator sources were observed for several days, as well as from daily measurements of the source fluxes. These observations were interleaved with observations of the Ring, so that every twelfth Ring field ($\sim$ every eight hours) was replaced by a 40-minute scan on a calibrator source. To avoid selective depletion of data from any three fields, the set of secondary calibrators was chosen so that at least one would be visible at any time, and the calibrator scans were precessed daily by one field, resulting in a uniform reduction in sensitivity of only 4% over the entire Ring.

3.1.1 Relative Flux Measurements

Of the sources bright enough at 31.7 GHz to use as calibrators for the 5.5-meter telescope (with sensitivity to point sources in antenna temperature given by 4.1×10^{-3} K/Jy), we used 3C 286, the supernova remnants Cas A and Tau A (the Crab) and DR 21. While Cas A and Tau A are large compared to the beam, pointing on these sources has proven reproducible to high precision, making them excellent relative calibrators. Measurements of the source flux densities relative to Jupiter were made during three observing sessions conducted on $08-10$ Jan. 96, $27-29$ Feb. 96 and $07-10$ May 96, during which all of the calibrators were observed. Results of these observations are given in Table 3.2, expressed as ratios to DR 21, while the flux density of DR 21 is given relative to Jupiter's brightness temperature in units of 100 K. These ratios are found to be in excellent agreement with the means of the daily ratios. The resulting absolute flux scale is given in Table 3.3.

Ku-Band measurements were restricted to be within $\pm 5^\circ$ of the zenith angle of the Ring, and a correspondingly larger set of secondary calibrators was used. These

calibrators were measured on 20 – 23 March 96 and 07 – 10 May 96. Results are summarized in Tables 3.4 and 3.5.

3.1.2 DR 21

DR 21 (Downes & Rinehart 1966) is a bright, compact HII region in Cyg X, with a total flux density above 3 GHz of about 20 Jy. The flatness of DR 21's spectrum above 3 GHz, coupled with a compact morphology ($\theta_s < 1'$), make it an ideal source for the calibration of large beam-width radio telescopes.

Dent (1972) has studied DR 21 in considerable detail using the 120-foot Haystack antenna at 7.8 GHz and 15.5 GHz, and the 36-foot antenna at 31.4 GHz. Using measurements of 3C 123 and Cyg A relative to Cas A at 7.8 GHz, 3C 274 and 3C 218 relative to Cas A at 15.5 GHz, and absolute measurements of Jupiter and Saturn at 31.4 GHz, he determines a fit to the spectrum of DR 21 between 7.8 GHz and 31.4 GHz to be

$$S_\nu = 26.78 - 5.63 \log \nu_{\rm GHz}, \tag{3.1}$$

with an associated error of $\pm 3\%$. Ideally, the absolute flux scale for both telescopes would be based on DR 21 directly; unfortunately, the location of DR 21 in a complicated region of the Galactic plane severely limits its use for a dual-feed system with a wide beam throw. Maps of the DR 21 region suggest that the compact components of the source may be superimposed on a weak, extended source as broad as $\sim 1^\circ$, so that the large beam size of the OVRO telescopes relative to the $\sim 1'$ resolution of the 36-foot telescope will complicate comparisons with Dent's derived flux. Dent has demonstrated that for offset positions $< 18'$ from the core of DR 21, the background is sufficiently linear to contribute less than 1% to the measured brightness temperature. Given the large beam and beam throw ($\sim 22'$) of the OVRO telescopes, however, the flux of DR 21 is significantly contaminated by background emission in the reference

fields (see Figure 3.1).

Based on Dent's fit to DR 21's spectrum and measurements at 31.4 GHz of the ratio of Jupiter's flux density to DR 21, the equivalent brightness temperature of Jupiter is determined to be

$$T_J = 152 \pm 5 \text{ K}, \tag{3.2}$$

and this is the measurement on which the Ring5m absolute scale at 31.7 GHz is based. Although Dent's fit to the spectrum of DR 21 is itself based on absolute measurements of Cas A, Jupiter and Saturn at three different frequencies, we feel that this bootstrapped spectrum is less likely than any single-point measurement to be corrupted by systematic errors. Moreover, Dent's value for Jupiter is consistent with the two absolute measures at the same frequency reported in the compilation by Berge & Gulkis (1976).

Since the reference fields are displaced azimuthally by 22′, as DR 21 is tracked on the sky, emission in the ring of radius 22′ around the source rotates through the reference beams; although DR 21 cannot be used as an absolute calibrator, the resultant variation of DR 21's flux is quite reproducible and can be removed, making DR 21 suitable as a relative calibrator. The *parallactic angle*, ψ, defined as the angle between the direction of the North Celestial Pole and the zenith, is convenient for specifying the location of the reference fields relative to the source — for a given ψ, the reference fields will be $\pm 90°$ away. For sources which transit north of the observing latitude, the parallactic angle changes discontinuously at transit from $+180°$ to $-180°$, and it is convenient to use the *principal parallactic angle*, ψ_p, defined as the parallactic angle folded into the range $(-90°, +90°)$. A 5-parameter polynomial fit to $S_{DR\ 21}(\psi_p)$ which gives the smallest residual slope in ψ_p was derived from 34 tracks of DR 21 taken over the course of 1995 (see Table 3.1). In this compilation, each scan was normalized to the flux averaged over $\psi_p = (-80°, -70°)$. Although the actual peak occurs near $\psi_p = -65°$, the range $-80°$ to $-70°$ was used since all of the scans contained data in

TABLE 3.1
FIT TO $S_{DR\ 21}(\psi_p)$

a_1	9.19×10^{-1}
a_2	-1.92×10^{-3}
a_3	3.71×10^{-6}
a_4	2.36×10^{-7}
a_5	2.32×10^{-10}

this range. The fit was then normalized to the peak flux (since DR 21 is used only as a relative calibrator, the normalization can be arbitrary; nevertheless, contamination of the reference fields can only *decrease* the measured flux, and the peak will most nearly approximate the true flux of DR 21).

It was found that the fit derived at 31.7 GHz successfully removed the parallactic angle dependence of the 14.5 GHz DR 21 flux as well, indicating that the contaminating flux in the reference beam has very nearly the same spectral index between 31.7 and 14.5 GHz as does DR 21. This is not surprising, given that all the flux in the region of Cyg X surrounding DR 21 is thought to be part of a large HII complex. Although the observed flux density of DR 21 is not expected to be representative of the true flux density at either frequency, that the frequency dependence of the contaminating flux is separable from the parallactic angle dependence implies that the observed flux *ratio* at the two frequencies is, and this fact can be exploited to determine the Ku-Band flux density scale relative to the same measurement (3.2) of Jupiter at 31.4 GHz. Any uncertainty in the flux scale will thus translate into a single scaling of the measured temperatures at both frequencies. As can be seen in Table 3.3, the flux scale so derived is in excellent agreement with the flux scale based on the absolute measurement of Jupiter's brightness temperature at 14.5 GHz by Gary (1974). Therefore this scale, with the 3% errors reported by Gary, is the one used to calibrate the 14.5 GHz data.

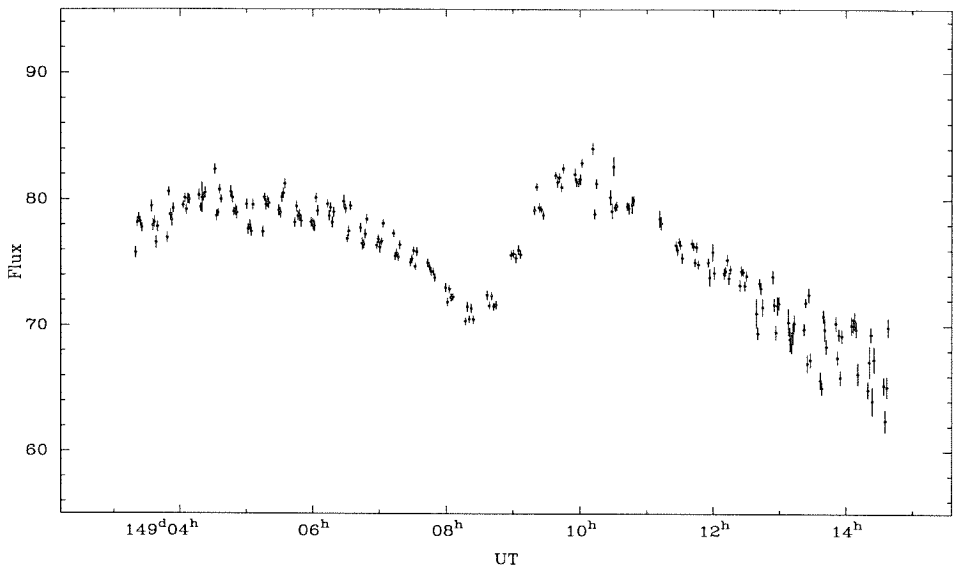

Figure 3.1 A typical uncalibrated scan on DR 21. The measured flux (shown here in digitizer units) is dominated by contamination in the reference fields and is a strong function of parallactic angle.

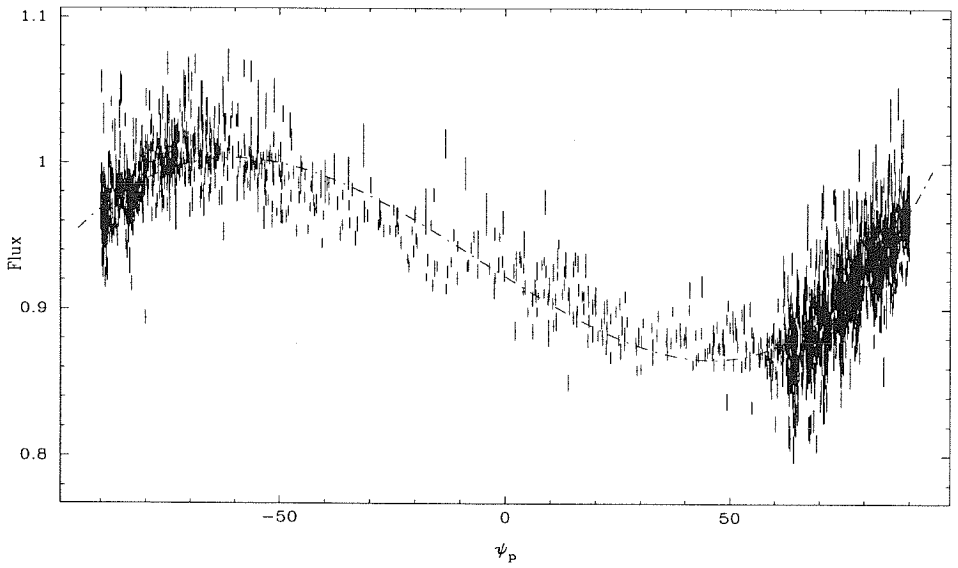

Figure 3.2 Dependence of the switched flux on parallactic angle, shown here in a compilation of 34 individual tracks of DR 21 from 1995. Each scan was separately calibrated and normalized to the flux over the ψ_p interval $(-80°, -70°)$. Shown also is the best fit model for the ψ_p dependence.

3.1.3 Cas A

Recently, the Saskatoon experiment has reported a measurement of intrinsic anisotropy on degree scales, referenced to an estimate of the flux density of Cas A of 186.5 ± 25 Jy at 32 GHz from fits to Cas A's spectrum (Netterfield et al. 1997). The power they detect on degree scales, in excess of some favorite cosmologies, has lead to speculation that their assumed flux for Cas A may be too high; moreover, the 14% uncertainty in their fit to the flux density of Cas A is a significant source of error. Since Cas A is used as a calibrator source in the Ring5m experiment, the OVRO observations of Cas A not only provide a corroborative check on the Saskatoon calibration, but can in principal reference their measurements to a flux scale based on Jupiter, thereby reducing their calibration uncertainties to a few percent. Since Cas A is comparable in size to the 5.5-meter beam, however, our measurement cannot be compared directly with the Saskatoon value. In an observation of Cas A, the flux density measured on the 5.5-meter telescope is given by

$$S_{ovro} = \iint_{\Omega_m} I(\theta,\phi) P_{ovro}(\theta,\phi) d\Omega, \tag{3.3}$$

where $P_{ovro}(\theta,\phi)$ is the normalized antenna power pattern $P_n(\theta,\phi)$ discussed in §2.10. In an experiment with $\Omega_m \gg \Omega_{Cas}$, such as Saskatoon, the measured flux density is

$$S_{sask} = \iint_{\Omega_m} I(\theta,\phi) P_{sask}(\theta,\phi) d\Omega \simeq \iint_{\Omega_m} I(\theta,\phi) P_{sask}(0,0) d\Omega = \iint_{\Omega_{Cas}} I(\theta,\phi) d\Omega \tag{3.4}$$

since most of the flux of the source will be concentrated near the peak of the antenna response pattern $P_{sask}(0,0) = 1$. Thus to compare these two measurements, S_{ovro} must be multiplied by the factor

$$f = \frac{\iint_{\Omega_{Cas}} I(\theta,\phi) d\Omega}{\iint_{\Omega_m} I(\theta,\phi) P_{ovro}(\theta,\phi) d\Omega} = \frac{\iint_{\Omega_{Cas}} P_{Cas}(\theta,\phi) d\Omega}{\iint_{\Omega_{Cas}} P_{Cas}(\theta,\phi) P_{ovro}(\theta,\phi) d\Omega}, \tag{3.5}$$

where $P_{Cas}(\theta,\phi)$ is the source structure function.

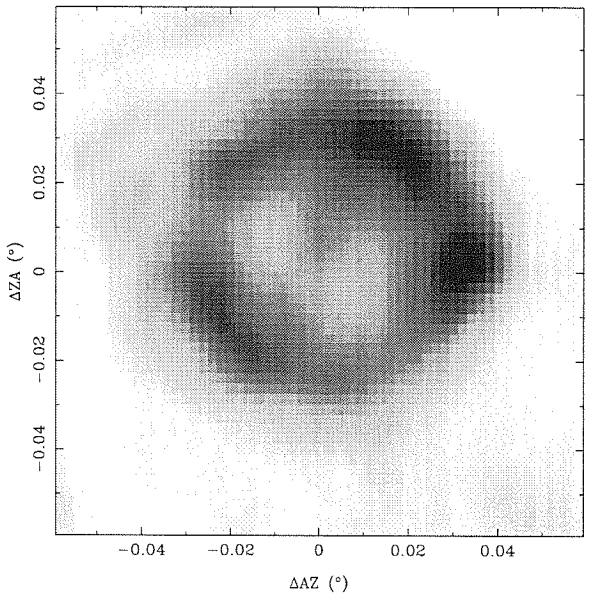

Figure 3.3 Map of Cas A at 32 GHz, from the Effelsberg 100-meter telescope

To avoid complications with spectral index variation across the face of Cas A, we obtained a 32 GHz map of Cas A made with the Effelsberg telescope (Morsi 1997) (see Figure 3.3), which we use as a template for $P_{Cas}(\theta, \phi)$ in determining the correction factor from (3.5). Uncertainties in the 5.5-meter pointing, as well as in the determination of the 5.5-meter beam will affect the correction factor; this effect is modeled via Monte Carlo simulation. Gaussian-distributed pointing positions were generated for 10^5 events, with $\sigma_{az} = \sigma_{za} = 0\farcm3$ centered on the nominal pointing position; beam widths were drawn from Gaussian distributions centered on the best-fit θ_{min} and θ_{maj}. The 1σ confidence interval of the resulting distribution is given by

$$f = 1.18^{+0.02}_{-0.01}. \tag{3.6}$$

With $S_{ovro} = 164.18 \pm 5.45$ Jy, application of the derived correction factor yields

$$S_{sask} = 193.73^{+7.22}_{-6.64} \text{ Jy}, \tag{3.7}$$

or

$$1.04 \pm 0.04 \tag{3.8}$$

relative to Saskatoon's fitted value of 186.5 Jy.

The flux density of Cas A is known to decrease with time as a function of frequency (Baars et al. 1977) according to

$$\delta S/S = 0.0097(\pm 0.0004) - 0.0030(\pm 0.0004) \log \nu_{\mathrm{GHz}}\ \mathrm{yr}^{-1}, \tag{3.9}$$

so that the factor by which Cas A has dimmed after t years is given by $(1 - \frac{\delta S}{S})^t$. The OVRO measurement of the flux density of Cas A adjusted to 1994 is therefore

$$S_{ovro} = (1.05 \pm 0.04) S_{sask} \tag{3.10}$$

or marginally consistent with the Saskatoon calibration.

TABLE 3.2
RELATIVE FLUX SCALE (31.7 GHz)

Name	S/S_{DR21}	S/T_{Jup} (Jy/100 K)
DR 21	1	13.55 ± 0.04
Cas A	7.97 ± 0.03	—
Tau A	14.91 ± 0.017	—
3C 286	0.0980 ± 0.0006	—

TABLE 3.3
ABSOLUTE FLUX SCALE (31.7 GHz)

Name	S (Jy) or T (K)
Jupiter	$\mathbf{152 \pm 5}$ K
DR 21	$20.60 \pm 0.68^{\dagger}$
Cas A	$164.18 \pm 5.45^{\dagger}$
Tau A	$307.15 \pm 10.14^{\dagger}$
3C 286	2.02 ± 0.07

† Not an accurate measure of absolute flux

TABLE 3.4
RELATIVE FLUX SCALE (14.5 GHz)

Name	S/S_{DR21}	S/T_{Jup} (Jy/100 K)
3C 84	1.13 ± 0.01	—
3C 123	0.256 ± 0.002	—
3C 218	0.2053 ± 0.0008	—
3C 286	0.166 ± 0.003	—
3C 353	0.369 ± 0.002	—
Cas A	13.69 ± 0.06	—
Tau A	18.67 ± 0.09	—
DR 21	1	13.09 ± 0.11
NGC 7027	0.271 ± 0.002	—

TABLE 3.5
ABSOLUTE FLUX SCALE (14.5 GHz)

Name	S (Jy) or T (K)[1]	S (Jy) or T (K)[2]	S (Jy) or T (K)[3]
Jupiter	**175 ± 5** K	155 ± 5 K	175 ± 10 K
DR 21	22.91 ± 0.64	**20.23 ± 0.61**	**22.87 ± 1.28**
3C 84	25.88 ± 0.76	22.66 ± 0.79	25.84 ± 1.46
3C 123	5.86 ± 0.17	5.18 ± 0.16	5.85 ± 0.33
3C 218	4.70 ± 0.13	4.15 ± 0.13	4.69 ± 0.26
3C 286	3.81 ± 0.13	3.36 ± 0.12	3.80 ± 0.22
3C 353	8.45 ± 0.24	7.46 ± 0.23	8.44 ± 0.47
Cas A	313.6 ± 8.9	276.95 ± 8.43	313.04 ± 17.54
Tau A	427.7 ± 12.1	377.7 ± 11.5	426.9 ± 23.9
NGC 7027	6.21 ± 0.18	5.48 ± 0.17	6.20 ± 0.35

[1]Flux Scale based on $T_J(14.5\text{ GHz}) = 175 \pm 5$ K
[2]Flux Scale based on $S_{DR21}(14.5\text{ GHz}) = 20.23 \pm 0.61$ K.
[3]Flux Scale based on $T_J(31.4\text{ GHz}) = 152 \pm 5$ K, assuming Dent's value for $S_{DR21}(31.4\text{ GHz})/S_{DR21}(14.5\text{ GHz})$.

Chapter 4

Telescope Calibration

4.1 Conversion to Physical Units

Most "radio" astronomy is done at wavelengths where $h\nu \ll kT$, so that for generic blackbody sources, the emitted power is most naturally expressed in temperature units. The signal from a celestial source can be expressed as the temperature of a blackbody filling the beam solid angle which produces the same power; since data are generally calibrated by comparison with blackbody loads filling the beam solid angle (i.e., the noise diodes), this *antenna temperature*, denoted T_A, is the unit used when comparing data taken on the same telescope (see §4.1.2). Because beam solid angle is a telescope-dependent quantity, however, antenna temperature is not a useful convention when comparing data from different telescopes, and we prefer a physical unit which reflects only information about the astronomical source. One possibility is to use the equivalent brightness temperature of a blackbody filling the *main* beam solid angle to convert to physical units; ultimately, this is what will be used for signals from the CMBR. In general, though, the equivalent brightness temperature is an arbitrary designation with little or no physical meaning except in the case of pure blackbody radiation; even for blackbody radiation, (4.17) must be corrected for deviations from

perfect Rayleigh-Jeans behavior (see §4.1.3), so that any statements about brightness temperature involve an implicit assumption about the source spectrum. Since the observed signals are typically a superposition of microwave background, thermal bremsstrahlung and synchrotron sources, in what follows, results at Ka-Band and Ku-Band will in general be compared in *intensity* (Jy/sr), which is independent of any such assumptions, and depends only on the assumption that the source fills the main beam. Calibration of the Ring5m data in each of these units is briefly reviewed below.

4.1.1 Intensity Calibration

When a plane wave is incident on an antenna, the ratio of the power density intercepted to the power density in the wave defines an effective cross-section for the antenna, which we call the *effective aperture* A_e. In general, the effective aperture is parameterized by the *aperture efficiency*, $\eta_a \equiv A_e/A_p$, which is the ratio of the effective aperture to the physical aperture.

The power received from a source of intensity $I(\nu, \theta, \phi)$ is then given by

$$P = \frac{1}{2} \int A_e(\nu) d\nu \iint I(\nu, \theta, \phi) P_n(\theta, \phi) d\Omega, \tag{4.1}$$

where $P_n(\theta, \phi)$ is the normalized power pattern of the telescope, defined in §2.10. This is the fundamental relation from which all our subsequent analysis derives. If $I(\nu, \theta, \phi)$ is the intensity of a source uniformly filling the main beam Ω_m of the telescope power pattern, so that $I(\nu, \theta, \phi) = I(\nu)$, and if we furthermore take the bandwidth to be sufficiently small that $I(\nu)$ can be considered uniform over the bandpass of the receiver, i.e., $I(\nu) \simeq I$, we can write

$$P = \frac{1}{2} I A_p \eta_a \Omega_m \Delta\nu \tag{4.2}$$

for the total power received. The measured power in digitizer units (DU) is converted

to physical units by referencing to the power from a calibrator source of known intensity I_{cal}. Since the radiation from a noise diode internal to the receiver fills the beam pattern Ω_a of the telescope, the detected power is given by

$$P_{cal} = \frac{1}{2} I_{cal} A_p \eta_a \Omega_a \Delta\nu, \tag{4.3}$$

and

$$\frac{P}{P_{cal}} = \frac{I\Omega_m}{I_{cal}\Omega_a} \equiv \frac{I\Omega_m}{S_{cal}}, \tag{4.4}$$

so that the intensity for a source filling the beam is given simply by

$$I = \left(\frac{P}{P_{cal}}\right) \frac{S_{cal}}{\Omega_m}. \tag{4.5}$$

Atmospheric attenuation reduces the observed intensity of a source by a factor

$$\kappa(za) = e^{-\tau A(za)} \tag{4.6}$$

where τ is the atmospheric optical depth, and $A(za) \simeq \sec za$ is the *airmass*. Furthermore, deformation of the telescope dish makes the gain of the telescope a function of zenith angle, so that the observed intensity from a source of intrinsic intensity I_0 is given by

$$I(za) = I_0\, g(za)\kappa(za) \tag{4.7}$$

To recover the intensity of a source above the atmosphere, then, we must compute

$$I_0 = I(za)\frac{1}{g(za)\kappa(za)} = \left(\frac{P}{P_{cal}}\right)\left(\frac{S_{cal}}{\Omega_m}\right)\frac{1}{g(za)\kappa(za)}. \tag{4.8}$$

This is the appropriate form of the calibration when the CAL flux density is measured directly against external sources. Often, however, the antenna temperature T_{cal} is measured instead. Since the calibration diode is internal to the receiver, it can be thought of as a blackbody filling the power pattern Ω_a of the telescope, and its equivalent flux in the Rayleigh-Jeans regime is given by

$$S_{cal} = \frac{2kT_{cal}}{\lambda^2}\Omega_a, \tag{4.9}$$

so that I_0 can also be written as

$$I_0 = \left(\frac{P}{P_{cal}}\right)\left(\frac{2kT_{cal}}{\lambda^2}\frac{\Omega_a}{\Omega_m}\right)\frac{1}{g(za)\kappa(za)}. \tag{4.10}$$

When the data are calibrated according to (4.10), a separate measurement of Ω_a is required from (4.9), and uncertainties in the temperature scale of the noise diodes will enter into the final calibration twice, along with the uncertainty in the absolute flux scale. If calibrator sources are observed on a regular basis, this intermediate step can be eliminated, so that calibration uncertainties are limited by uncertainties in the absolute flux scale alone.

For the Ring data from 1994-1995, only sporadic measurements of calibrator sources were obtained, and the diode temperatures (4.10) are used to achieve calibration. For the 1996 data, however, the daily record of secondary calibration standards referenced to Jupiter provides a direct record of S_{cal}. In practice, then, calibration requires a determination of T_{cal}, S_{cal}, Ω_a and τ, and these are discussed in turn in §4.2 - §4.4.

4.1.2 Antenna Temperature

Radio astronomers like to express the observed power in units of *antenna temperature*, which is the temperature of an incoherent noise source filling the telescope power pattern which produces the equivalent power per Hertz:

$$kT_A = P/\Delta\nu. \tag{4.11}$$

When the observed power is from a blackbody of brightness temperature T_B filling the beam solid angle, we see from (4.1) that in the Rayleigh-Jeans limit, the antenna temperature is equal to the physical brightness temperature, since

$$\Omega_a = \frac{\lambda^2}{A_p\eta_a} \tag{4.12}$$

(Kraus 1986, p. 6-2). When the data are calibrated against the noise diode temperatures, the equivalent antenna temperature is given from (4.10) by

$$T_A = \left(\frac{P}{P_{cal}}\right)(T_{cal})\,\frac{1}{g(za)\kappa(za)}. \tag{4.13}$$

When the diode flux densities are measured instead, (4.9) gives

$$T_A = \left(\frac{P}{P_{cal}}\right)\left(\frac{\lambda^2}{2k\Omega_a}S_{cal}\right)\frac{1}{g(za)\kappa(za)}. \tag{4.14}$$

4.1.3 Brightness Temperature

When a generic source fills the main beam of the telescope, the *equivalent brightness temperature* is defined by

$$S_0 = \frac{2kT_B}{\lambda^2}\Omega_m. \tag{4.15}$$

Since the antenna temperature is the blackbody temperature of a source filling the beam solid angle, the equivalent brightness temperature is given by

$$T_B = T_A\frac{\Omega_a}{\Omega_m}, \tag{4.16}$$

so that defining the *beam efficiency* to be $\eta_b \equiv \Omega_m/\Omega_a$, we have

$$T_B = \frac{T_A}{\eta_b}. \tag{4.17}$$

Throughout the foregoing discussion, it was implicitly assumed that at 31.7 GHz, the low-frequency Rayleigh-Jeans formula (4.15) is an adequate approximation to the Planck law. Including the receiver bandpass $G(\nu)$, the power per Hz from any real blackbody filling Ω_a is given by

$$\frac{P_r}{\Delta\nu} = \frac{1}{2}\int G_n(\nu)B(\nu)A_p\eta_a\Omega_a d\nu \tag{4.18}$$

$$= \frac{1}{2}\int G_n(\nu)B(\nu)\frac{c^2}{\nu^2}d\nu, \tag{4.19}$$

from (4.12), where $G_n(\nu) \equiv G(\nu)/\int_{-\infty}^{+\infty} G(\nu)d\nu$. Substituting the Planck law for $B(\nu)$, we obtain

$$\frac{P_r}{\Delta\nu} = \int G_n(\nu)\frac{h\nu}{e^{h\nu/kT}-1}d\nu, \tag{4.20}$$

from which it is clear that $G_n(\nu)$ is just an additional weighting function for photons of energy $h\nu$. If we equate (4.20) to kT_A, we obtain

$$T_A = T\int G_n(\nu)\frac{h\nu/kT}{e^{h\nu/kT}-1}d\nu \tag{4.21}$$

$$\equiv T\{1-\delta(T)\}. \tag{4.22}$$

The result is essentially independent of the bandpass, and depends only on the appropriateness of the R-J approximation, which even for a load temperature of 76 K, gives $\delta(T) < 0.01$.

When measuring signals from the microwave background, however, the R-J approximation at 31.7 GHz underestimates the true brightness temperature by 25%. When we consider the *incremental* change in antenna temperature with an incremental change in brightness temperature, (4.21) gives

$$\frac{\partial T_A}{\partial T} = \int G_n(\nu)\frac{x^2e^x}{(e^x-1)^2}d\nu, \tag{4.23}$$

where $x \equiv h\nu/kT$. For $T = 2.73$ K, $\partial T_A/\partial T = 0.974$, and we must correct brightness temperatures measured according to (4.17) by $\partial T_A/\partial T^{-1} = 1.027$.

4.2 Calibration Diodes

Gain fluctuations from temperature-dependent components in the receiver are removed by dividing the FLUX record for a source by the CAL record over the same time period. To convert FLUX measurements to antenna temperature, these ratios must be multiplied by the CAL diode temperatures as indicated in (4.13). The physical temperature of the noise diodes is determined by comparison with external

loads of known absolute temperature. The brightness temperatures of the loads are assumed to be equal to the measured physical temperatures, an assumption whose validity depends on the reflective properties of the loads, as well as the validity of the R-J approximation for typical load temperatures (which we just determined was quite good). In practice, two loads of different temperatures are placed in front of the feeds. Against a hot external load of temperature T_H, the measured antenna temperature on the ANT side is (see Figure 4.1)

$$\begin{aligned} T_A &= T_{AH} + \xi_{AL} T_{AL} + T_{WG} + (1+\xi_A) T_H + \xi_A \xi_{RL} T_{RL} + \xi_A T_{RH} \qquad (4.24) \\ &\simeq (T_{AH} + \xi_{AL} T_{AL} + T_{WG}) + (1+\xi_A) T_H \\ &\equiv T_{Rx,A} + (1+\xi_A) T_H, \qquad (4.25) \end{aligned}$$

defining the *receiver temperature*, T_{Rx}. Here, $T_{\{A,R\}H}$ is the contribution to the system noise temperature from the feed horns, $T_{\{A,R\}L}$ the contribution from the internal loads and T_{WG} the summed contribution from all waveguide components. The isolation of the load switches and Dicke switch are given by $\xi_{\{A,R\}L}$ and $\xi_{A,R}$, respectively. Against a cold load, the temperature is given by

$$T_A = T_{Rx,A} + (1+\xi_A) T_C. \qquad (4.26)$$

Letting

$$y \equiv \frac{T_{Rx,A} + (1+\xi_A) T_H}{T_{Rx,A} + (1+\xi_A) T_C}, \qquad (4.27)$$

we have

$$T_{Rx,A} = (1+\xi_A) \frac{T_H - y T_C}{y - 1}. \qquad (4.28)$$

In normal observing mode, the Dicke switch spends half of the time in each switch position, so that the dynamic receiver temperature is given by the average of $T_{Rx,A}$ and $T_{Rx,R}$. Since the measured receiver temperature is used only for checks on the system performance and enters into the data analysis as a rejection criterion only

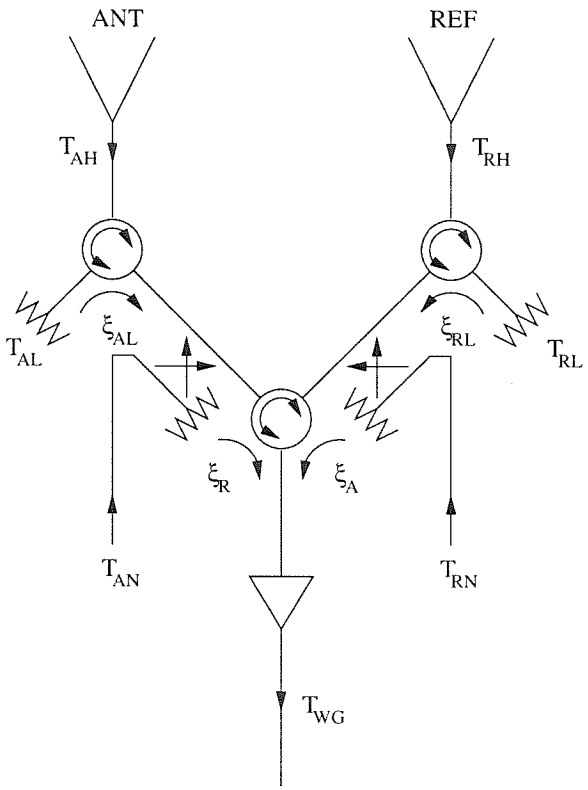

Figure 4.1 A schematic of the Ka-Band front end. T_{AH} and T_{RH} represent the contribution to the system temperature of the ANT and REF feed horns, respectively. Similarly, T_{AL} and T_{AN} are the temperature contributions of the internal load and NOISE diode on the ANT side. T_{WG} is the summed noise temperature of all waveguide components after the switch. The isolation of the Dicke switch when pointed at the ANT side is indicated by ξ_A and when pointed to the REF side, by ξ_R.

(see next chapter), $T_{Rx,R}$ is not in general measured, and only $T_{Rx,A}$ is recorded in Tables 4.1 and 4.2.

Similarly, turning the CAL diode on against an external load of temperature T_L, we measure

$$T_A^{on} = T_{Rx,A} + (1+\xi_A)T_L + T_{cal} \tag{4.29}$$

$$T_A^{off} = T_{Rx,A} + (1+\xi_A)T_L \tag{4.30}$$

from which

$$y_c \equiv \frac{T_A^{on} - T_A^{off}}{T_A^{off}} = \frac{T_{cal}}{T_{Rx,A} + (1+\xi_A)T_L}, \tag{4.31}$$

so that

$$T_{cal} = y_c \{T_{Rx,A} + (1 + \xi_A)T_L\}, \tag{4.32}$$

once $T_{Rx,A}$ is known. Since the CAL diode is injected into the signal path with 50 dB of attenuation, its signal is quite weak, and only the NOISE diode is measured directly against the loads, as in (4.32). The temperature of the CAL diode is determined by measuring its FLUX relative to the FLUX of the NOISE diode, since the switched power measured in a FLUX procedure is a much more stable method of measuring small power increments than differencing direct measures of the total power.

4.2.1 Switched CALs

When the CAL diode is measured in switched mode during normal observing, the effective temperature of the CAL in the ANT side is

$$T_{cal}^{sw} = T_{cal}(1 - \xi_R), \tag{4.33}$$

since the CAL diode is seen in the REF side as $\xi_R T_{cal}$. Because the directional isolations ξ_A and ξ_R are not identical, this introduces a slight error in the measured temperature of a signal on the sky observed in double-sided switching mode, as the normalized FLUX is given by

$$T_s^{sw} = T_s \frac{1}{2}\{(1 - \xi_R) + (1 - \xi_A)\}. \tag{4.34}$$

For $-10 \log \xi_R = 17.7$ dB and $-10 \log \xi_A = 16.55$ dB, this asymmetry results in a 0.2% error in the ratio of FLUXes to CALs measured in total power mode.

4.2.2 Error in the CAL Diode Measurement

When the NOISE diode is measured against the loads, errors in the non-linearity correction propagate into the measurement of the diode's physical temperature. The

diode temperature is proportional to the ratio of the power increment when the diode is on to the total power with it off, call it α:

$$\alpha = \frac{P_{on} - P_{off}}{P_{off}}. \tag{4.35}$$

(The error in the temperature of the load + receiver which multiplies this ratio is quite small, and we treat it as effectively zero in the following analysis.) Since any observed power P_o is converted to a true power via $P = P_o/(1 + bP_o)$ (see §2.7), the error in P is

$$\frac{\sigma_P}{P} = P\sigma_b, \tag{4.36}$$

and the error in α is given by

$$\frac{\sigma_\alpha^2}{\alpha^2} = \frac{\sigma_{P_{on}}^2}{P_{on}^2} + \frac{\sigma_{P_{off}}^2}{P_{off}^2} = (P_{on}^2 + P_{off}^2)\sigma_b^2. \tag{4.37}$$

For typical Ka-Band values of $b = -8 \times 10^{-7}$, $\sigma_b/b \sim 11\%$, $P_{on} \simeq 45,000$ and $P_{off} \simeq 30,000$, the error introduced in the NOISE diode temperature is $\sigma_\alpha/\alpha \simeq 0.5\%$.

When the ratio of the CAL diode to the NOISE diode is measured, we have again

$$\alpha = \frac{F_C}{P_{on} - P_{off}}, \tag{4.38}$$

where F_C is the differential power measured in a CAL procedure. For differential measurements, $F = F_o/(1 + bP_o)^2$, so that

$$\frac{\sigma_F}{F} = 2P_o\sigma_b, \tag{4.39}$$

and we have

$$\frac{\sigma_\alpha^2}{\alpha^2} = (4P_o^2 + P_{on}^2 + P_{off}^2)\sigma_b^2 \tag{4.40}$$

$$\simeq (5P_{off}^2 + P_{on}^2)\sigma_b^2, \tag{4.41}$$

or, with the values given above, $\sigma_\alpha/\alpha \simeq 0.7\%$. The total error introduced in the temperature of the CAL diode will then be the quadrature sum of these contributions, or about 1%. For the Ku-Band receiver, the error in b is only 3%, but $P_{on} \sim 50,000$, so that the error introduced is roughly the same as for the Ka-Band receiver.

4.2.3 Loads

Ideally, the loads used in the calibration procedure described in §4.2 should be perfect blackbodies of known absolute physical temperature. The hot load consists of Eccosorb AN72 foam (Emerson & Cuming 1979) at ambient temperature ($T_H \sim 300$ K), while for the cold load, a piece of Eccosorb CV-3 immersed in liquid nitrogen (LN_2) provides a blackbody at a widely separated temperature ($T_C = 76.3$ K at the OVRO). These absorbers are varieties of lightweight plastic epoxy foam, with varying amounts of magnetic loading to match the refractive index of air at a range of frequencies; at 31.7 GHz, the reflectivity of Eccosorb AN72 is better than -22 dB (Emerson & Cuming 1979), while the reflectivity of Eccosorb CV-3 is better than -40 dB for frequencies > 9 GHz (Emerson & Cuming 1982).

Cone loads were used during the first year of the Ring5m experiment, despite the discourse on the horrors of these primitive devices by Herbig (1994). These loads consist of copper-backed cones of Eccosorb, which are immersed in LN_2, then held manually in front of the feeds. During measurements against the cold loads, the power levels can clearly be seen to rise as the LN_2 boils off, on typical timescales of ~ 20 seconds. By early 1995, driven by concerns over apparent changes in the noise diode temperatures, we resurrected the remains of a significantly more stable cold load described by Herbig (1994). A thick piece of pyramidal absorber is immersed in a bath of LN_2 contained in a translucent polyethylene foam box capable of providing stable load temperatures for up to an hour. The foam box is in turn contained in a plywood box which can be hung off the end of the receiver package, eliminating any stray radiation introduced by a cone load held with an unsteady hand. A hole cut in the side of the plywood box allows the Ka-Band receiver to make direct contact with the foam wall, in which an anti-reflection hole pattern has been drilled to approximate the refractive index of air. (No measurable difference in power has ever been detected between this "matched" side of the cold load and the solid foam side, an indication

that reflection at the boundary layer is not a significant concern.) The opposite side of the box was machined to match the end of the Ku-Band receiver can, and this refurbished cold load has been used to calibrate both receivers since 1995.

Prior to fall of 1995, the hot load consisted simply of a flat disk of Eccosorb, backed by an aluminum plate to prevent transmission of radiation through the foam. The temperature of the load was determined by averaging readings from a thermocouple device around the perimeter of the load. These measurements often varied by several degrees across the plate, raising concerns about ambient heating of the load, as well as the accuracy to which temperature readings from the metal backing of the load reflected the temperature of the Eccosorb foam. In the fall of 1995, during tests of a new HEMT in the Ka-Band set, it was discovered that the combination of gross absorber geometry (i.e., pyramidal vs. flat absorber) and orientation of the hot load (i.e., simply rotating the disk) could cause the the measured receiver temperature to vary by as much as 10 K, orientation alone accounting for as much as 5 K. Moreover, significant hysteresis in the power levels was detected between measurements of the cold and hot loads, i.e., if the hot load was placed in front of the feeds immediately after removing the cold load, the power levels would continue to rise for up to a minute. In short, we found that in the absence of ideal loads, consistency in the application of the loads plays as important a role in the reproducibility of the telescope calibrations as does the load design itself.

The hot load was consequently redesigned, using flat Eccosorb AN72, the type found consistently to yield the lowest measured receiver temperature, and thus most likely to represent the true receiver temperature, since reflections will generally increase the measured T_{Rx}. To suppress ambient heating of the hot load, a thick piece of insulating styrofoam was fixed to the back surface of the aluminum plate. In addition, three temperature-sensitive AD590 ICs were embedded beneath the styrofoam backing; the average of these temperature readings is input directly to the computer

via a coax port on the hot load, and is found to vary by less than 0.3% over periods of 20 minutes. The orientation of the hot load which consistently gave the lowest receiver temperature was noted, and the load has been attached in this orientation since fall of 1995. Moreover, the cold and hot loads are consistently alternated in the same order, with sufficient time between them to allow any temperature hysteresis to settle.

4.2.4 Ka-Band Measurements

Since fall of 1995, system calibrations were conducted at least every two weeks, in the manner described in §4.2. For the period spanning 30 Jan 96 - 22 May 96, during which 13 system calibrations were performed, the receiver temperature was found to be

$$T_{Rx} = 32.59 \pm 1.65 \text{ K}, \tag{4.42}$$

where 1.65 is the standard deviation of the measurements. Likewise, the temperature of the NOISE diode from 9 measurements between which no receiver changes were made was

$$T_{noise} = 32.55 \pm 0.29 \text{ K}. \tag{4.43}$$

The CAL diode remained stable over 13 measurements to within 1% at

$$T_{cal} = 0.370 \pm 0.004 \text{ K}. \tag{4.44}$$

All quoted errors are standard deviations, demonstrating that apart from gross failure of the noise diodes, which is always obvious, any fluctuations in the physical temperature of the diodes are quite small. This is consistent with variations in the CAL diode seen against calibrator sources during the long calibration sessions from winter of 1996, which showed only a 1% diurnal variation of the CAL flux. For periods during which calibration was performed only sporadically, the larger scatter of

TABLE 4.1
KA-BAND RECEIVER MEASUREMENTS

Date			$T_{Rx,A}$ (K)	$T_{noise,A}$ (K)	$T_{cal,A}$ (K)
19 Apr 93	93/109	(49461)	33.00 ± 1.60		0.557 ± 0.020
19 Apr 93	93/109	(49461)	54.80 ± 1.70		0.628 ± 0.020
31 Oct 94	94/304	(49656)	57.19 ± 1.09	29.37 ± 0.30	0.641 ± 0.007
25 Apr 95	95/115	(49832)	56.89 ± 2.17	27.84 ± 0.74	0.587 ± 0.016
26 Apr 95	95/116	(49833)	60.19 ± 3.56	28.77 ± 1.37	0.606 ± 0.027
27 Sep 95	95/270	(49987)	54.01 ± 1.30	27.17 ± 0.47	
03 Oct 95	95/276	(49993)	52.48 ± 3.14	27.12 ± 1.13	
13 Nov 95	95/317	(50034)	34.33 ± 1.28	15.39 ± 0.17	$0.373 \pm 0.004^{\ddagger}$
04 Dec 95	95/338	(50055)	32.54 ± 0.40	15.13 ± 0.05	$0.364 \pm 0.001^{\ddagger}$
29 Dec 95	95/363	(50080)	31.45 ± 0.56	15.07 ± 0.06	0.369 ± 0.002
11 Jan 96	96/011	(50093)	33.08 ± 0.83	15.28 ± 0.12	0.374 ± 0.003
30 Jan 96	96/030	(50112)	32.44 ± 0.18	32.73 ± 0.05	0.374 ± 0.001
12 Feb 96	96/043	(50125)	37.21 ± 0.27	33.08 ± 0.07	0.376 ± 0.001
26 Feb 96	96/057	(50139)	32.57 ± 0.73	32.23 ± 0.21	0.367 ± 0.002
11 Mar 96	96/071	(50153)	31.78 ± 0.25	32.20 ± 0.08	0.367 ± 0.001
26 Mar 96	96/087	(50169)	31.01 ± 0.27	32.24 ± 0.08	0.366 ± 0.001
09 Apr 96	96/100	(50182)	32.15 ± 0.61	32.58 ± 0.20	0.370 ± 0.002
22 Apr 96	96/112	(50195)	31.53 ± 0.36	32.58 ± 0.11	0.370 ± 0.001
06 May 96	96/127	(50209)	31.11 ± 0.14	32.61 ± 0.04	0.371 ± 0.001
22 May 96	96/143	(50225)	32.52 ± 0.13	32.70 ± 0.03	0.371 ± 0.001

‡ Corrected for the variation of T_{noise} with zenith angle.

3% in temperatures measured prior to fall 1995, in quadrature sum with propagated errors from the non-linearity corrections, are the appropriate uncertainties on T_{cal}.

In November of 1995, it was discovered that the NOISE diode power correlated with zenith angle. This problem was eventually tracked to two variable attenuators in front of the NOISE diodes. These had been disconnected electrically, but had been left in the set to provide a fixed attenuation. Apparently due to mechanical motion of components in the attenuators, the NOISE diode fluxes were reproducibly reduced in flux as the telescope tracked to smaller zenith angles, by an amount

$$F(za)/F(90) = 0.913 + 5.72 \times 10^{-4} za + 4.33 \times 10^{-6} za^2 \tag{4.45}$$

where $F(90)$ is the measured flux at $za = 90°$. As a result, measurements of T_{cal} made

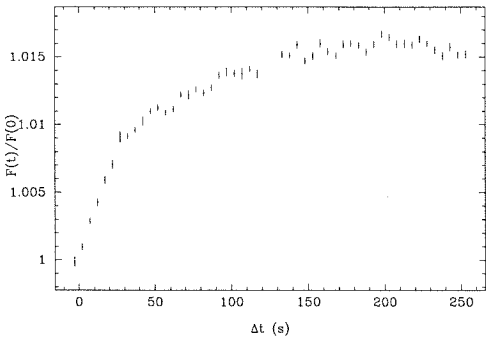

Figure 4.2 The NOISE diode flux on the 5.5-m, as a function of time from turn-on.

during this period will be accurate only if the CAL diode is compared to the NOISE diode at $za = 90°$, where the physical temperature of the NOISE diode is measured. Two measurements of T_{cal} in Table (4.1) have been corrected for this effect.

Turn-on Values

It was also noted that the power output of the Ka-Band noise diodes was a function of how long the diodes remained on. This was investigated on 25 April 95, by taking averages of the total power against the internal loads while the NOISE diode remained on. The power output of the diode was seen to stabilize after approximately 200 s, with a peak flux variation of 1.5%. To minimize the scatter in successive measurements of the CAL diode flux, therefore, we require a time interval between CALs which is longer than the hysteresis in the diode, so that each integration begins at approximately the same point on the rise curve. It was found by comparing CALs taken at successively shorter intervals that the integrated flux for CAL procedures separated by as little as 1 minute differed by $< 0.1\%$, which for the CAL diode, is smaller than the typical standard deviation of an individual measurement. During the Ring5m observations, measurements of the CAL diode were therefore interspersed with measurements of the NOISE diode to keep $\Delta t > 1$ minute.

TABLE 4.2
KU-BAND RECEIVER MEASUREMENTS

Date			T_{rx} (K)	$T_{antnoise}$ (K)	T_{antcal} (K)
25 Apr 94	94/115	(49467)	68.94 ± 4.79	46.03 ± 2.47	0.936 ± 0.050
01 Dec 94	94/334	(49686)	52.63 ± 1.28	48.93 ± 0.84	0.962 ± 0.017
13 Nov 95	95/317	(50034)	54.62 ± 0.31	50.42 ± 0.12	0.988 ± 0.002
04 Dec 95	95/338	(50055)	54.15 ± 0.17	49.59 ± 0.05	0.966 ± 0.002
11 Jan 96	96/011	(50093)	54.68 ± 0.68	50.22 ± 0.26	0.980 ± 0.005
30 Jan 96	96/030	(50112)	52.66 ± 0.14	50.13 ± 0.05	0.962 ± 0.002
12 Feb 96	96/043	(50125)	53.84 ± 0.16	50.25 ± 0.04	0.958 ± 0.001
26 Feb 96	96/057	(50139)	51.44 ± 0.18	49.61 ± 0.07	$0.713 \pm 0.001^{\dagger}$
11 Mar 96	96/071	(50153)	53.18 ± 0.16	49.83 ± 0.05	$0.969 \pm 0.001^{\ddagger}$
26 Mar 96	96/086	(50168)	52.90 ± 0.29	49.97 ± 0.09	0.976 ± 0.002
09 Apr 96	96/100	(50182)	53.48 ± 0.21	50.05 ± 0.06	0.996 ± 0.001
22 Apr 96	96/113	(50195)	52.98 ± 0.08	50.18 ± 0.04	0.997 ± 0.001
02 May 96	96/123	(50205)	53.96 ± 0.11	77.34 ± 0.06	$1.065 \pm 0.001^{\dagger\dagger}$
16 May 96	96/137	(50219)	53.53 ± 0.06	76.76 ± 0.06	1.062 ± 0.001

†The ANT CAL diode was swapped with the REF CAL diode on 14 Feb 96.
‡The ANT CAL diode was swapped back in on 26 Feb 96.
††Replaced semi-rigid coax at the back of the dewar on 22 Apr 96.

4.2.5 Ku-Band Measurements

For the period spanning 13 Nov. 95 - 16 May 96, during which 12 system calibrations were performed, the receiver temperature was found to vary by less than 2%;

$$T_{Rx} = 53.39 \pm 0.90 \text{ K}. \tag{4.46}$$

Likewise, the temperature of the NOISE diode over 10 measurements was

$$T_{noise} = 50.03 \pm 0.28 \text{ K}, \tag{4.47}$$

or non-variable to better than a percent. The CAL diode remained stable to within less than 2% at

$$T_{cal} = 0.975 \pm 0.014 \text{ K}. \tag{4.48}$$

All quoted errors are standard deviations.

The CAL diode was known to be bi-stable, the origin of the 2% variation in the measured CAL diode temperature. This was eventually traced to the A/D converter; whenever the input total power exceeded 32,930 DU, the output power was seen to drop by 10 DU. As described in §2.4.3, CAL procedures measure the difference between powers with the diode on and off; thus, if the off power level was just below this threshold, turning on the diode would bring the power above this threshold, resulting in a 10 DU drop in the measured diode flux, or about 2-3%. Further inspection with a signal generator over the full 16-bit power range revealed similar glitches near the 1/2, 1/4 and 1/8 power points, indicating a problem with the ladder structure of the A/D converter. Fortunately, few of the Ring FLUXes were directly affected, as these power levels were typically reached only when the noise diode was on. Data which were affected have been excised from the analysis. Although the system calibrations are typically performed at higher than average power levels, so that the CAL diode is unlikely to have crossed this power threshold during the calibration, the 2% uncertainty in the diode temperature scale will be included in the Ring5m calibration uncertainty.

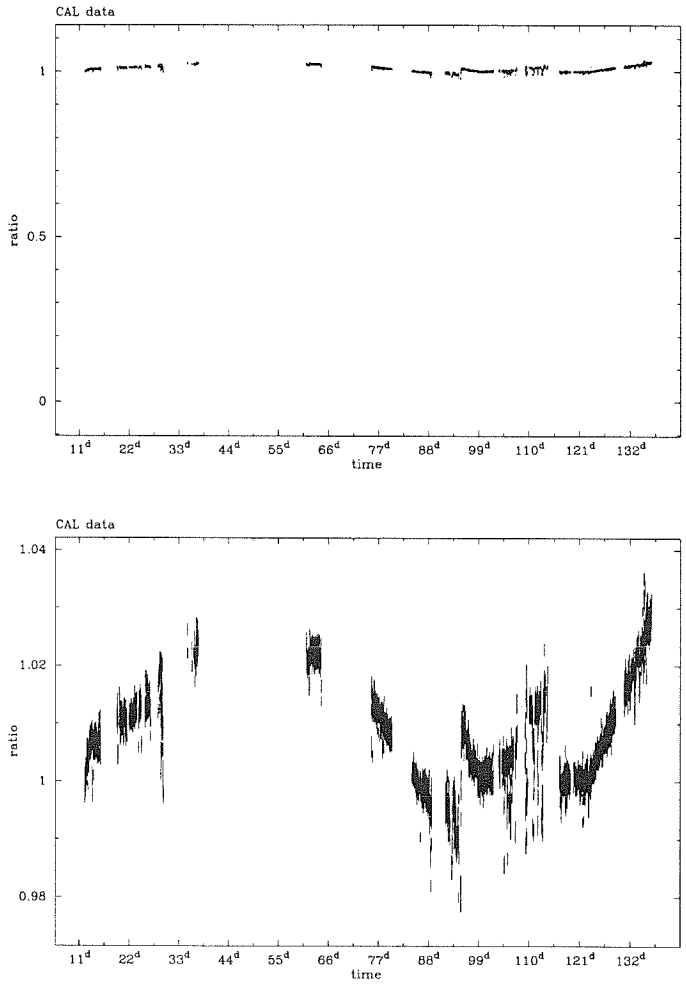

Figure 4.3 Two views of the ratio of the Ku-Band NOISE diode to the CAL diode fluxes, 1996. Both diodes were calibrated by their measured temperatures, then divided. The top panel shows that the ratio is $1 \pm 1\%$ (standard deviation), while the second panel shows that the 1% variation of the ratio is due to long-term systematic fluctuations in the diode temperatures. The step in the ratio near day 99 is due to the A/D converter glitch discussed in §4.2.5.

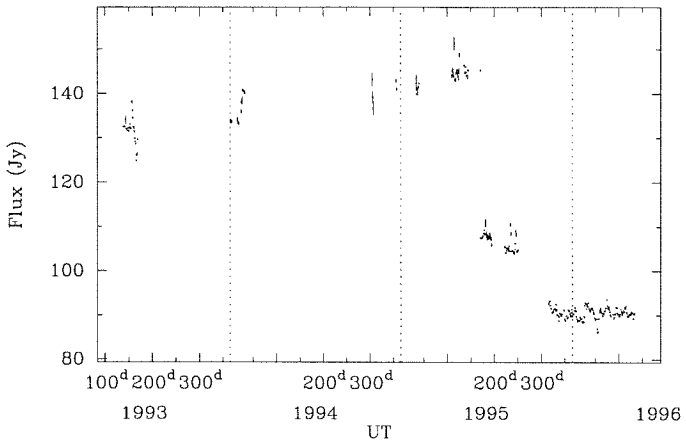

Figure 4.4 S_{cal}^{Ka} as determined from calibrator source measurements.

4.2.6 CAL Diode Flux Density Measurements

As discussed in §4.1, the calibrator sources observed during the 1996 season provide a direct measure of the CAL diode flux density. Prior to 1996, observations of calibrator sources were sporadic, and the diode temperatures from this period are used to calibrate the Ring data. Nevertheless, as shown in Fig 4.4, serendipitous observations of DR 21, Cas A, Tau A and 3C286 made during this time period provide a consistent picture of CAL diode variability, indicating that at least some of the long-term variation observed in the CAL temperatures is real. The end of the summer of 1995 saw a catastrophic failure of the CAL diode, and this device was replaced prior to the 1996 observing season. The mean of all 1996 measurements against the internal loads was

$$S_{cal}^{Ka} = 90.48 \pm 0.09\ (\pm 1.2)\ \text{Jy}, \tag{4.49}$$

where the second error is the standard deviation, indicating that the CAL flux was constant to $\sim 1\%$.

At Ku-Band, calibrator sources were observed only in 1996. A variety of instrumental changes prevent the use of a single value for the diode flux during this season, and the interpolated flux record is used in calibrating the 1996 Ku-Band data. The

average over a representative $1\frac{1}{2}$ months during which no changes were made to the receiver yields

$$S_{cal}^{Ku} = 46.01 \pm 0.09\ (\pm 0.54)\ \text{Jy}. \tag{4.50}$$

4.3 Sensitivity and Telescope Efficiencies

In §4.1, we derived the power received from a source filling the main beam of the telescope power pattern. When observing a source of flux density S_ν, with angular diameter small compared to the telescope beam, so that $S(\nu, \theta, \phi) \simeq S(\nu)\delta(0,0)$, the received power is given from (4.1) by

$$kT_A d\nu = \frac{1}{2} A_p \eta_a S_\nu d\nu, \tag{4.51}$$

so that the antenna temperature is given by

$$T_A = \Gamma S_\nu, \tag{4.52}$$

where $\Gamma \equiv A_p \eta_a / 2k$ is known as the *sensitivity* of the telescope, measured in K/Jy. Once the CAL diode flux density is known, we can determine the sensitivity by measuring

$$\Gamma = \frac{T_{cal}}{S_{cal}}, \tag{4.53}$$

and (4.9) can be used to determine the beam solid angle as

$$\Omega_a = \frac{\lambda^2}{2k\Gamma}. \tag{4.54}$$

The beam efficiency is then given simply by comparison with the main beam solid angle measured from the beam maps in §2.10

$$\eta_b \equiv \frac{\Omega_m}{\Omega_a} = \frac{2k\Omega_m}{\lambda^2}\Gamma, \tag{4.55}$$

while the aperture efficiency is

$$\eta_a = \frac{2k}{A_p}\Gamma. \tag{4.56}$$

These measurements are described below, and are summarized in Table 4.3.

4.3.1 Ka-Band

Plots of the sensitivity derived from the measured diode fluxes and temperatures from 1996 are presented in Fig. 4.5 for both noise diodes. Since the backing structure of the 5.5-meter is sufficiently rigid to prevent significant deformation of the dish with zenith angle, we take the relative gain in (4.8) and (4.10) to be $g(za) = 1$ for all zenith angles, and the average sensitivity determined from both noise diodes is given by

$$\Gamma = (4.098 \pm 0.004) \times 10^{-3} \text{ K/Jy}, \tag{4.57}$$

or, taking errors in the flux and temperature scale into account (1% measurement error on the diode temperatures, 1% error propagated from the non-linearity correction, plus 3.3% estimated error in the flux scale),

$$\Gamma = (4.10 \pm 0.15) \times 10^{-3} \text{ K/Jy}, \tag{4.58}$$

and

$$\Omega_a = (7.92 \pm 0.28) \times 10^{-6} \text{ sr}. \tag{4.59}$$

The true uncertainty in η_b will be given by the quadrature sum of errors in the beam, the temperature scale for the diodes, the flux scale and the measurement error in the sensitivity:

$$\frac{\sigma^2_{\eta_b}}{\eta_b^2} = \frac{\sigma^2_{\Omega_m}}{\Omega_m^2} + \frac{\sigma^2_{T_{cal}}}{T^2_{cal}} + \frac{\sigma^2_{S_{cal}}}{S^2_{cal}} + \frac{\sigma^2_{\Gamma}}{\Gamma^2}. \tag{4.60}$$

For the Ka-Band receiver, these terms are approximately

$$(0.6\%)^2_{\Omega_m} + (1.4\%)^2_{T_{cal}} + (3.3\%)^2_{S_{cal}} + (0.1\%)^2_{\Gamma}. \tag{4.61}$$

For $\Omega_m = (5.21 \pm 0.03) \times 10^{-6}$ sr, we have

$$\eta_b = 0.658 \pm 0.024. \tag{4.62}$$

For the 5.5-meter telescope, $A_p = 2.376 \times 10^5$ cm^2, and

$$\eta_a = 0.476 \pm 0.017. \tag{4.63}$$

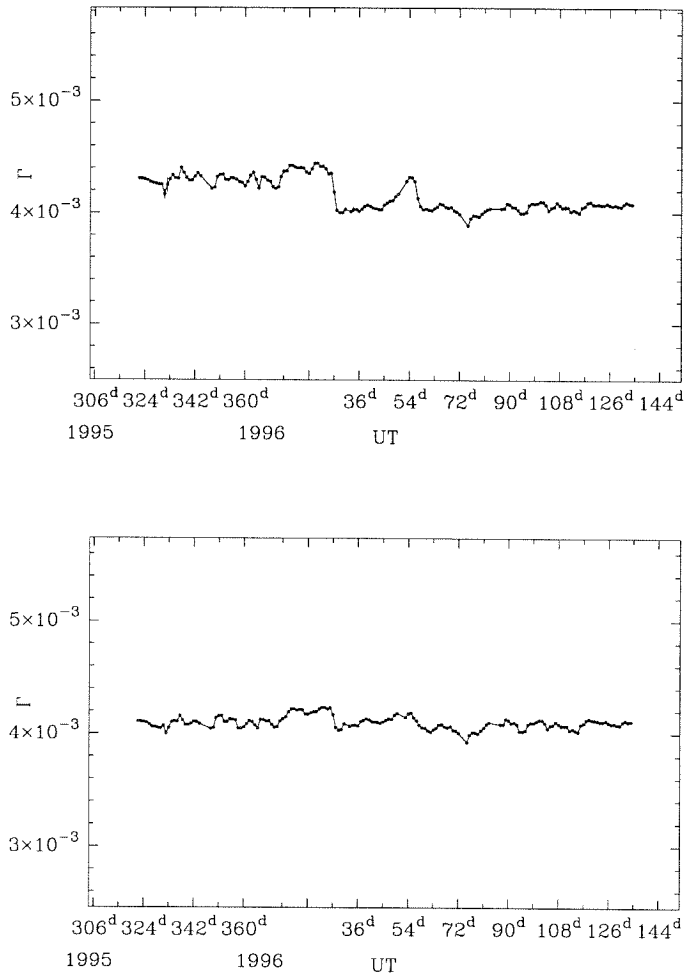

Figure 4.5 Measured Ka-Band sensitivity (in K/Jy) from the NOISE diode (top panel) and the CAL diode (bottom panel). The correlation between diode flux records suggests that these fluctuations are either real fluctuations in the diode temperatures, due presumably to fluctuations in the common power supply, or incomplete cancelation of the system gain. The *za* dependence of the NOISE diode flux is clearly visible in the data from the first half of 1996, and is consistent with the independently determined correction given in (4.45).

4.3.2 Ku-Band

At Ku-band, recall that the large change in beam width with offset of the receiver package along the optical axis makes the beam width a function of *za*, which mimics the gain of the telescope. We therefore did not attempt to determine the gain of the telescope at 14.5 GHz, and instead focused on calibrating the receiver at a small range of *za* about the *za* of the RING. As a result, telescope parameters can be determined only modulo a factor $\overline{g}$, where $\overline{g}$ is the average gain factor due to deformation of the dish over the (small) range in observing zenith angle. These quantities are referred to as Γ^*, η_b^*, etc.

From day 11-66 in 1996, the azimuthal offset for the FLUX procedure was reversed; i.e., for the off-source position, the telescope slewed so that the source was in neither beam, instead of the usual procedure which puts the source in the REF beam during the off-source integration. As a result, the effective beam for these measurements is the ANT beam instead of the MEAN beam, and application of (4.53)–(4.54) results in

$$\Gamma^*_{ant} = (2.220 \pm 0.086) \times 10^{-2} \text{ K/Jy} \tag{4.64}$$

$$\Gamma^*_{mean} = (2.130 \pm 0.082) \times 10^{-2} \text{ K/Jy}, \tag{4.65}$$

and

$$\Omega^*_{a_{ant}} = (6.99 \pm 0.27) \times 10^{-6} \text{ sr} \tag{4.66}$$

$$\Omega^*_{a_{mean}} = (7.28 \pm 0.28) \times 10^{-6} \text{ sr}. \tag{4.67}$$

The diode records from long tracks against calibrator sources indicate that even in the absence of the bi-stable behavior observed during most of 1996, fluctuations in the CAL temperature of $\sim 1\%$ are expected, and the error in the temperature scale will be the convolution of this uncertainty with the 1% uncertainty introduced by the

TABLE 4.3
TELESCOPE MEAN BEAM CALIBRATION PARAMETERS

Parameter		Ka	Ku
Sensitivity (K/Jy)	Γ	$(4.10 \pm 0.15) \times 10^{-3}$	$(2.130 \pm 0.082) \times 10^{-2}$
Beam Solid Angle (sr)	Ω_a	$(7.92 \pm 0.28) \times 10^{-6}$	$(7.28 \pm 0.28) \times 10^{-6}$
Beam Efficiency	η_b	0.658 ± 0.024	0.735 ± 0.029
Aperture Efficiency	η_a	0.476 ± 0.017	—

nonlinearity correction and the 2% fluctuations due to the A/D effect discussed in §4.2.5. The variance in our estimate of the beam efficiencies is then given by

$$(0.6\%)^2_{\Omega_m} + (2.4\%)^2_{T_{cal}} + (3.0\%)^2_{S_{cal}} + (0.3\%)^2_{\Gamma}, \tag{4.68}$$

yielding

$$\eta^*_{b\,ant} = 0.688 \pm 0.027, \tag{4.69}$$

and

$$\eta^*_{b\,mean} = 0.735 \pm 0.029. \tag{4.70}$$

Since the receiver under-illuminates the 40-meter dish, the physical aperture and thus η_a cannot separately be measured.

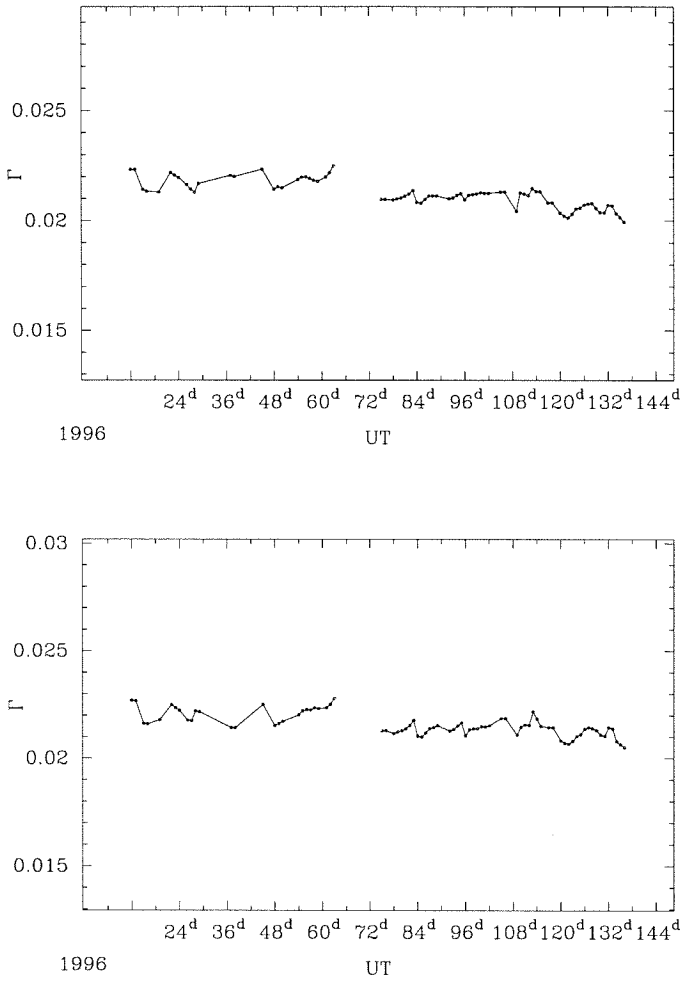

Figure 4.6 Measured Ku-Band sensitivity (in K/Jy) from the NOISE (top) and CAL (bottom) diodes. Note the higher sensitivity obtained in the first part of 1996 (day 11-66). During this period, the azimuthal offset in the FLUX procedure was reversed, so that the effective beam was the ant beam, instead of the mean beam.

4.4 Ground Spillover and Atmospheric Opacity

If we take the atmosphere to be a blackbody at physical temperature T_{atm}, the brightness observed against blank sky is given by standard radiative transfer (see, e.g., Rybicki & Lightman 1979) as

$$B(T_{sky}) = B(T_{atm})(1 - e^{-\tau A}) + B(T_{cmb})e^{-\tau A}, \tag{4.71}$$

where $B(T)$ is just the Planck function,

$$B(T) = \frac{2h\nu^3}{c^2}\frac{1}{\exp(h\nu/kT) - 1}, \tag{4.72}$$

and $A(za) \equiv \sec za$ is the airmass. For a blackbody at $T_{atm} \simeq 300$ K, $h\nu/kT \ll 1$, and we can write (4.71) as

$$T_{sky} = T_{atm}(1 - e^{-\tau A}) + J(T_{cmb})e^{-\tau A}, \tag{4.73}$$

where

$$J(T) = \frac{h\nu/k}{\exp(h\nu/kT) - 1}. \tag{4.74}$$

For $\tau A \ll 1$, $e^{-\tau A} \simeq 1 - \tau A$, and we have

$$T_{sky} = J(T_{cmb}) + \tau A \left\{T_{atm} - J(T_{cmb})\right\}. \tag{4.75}$$

When the sky is observed with a real radio telescope, the receiver temperature will contribute to the measured antenna temperature, and radiation from the ground will enter into sidelobes of the telescope power pattern. To first order, we can approximate the ground as an infinite sheet of uniform temperature, so that the sidelobes see the same temperature at all zenith angles, giving

$$T_{sky} = T_{fix} + \tau A \left\{T_{atm} - J(T_{cmb})\right\}, \tag{4.76}$$

where

$$T_{fix} \equiv T_{Rx} + T_{ground} + J(T_{cmb}). \tag{4.77}$$

A measure of the antenna temperature vs. airmass (commonly referred to as a *skydip*) can thus determine T_{ground} and τ once the receiver temperature is known. Although the Rayleigh-Jeans approximation is inappropriate even at 31.7 GHz for a 3 K blackbody ($h\nu/kT \simeq 0.57$), we will incur a negligible error in the measure of T_{fix} and τ by taking $J(T_{cmb}) \simeq T_{cmb}$.

4.4.1 Ka-Band

On the 5.5-meter, skydips were performed on 19 Jan. 95, 12 April 95, 25-26 April 95 and 12 July 96, yielding a mean ground spillover of

$$T_{ground} = 5.9 \pm 1.9 \text{ K}, \tag{4.78}$$

where the standard deviation $\sim$ 2 K presumably reflects actual variations in the temperature over a 6-month period. The mean atmospheric opacity τ determined from these time periods ranged from $0.028 - 0.039$, but these skydips were done during periods of good weather and are not necessarily an indication of the true average opacity at 31.7 GHz at the Owens Valley.

For 1996, a better estimate of the mean atmospheric opacity can be obtained from the daily scans on calibrator sources. As described above, the flux density of the CAL diode can be be measured by comparison with sources; uncorrected for atmospheric absorption, the diode flux density is then given by

$$S'(t, za) = S_{cal}(t) e^{\tau(t) A(za)}, \tag{4.79}$$

or

$$\ln S'(t, za) = \ln S_{cal}(t) + \tau(t) A(za). \tag{4.80}$$

A fit to the entire year's data is then equivalent to fitting to

$$\frac{1}{\Delta t} \int \ln S'(t, za)\, dt = \frac{1}{\Delta t} \int \ln S_{cal}(t)\, dt + \frac{1}{\Delta t} \int \tau(t)\, dt\, A(za) \tag{4.81}$$

$$= \overline{\ln S}_{cal} + \overline{\tau} A(za), \tag{4.82}$$

from which we obtain

$$\overline{S}_{cal} \equiv \left(\prod_i^N S_i\right)^{\frac{1}{N}} \tag{4.83}$$

$$= 90.35 \pm 0.22 \text{ Jy}, \tag{4.84}$$

and

$$\overline{\tau} = 0.045 \pm 0.002, \tag{4.85}$$

where the estimated errors were obtained by fitting to the binned version of the data shown in Figure 4.7.

With sufficient calibrator source data, $\tau(t)$ itself could be recovered, but in practice, airmass coverage during a single calibrator scan is insufficient to obtain an accurate fit. The daily opacities obtained in this manner, however, agree broadly with the yearly mean quoted above (see Figure 4.8).

The effect on CMBR data of assuming a constant value for the opacity can be estimated as follows. Since the airmass is constant for Ring field observations (fields are observed at transit only), the measured flux density for each field is

$$\overline{S}_{cmb} = \frac{1}{N}\sum_{i=1}^{N} S_0 \left(\frac{e^{\overline{\tau}A}}{e^{\tau_i A}}\right) = S_0 \frac{1}{N}\sum_{i=1}^{N} e^{(\overline{\tau}-\tau_i)A} \tag{4.86}$$

$$= S_0 \frac{1}{N}\sum_{i=1}^{N}\{1 + (\overline{\tau}-\tau_i)A + (\overline{\tau}-\tau_i)^2\frac{A^2}{2!} + \ldots\} \tag{4.87}$$

$$\simeq S_0\left(1 + \frac{A^2}{2!}\frac{1}{N}\sum_{i=1}^{N}(\tau_i - \overline{\tau})^2\right) \tag{4.88}$$

$$= S_0\left(1 + \frac{A^2}{2!}V(\tau)\right), \tag{4.89}$$

where $V(\tau)$ is the variance. For $za_{Ring} = 50°$, $A = 1.56$, and assuming a conservative value of $\Delta\tau \sim 0.02$ for the variance, this amounts to only a 0.05% error in the final CMBR flux.

A water vapor radiometry system (WVR), which reports fits to the zenith brightness temperature at 20 and 31.4 GHz, has been in operation at the OVRO since

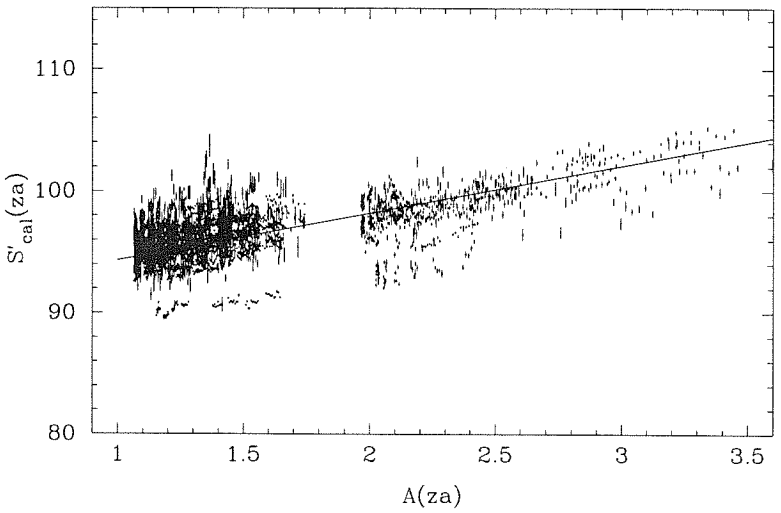

Figure 4.7 1996 CAL diode flux densities, measured relative to calibrator source data uncorrected for atmospheric absorption. Also shown is the best linear fit in airmass $A(za) \simeq \sec za$, yielding the mean opacity $\overline{\tau} = 0.045$ for 1996 used to calibrate the Ring CMBR data.

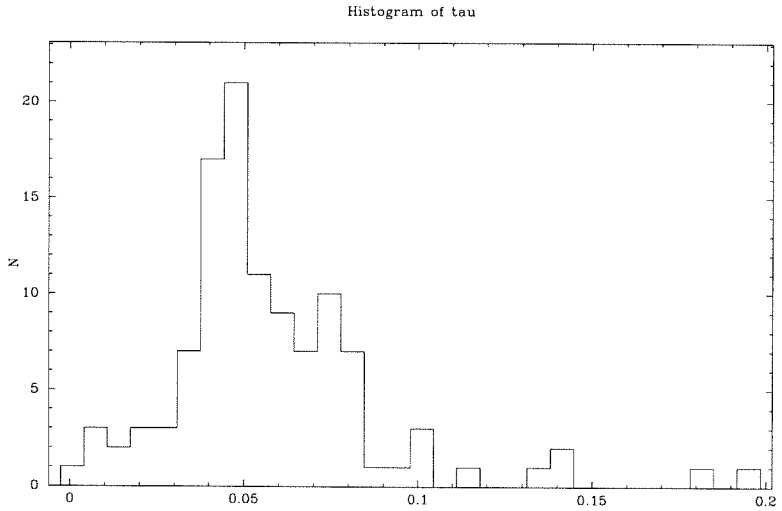

Figure 4.8 Daily opacities from 1996, obtained by fitting to individual calibrator scans. In general, individual tracks on calibrator sources interleaved with the Ring observations provide insufficient coverage in airmass for an accurate determination of $\tau(t)$, the source of the large outlier values in the histogram (no data actually taken at an atmospheric opacity of 0.2 would pass our data filters). Nevertheless, the daily opacities determined in this manner agree broadly with the mean fitted value.

the 1980s. This system has never been documented, and these measurements were not deemed trustworthy for direct use. Nevertheless, the *relative* mean opacities for different years should be a reasonably good indicator of how appropriate the value for $\overline{\tau}$ derived from the 1996 source data is for the previous 2 years, and the variance estimated from these data over 1996 is likely to be accurate. After editing data from the WVR taken when the system was clearly saturated (corresponding roughly to the acceptable source data from the 5.5-meter), the mean opacity from Nov.-May was found to be

$$\overline{\tau}_{96} = 0.043, \tag{4.90}$$

with variance given by

$$V(\tau) = 1.4 \times 10^{-4}, \tag{4.91}$$

implying from (4.89) that the error introduced by assuming a constant value of τ is less than 0.02%. Similarly, from the 1995 WVR data we find

$$\overline{\tau}_{95} = 0.046, \tag{4.92}$$

and from the 1994 WVR data,

$$\overline{\tau}_{94} = 0.045, \tag{4.93}$$

justifying the use of a single value for $\overline{\tau} = 0.45$ for all of the Ring data.

4.4.2 Ku-Band

On 16 Feb. 95, a series of skydips were done on the 40-meter telescope, yielding

$$T_{sky} = 53.49 + 2.65 \sec za. \tag{4.94}$$

The receiver temperature was $T_{Rx} = 53.2$ K, giving

$$T_{ground} < 1 \text{ K}. \tag{4.95}$$

It is clear that under-illumination of the 40-meter dish by the Ku-Band receiver provides excellent rejection of ground spillover, as expected, since the largest forward sidelobes of the feed power pattern are reflected back onto the sky and do not see the ground directly.

The ambient temperature was $T_{atm} = 283.4$ K, giving

$$\tau = 0.01. \tag{4.96}$$

Once again, this is likely to underestimate the true opacity averaged over the observing season, as these data were taken in selectively good weather. For the 1996 observing season, however, as calibrator sources were observed only within $\pm 5^{\circ}$ of the zenith angle of the Ring, when the CAL flux referenced to these source measurements is applied to the FLUX data on the Ring, absorption effects will cancel if no atmospheric correction is applied to the data.

The 1995 Ku-Band data, however, must be calibrated by reference to the noise diode temperatures, and the good agreement between the mean opacity estimated from the WVR and that determined from the 1996 source data will be exploited to estimate the mean opacity at 14.5 GHz. The mean opacity for 1996 obtained from the WVR at 20 GHz is 0.03, yielding an extrapolated opacity at 14.5 GHz of

$$\overline{\tau}_{Ku} = 0.023, \tag{4.97}$$

in good agreement with predictions from atmosphere modeling, which indicate that fluctuations at 14.5 GHz should be roughly a factor of 2 lower than at 31.4 GHz (Gulkis 1997; see also Herbig 1994).

Chapter 5

Data Reduction

HANNAH: Noise?

VALENTINE: Distortions. Interference. Real data is messy. There's a thousand acres of moorland that had grouse on it, always did till about 1930. But nobody counted the grouse. They shot them. So you count the grouse they shot. But burning the heather interferes, it improves the food supply. A good year for foxes interferes the other way, they eat the chicks. And then there's the weather. It's all very, very noisy out there. Very hard to spot the tune. Like a piano in the next room, it's playing your song, but unfortunately it's out of whack, some of the strings are missing, and the pianist is tone deaf and drunk — I mean, the noise! Impossible!

Tom Stoppard, *Arcadia*

5.1 Introduction

By comparison with observations of objects at $z \ll 1000$, the interpretation of observations of the microwave background is thought to be quite simple, reflecting the relative simplicity of the physics which governs the early universe. For the Gaussian fluctuation models predicted by inflation, all the information provided by the CMBR is revealed in the average properties of the radiation field, specifically in the angular power spectrum of temperature fluctuations. The *reductio ad absurdum* of microwave background experiments with limited angular resolution is the measure of the variance in a set of samples drawn from the underlying distribution of temperature fluctuations at a given angular scale on the sky. Thus to first order, reduction of

CMBR data requires nothing more than getting the factor of $1/(N-1)$ right when computing a standard deviation.

The fundamental difficulty with measuring a signal $\sim 10^{-7}\times$ the temperature of the Earth's atmosphere, however, lies not with the interpretation of the data but in distinguishing photons which originate in the primordial fireball from those which are artifacts of the experiment's local environment, and from those whose origin is in the detritus of 10 billion years of structure formation which intervene. The first challenge is addressed in this chapter, while the second is relegated to Chapters 6 and 7.

5.2 Data Subdivision

On the 5.5-meter telescope, data were acquired from winter of 1993 to spring of 1996. The typical observing season at the OVRO lasts from early October until mid May, so that a "season" of data refers broadly to this time period, and is not a calendar convention. (Thus the "1994 season" refers to data taken from fall of 1993 through spring of 1994, etc.) On the 5.5-meter, a total of three seasons of data were obtained. These data sets are processed separately; since each data set typically has problems unique to the season, it seems logical to maintain this distinction. Moreover, it provides a natural time span over which data sets can be compared for consistency (see §5.4.5).

On the 40-meter telescope, construction of the Ku-Band receiver was completed in spring of 1994, and all together two seasons of data were obtained, the first spanning fall of 1994 to spring of 1995, and the second, fall of 1995 to spring of 1996. On the Ku-Band receiver, the designation of the ANT and REF feeds is reversed with respect to the 5.5-meter Ka-Band receiver. As a result, whereas the 5.5-meter telescope slews in the negative azimuthal direction to bring the REF beam on source during a FLUX procedure, the 40-meter telescope must slew in the positive direction. The schedule

files which control the 5.5-meter during observations of the Ring5m were recycled for the 40-meter, and for the first half of the 1996 observing season, the telescope slewed in the wrong direction, so that neither beam was on-source during the B and C integrations of the FLUX procedure (see §2.4.2). Fortunately, these data are recoverable, since the interlocked geometry of the Ring ensures that each beam is always on a Ring field (see §5.4.3). Nevertheless these data have been separated from data taken during the second half of 1996, resulting in two seasons referred to as the 1996_1 and 1996_2 seasons, respectively.

5.3 Data Editing

The primary obstacles to observations of the CMBR are sources of systematic and stochastic noise originating outside the telescope. With the advent of stable, low-noise HEMT amplifiers and at higher frequencies, bolometers, CMBR experiments are no longer limited by receiver sensitivity, except in the number of spatial samples which can be obtained over the reasonable lifetime of an experiment, or of an astronomer. After only a single season of data from the Ring5m experiment, our estimate of the sky variance was limited by the number of patches sampled, not by instrumental noise. As is discussed below, the two additional seasons were required for the attendant reduction in psychological variance only, as observations from the second season reassured us that the extraordinary signals we had detected were not figments of an avid astronomer's imagination, while the third proved not only that they originated outside the telescopes, but that they were astronomical in origin.

As described in §1.1, the Ring5m experiment was designed to suppress obvious sources of systematic error: observations at a fixed position relative to the ground should provide good rejection of variable ground spillover, while the double-switched

beam response effectively provides a curvature filter, with zero response to large-scale temperature gradients from the ground or the atmosphere. Dicke-switching at 500 Hz eliminates noise power from $1/f$ system gain fluctuations, at the same time removing atmospheric fluctuations which occur in both beams. In practice, none of these techniques is perfect, particularly not the last, and our approach is selectively to cull data which are affected by known sources of noise. As considerable care must be taken when editing the data to avoid the introduction of systematic biases, these edits are discussed in some detail below.

5.3.1 CAL Editing

The simplest way to avoid introducing bias when editing data is to avoid using the data values themselves as a rejection criterion. As discussed in §4.2, temperature-dependent gain fluctuations are removed from the data by referencing to the record of CAL diode fluxes. Since the CAL diode is internal to the receiver and is measured at regular intervals, the CAL knows nothing about what is observed through the front of the feeds, and editing of the CAL record can introduce no bias into the final data set. CALs measured against the sky are subject to atmospheric fluctuations, making measurement of their flux unreliable during periods of bad weather. Due to imperfect isolation of the load switches, not even CALs measured against the internal loads are completely immune to atmospheric conditions, although the effect is greatly attenuated. In addition, LOAD CALs suffer from power fluctuations in the loads themselves, glitches in the programmable attenuators, and fluctuations in the supplies powering the diodes. While these devices are known to degrade on timescales of years, their intrinsic temperature on timescales of days is known to be stable to within 1% from comparison with calibrator sources. Moreover, the system gain, tracked by the diodes in good weather, typically shows only a slow diurnal variation. Fast variations of large amplitude observed in the CAL record are thus not

representative of the true system gain, and these CALs must be removed to avoid contaminating valid FLUX data. If sufficient CALs are rejected that a given FLUX procedure has no gain reference within the typical timescale for significant system gain variations ($\Delta t_g \sim 1$hr), the FLUX is rejected.

First, CAL measurements for which any of the A–D (see §2.4.2) averages is exactly 0 are rejected, as these occur only when the total power saturates the detector. Negative CAL values are also rejected, as these only occur when the detector is saturated during an OFF segment of the CAL procedure, but not during the ON segment (unlikely, but known to occur). During the first part of 1996, the 16-bit A/D converter in the Ku-Band backend showed a power glitch near a special data value, corresponding roughly to the 15^{th} bit (see §4.2.5). This is manifested as a drop in the CAL flux when the power levels during the CAL-ON and CAL-OFF integrations respectively lie on either side of this data value. Measurements which are the difference of power levels lying entirely above or entirely below this threshold are unaffected. During 1996, the total power was recorded during each segment of the FLUX and CAL procedures, and any CAL or FLUX data which cross this threshold are excised.

As part of the CMBPROG package (see Appendix D) with which this data was processed, an automated procedure was devised to edit the CALs using flexible, user-defined statistical filters. Any editing involves an element of subjectivity in the choice of cutoffs, and this procedure is no exception; the routine is effectively an attempt to quantify the intuition that years of experience with these receivers provides. Nevertheless, it has proven eminently capable of rejecting obviously spurious CALs while discriminating genuine temperature or attenuator changes. The increased efficiency over manual editing for large data sets allows great latitude in experimenting with different editing techniques.

A series of sliding buffer edits, described in more detail in §5.3, forms the basis

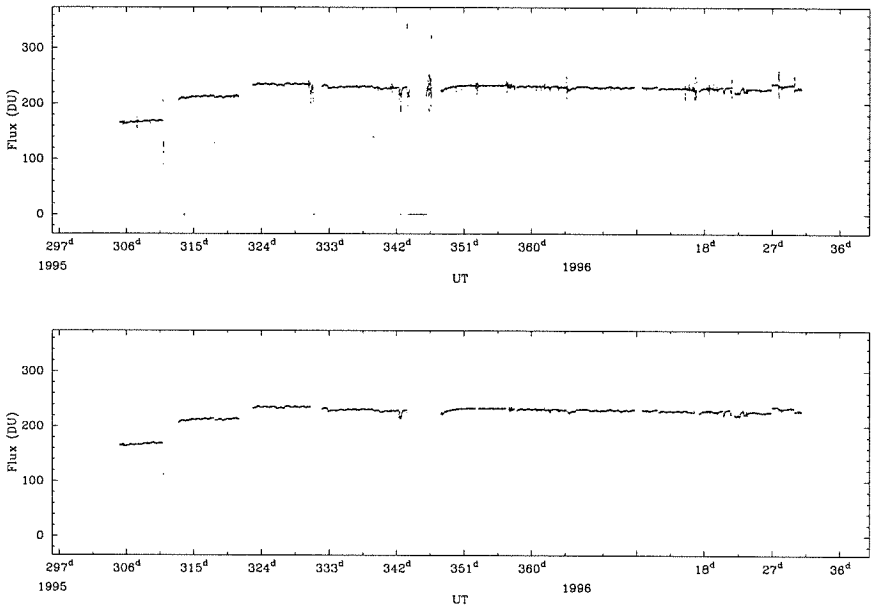

Figure 5.1 Results of automated CAL editing from the 1996 Ka-Band data. Top panel is the unedited CAL record, while the bottom panel shows CALs passed by the filter. All drops in the CAL record at bottom are genuine system gain or attenuation changes, including the small dropout near day 95/311.

for this procedure. The CAL SD is first normalized by the CAL FLUX, to allow comparison of CALs taken at different attenuator settings. CALs whose normalized SDs are $> 3\sigma_{buf}$ are then iteratively rejected, where σ_{buf} is the standard deviation in day-long buffers of CALs. Next, two-hour buffers whose normalized standard deviation is larger than the sd for the entire data set are rejected. An iterative rejection of the CAL FLUXes in day-long buffers is also done, followed by rejection of two-hour CAL FLUX buffers whose standard deviation was greater than 10 (in DU). Results of a typical editing session are shown in Fig. 5.1.

Since LOAD CALs are measured against a different total power than the SKY FLUXes, they must be corrected for non-linearity (see §2.7), requiring separate measurements of the total power. Any CALs for which no bracketing power measurements are found within 1 hour are rejected. From fall of 1995 onward, the total power was

recorded as part of the CAL procedure, so that no CALs from this time period are rejected on this basis.

5.3.2 FLUX Editing

The first level of FLUX editing consists of rejecting all data taken when the receiver was saturated during periods of high atmospheric water vapor content. Since the receiver typically remains saturated (at 2^{16} DU for a 16-bit A/D converter) during all four segments of the FLUX procedure, these FLUXes are readily identified as FLUXes with standard deviations identically zero. This rejects less than 1% of the data. Next, FLUXes taken during excessively windy conditions, leading to tracking errors, are identified by the excess time taken for the procedure to complete. Any FLUXes for which the difference between the actual and expected duration is more than 1 second are excised, eliminating between $1 - 10\%$ of the data.

When LOAD CALs are used in gain calibration, FLUX procedures must also be corrected for non-linearity, and for data prior to fall of 1995, the total powers must be interpolated onto the FLUXes, as with the CAL measurements. Any FLUX for which no bracketing power measurements are found within 1 hour is rejected, typically affecting 1% or less of the data. Since on the 40-meter telescope, CALs are only measured against the sky, no non-linearity correction is applied to the Ku-Band data.

Referencing of the CALs constitutes the next level of editing for the FLUX data. CALs are boxcar-smoothed onto the FLUXes in one-hour buffers, providing an accurate measure of the mean CAL level; any FLUX for which fewer than 3 CAL measurements are found during that period, or for which the maximum and minimum CAL values in the buffer differ by more than 10% are flagged. Although spurious CALs have previously been removed by the editing described in §5.3.1, this eliminates data taken during a change in attenuation or other uncalibrated but legitimate step in the

level of the CAL. In this manner, $4-11\%$ of the Ka-Band FLUX data is rejected. In the Ku-Band receiver, there are no internal loads, and CALs are measured against the sky. As a result, many more CALs are rejected by the previous step of CAL filtering, and CAL referencing constitutes the most stringent filter at Ku-Band, rejecting between $12-40\%$ of the FLUX data.

5.3.3 Atmosphere

In each FLUX measurement, the receiver input is switched at 500 Hz between two horns separated in azimuth by $\sim 22'$ on the sky, as indicated schematically in Fig. 2.2. As described in §2.4.2, the telescope integrates for equal amounts of time in each of the A, B, C and D configurations. For each set of such measurements, the quantity $F = \frac{1}{2}(B+C-A-D)$ is formed, so that if the temperature in the i^{th} field is denoted by $T_i \equiv T(\phi_i)$, the quantity which results is given by

$$F_i \simeq \Delta\phi^2 \left.\frac{\partial^2 T}{\partial \phi^2}\right|_{\phi_i}. \tag{5.1}$$

Now assume that $T_i = T_{i_{cmb}} + T_{i_{atm}}$, where $T_{i_{cmb}}$ is the component of the sky temperature due to the CMBR, and $T_{i_{atm}}$ is that due to stationary (over the timescale of a single FLUX measurement) structure in the atmosphere. Then if the sky temperature field is linear over $2\Delta\phi$, the second derivative will vanish, and we are left with

$$F_i \simeq \Delta\phi^2 \left.\frac{\partial^2 T_{cmb}}{\partial \phi^2}\right|_{\phi_i}. \tag{5.2}$$

In addition to any constant spatial component, however, the atmosphere contributes a time-varying component to each integration equal to

$$\delta F_k = \frac{1}{\Delta t}\int_{t_k}^{t_{k+1}} \delta T dt. \tag{5.3}$$

For the 5.5-meter telescope, with beam throw of 22.'16, the beams diverge 853 meters above the ground, so that fluctuations in atmospheric water vapor below this altitude

will occur in both beams simultaneously. Since the 500 Hz switching is faster than most coherent atmospheric fluctuations, we expect that these fluctuations will at least partially cancel. On the shortest timescales, incomplete cancelation of fluctuations will add in quadrature to the measured variance of the FLUXes, and the ratio of the measured SD to the SD expected from instrumental noise alone (see §2.6) is used as a rejection criterion. On longer timescales, the presence of time-varying instrumental contributions and incomplete cancelation can be probed by forming the quantities $SW1 = \frac{1}{2}(C - A + D - B)$ (Myers et al. 1997), since any signal in the far field will cancel, leaving only

$$\begin{aligned} SW1 &= \frac{1}{2}\{(\delta F_{i_C} - \delta F_{i_A}) + (\delta F_{i_D} - \delta F_{i_B})\} && (5.4) \\ &\simeq \Delta t \left(\left.\frac{\partial F}{\partial t}\right|_{t+2\Delta t} - \left.\frac{\partial F}{\partial t}\right|_{t} \right) && (5.5) \\ &\simeq 2\Delta t^2 \frac{\partial^2 F}{\partial t^2}, && (5.6) \end{aligned}$$

on timescales of $2\Delta t$. Likewise the quantity $SW2 = \frac{1}{2}(B - A + D - C)$ cancels the signal in the far field, leaving

$$\begin{aligned} SW2 &= \frac{1}{2}\{(\delta F_{i_B} - \delta F_{i_A}) + (\delta F_{i_D} - \delta F_{i_C})\} && (5.7) \\ &\simeq \Delta t \left(\left.\frac{\partial F}{\partial t}\right|_{t+\Delta t} - \left.\frac{\partial F}{\partial t}\right|_{t} \right) && (5.8) \\ &\simeq \Delta t^2 \frac{\partial^2 F}{\partial t^2}, && (5.9) \end{aligned}$$

on timescales of Δt.

Statistical Edits

In practice, atmospheric culling is achieved via a series of statistical edits applied to the FLUXes. These have previously been described in Myers et al. (1997), and the same notation is retained here for consistency. A combination of sliding buffer edits

is implemented, where in each case we form the test statistic

$$t_i = X_i/\sigma_{i_{th}}, \tag{5.10}$$

where the data have been divided by $\sigma_{i_{th}}$, the expected thermal noise for the i^{th} measurement, given by (2.23). The tested quantity X can be the FLUX, SD, SW1 or SW2. Successive buffers of N points are constructed, where N is typically $10-25$. For each buffer j, we compute the mean

$$\bar{t}_j = \frac{1}{N}\sum_{i=j}^{j+N-1} t_i, \tag{5.11}$$

and standard deviation

$$\sigma_j = \left[\frac{1}{N-1}\sum_{i=j}^{j+N-1}(t_i - \bar{t}_j)^2\right]^{1/2}. \tag{5.12}$$

Successive buffers in time are constructed, where the width of a buffer is constrained to be no more than two hours. A point is rejected if there exists no buffer containing that point for which either $\bar{t}_j < \bar{t}_{max}$ or $\sigma_j < \sigma_{max}$, designated "meanX[N, $\bar{t}_{max}$]" and "sigX[N, σ_{max}]," respectively. These filters are applied to the combined data from all Ring5m fields, as their primary purpose is to reject data affected by weather, regardless of the field being observed. In addition to these buffer edits, we employ a simple point-by-point filter which rejects data for which $t_i > t_{max}$, designated "X[t_{max}]."

The last edit applied to the data is the only edit in which the data values themselves are used as a rejection criterion. We perform an outlier rejection, denoted "rejX[N]," in which FLUX data for which $|f_i - \bar{f}| > N\sigma$ are rejected, where σ is the standard deviation of the FLUXes. This rejection is iterative, and the mean is recomputed after each rejected point to avoid biasing the final data distribution. The rejX[N] filter is effected on a field-by-field basis, to allow for possible contamination of a field by real structure in the far field (i.e., Galactic foregrounds or discrete sources).

This serves to remove spurious signals due to radio frequency interference (RFI), and typically rejects $< 0.5\%$ of all data.

In the analysis of data from both telescopes, the following combination of filters was selected: meanSD[25, 2.0], SD[2.5], sigSW1[25, 7.5] and rejFLUX[4]. The effect of different filtering methods on the 36 Ring5m field means was explored by reducing the 1994 Ring5m data with the following grid of filter combinations:

1) Reject points with high SD, using $t_{max} \in \{\infty, 2, 2.5, 3\}$ (SD[2] – SD[3], where SD[∞] is equivalent to no rejection)

2) Filter on the mean SD, with $N = 25$ and $\bar{t}_{max} \in \{\infty, 1.5, 2.0, 2.5\}$ (none, meanSD[25, 1.5] – meanSD[25, 2.5])

3) Filter on the standard deviation of SW1, with $N = 25$, and $\sigma_{max} \in \{\infty, 6.0, 7.5\}$ (none, sigSW1[25, 6.0] – sigSW1[25, 7.5]).

4) Outlier reject $|f_i - \overline{f}| > N\sigma$, with $N \in \{\infty, 3, 4, 5\}$ (none, rejFLUX[3] – rejFLUX[5]).

Results are shown in Fig. 5.2, for both unweighted means and weighted field means (see below), demonstrating that the editing is robust to small changes in cutoff levels. Even when the unweighted means are computed for each field, the variance among the different editing schemes is smaller than the standard error in the field means; for the weighted models, all errors are $\lesssim 5$ μK. Table 5.1 summarizes all data edits for both the Ka and Ku-Band data sets.

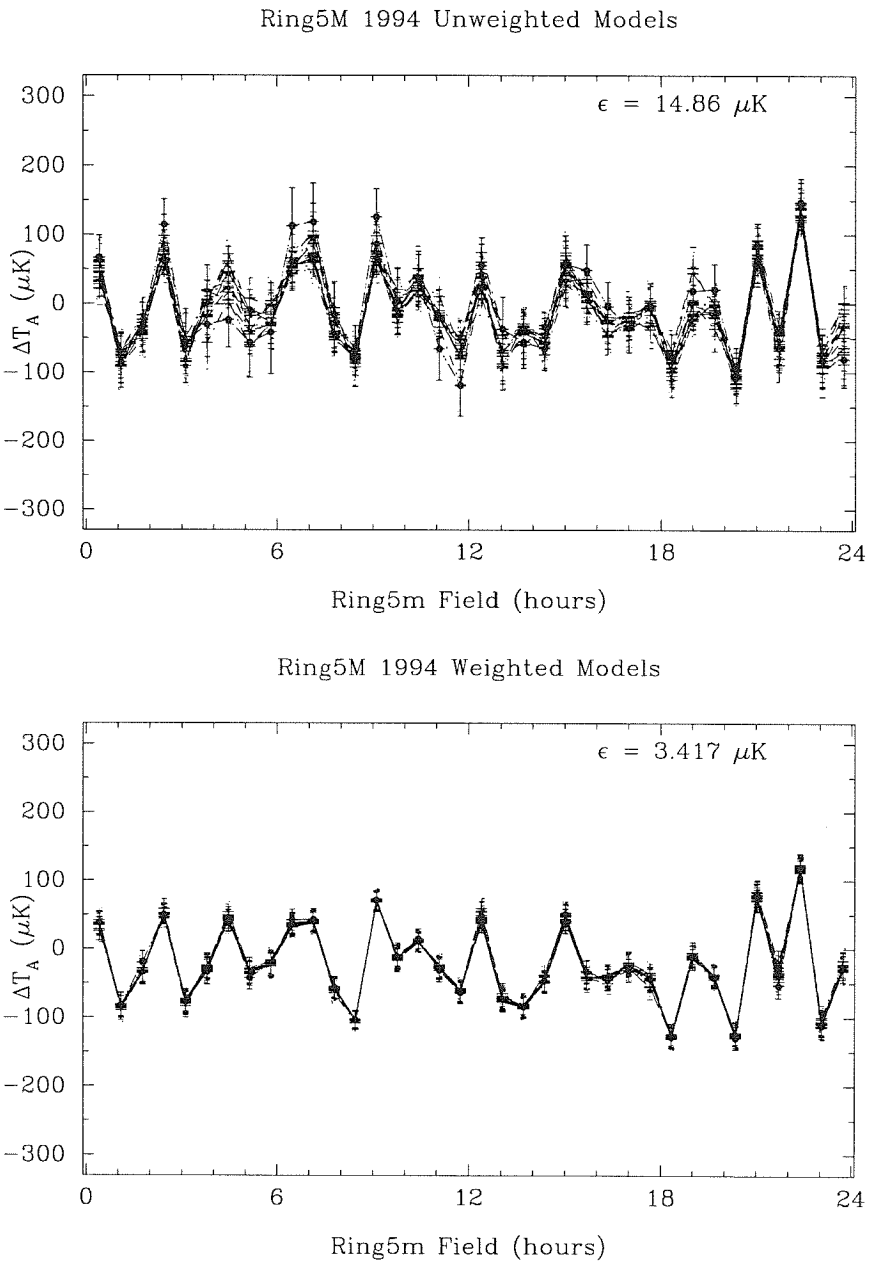

Figure 5.2 Reduction of the 1994 Ring5m Ka-Band data for 15 unweighted models (top panel), and 15 weighted models (bottom panel). Even in the case of the unweighted editing schemes, the mean standard deviation in each field (the mean sd is shown at the top right of each plot) is smaller than the statistical error bars, and in the case of the weighted models, is practically negligible.

TABLE 5.1
DATA EDITS

	Ka			Ku		
Edit	1994	1995	1996	1995	1996_1	1996_2
Saturated	0.05%†	0.77%	0.15%	0.20%	0.64%	0.03%
RejFLUX	0.46%	0.24%	0.14%	0.21%	0.15%	0.37%
Power	0.69%	1.41%	0.00%	0.00%	0.00%	0.00%
SD	1.87%	1.77%	2.34%	2.34%	1.92%	2.72%
SigSW1	2.25%	1.67%	2.07%	0.02%	0.00%	0.00%
No CALs	3.99%	4.06%	11.39%	24.61%	39.80%	13.58%
Excess	9.72%	1.00%	3.92%	24.60%	1.29%	3.67%
MeanSD	22.64%	36.87%	35.53%	3.16%	1.11%	1.38%
Rejected	41.67%	47.78%	55.53%	55.13%	44.91%	21.75%
Total‡	68,359	98,617	107,494	32,743	29,209	40,584

†Percent rejected.
‡Total number of data points before editing.

5.4 Results

After the data are filtered, the weighted mean $\overline{\Delta T} \pm \epsilon$ for each of the 36 Ring5m fields is computed as follows:

$$\overline{\Delta T} = \frac{1}{W_1} \sum_{j=1}^{N} w_j \Delta T_j \tag{5.13}$$

$$\epsilon^2 = \frac{W_2}{W_1^2} \sigma^2 \tag{5.14}$$

$$\sigma^2 = \frac{N}{N-1} \frac{1}{W_2} \sum_{j=1}^{N} w_j^2 (\Delta T_j - \overline{\Delta T})^2 \tag{5.15}$$

$$W_1 = \sum_{j=1}^{N} w_j \tag{5.16}$$

$$W_2 = \sum_{j=1}^{N} w_j^2. \tag{5.17}$$

The weights used in determining the field means (5.13) follow straightforwardly from a maximization of the likelihood for data drawn from a Gaussian distribution:

$$\mathcal{L} \propto \prod_{j}^{N} \exp \left\{ \frac{-(\Delta T_j - \overline{\Delta T})^2}{2\sigma_j^2} \right\}, \tag{5.18}$$

or

$$\ln \mathcal{L} \sim -\sum_{j}^{N} \frac{(\Delta T_j - \overline{\Delta T})^2}{2\sigma_j^2}, \tag{5.19}$$

such that

$$\frac{\partial \ln \mathcal{L}}{\partial \overline{\Delta T}} = 0 \;\Rightarrow\; \sum_{j}^{N} \frac{(\Delta T_j - \overline{\Delta T})}{\sigma_j^2} = 0 \tag{5.20}$$

$$\Rightarrow\; \overline{\Delta T} = \frac{\sum_j^N \Delta T_j/\sigma_j^2}{\sum_j^N 1/\sigma_j^2}, \tag{5.21}$$

so that the sample mean weighted by $w_j = \sigma_j^{-2}$ is a maximum likelihood estimator for the mean of the underlying distribution. A typical scan on a single Ring5m field lasts approximately 40 minutes, during which $\sim$ 21 FLUXes are collected. In general, the standard error σ_j reported with each datum underestimates the scan variance by a factor of 2-3, in the best weather approaching the data standard error (typically $\sim 1.5\times$ the thermal noise), presumably due to atmospheric fluctuations on timescales longer than a single FLUX measurement. The scan variance $\sigma_{j\,sc}^2$ is thus a better estimate of the true error, and we take $w_j = (\sigma_j^2 + \sigma_{j\,sc}^2)^{-1}$ when computing statistics for the Ring5m fields.

5.4.1 Atmosphere

On the 5.5-meter telescope, CAL procedures done against the loads can be used to estimate the contribution of the atmosphere to the measured sds. Against the loads, the measured temperature is

$$T_{Rx} + T_{load}, \tag{5.22}$$

while against the sky, the measured temperature is T_{sky}, given by (4.76). The expected sd for a measurement of duration τ_C is then

$$\sigma_{T_C} = \sigma_{T_F} \times \frac{T_{Rx} + T_{load}}{T_{sky}} \sqrt{\frac{\tau_F}{\tau_C}} \tag{5.23}$$

relative to the expected thermal sd σ_{T_F} for a FLUX measurement (see §2.6). Figure 5.3 shows the histogram of individual standard deviations from FLUX procedures passed by the data rejection filters (see §5.3.2) and from CAL procedures done against the internal loads.

The expected thermal sd can be computed from (2.23) using the CALs to convert the observed total power to antenna temperature units. The expected thermal sd has its own sampling distribution, given by

$$\exp(-N\sigma^2/2)\sigma^{N-2}, \tag{5.24}$$

up to a normalization (Kendall 1955), plotted as the smooth solid line in Fig. 5.3. The FLUX distribution shows considerable skew to high sds, reaching the thermal limit only in the best weather, while the CAL SDs against the internal loads consistently achieve close to the thermal limit, showing a small tail to higher sds, possibly due to atmospheric fluctuations which leak through the load switches or to small fluctuations in the load powers themselves.

On the 40-meter telescope, FLUX procedures routinely achieve standard deviations close to the thermal limit, as can be seen in the bottom panel of Fig. 5.3. Although atmospheric fluctuations are expected to be approximately a factor of 2 smaller at 14.5 GHz, part of the good agreement is an artifact of the higher system temperature of the Ku-Band receiver, so that the relative contribution to the system noise of the atmosphere is attenuated. Moreover, as the Ku-Band feeds illuminate a patch on the 40-meter dish surface approximately 11 meters in diameter, the column of air common to both feeds persists to $\sim$ 1700 m, canceling fluctuations a factor of 2 higher in the atmosphere than on the 5.5-meter telescope.

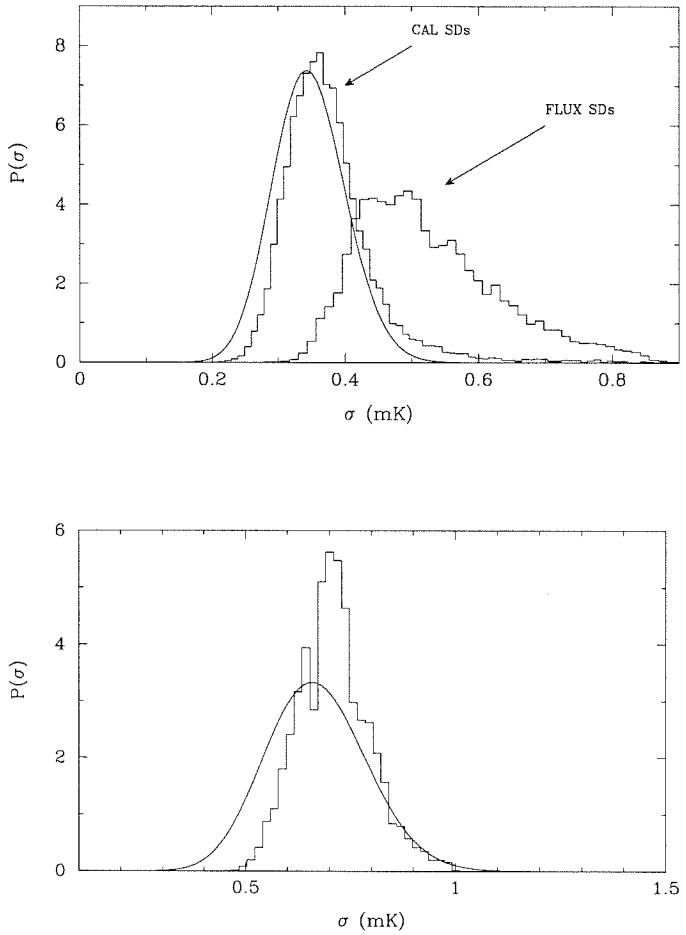

Figure 5.3 (top panel) Histogram of CAL sds against the internal loads, and of FLUX sds on sky, from the 1996 Ka-Band data. The distribution of expected thermal sds is plotted as the smooth solid line (see text). (bottom) Expected and actual standard deviations from the 1996 Ku-Band FLUX data. Histograms have been normalized to have unit area.

5.4.2 Mean Levels

Shown in Fig. 5.4 are the Ka-Band Ring5m field means for 1994 – 1996, demonstrating that the mean level for the Ring changed between 1994 and 1995 by approximately 120 μK, while between 1995 and 1996, the difference is consistent with zero. Subtraction of the 1994 and 1995 data sets shows that the shift is consistent with a constant offset in each field (a variable point source contributes to the measured signal in the

first field (see next chapter), which affects the two neighboring fields through the double switching), implying that the mean level is either instrumental in origin, or at least fixed relative to the telescope. Since the shift is constant from field to field, it does not affect our computation of the sky variance.

The Ring mean averaged over all 36 fields is plotted as a function of time in Fig. 5.5, revealing that the largest jump in the mean level occurred just after the TRW HEMT was changed out of the set on day 94/091 (indicated in Fig. 5.5 by the dotted line) and replaced by NRAO A12.

The explanation for the change in mean level of the Ring may lie with the directional isolation discussed in §2.8.1. There, it was demonstrated that a mismatch in the directional isolations of the Dicke switch can lead to incomplete cancelation of ground or atmospheric temperature gradients. The residual term is proportional to the difference in isolations with the Dicke switch in either ANT or REF positions. Replacement of the HEMT will undoubtedly change the impedance at the output port of the switch, quite likely resulting in a change in isolation. Three measurements were made of the isolations, one before the HEMT changeover, and two after. We find that when the putative error term given by (2.50) is normalized to the Ring5m mean in 1993, the mean levels predicted by the measured isolations in 1994 and 1995 (shown as open triangles in the bottom panel of Fig. 5.5) are in excellent agreement with the data, implying a constant temperature gradient of

$$\Delta\phi\frac{\partial T}{\partial\phi} = -16 \text{ mK} \tag{5.25}$$

across the beam throw of the telescope.

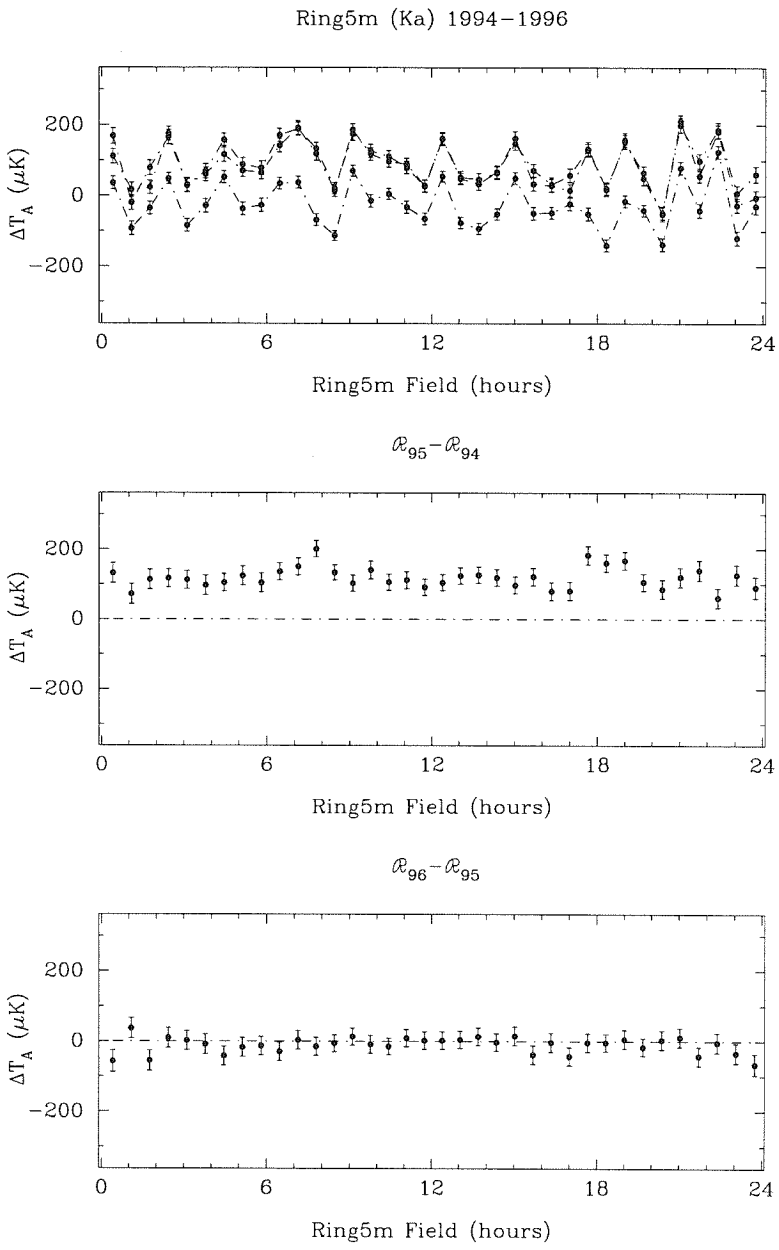

Figure 5.4 Ring5m results for 1994-1996. (Top panel) Three years of data, with no means subtracted. Subtraction of the 1994 and 1995 data sets (middle panel) shows that the Ring has changed by a constant offset ($\Delta T = 119.41$ μK, $\chi_r^2 = 1.34$), while the 1996 and 1995 data sets are consistent with a change of $\Delta T = -9.93$ μK ($\chi_r^2 = 0.71$) (bottom panel).

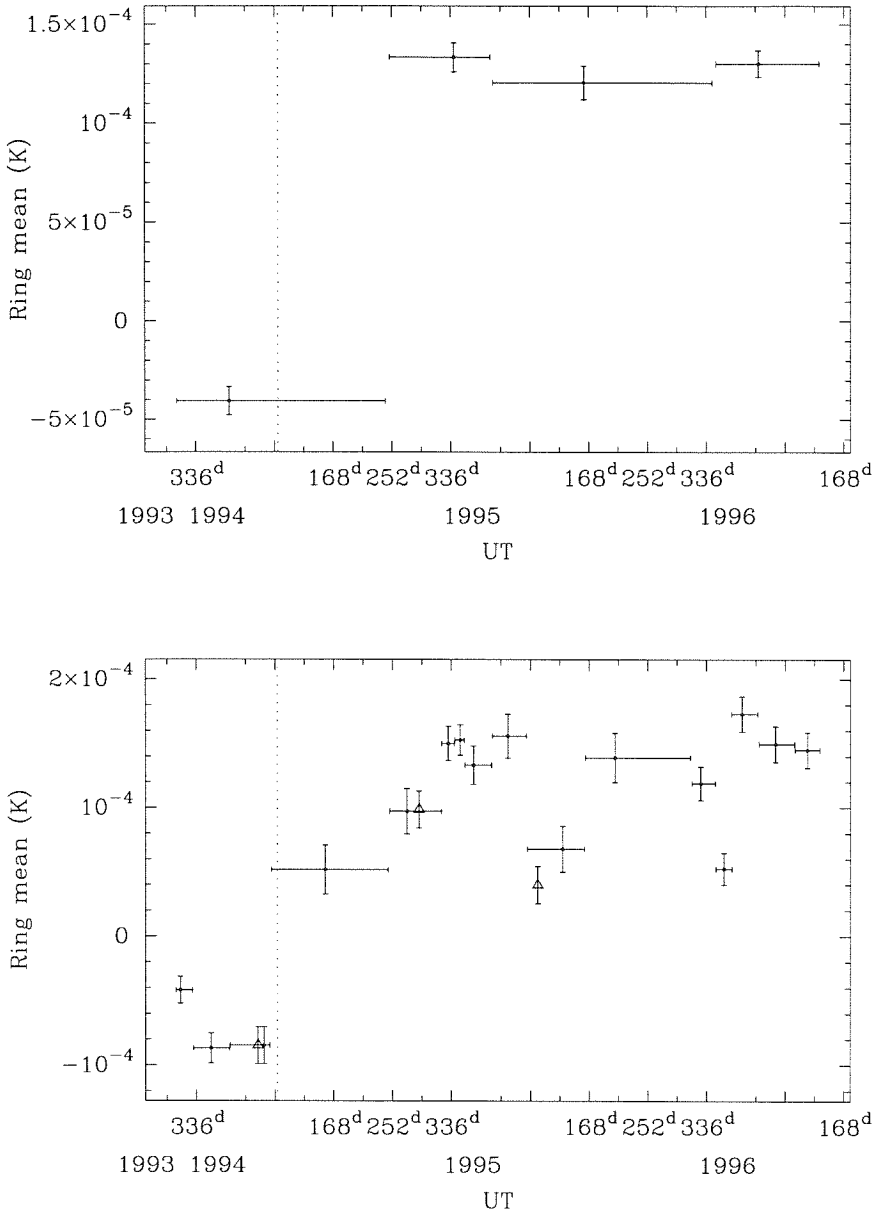

Figure 5.5 Mean levels for the Ka-Band Ring, 1994-1996, where bins are chosen to contain equal amounts of data. The long-term means have been quite stable since early 1994. The large step in the mean level coincides with a HEMT change on day 91, 1994 (indicated by the dotted line), as can readily be seen in a plot of the short-term means (bottom panel). Scatter in the mean level, as well as the change in sign, may be related to changing directional isolation in the Dicke switch (see section §2.8). If we assume that the mean levels are due to this effect, we can compute the expected mean of the Ring, relative to the observed value in 1993, at the two epochs in 1994 and 1995 when measurements of the directional isolations were made. These predictions are indicated by open triangles on the plot and agree quite well with the observed levels.

5.4.3 Ku-Band

In this section, we investigate the effect of reversing the azimuthal offset in a FLUX procedure, as occurred at Ku-Band during the first half of the 1996 season (see §5.2). Since the beam throw is small compared to the curvature of the Ring, when the fields are observed near transit, the field separation is approximately azimuthal. Since the Ring5m field spacing is matched to the separation $\Delta\phi$ of the telescope beams, if we denote the temperature in the Ring field $+\Delta\phi$ away from the i^{th} field by T_{i+1}, and the field located $-\Delta\phi$ away by T_{i-1}, as depicted below, where the sense of the ANT and REF beams is appropriate for the Ku-Band receiver,

	T_{i-2}	T_{i-1}	T_i	T_{i+1}
A			ⓡ	ⓐ
B		ⓡ	ⓐ	
C		ⓡ	ⓐ	
D			ⓡ	ⓐ

what we measure in a double-switched FLUX procedure is then

$$\Delta T_i^+ \equiv 2T_i - (T_{i+1} + T_{i-1})\,. \tag{5.26}$$

With the sense of the azimuthal offset reversed, we have:

	T_{i-2}	T_{i-1}	T_i	T_{i+1}
A	ⓡ	ⓐ		
B		ⓡ	ⓐ	
C		ⓡ	ⓐ	
D	ⓡ	ⓐ		

so that the double-switched FLUX is now

$$\Delta T_i^- \equiv -2T_{i-1} + (T_i + T_{i-2})\,. \tag{5.27}$$

Thus to transform, we have simply:

$$\Delta T_i^+ = -\Delta T_{i+1}^-. \tag{5.28}$$

In reality, this is only approximately true. Under normal circumstances, a field is observed for a small range in parallactic angle $\psi_p = 0 \pm 5^\circ$ about upper culmination (transit), so that deviations from purely azimuthal separation of neighboring fields are less than 1.'9. The transformation in Equation (5.28), however, is equivalent to observing the i^{th} field over the parallactic angle range $\psi_p = 5 \pm 5^\circ$, so that the resulting beam is rotated, as in Fig. 5.6. The agreement between the data from 1996_1 and 1996_2 will thus depend on the angular scale of the structure producing the signals, improving with increasing angular scale. Also note that the effective pattern of the FLUX procedure has been inverted, so that the A and D integrations are now on-source, while the B and C are off-source. As Fig. 5.7 shows, most of the signals are produced by structure sufficiently large that the rotation of the effective beam pattern is not a significant effect, while the signals in some fields clearly have contributions from structure on smaller scales. Several of these, notably the first and fourth, contain point sources, as will be seen in the next chapter, and must be corrected before being compared.

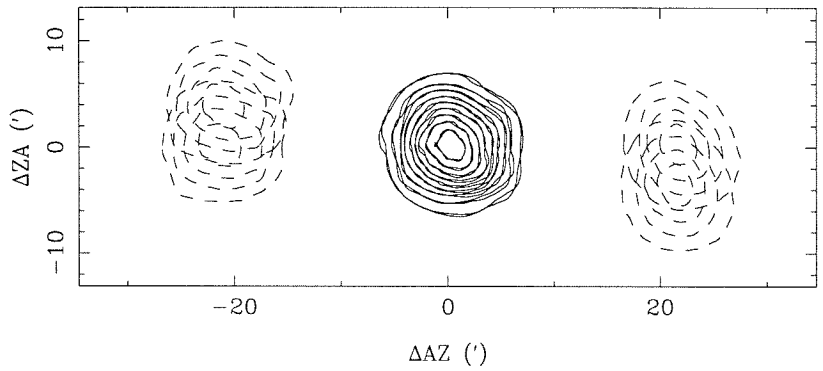

Figure 5.6 (top panel) The effective beam pattern for Ku-Band observations from the first half of 1996, superimposed on the beam pattern for the second half.

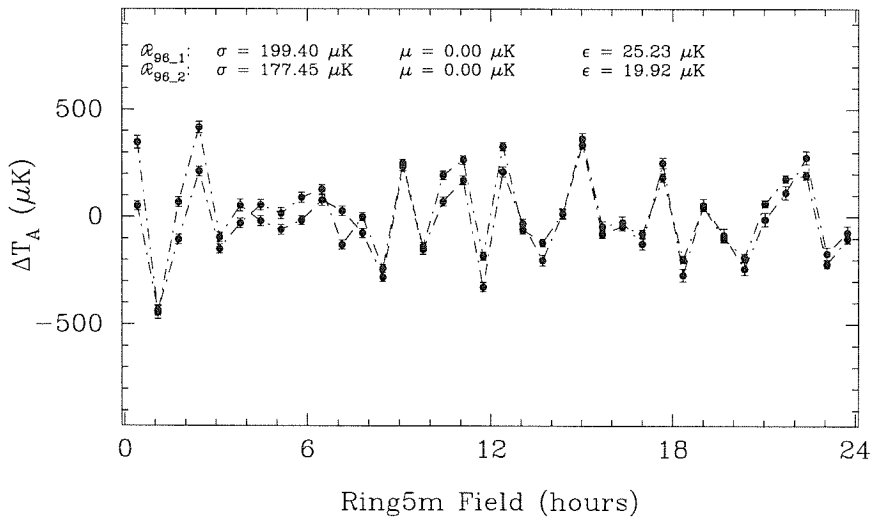

Figure 5.7 Final Ring5m field means for the two halves of the 1996 Ku-Band data, showing that most of the signals are produced by structure of angular scale larger than the beam, so that the beam rotation is not a significant effect.

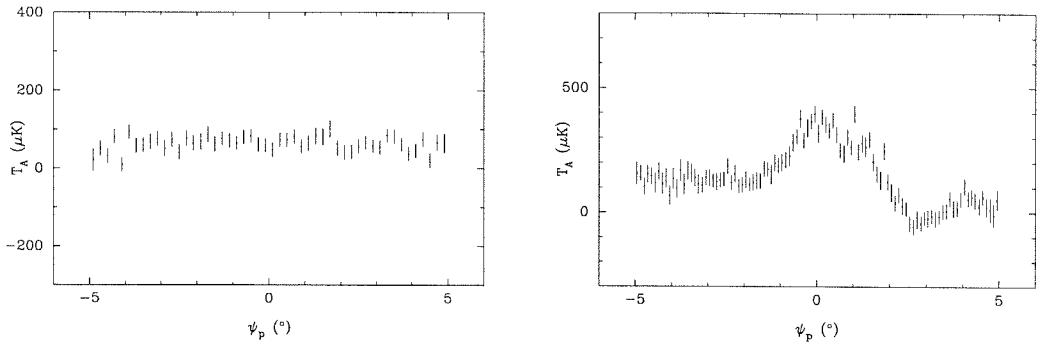

Figure 5.8 Parallactic angle dependence of the Ring Ka-Band data (left), and Ku-Band (right). The Ku-Band data show the characteristic signature of interference from the ground, while the Ka-Band data appear free of contamination.

5.4.4 Parallactic Angle Dependence

Local radio frequency interference (RFI) is an unlikely source of structure which appears fixed to the sky, since each field is observed over the same set of positions relative to the ground; to contribute anything other than a mean level to the Ring, local RFI would have to modulate repeatably with sidereal time over a period of many years. Nevertheless, for a signal fixed to the ground, the change in telescope elevation as a field is tracked through transit will introduce a characteristic parallactic angle dependence to the flux (see §3.1.2), and we can look for this signature in the Ring data.

The Ring5m means for all fields are shown in Fig. 5.8, binned in parallactic angle. We find no parallactic angle dependence in the Ka-Band data, indicating that the data are free from RFI contamination. The Ku-Band data, on the other hand, show a large variation in amplitude with parallactic angle, indicating significant contamination. The pattern, however, occurs with the same amplitude in each field, suggesting that RFI contributes only a mean level, constant over long timescales, to the Ring, so that our measurement of the variance should be unaffected. In spring of 1997, we observed a significant increase in interference at Ku-Band while observing near the NCP. This

was tracked to a series of large-amplitude spikes spanning 12.984-13.003 GHz and we were forced to shift our bandpass by 0.5 GHz to avoid these signals. Although this occurred after the data for the Ring experiment were acquired, the parallactic dependence of the Ku-Band Ring data can probably be traced to the same source.

5.4.5 Concordance

Final edited and calibrated means for the 36 Ka-Band and Ku-Band Ring fields are presented in Figures 5.9-5.14. Both data sets show structure well above the noise. In the first part of this chapter, we described a data editing scheme designed to eliminate data badly contaminated by known sources of systematic error; in the preceding few sections, we examined the edited data for any residual systematic effects and attempted to identify their source. Although we found evidence for long term changes in the mean for the Ring at Ka-Band, and evidence that the Ku-Band data may be affected by terrestrial interference, the data indicate that neither of these effects should compromise our measure of real structure in the CMBR. Although we have already mentioned in section §5.4.2 that the Ka-Band data are consistent with structure which repeats from year to year, we examine the internal consistency of both data sets more rigorously here.

We can test for consistency by breaking each data set into two halves in time, as shown in Figure 5.9 and Figure 5.10 for the three data divisions at each frequency, described in §5.2. The division was made such that each half contains equal amounts of data. While the time spanned by one season is insufficient to permit a sensible division of the data into halves relative to civil time (i.e., data taken during the day vs. data taken at night), we nonetheless find that on timescales over which the field positions have precessed significantly relative to the solar reference frame, the agreement between halves is excellent.

At Ka-Band (Figure 5.9), the differences in field means from one half to another

are consistent with zero, to within Gaussian statistics (i.e., $\mathcal{R}_{96\_1}$ deviates from $\mathcal{R}_{96\_2}$ by $> 1\sigma$ in fewer than a third of the fields, and by $> 2\sigma$ in one). Note that although each half contains equal amounts of data, $\mathcal{R}_{94\_2}$ has larger error bars than $\mathcal{R}_{94\_1}$, due to the large change in field means which were attributed to a change in the directional isolation of the Dicke switch in §5.4.2.

At Ku-Band (Figure 5.10), the agreement between halves is also quite good, although a few features should be noted. The first and second fields, which are dominated by a bright variable point source (discussed in the next chapter) in the wings of the Ku-Band beam, show considerable variation from year to year. Although no monitoring data exist for this source prior to late 1995 (see next chapter), absence of this source in the $\mathcal{R}_{95}$ (winter 1994 - spring 1995) data is consistent with the long-term trend seen in the source flux, which increased steadily by nearly 50% during the winter of 1995. The discrepancy in these fields between the $\mathcal{R}_{96\_1\_1}$ and $\mathcal{R}_{96\_1\_2}$ data is also qualitatively consistent with the change in source flux, although the magnitude of the change suggests that these fields are dominated by pointing errors, as discussed in the next chapter.

The systematic offset seen in the $\mathcal{R}_{96\_2}$ data may be due to a systematic pointing offset, which would not be surprising, given the number of instrumental changes which were made to the Ku-Band receiver during this time period. Note, however, that the field means from $\mathcal{R}_{96\_2\_1}$ are systematically low from 9h$-$19h LST, and systematically high from 19h $-$ 9h, relative to the means from $\mathcal{R}_{96\_2\_2}$. As these ranges correspond broadly to nighttime and daytime during this period, this effect is most likely due to the sun entering a sidelobe of the antenna power pattern.

One notable anomaly persists, namely the large discrepancy in fields OV5M1944 and OV5M2104 between the $\mathcal{R}_{94\_1}$ and $\mathcal{R}_{94\_2}$ data. As will be seen in the next chapter, there is no point source near these fields bright enough to produce this signal, either through variability or pointing errors, and this deviation remains unexplained.

TABLE 5.2
DATA CORRELATIONS

Ka			Ku		
C	r_{obs}	$p(r > r_{obs})$	C	r_{obs}	$p(r > r_{obs})$
r_{9412}	0.79	9.7×10^{-7}	r_{9512}	0.89	5.1×10^{-8}
r_{9512}	0.84	2.1×10^{-7}	r_{96_112}	0.85	1.9×10^{-7}
r_{9612}	0.73	6.7×10^{-6}	r_{96_212}	0.84	2.5×10^{-7}
r_{94-95}	0.89	4.3×10^{-8}	r_{95-96_1}	0.72	8.0×10^{-6}
r_{95-96}	0.94	8.7×10^{-9}	$r_{96\_1-96\_2}$	0.87	8.2×10^{-8}

Correlation coefficients are Pearson's r, for various combinations of data sets. Correlation between two halves of a season are denoted $r_{yr_{12}}$, while correlations between years are denoted $r_{yr1-yr2}$.

We note, however, that it appears only in the first half of 1995 and does not contribute significantly to the final field mean when all of the Ku-Band Ring data are averaged together.

Using *Pearson's r* (Press et al. 1988) to quantify the correlation between halves, we find that for all seasons, the data from both telescopes exhibit a remarkable degree of correlation, with the probability of obtaining a higher correlation by chance ranging from $6.7 \times 10^{-6} - 5.0 \times 10^{-8}$ (see Table 5.2). As repeatability is the first test of reality, the good agreement between independent data sets gives us confidence that what we are seeing at both frequencies is not due to instrumental transients. Note that for the Ring, the significance of any observed correlation is reduced by the double switching; as the fields are interlocked, the double-switching will introduce artificial correlations between initially uncorrelated data, and the quoted significances, appropriate for 36 *independent* samples, are typically reduced by a factor of ~ 100 (see §7.7).

Comparing the combined data sets from year to year (see Fig. 5.11 and Fig. 5.12), we find that over longer timescales (and over many receiver changes), both the Ka-Band and Ku-Band data are highly correlated, with probabilities as small as $few \times 10^{-8}$, leaving no doubt that the observed structure in the Ring is real.

To take the most cynical approach, having demonstrated that the signals are real, it now remains to show that the structure in the Ring originates outside the telescopes. As shown in Fig. 5.13, when the three seasons of Ka and Ku-Band data are combined to create a mean data set at each frequency, the observed correlation between the two data sets is remarkably high, with a linear correlation coefficient of $r_{obs} = 0.81$, and probability of observing a correlation higher than this under the hypothesis that the data are uncorrelated given by $p(r > r_{obs}) = 6.5 \times 10^{-7}$. The good agreement between several years of data from two independent telescopes demonstrates that the observed structure in the Ring is independent of instruments and must be celestial in origin. (As noted in §5.4.4, each field is observed at what is essentially a fixed position relative to the ground, so that contamination from RFI should affect each field equally, unless conspiratorially arranged to produce repeatable sidereal fluctuations over many years.)

Since the differential CMBR intensity is approximately $\Delta I = 2k\Delta T_B \nu^2/c^2$, signals produced by the microwave background should be reduced at 14.5 GHz by a factor of ~ 5 relative to 31.7 GHz. When displayed to equal intensity scales, as in Fig. 5.13, the Ring data show several fields, notably in the regions 0h – 3h and 12h – 18h, with equal intensities at the two frequencies, implying that $\alpha \simeq 0$ (where $\Delta I \propto \nu^{\alpha}$), the approximate signature of thermal bremsstrahlung emission. The origin of these signals is investigated in the next two chapters. On the other hand, we note that the regions 4h – 8h and 18h – 0h show the spectral signature of the microwave background, as can more readily be seen when the data are plotted to equal temperature scales, as in Fig. 5.14, since the CMBR temperature is independent of frequency to first order.

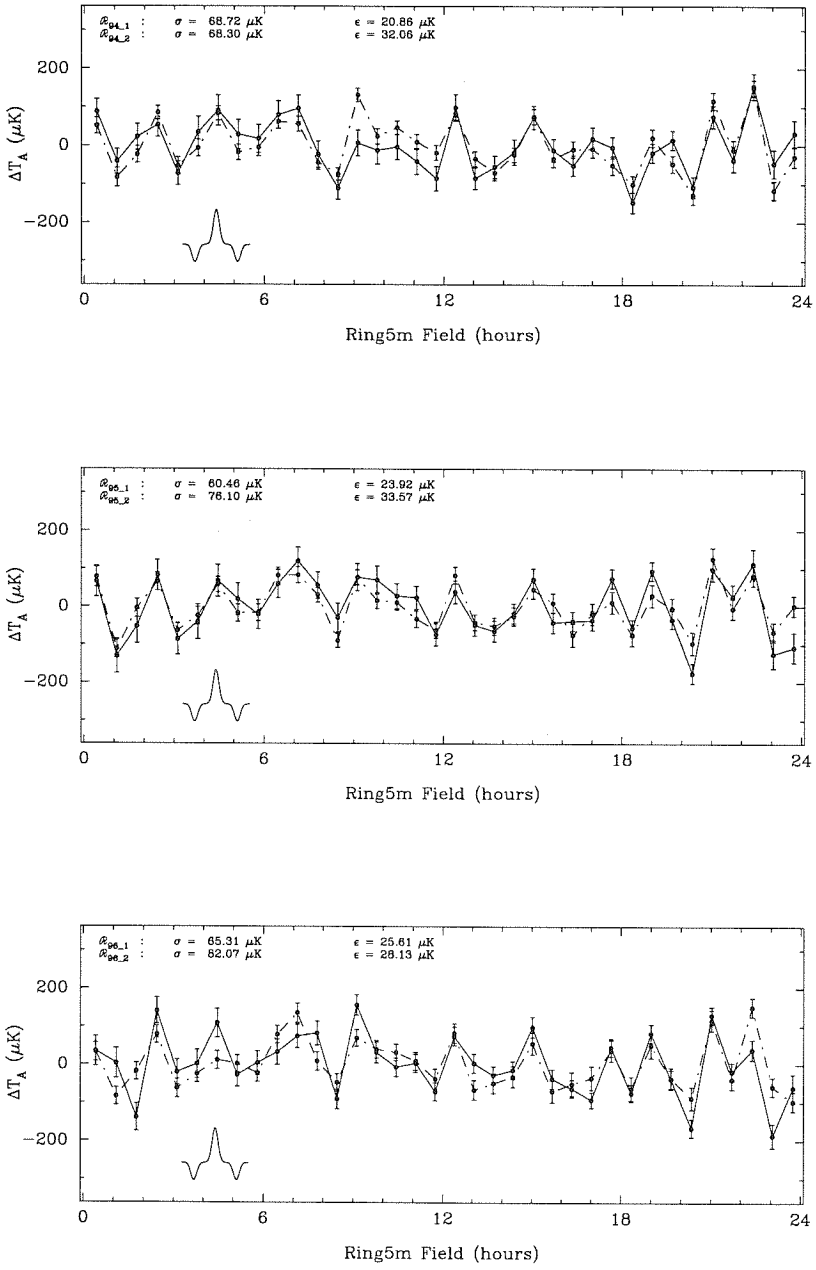

Figure 5.9 Comparison of Ka-Band data, by division into equal halves in time, for 1994 (top panel), 1995 (middle) and 1996 (bottom). The first half is indicated by the dot-dashed line, while the second is the solid line. The data sets show a high degree of correlation over timescales during which the field positions have precessed significantly relative to the solar frame. The larger error bars for $\mathcal{R}_{94\_2}$ are due to the fact that these data straddle the large change in the Ring mean which occurred when the TRW HEMT was replaced.

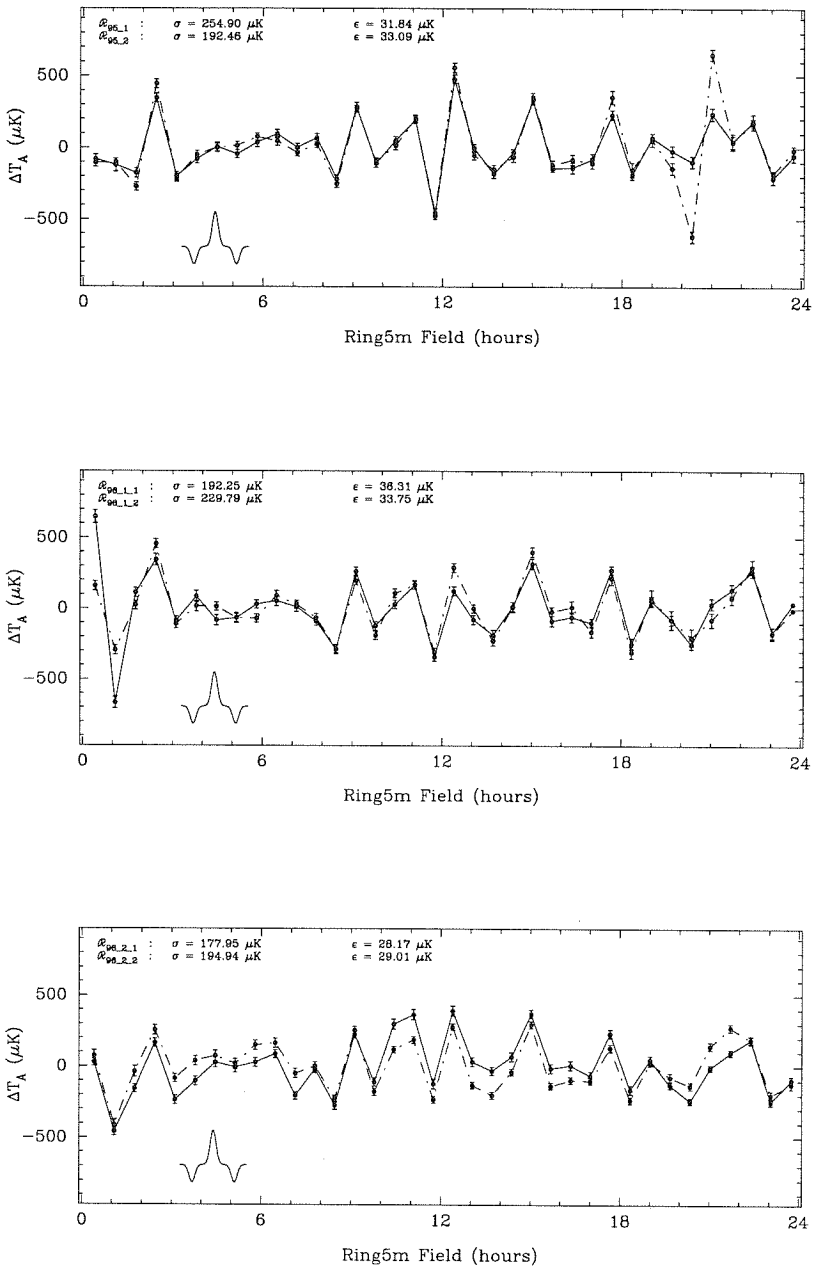

Figure 5.10 Comparison of Ku-Band data, by division into equal halves in time, for 1995 (top panel), 1996_1 (middle) and 1996_2 (bottom). The first half is indicated by the dot-dashed line, while the second is the solid line. The anomalous signal in fields OV5M2024 and OV5M2104 in the first half of 1995 remains unexplained by known point sources, and may be due to extended structure on the sky at 14.5 GHz. Note also the systematic offsets between $\mathcal{R}_{96\_2\_1}$ and $\mathcal{R}_{96\_2\_2}$, which appear to be diurnal.

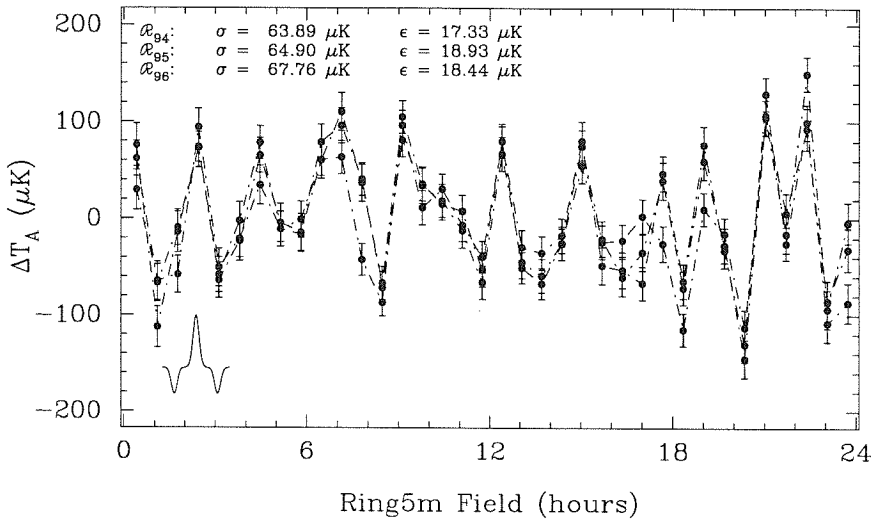

Figure 5.11 Ring5m Ka-Band data from winter of 1993 ($\mathcal{R}_{94}$) to winter of 1995 ($\mathcal{R}_{96}$). At bottom left is the effective beam pattern produced by the double-switching, i.e., the effective point-spread function for the OVRO telescopes.

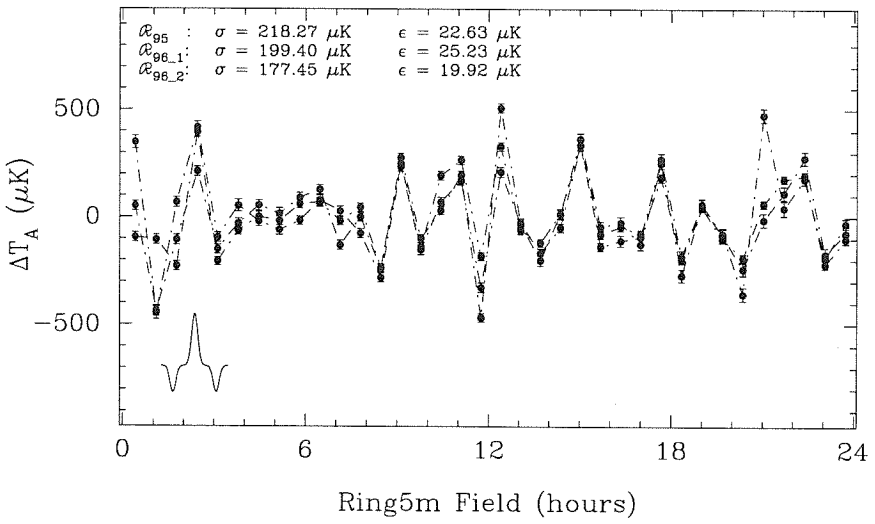

Figure 5.12 Ring5m Ku-Band data from winter of 1994 ($\mathcal{R}_{95}$) to winter of 1995 ($\mathcal{R}_{96}$)

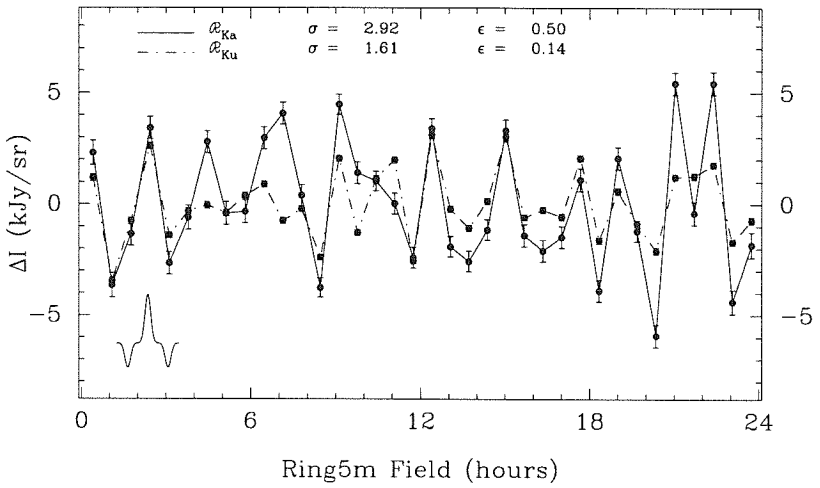

Figure 5.13 Comparison of the mean Ring5m Ka data (solid line) with the mean Ring5m Ku-Band data (dotted line) from 1994-1996. Both are plotted to the same intensity scale, in kJy/sr.

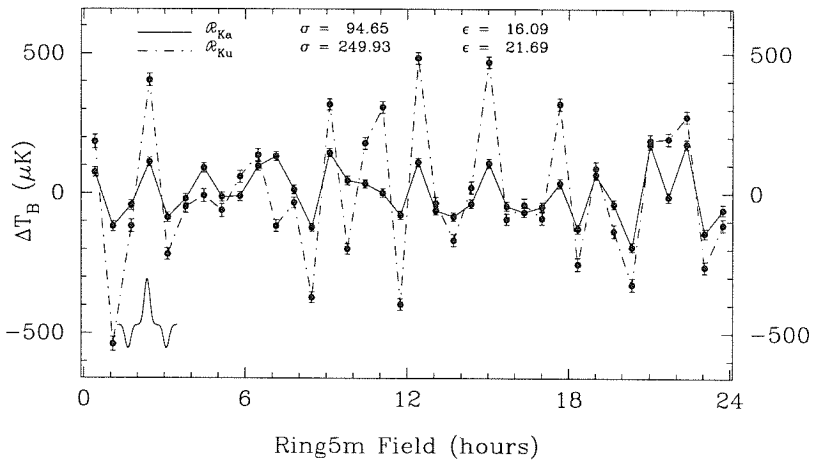

Figure 5.14 Comparison of the mean Ring5m Ka data (solid line) with the mean Ring5m Ku-Band data (dotted line) from 1994-1996. Both are plotted to the same brightness temperature scale, in μK.

TABLE 5.3
RING FIELD MEANS[†]

Field	ΔT_{Ka} (μK)	σ_{Ka} (μK)	ΔT_{Ku} (μK)	σ_{Ku} (μK)
OV5M0024	144.46	17.70	332.21	24.34
OV5M0104	−48.95	17.83	−390.41	25.07
OV5M0144	26.18	17.20	30.69	23.05
OV5M0224	180.55	15.90	552.72	22.41
OV5M0304	−16.76	16.48	−69.90	20.81
OV5M0344	49.80	17.49	99.78	21.87
OV5M0424	160.00	16.19	139.19	23.16
OV5M0504	55.98	16.51	86.40	23.56
OV5M0544	58.33	16.58	207.17	21.50
OV5M0624	165.62	15.80	284.51	21.95
OV5M0704	201.69	16.14	31.40	21.14
OV5M0744	82.11	15.71	114.23	18.91
OV5M0824	−52.72	14.10	−224.10	19.52
OV5M0904	214.62	14.73	465.66	19.75
OV5M0944	114.95	15.93	−50.65	18.82
OV5M1024	102.99	14.37	326.20	21.32
OV5M1104	70.14	15.25	455.32	20.71
OV5M1144	−8.70	15.17	−248.90	20.83
OV5M1224	179.49	14.78	631.48	21.48
OV5M1304	7.38	14.98	112.23	21.14
OV5M1344	−14.28	15.04	−20.52	21.14
OV5M1424	31.85	15.18	168.04	21.72
OV5M1504	176.52	15.91	616.84	20.24
OV5M1544	23.53	16.24	55.14	20.18
OV5M1624	1.22	15.92	106.65	22.19
OV5M1704	21.43	15.73	58.56	22.42
OV5M1744	104.87	16.48	467.21	22.20
OV5M1824	−56.98	15.65	−105.51	22.70
OV5M1904	136.23	16.27	237.57	22.88
OV5M1944	30.41	15.39	12.49	22.89
OV5M2024	−122.97	16.51	−177.99	22.74
OV5M2104	245.30	16.27	336.88	21.98
OV5M2144	56.29	16.66	342.49	22.29
OV5M2224	245.74	16.65	422.02	21.40
OV5M2304	−73.07	17.75	−115.77	20.90
OV5M2344	9.94	18.64	34.51	21.77

[†]Equivalent R-J brightness temperature

Chapter 6

Discrete Source Contamination

6.1 VLA X-Band Survey

In December of 1994, the Ring fields were observed for 10 hours at $8 - 8.5$ GHz (X-Band), using the VLA in C configuration. The half-power point of the VLA primary beam at X-Band ($8 - 8.5$ GHz) is at 2.7, corresponding to the 67% point of the 5.5-meter beam. To extend our coverage of the Ring fields, we performed a hexagonal 7-field mosaic of observations centered on each field, providing uniform sensitivity out to the 23% contour of the 5.5-meter beam, with a reduction in sensitivity to 50% only at the $\sim 3\%$ contour of each Ring field. Phase calibration was performed every 12 minutes using the nearby sources 1058+812, 1632+825 and 0626+820. The flux density scale was determined by observations of 3C 286, whose flux density at 8 GHz is assumed to be 5.23 Jy (Baars et al. 1977). Calibration and editing of these data were performed at the VLA site using the NRAO AIPS software package. Slightly less than 2 minutes of data were obtained on each pointing, yielding a uniform sensitivity of $\lesssim 0.21$ mJy to the 23% contour of each Ring field. Since the sensitivity of the 5.5-meter to point sources is 4.1×10^{-3} K Jy^{-1}, for sources with spectral indices in the range $\alpha \leq +1$ (where $S_\nu \propto \nu^\alpha$), any residual contribution to the Ring5m from subtraction of these sources will be < 3 μK.

An automatic mapping procedure was developed using the Caltech difference mapping package DIFMAP (Shepherd et al. 1995). The UV data for each field was initially gridded and Fourier transformed to a 1024×1024 grid with $1''$ resolution, covering the VLA primary beam out to the first nulls. An initial phase self-calibration (Perley 1988, Thompson 1991) was performed on the highest peak if the map contained any sources $> 8\sigma$, where σ is the *rms* in the dirty map. Sources were then iteratively located by successively finding the highest peak $> 6\sigma$ above the noise. A smaller map on a 512×512 grid with $0\farcs5$ resolution was made at the location of each source, the VLA beam response was deconvolved via a CLEAN algorithm (Perley 1988) and the map self-calibrated to the updated model. When no further sources were detected above 6σ, the clean components were deleted and Gaussian models fitted to each peak. This procedure was checked by manual inspection of the residual maps after the final model fit. The resulting catalogue of 39 distinct sources with brightest components having $S_{8\mathrm{GHz}} > 1.7$ mJy is presented in Table 6.3. Several of these sources have multiple components, consisting of a core and one or two prominent lobes, while others show two point-like components closer than one would expect from random superpositions of unrelated sources. Flux densities for these components were determined from subsequent observations (see below) by fitting multi-component UV models. The location of each model component is listed in Table 6.3.

6.2 Variability Observations

During the period bracketing the 1996 Ring5m season, we obtained monthly VLA observations at X and U-Band (14.6-15.3 GHz) of sources found in the initial X-Band survey, allowing removal of variable contributions to the Ring data from sources which vary on timescales of $\gtrsim 1$ month. The U-Band observations are a direct

TABLE 6.1
SUMMARY OF VLA OBSERVATIONS

Date			X-Band	U-Band	K-Band
31 Dec 94	94/365	(49717)	√		
02 Oct 95	95/275	(49992)	√	√	
05 Nov 95	95/309	(50026)	√	√	√
24 Nov 95	95/328	(50045)	√	√	
07 Dec 95	95/341	(50058)	√	√	
17 Dec 95	95/351	(50068)	√	√	
30 Dec 95	95/364	(50081)	√		√
14 Jan 96	96/014	(50096)	√	√	√
09 Feb 96	96/040	(50122)	√	√	√
23 Mar 96	96/083	(50165)	√	√	
25 Apr 96	96/116	(50198)	√	√	√
12 Nov 96	96/317	(50399)	√	√	

record of source contributions to our lowest frequency data, while the simultaneous measurements at X-Band allow extrapolation of the source flux densities to Ka-Band. For the brightest sources, some observations at K-Band (20 GHz) were also obtained.

From October 1995 – May 1996, Ring5m sources were observed at 11 separate epochs, in BnA, B, CnB, C and DnC configurations. Due to the time constraints of the U-Band observations (the approximate 10 minute sensitivity of the VLA at U-Band is 0.17 mJy, compared to 0.045 mJy at X-Band, so that 80% of our observing time was spent at U-Band), not all sources could be observed at each epoch. Sources which early-on showed significant variability were observed at each epoch, while any remaining sources which could not be observed at a given epoch were observed during the next. Typical *rms* noise in the X-Band maps was 0.25 mJy, while at U-Band, sensitivities of 0.5 mJy were achieved.

The UV data from all epochs at which a source was observed are combined to form a single map at each frequency for each source in the original survey. This provides a high-sensitivity map from which an accurate model for the source spatial structure can be determined. Model-fits to the combined maps also provide a measurement of

the mean flux at each frequency. These are given in Table 6.4.

To determine which sources are variable, the UV data from each epoch are fit to the spatial template derived from the mean X-Band map for each source. The signal-to-noise ratio (SNR) in the dirty map is used as a rejection criterion; although the individual epoch maps are not of uniform quality, it is found by inspection that rejecting fluxes for which SNR < 5 eliminates most observations in which a source is clearly not detected. In addition, data with SNR < 5 in the residual map are also rejected. In general, it is found that sources with $S_X < 2$ mJy were not reliably detected in the individual epoch maps.

To reduce systematic gain calibration errors from epoch to epoch, sources for which > 5 detections were obtained (allowing a reasonable estimate of the mean flux) are used to derive a gain curve directly from the sources. The flux record for each source is divided by the mean, and all normalized fluxes at each epoch are averaged together to form a relative gain curve at each frequency. The resulting averages of the X-Band flux densities from the individual maps are in good agreement with the fluxes derived from the mean maps (see Table 6.4), and this procedure reduces the scatter in the flux records of most sources.

The flux records at X-Band are fitted to a mean level, and we take to be variable any source for which $\chi^2_r > 1 + \sqrt{2/(N-1)}$, where $\sqrt{2/(N-1)}$ is the expected standard deviation of χ^2_r (see Appendix C); since $N = 8$ for most sources, we treat as non-variable any source for which $\chi^2_r \leq 1.5$. In all, three sources are clearly variable at both X and U band: 0032+50_0, 1745+44_0, and 2317+52_0. Five other sources show possible variability at X-band; of these, 0702+45_0, 1148+42_0 and 1216+51_0 show no variability at U-Band, perhaps because of the larger error bars, and 1427+47_0 and 1901+51_0 are too weak for reliable detection at U-Band on an epoch-by-epoch basis. Several of the multi-component sources have $\chi^2 > 1.5$, but this is an artifact of the model fitting. When the spatial template for a source is fit

to the UV data at each epoch, the amplitudes of the components are allowed to vary; given the weakness of some of the components, there is typically degeneracy between models with different relative amplitudes for the fluxes of different components. The total flux, however, is conserved and is a better indicator of true variability for these sources. The χ^2 resulting from a fit to the mean total flux is given in the far right column of Table 6.4.

For sources which show no variability at X-Band, we assume no variability at U-Band and use the spectral index derived from the mean map when extrapolating the flux of these sources to Ka-Band. For those sources which are variable, if the spectral index measured at individual epochs shows no variability (within errors), or if the source is too weak to be detected at U-Band, we use the interpolated X-Band flux record, plus the spectral index derived from the mean maps. If the spectrum of a source is varying, the spectral index at each epoch must be used when estimating the contribution of a source at Ka-Band. Figure 6.1 shows that only 0032+50_0 and 1745+44_0 show clear signs of spectral variability.

In summary, when extrapolating to Ka-band, the mean flux densities and spectral indices derived from the combined maps will be used for all sources, except:

- for 0702+45_0, 1148+42_0, 1216+51_0, 1427+47_0, 1901+51_0 and 2317+52_0, we use the X-Band flux record, along with the mean spectral index
- for 0032+50_0, and 1745+44_0, we use the spectral index and flux density at each epoch,
- for these sources, for years prior to 1996, we use the mean of the extrapolated Ku-Band and Ka-band fluxes, with errors given by the standard deviation of these extrapolated quantities in 1996.

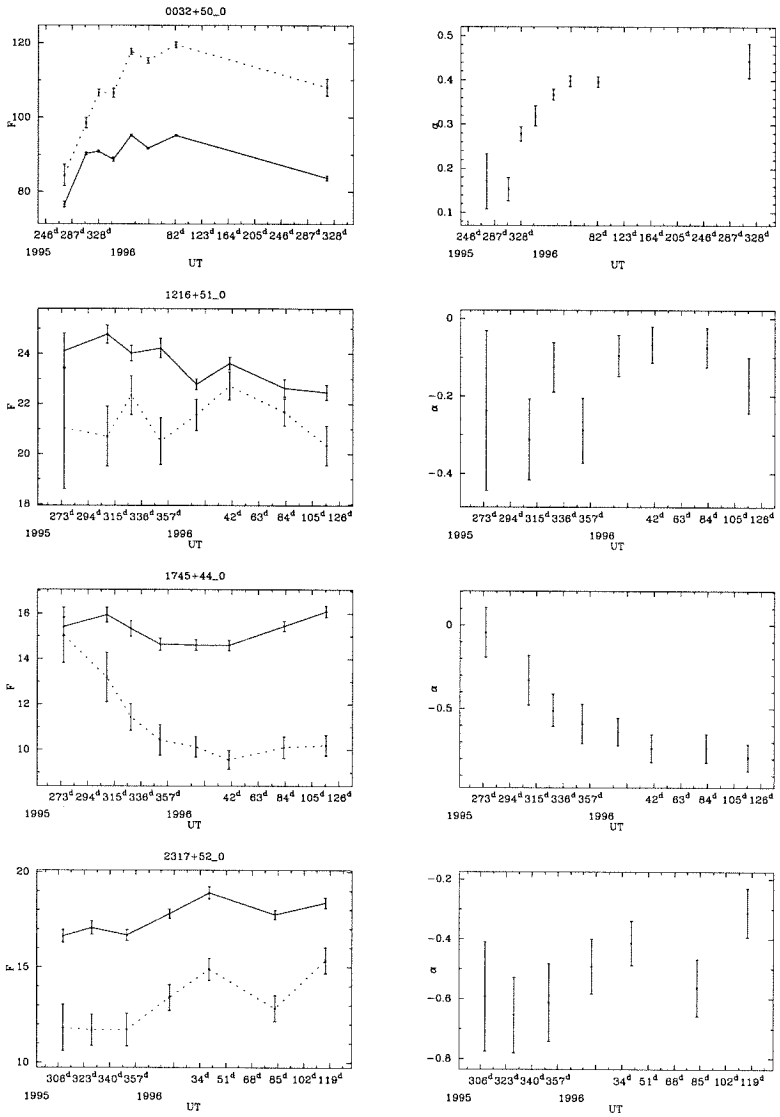

Figure 6.1 (left) X and U-Band (dotted line) flux records of the four bright variable sources (in mJy). (right) Spectral index records. Of the four, only 0032+50_0 and 1745+44_0 have $\chi^2_r > 1 + \sqrt{2/(N-1)}$, indicating spectral index variability.

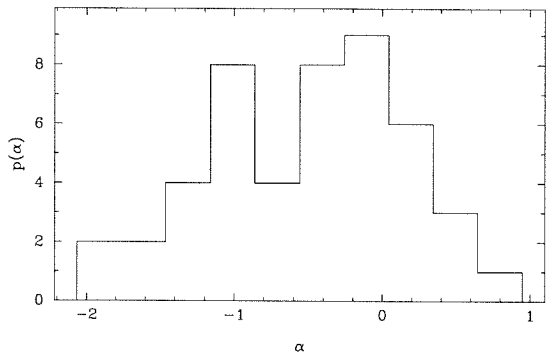

Figure 6.2 The distribution of spectral indices, $p(\alpha)$, as derived from the 47 discrete sources detected at both X and U-Band.

6.3 Non-Detections

For any source not detected at U-Band, we can take a Bayesian approach (Sivia 1996) to estimate its flux density at higher frequencies. The probability distribution for the flux density at U-Band, given a detection at X-Band and an upper limit at U-Band, can be written, up to an arbitrary normalization, as

$$p(f_U|D) \propto p(D|f_U) \times p(f_U), \tag{6.1}$$

where $p(D|f_U)$ is the probability of the data (i.e., of not detecting a source of flux density f_U), and $p(f_U)$ represents our prior knowledge about the U-Band flux, given all available background information. (In the following, it is to be understood that $p(x)$ is symbolic notation for the probability distribution of the variate x, and is not to be taken literally as a functional form; i.e., $p(x)$ should really be written as $p_x(x)$.) At the very worst, since we know from radio surveys that spectral indices outside of some range $\alpha_{min} \leq \alpha \leq \alpha_{max}$ rarely occur, we could construct $p(f_U)$ from the observed X-Band flux by assuming $p(\alpha)$ to be uniform within this range. In fact, we can do quite a bit better than this, since $p(\alpha)$ can be constructed directly from the sources for which firm detections at both frequencies were obtained. The distribution

TABLE 6.2

MAXIMUM LIKELIHOOD ESTIMATES OF FLUX DENSITIES FOR UNDETECTED SOURCES

Name	$\bar{S}_U$ (mJy)	$\bar{S}_{Ka}$ (mJy)
0022+53_0:	$0.78^{+0.16}_{-0.06}$	$0.20^{+0.11}_{-0.04}$
0630+53_0:	$0.69^{+0.19}_{-0.06}$	$0.18^{+0.14}_{-0.04}$
0630+53_1:	$0.32^{+0.17}_{-0.10}$	$0.09^{+0.22}_{-0.05}$
0634+56_0:	$1.01^{+0.14}_{-0.06}$	$0.26^{+0.09}_{-0.04}$
0938+50_0:	$0.84^{+0.13}_{-0.09}$	$0.22^{+0.10}_{-0.05}$
1146+54_1:	$0.39^{+0.15}_{-0.05}$	$0.11^{+0.12}_{-0.04}$
1433+51_0:	$1.06^{+0.11}_{-0.07}$	$0.27^{+0.08}_{-0.04}$
1511+55_1:	$0.49^{+0.21}_{-0.06}$	$0.14^{+0.17}_{-0.05}$
1731+56_0:	$0.83^{+0.29}_{-0.10}$	$0.23^{+0.21}_{-0.09}$

of α measured from the 47 discrete source components (recall that of the 39 sources, several have multiple components) is shown in Fig. 6.2. Given $p(\alpha)$ and $p(f_X)$, which we assume to be a Gaussian of width σ_X, where σ_X is the noise in the corresponding X-Band map, we can derive $p(f_U)$ by the usual transformation of variables. The null detection at U-Band implies that $p(D|f_U)$ is just the noise distribution in the U-band map, since a null detection implies that any source flux is counteracted by noise at the same level.

In practice, we take the computationally simpler route of computing $p(f_U|D)$ via Monte Carlo simulation for each of the 9 sources not detected at U-Band. The distribution $p(f_U)$ is first constructed by drawing random deviates from $p(f_X)$ and $p(\alpha)$. Once $p(f_U)$ is known, we can construct $p(f_{Ka}|D)$ from $p(f_X)$ and $p(f_U|D)$. Maximum likelihood estimates for the source flux at Ku and Ka-Band are then obtained by maximizing $p(f_U|D)$ and $p(f_{Ka}|D)$, respectively, and are given in Table 6.2. A sample calculation is shown in Fig. 6.3 for the source 1731+56_0.

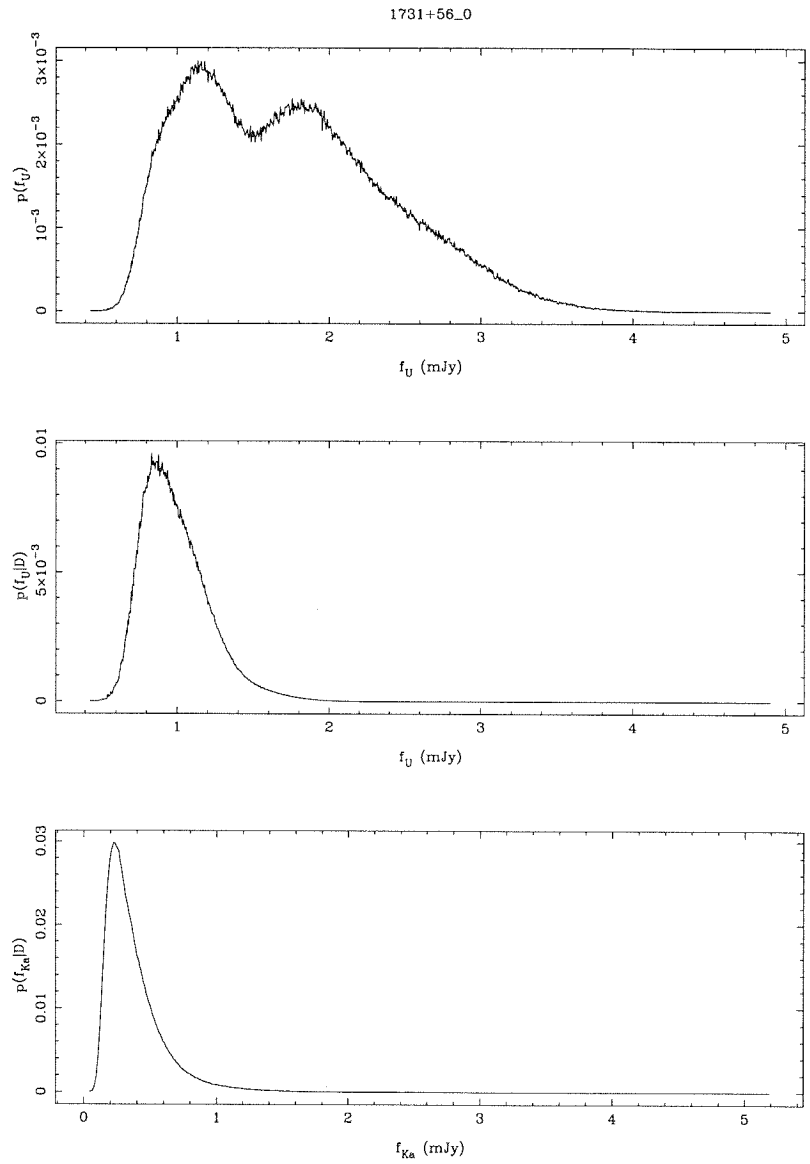

Figure 6.3 Maximum Likelihood analysis for 1731+56_0. Top panel is $p(f_U)$, the prior distribution for f_U, determined from the spectral index distribution $p(\alpha)$ and the detected flux at X-Band. Note the double peak, which occurs because $p(\alpha)$ is bimodal (see Figure 6.2). Middle panel is $p(f_U|D)$, the distribution of U-Band fluxes given the data, i.e., the upper limit at U-Band. At bottom is the distribution of Ka-Band fluxes $p(f_{Ka}|D)$ determined from $p(f_X)$ and $p(f_U|D)$.

6.4 Effect of Point Sources on the Ring5m Fields

Once the discrete source contribution to the Ring fields has been characterized, their effect can in principal be removed on a point-by-point basis. The Dicke-switching is always azimuthal, so that astronomical sources rotate through the beam pattern as a Ring field is tracked for a finite range of parallactic angle about transit. Thus the flux from a given source is weighted by the effective beam pattern at the location of the source during each measurement.

Consider the measured signal in the i^{th} field. In the presence of point sources, what we measure is

$$\Delta T_{i,j}^{meas} = T_i - \frac{1}{2}(T_{i+1} + T_{i-1}) + N_{i,j} + \sum_k b_{i,j,k} F_{j,k}^{true}. \tag{6.2}$$

Here, $b_{i,j,k}$ is the beam weighting factor for the k^{th} source in the i^{th} field at the time of the j^{th} measurement, and similarly $F_{j,k}$ is the flux of the k^{th} source at the time of the j^{th} measurement, modulo the telescope sensitivity (4.52), which converts Jy to antenna temperature. $N_{i,j}$ is the random noise in the i^{th} field at the j^{th} time.

If we could measure the flux density of each source at the time of each Ring5m observation to some accuracy $\sigma_{j,k}$, this would mean that we have measured

$$F_{j,k} = F_{j,k}^{true} + N_{j,k}, \tag{6.3}$$

where $N_{j,k}$ is the noise (*rms* in a VLA map, say) in the measurement of source k at time j, with associated variance $\sigma_{j,k}^2$. Then the signal from the CMBR alone would be constructed by forming the difference

$$\Delta T_{i,j}^{cmb} \equiv \Delta T_{i,j}^{meas} - \sum_k b_{i,j,k} F_{j,k}, \tag{6.4}$$

which gives

$$\Delta T_{i,j}^{cmb} = T_i - \frac{1}{2}(T_{i+1} + T_{i-1}) + N_{i,j} - \sum_k b_{i,j,k} N_{j,k}. \tag{6.5}$$

The variance of ΔT_i^{cmb} is then given (assuming covariances vanish, as the noise in the source maps is uncorrelated with the noise in the CMBR data) by

$$V(\Delta T_i^{cmb}) = V(N_i) + \sum_k V(b_{i,k} N_k). \tag{6.6}$$

The variance of the product of two variables is given by

$$V(x_1 x_2) = V(x_1)V(x_2) + \langle x_2 \rangle^2 V(x_1) + \langle x_1 \rangle^2 V(x_2), \tag{6.7}$$

where $\langle\ \rangle$ denotes expectation, or time average, so that we have

$$\sum_k V(b_{i,k} N_k) = \sum_k \left\{ V(b_{i,k})V(N_k) + \langle N_k \rangle^2 V(b_{i,k}) + \langle b_{i,k} \rangle^2 V(N_k) \right\} \tag{6.8}$$

$$= \sum_k \langle b_{i,k}^2 \rangle V(N_k), \tag{6.9}$$

since $\langle N_k \rangle = 0$.

From (6.6), the variance in each field is then given by

$$C_{ii} = \sigma_i^2 + \sum_k \langle b_{i,k}^2 \rangle \sigma_k^2, \tag{6.10}$$

where σ_i is the variance in the CMBR measurements, and σ_k^2 is the variance in the flux for source k. (Here, we denote the variance as C_{ii} to make contact with the covariance matrix discussed in the next two chapters.) This is the appropriate form of the variance to use if the sources are measured on a point-by-point basis. If the sources are not variable, so that we can take $F_{j,k} = \langle F_k \rangle$, σ_k above is just given by the error in the mean source flux.

If the sources are variable, and only the long-term mean is known, this is equivalent to forming the quantity

$$\Delta T_{i,j}^{cmb} \equiv \Delta T_{i,j}^{meas} - \sum_k b_{i,j,k} \langle F_k \rangle. \tag{6.11}$$

Then we have

$$\Delta T_{i,j}^{cmb} = T_i - \frac{1}{2}(T_{i+1} + T_{i-1}) + N_{i,j} - \sum_k b_{i,j,k}(F_{j,k}^{true} - \langle F_k \rangle), \tag{6.12}$$

and

$$V(\Delta T_i^{cmb}) = V(N_i) + \sum_k V(b_{i,k}(F_k^{true} - \langle F_k \rangle)), \tag{6.13}$$

or

$$C_{ii} = \sigma_i^2 + \sum_k \langle b_{i,k}^2 \rangle V(F_k), \tag{6.14}$$

where $V(F_k)$ is the variance of the source flux due to variability.

6.4.1 Weighted Means

In §5.4, it was demonstrated that the maximum likelihood estimator for the mean is the sample mean weighted by the individual variances. The variance associated with each quantity

$$\Delta T_{i,j}^{cmb} \equiv \Delta T_{i,j}^{meas} - \sum_k b_{i,j,k} F_{j,k} \tag{6.15}$$

is given by the estimated variance from the system noise, plus the variance due to the source flux subtraction:

$$\epsilon_{i,j}^2 = \sigma_{i,j}^2 + \sum_k b_{i,j,k}^2 \sigma_{j,k}^2, \tag{6.16}$$

suggesting that the maximum likelihood estimate of the mean is

$$\langle \Delta T_{i,j}^{cmb} \rangle = \frac{\sum_j \left\{ \Delta T_{i,j}^{meas} - \sum_k b_{i,j,k} F_{j,k} \right\} / \epsilon_{i,j}^2}{\sum_j 1/\epsilon_{i,j}^2}, \tag{6.17}$$

which is just another way of saying that data most strongly affected by point sources should be down-weighted when computing the mean from the CMBR signal.

6.4.2 Results

The estimated contribution of point sources to the 1996 Ka and Ku-Band data is shown in Fig. 6.4. Very few of the point sources are strong enough or close enough to a field center to contribute a significant signal, with the notable exception of 0032+50,

which dominates the signal in the first field, and affects the two adjacent fields through the double switching. Because the sources were monitored during 1996, formal errors from the point source subtraction are quite small, typically a few μK. Since many of the Ring5m sources lie on the exponential cutoff of the 7.'35 beams, however, small errors in pointing can produce dramatic changes in the flux received from a source, so that the variance due to pointing errors will dominate the uncertainties. Field errors in Fig. 6.4 are the computed field-to-field variance, assuming Gaussian *az* and *za* pointing errors with $\sigma_{az} = \sigma_{za} = 0.'3$ (see §2.9). At Ka-Band, the largest uncertainty due to pointing is 17 μK, while at Ku-Band, the largest error is 70 μK, comparable to the variance of the brightest variable source in the Ring, making pointing the dominant uncertainty even for periods when the sources were not monitored.

In all subsequent analysis, a single combined data set will be used at each frequency. Although the errors due to point-source variability are not comparable from year to year, we can define a mean error for each field

$$\sigma = \frac{\sum_j \sigma_j w_j}{\sum_j w_j}, \tag{6.18}$$

where σ_j is the error from source subtraction from season j, and w_j is the sum of the weights

$$w_j = \sum_k^{N_j} 1/\epsilon_{jk}^2 \tag{6.19}$$

from season j. This mean error should accurately reflect the relative contribution to the mean of data for which we have source monitoring. To these we add in quadrature the statistical errors for each field mean, and the error per field due to pointing uncertainties. The final mean data sets for the Ring are shown in Fig. 6.6 and Fig. 6.7.

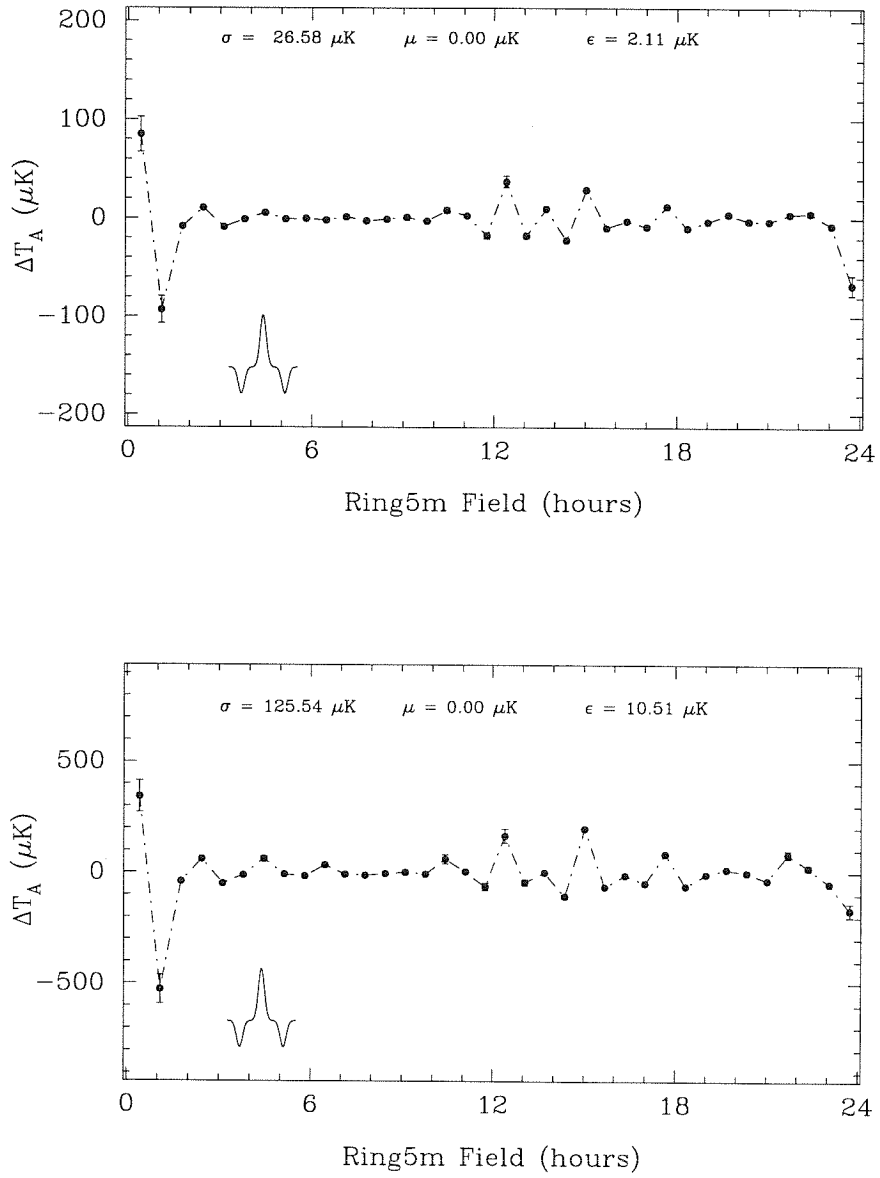

Figure 6.4 Point source contribution to the Ka-Band Ring data (top), and to the Ku-Band data (bottom), extrapolated from VLA monitoring at X and U-Band. Error bars reflect uncertainties in the source flux due to pointing only. At bottom left is the effective response to a point source near a Ring field center.

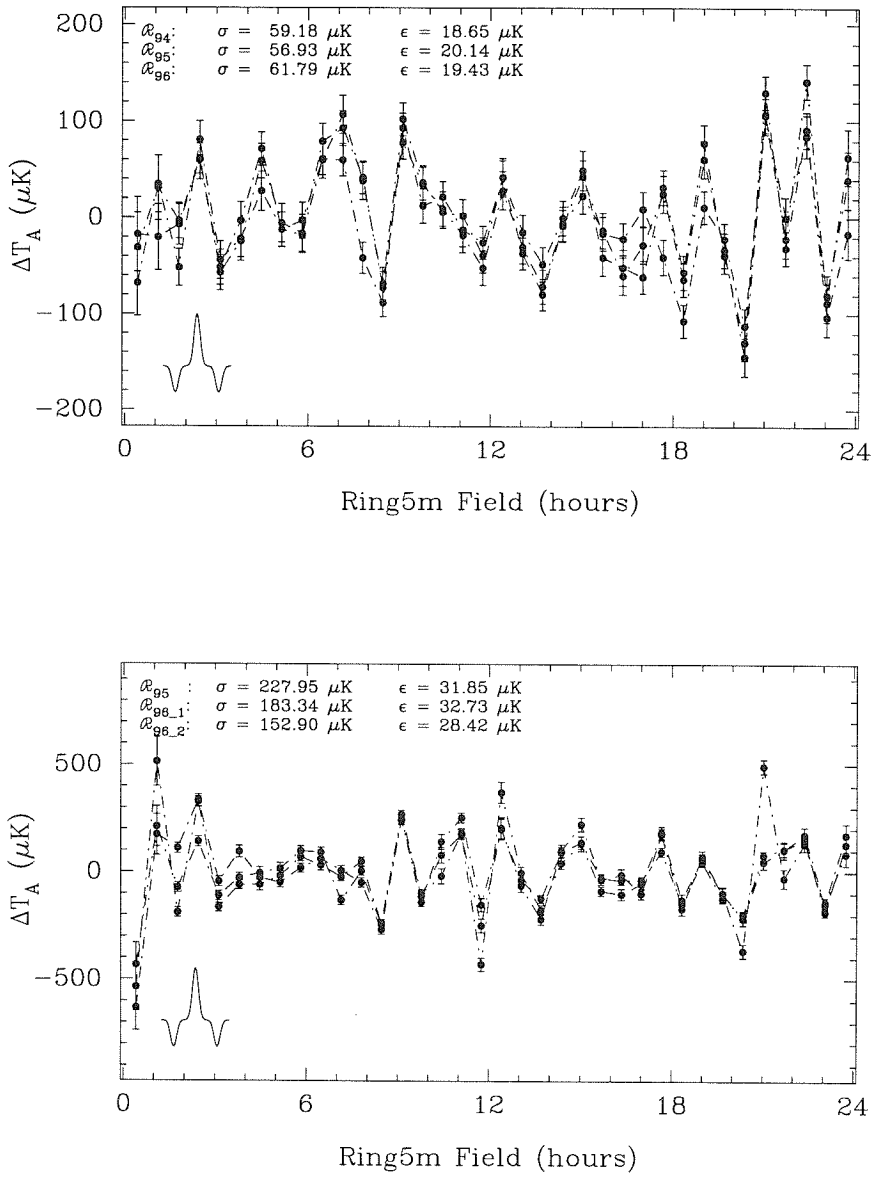

Figure 6.5 Source-subtracted Ka-Band (top) and Ku-Band (bottom) Ring data.

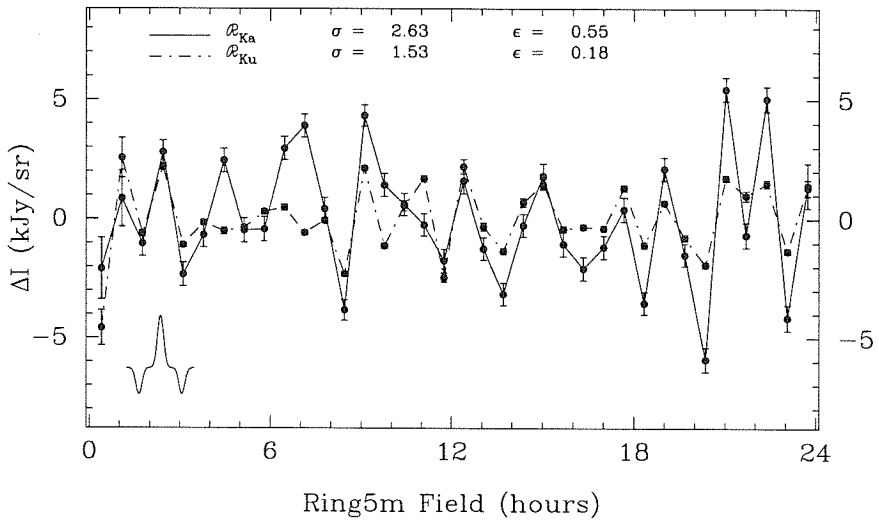

Figure 6.6 Mean source-subtracted Ka (solid line) and Ku-Band (dotted line) Ring data, to equal intensity scales.

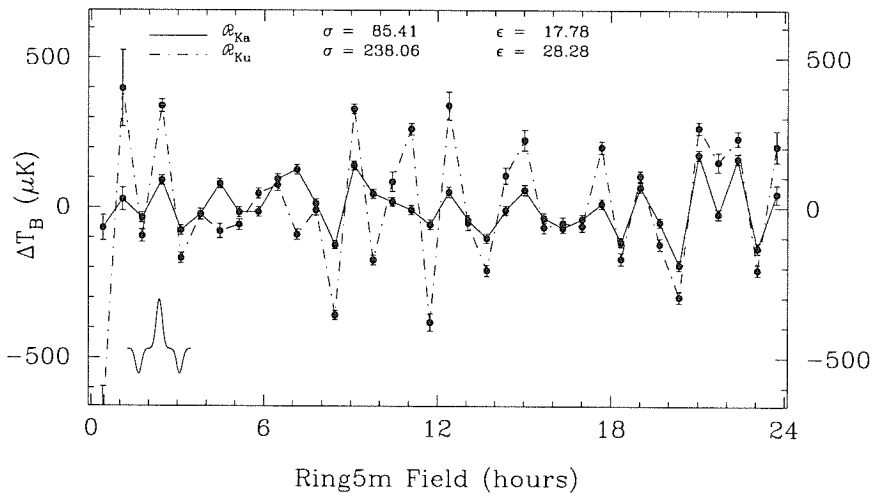

Figure 6.7 Mean source-subtracted Ka (solid line) and Ku-Band (dotted line) Ring data, plotted to equal R-J brightness temperature scale.

TABLE 6.3
X-BAND RING5M SOURCES

Name	α (2000)	δ (2000)	Comments
0022+53_0	00:22:12.97	87:53:56.64	
0032+50_0	00:32:41.48	87:50:43.61	
0222+52_0	02:22:09.58	87:52:18.73	
0231+49_0	02:31:45.60	87:49:10.76	
0428+58_0	04:28:27.47	87:58:32.65	
0630+53_0	06:30:29.55	87:53:19.64	Bright core with some suggestion of a faint single-sided lobe.
0630+53_1	06:30:29.55	87:53:18.41	
0634+56_0	06:34:14.18	87:56:23.83	
0702+45_0	07:02:43.09	87:45:09.00	
0856+47_0	08:56:31.32	87:47:58.19	
0938+50_0	09:38:58.18	87:50:52.59	
1017+56_0	10:18:52.68	87:56:08.52	
1017+56_1	10:20:12.52	87:56:11.76	Core with two bright lobes.
1017+56_2	10:21:12.46	87:56:00.62	
1056+47_0	10:56:50.10	87:47:46.16	
1146+54_0	11:46:15.05	87:54:55.13	Double source.
1146+54_1	11:46:13.76	87:54:56.52	
1148+42_0	11:48:37.64	87:42:05.72	Double source.
1148+42_1	11:48:39.63	87:42:09.74	
1153+56_0	11:53:24.39	87:56:06.25	
1211+50_0	12:11:50.52	87:50:54.44	
1216+51_0	12:16:17.38	87:51:24.27	
1255+48_0	12:55:57.99	87:48:00.82	
1300+45_0	13:00:16.65	87:45:09.98	
1341+48_0	13:41:49.23	87:48:20.03	
1427+47_0	14:27:16.54	87:47:39.89	
1433+51_0	14:33:37.94	87:51:07.58	
1500+50_0	15:00:10.90	87:50:53.45	
1500+50_1	15:00:10.12	87:50:57.62	Double source, 3-component model.
1500+50_2	14:59:50.43	87:50:07.46	
1502+58_0	15:02:54.05	87:58:44.39	
1511+55_0	15:11:29.40	87:55:43.30	Double source.
1511+55_1	15:11:34.96	87:55:46.31	
1542+55_0	15:42:38.53	87:55:38.92	
1703+45_0	17:03:23.72	87:45:10.68	
1730+54_0	17:30:38.61	87:54:12.72	
1730+54_1	17:31:05.73	87:54:12.77	Double source, 3-component model.
1730+54_2	17:30:37.89	87:54:16.49	
1731+56_0	17:31:04.27	87:56:33.13	
1739+49_0	17:39:48.20	87:49:52.79	
1745+44_0	17:45:23.55	87:44:33.37	

TABLE 6.3
X-BAND RING5M SOURCES (CONT.)

Name	RA (2000)	Dec (2000)	Comments
1901+61_0	19:00:58.12	88:01:38.76	
1929+55_0	19:29:34.27	87:55:02.19	
1941+46_0	19:41:43.37	87:46:35.91	
2032+59_0	20:32:28.60	87:59:31.15	
2032+59_1	20:32:49.85	87:59:25.76	Bright core with single-sided lobe.
2032+59_2	20:32:52.51	20:32:30.54	
2032+59_3	87:59:24.91	87:59:30.94	
2140+58_0	21:41:01.80	87:58:10.62	
2140+58_1	21:41:53.75	87:57:51.41	
2140+58_2	21:41:52.32	87:57:53.02	Core with single lobe, bright knots of emission.
2140+58_3	21:41:03.45	87:58:10.02	
2140+58_4	21:41:41.22	87:57:55.77	
2228+50_0	22:28:10.05	87:50:37.98	
2316+49_0	23:16:20.13	87:49:41.46	
2317+52_0	23:17:25.40	87:52:58.42	

TABLE 6.4
VARIABILITY OF RING5M SOURCES AT X-BAND

Name	$\overline{S_X}^{\dagger}$ (mJy)	$\langle S_X \rangle^{\ddagger}$ (mJy)	χ^2_r	Comments
0022+53_0	2.10 ± 0.10	2.15 ± 0.02	0.01	
0032+50_0	89.86 ± 0.56	89.57 ± 1.67	150.85	
0222+52_0	4.14 ± 0.10	4.15 ± 0.06	0.19	
0231+49_0	4.49 ± 0.10	4.51 ± 0.11	1.39	
0428+58_0	17.89 ± 0.15	17.90 ± 0.10	1.01	
0630+53_0	1.84 ± 0.11			Below 2 mJy
0630+53_1	0.66 ± 0.11			Below 2 mJy
0634+56_0	2.78 ± 0.11	2.80 ± 0.05	0.07	
0702+45_0	7.67 ± 0.12	7.89 ± 0.68	12.07	
0856+47_0	1.70 ± 0.11			Below 2 mJy
0938+50_0	2.23 ± 0.12	2.43 ± 0.34	1.49	
1017+56_0	8.32 ± 0.09	8.20 ± 0.39	11.31	$\chi^2_r = 1.40$
1017+56_1	5.51 ± 0.09	5.60 ± 0.17	1.56	
1017+56_2	22.67 ± 0.09	24.31 ± 0.60	25.84	
1056+47_0	5.19 ± 0.10	5.17 ± 0.12	1.06	
1146+54_0	4.88 ± 0.08	4.81 ± 0.05	0.20	
1146+54_1	0.99 ± 0.08			Below 2 mJy
1148+42_0	13.13 ± 0.12	13.00 ± 0.18	2.85	
1148+42_1	2.62 ± 0.12	2.65 ± 0.09	0.59	
1153+56_0	7.07 ± 0.10	7.09 ± 0.06	0.41	
1211+50_0	11.88 ± 0.32	12.52 ± 0.14	1.30	
1216+51_0	20.45 ± 0.23	23.22 ± 0.36	6.78	
1255+48_0	3.72 ± 0.10	3.77 ± 0.08	0.38	
1300+45_0	9.16 ± 0.11	9.19 ± 0.09	0.68	
1341+48_0	1.89 ± 0.09			Below 2 mJy
1427+47_0	4.70 ± 0.16	4.89 ± 0.55	23.57	
1433+51_0	2.91 ± 0.11	3.05 ± 0.20	1.42	
1500+50_0	6.17 ± 0.13	6.37 ± 0.11	0.92	$\chi^2_r = 1.21$
1500+50_1	3.91 ± 0.13	4.32 ± 0.23	3.50	
1500+50_2	4.68 ± 0.13	4.80 ± 0.28	4.23	
1502+58_0	3.07 ± 0.12	3.19 ± 0.02	0.01	
1511+55_0	1.91 ± 0.11			Below 2 mJy
1511+55_1	1.24 ± 0.11			Below 2 mJy
1542+55_0	4.39 ± 0.10	4.47 ± 0.11	1.39	
1703+45_0	5.01 ± 0.09	5.11 ± 0.07	0.36	

† Fluxes from the combined maps.

‡ Unweighted averages of fluxes from the individual maps.

TABLE 6.4
VARIABILITY OF RING5M SOURCES AT X-BAND (CONT.)

Name	$\overline{S}_X$ [†]	$\langle S_X \rangle$ [‡] (mJy)	χ^2_r	Comments
1730+54_0	6.12 ± 0.13	6.18 ± 0.13	1.29	$\chi^2_r = 0.51$
1730+54_1	2.46 ± 0.13	2.62 ± 0.09	0.53	
1730+54_2	4.85 ± 0.13	4.99 ± 0.11	1.03	
1731+56_0	2.19 ± 0.24	2.36 ± 0.05	0.07	
1739+49_0	4.05 ± 0.08	4.07 ± 0.06	0.39	
1745+44_0	15.29 ± 0.13	15.30 ± 0.19	4.26	
1901+61_0	6.80 ± 0.12	6.56 ± 0.40	5.95	
1929+55_0	3.07 ± 0.09	3.09 ± 0.05	0.19	
1941+46_0	2.55 ± 0.11	2.56 ± 0.03	0.03	
2032+59_0	13.96 ± 0.15	13.99 ± 0.13	2.02	$\chi^2_r = 0.40$
2032+59_1	3.79 ± 0.15	3.87 ± 0.09	0.62	
2032+59_2	2.87 ± 0.15	2.79 ± 0.09	1.05	
2032+59_3	2.38 ± 0.15	2.73 ± 0.08	0.35	
2140+58_0	3.50 ± 0.07	2.96 ± 0.10	1.11	$\chi^2_r = 0.64$
2140+58_1	1.65 ± 0.07			Below 2 mJy
2140+58_2	4.31 ± 0.07	4.33 ± 0.18	2.90	
2140+58_3	5.59 ± 0.07	6.76 ± 0.30	7.14	
2140+58_4	2.02 ± 0.07	2.62 ± 0.10	0.45	
2228+50_0	9.02 ± 0.09	9.10 ± 0.17	1.80	
2316+49_0	7.71 ± 0.99	7.66 ± 0.06	0.14	
2317+52_0	17.73 ± 0.15	17.75 ± 0.46	10.00	

[†] Fluxes from the combined maps.
[‡] Unweighted averages of fluxes from the individual maps.

TABLE 6.5
SUMMARY OF SOURCE FLUXES

Name	$\overline{S}_X$ (mJy)	$\overline{S}_U$ (mJy)	$\overline{S}_{Ka}$ (mJy)
0022+53_0	2.10 ± 0.10	$0.78^{+0.16}_{-0.06}$	$0.20^{+0.11}_{-0.04}$
0032+50_0	89.86 ± 0.56	107.08 ± 0.49	126.44 ± 0.60
0222+52_0	4.14 ± 0.10	3.67 ± 0.26	3.12 ± 0.27
0231+49_0	4.49 ± 0.10	5.03 ± 0.34	5.85 ± 0.47
0428+58_0	17.89 ± 0.15	9.75 ± 0.31	4.33 ± 0.15
0630+53_0	1.84 ± 0.11	$0.69^{+0.19}_{-0.06}$	$0.18^{+0.14}_{-0.04}$
0630+53_1	0.66 ± 0.11	$0.32^{+0.17}_{-0.10}$	$0.09^{+0.22}_{-0.05}$
0634+56_0	2.78 ± 0.11	$1.01^{+0.14}_{-0.06}$	$0.26^{+0.09}_{-0.04}$
0702+45_0	7.67 ± 0.12	7.84 ± 0.40	8.07 ± 0.46
0856+47_0	1.70 ± 0.11	2.10 ± 0.28	2.79 ± 0.53
0938+50_0	2.23 ± 0.12	$0.84^{+0.13}_{-0.09}$	$0.22^{+0.10}_{-0.05}$
1017+56_0	8.32 ± 0.09	5.97 ± 0.42	3.83 ± 0.27
1017+56_1	5.51 ± 0.09	4.87 ± 0.37	4.13 ± 0.37
1017+56_2	22.67 ± 0.09	17.13 ± 0.41	11.78 ± 0.27
1056+47_0	5.19 ± 0.10	5.97 ± 0.33	7.76 ± 0.48
1146+54_0	4.88 ± 0.08	3.59 ± 0.29	2.38 ± 0.24
1146+54_1	0.99 ± 0.08	$0.39^{+0.15}_{-0.05}$	$0.11^{+0.12}_{-0.04}$
1148+42_0	13.13 ± 0.12	5.86 ± 0.30	1.99 ± 0.12
1148+42_1	2.62 ± 0.12	0.87 ± 0.30	0.20 ± 0.12
1153+56_0	7.07 ± 0.10	3.94 ± 0.30	1.80 ± 0.17
1211+50_0	11.88 ± 0.32	12.72 ± 0.31	13.94 ± 0.39
1216+51_0	20.45 ± 0.23	21.36 ± 0.31	18.76 ± 0.31
1255+48_0	3.72 ± 0.10	3.66 ± 0.27	3.58 ± 0.33
1300+45_0	9.16 ± 0.11	5.10 ± 0.30	2.33 ± 0.16
1341+48_0	1.89 ± 0.09	2.99 ± 0.29	5.52 ± 0.70
1427+47_0	4.70 ± 0.16	3.18 ± 0.26	1.89 ± 0.20
1433+51_0	2.91 ± 0.11	$1.06^{+0.11}_{-0.07}$	$0.27^{+0.08}_{-0.04}$
1500+50_0	6.17 ± 0.13	3.74 ± 0.61	1.92 ± 0.38
1500+50_1	3.91 ± 0.13	3.30 ± 0.61	2.63 ± 0.60
1500+50_2	4.68 ± 0.13	4.21 ± 0.72	3.65 ± 0.63
1502+58_0	3.07 ± 0.12	1.90 ± 0.38	1.00 ± 0.28
1511+55_0	1.91 ± 0.11	2.29 ± 0.39	2.92 ± 0.68
1511+55_1	1.24 ± 0.11	$0.49^{+0.21}_{-0.06}$	$0.14^{+0.17}_{-0.05}$
1542+55_0	4.39 ± 0.10	3.30 ± 0.31	2.25 ± 0.26
1703+45_0	5.01 ± 0.09	4.61 ± 0.30	4.12 ± 0.32

TABLE 6.5
SUMMARY OF SOURCE FLUXES (CONT.)

Name	$\bar{S}_X$ (mJy)	$\bar{S}_U$ (mJy)	$\bar{S}_{Ka}$ (mJy)
1730+54_0	6.12 ± 0.13	2.21 ± 0.25	0.57 ± 0.09
1730+54_1	2.46 ± 0.13	1.37 ± 0.25	0.63 ± 0.18
1730+54_2	4.85 ± 0.13	3.79 ± 0.26	2.73 ± 0.22
1731+56_0	2.19 ± 0.24	$0.83^{+0.29}_{-0.10}$	$0.23^{+0.21}_{-0.09}$
1739+49_0	4.05 ± 0.08	3.99 ± 0.31	3.91 ± 0.37
1745+44_0	15.29 ± 0.13	11.26 ± 0.28	7.48 ± 0.20
1901+61_0	6.80 ± 0.12	3.59 ± 0.36	1.53 ± 0.19
1929+55_0	3.07 ± 0.09	3.96 ± 0.27	5.56 ± 0.47
1941+46_0	2.55 ± 0.11	3.21 ± 0.38	4.37 ± 0.66
2032+59_0	13.96 ± 0.15	6.57 ± 0.28	2.40 ± 0.12
2032+59_1	3.79 ± 0.15	2.24 ± 0.28	1.11 ± 0.19
2032+59_2	2.87 ± 0.15	1.19 ± 0.28	0.37 ± 0.14
2032+59_3	2.38 ± 0.15	2.01 ± 0.28	1.60 ± 0.32
2140+58_0	3.50 ± 0.07	1.45 ± 0.27	0.45 ± 0.12
2140+58_1	1.65 ± 0.07	1.54 ± 0.30	1.40 ± 0.35
2140+58_2	4.31 ± 0.07	1.98 ± 0.29	0.70 ± 0.13
2140+58_3	5.59 ± 0.07	3.80 ± 0.27	2.27 ± 0.19
2140+58_4	2.02 ± 0.07	0.99 ± 0.28	0.38 ± 0.17
2228+50_0	9.02 ± 0.09	8.82 ± 0.30	7.98 ± 0.31
2316+49_0	7.71 ± 0.99	3.97 ± 0.41	1.63 ± 0.25
2317+52_0	17.73 ± 0.15	13.11 ± 0.30	8.77 ± 0.22

TABLE 6.6
SOURCE-SUBTRACTED RING FIELD MEANS[†]

Field	ΔT_{Ka} (μK)	σ_{Ka} (μK)	ΔT_{Ku} (μK)	σ_{Ku} (μK)
OV5M0024	5.02	41.97	−589.73	115.70
OV5M0104	100.75	38.56	518.78	128.07
OV5M0144	39.22	17.14	26.57	20.88
OV5M0224	163.53	15.94	460.86	21.61
OV5M0304	−2.81	16.39	−47.35	17.34
OV5M0344	51.26	17.35	98.03	18.66
OV5M0424	152.39	16.13	42.53	24.08
OV5M0504	57.31	16.31	64.66	18.35
OV5M0544	58.91	16.50	168.75	16.77
OV5M0624	168.76	15.76	196.72	19.45
OV5M0704	199.63	15.90	31.91	17.32
OV5M0744	86.67	15.32	113.43	18.10
OV5M0824	−51.32	13.88	−236.40	15.45
OV5M0904	213.34	14.56	450.90	15.60
OV5M0944	119.04	15.79	−53.27	16.61
OV5M1024	92.54	15.01	207.63	32.76
OV5M1104	64.98	15.28	383.60	19.26
OV5M1144	16.04	15.93	−260.65	28.25
OV5M1224	124.62	17.47	461.59	46.69
OV5M1304	32.29	15.45	70.31	25.32
OV5M1344	−29.55	15.38	−87.82	18.63
OV5M1424	63.96	15.57	228.18	27.32
OV5M1504	131.52	16.89	346.64	34.70
OV5M1544	38.40	16.25	55.60	20.28
OV5M1624	5.29	15.86	70.02	18.60
OV5M1704	34.53	15.77	59.80	17.94
OV5M1744	85.91	16.32	323.06	20.03
OV5M1824	−41.75	15.54	−49.38	19.97
OV5M1904	141.21	16.02	226.87	17.33
OV5M1944	24.20	15.31	−0.59	19.31
OV5M2024	−118.87	16.50	−176.35	19.65
OV5M2104	249.37	16.17	387.89	20.24
OV5M2144	51.21	17.02	273.60	32.10
OV5M2224	236.30	16.90	352.78	24.77
OV5M2304	−61.78	17.65	−85.95	18.58
OV5M2344	118.72	30.41	325.91	52.47

[†]Equivalent R-J brightness temperature

Chapter 7

Foregrounds

HANNAH: What do you do?

VALENTINE: You start guessing what the tune might be. You try to pick it out of the noise. You try this, you try that, you start to get something — it's half-baked but you start putting in notes which are missing or not quite the right ones... and bit by bit... (He starts to dumdi-da to the tune of 'Happy Birthday'.) Dumdi-dum-dum, dear Val-en-tine, dumdi-dum-dum to you — the lost algorithm!

HANNAH: (Soberly) Yes, I see. And then what?

VALENTINE: I publish.

HANNAH: Of course. Sorry. Jolly good.

Tom Stoppard, *Arcadia*

7.1 Introduction[†]

It was noted in Chapter 5 that while a number of the Ring fields have the spectral signature of microwave background emission, others show the spectral signature characteristic of thermal bremsstrahlung. In this chapter, we investigate the nature of these signals, and attempt to disentangle what portion of the observed variance in the Ring is due to the CMBR. Given sufficient spectral coverage, the CMBR could simply be projected out, by fitting a template of Galactic foregrounds with known spectral indices to the data. With only two frequency channels, however, we are quite

[†]The material presented in this chapter is a more detailed discussion of Leitch et al. (1997).

restricted in our ability to reconstruct the CMBR signal directly from the data. On the other hand, the factor of two difference in frequency provides adequate leverage for discriminating the CMBR signal under a restricted set of hypotheses.

7.2 Lower Culmination Tests

In the previous chapter, we found that with the exception of OV5M0024, the Ring fields are not strongly contaminated by point sources. As can clearly be seen in Fig. 6.7, even after point source subtraction, several fields with temperature spectral index $\beta \simeq -2$ remain, suggesting a Galactic origin for these data. As discussed in §5.4.4, terrestrial contamination is not expected to produce structure which varies with sidereal time; the parallactic angle dependence of the Ku-Band data is consistent with RFI contamination which is identical from field to field. Nevertheless, observing the Ring at *lower* culmination provides a simple test which can definitively rule out terrestrial contamination. Since observing at lower culmination changes the position of the telescope beams only relative to the ground, signals from the sky will remain unaltered, while any time-dependent fluctuations from the ground will be shifted by 12 hours. This test was performed from 16-30 Sept. 96. (The strength of the signals at Ku-Band permits a reasonable detection in this relatively short time.) The comparison of the mean upper culmination Ku-Band data set with the lower culmination data is shown in Fig. 7.1. Field errors are estimated by reducing the 1996 upper culmination data in 2-week subsets, and computing the error in the mean between subsets, typically about 85 μK, or 62 μK in antenna temperature.

The lower culmination data show the same structure, to within errors, as the upper culmination data, demonstrating that the origin of these signals is undoubtedly celestial. The large differences in fields OV5M0024, OV5M0104 and OV5M2344 are due in part to variability of 0032+50, which dominates the signal in field

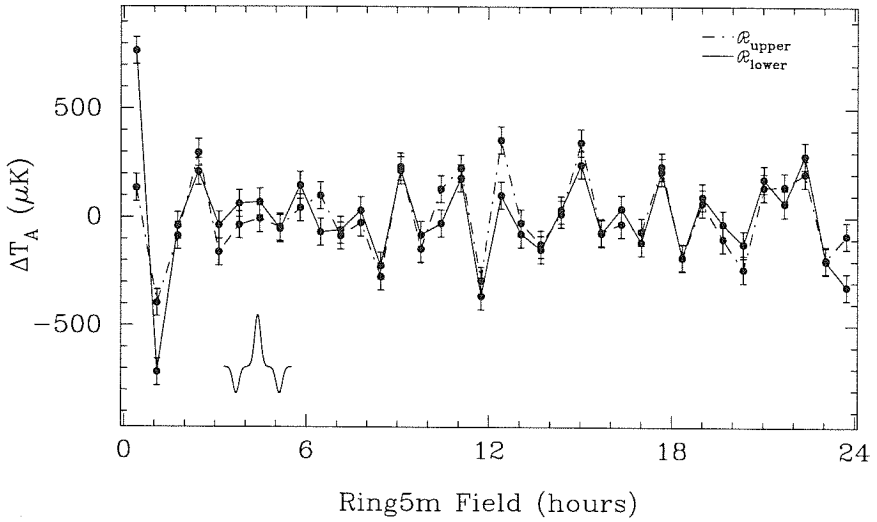

Figure 7.1 1996 Ku-Band upper culmination (dot-dashed line), shown with the lower culmination data (solid line). The good agreement of these to data sets effectively rules out terrestrial RFI as the source of the observed structure in the Ring. The large differences in the first, second and last fields are due to discrete sources (see text). At bottom left is the effective beam pattern for double-switched observations.

OV5M0024, and to the asymmetric Ku-Band beam pattern, which is inverted at lower culmination relative to the upper culmination beam.

7.3 Likelihood Analysis

In this section, we explore in a somewhat more rigorous manner what the Ka-Band and Ku-Band data themselves have to say about the frequency spectrum of the observed fluctuations. The approach taken to estimating parameters from the data is the standard approach of Maximum Likelihood estimation, described in passing in §5.4, and in detail by Myers (1990), Sivia (1996) and others. In short, we assume that our data are drawn from a Gaussian distribution on the sky, so that the joint probability of the entire data set can be constructed analytically. (Note that the Gaussian approximation is likely to be quite good for a maximum likelihood test,

since it is just equivalent to retaining the first three terms in the Taylor expansion of any arbitrary distribution about its maximum (see Appendix C).) The calculation is then a straightforward application of Bayes' theorem (cf. §6.3)

$$p(hypothesis|data) \propto p(data|hypothesis) \times p(hypothesis), \tag{7.1}$$

which states simply that the probability that a given hypothesis is true is just proportional to the probability that we would observe the measured data if the hypothesis were true. In our case, the latter probability is given by the joint probability discussed above. The term $p(hypothesis)$ represents our prior knowledge (or lack thereof) about the truth of the hypothesis under investigation. In the absence of any prior information, this is typically taken to be an "uninformative prior," i.e., we make the assumption that all hypotheses are equally likely, at least those for which $p(data|hypothesis)$ has some interesting value.

With this in mind, we can write the joint likelihood $\mathcal{L}$ of the Ring data as

$$\mathcal{L} = \frac{\exp(-\frac{1}{2}\mathbf{t}^T\mathbf{C}^{-1}\mathbf{t})}{(2\pi)^{N/2}\,|\mathbf{C}|^{1/2}}. \tag{7.2}$$

Here, $\mathbf{t}$ is the data vector, with elements ΔT_i, and $\mathbf{C}$ is the associated 36×36 covariance matrix. In general, the elements of $\mathbf{C}$ can be written

$$C_{ij} = \sigma_{ij}^2 + C_{ij\,sky}, \tag{7.3}$$

where the σ_{ij}^2 are the temporal covariances from the data (the diagonal elements σ_{ii}^2 are just the variances of the field means). The $C_{ij\,sky}$ describe the predicted spatial variance from the sky, and in general are given by the 2-pt correlation of the effective antenna pattern $B(\mathbf{x})$ convolved with the sky temperature field $T(\mathbf{x})$,

$$C_{ij\,sky} = \int d\mathbf{x}_1 \int d\mathbf{x}_2 B_i(\mathbf{x}_1) B_j(\mathbf{x}_2) \langle T(\mathbf{x}_1) T(\mathbf{x}_2) \rangle. \tag{7.4}$$

The computation of the spatial covariance matrix will be taken up in more detail in §8.1.

If covariances are ignored, off-diagonal elements of $\mathbf{C}$ will not contribute to the likelihood, and (7.2) reduces to the more familiar form

$$\mathcal{L} = \prod_{i=1}^{36} \frac{1}{\sqrt{2\pi C_{ii}}} \exp\left[\frac{-\Delta T_i^2}{2C_{ii}}\right], \tag{7.5}$$

where the C_{ii} are given by (7.3). (Note, however, that the interlocked geometry of the Ring effectively converts 36 independent temperatures T_i into 12 independent triplets $(\Delta T_{i-1}, \Delta T_i, \Delta T_{i+1})$, so that the spatial covariance matrix is *not* diagonal, but banded.)

Once $\mathcal{L}$ is expressed as a function of the parameters of interest, these parameters are varied to maximize $\mathcal{L}$. The α-confidence interval on any estimated parameter is then given by the smallest interval (the *highest probability density*, or HPD) which contains the specified probability α.

7.4 Spectral Index of the Ring

Under the assumption that a single process is responsible for the structure observed near the NCP at both frequencies, the formalism described in §7.3 can be used to set a limit on the frequency spectral index of the Ring. We construct the likelihood as a function of the sky variance ΔT_{sky}^2 and the foreground spectral index β by assuming that the sky correlations $C_{ij\,sky}$ are given by

$$C_{ij\,sky} = \Delta T_{sky}^2 \left(\frac{\nu_i}{\nu_0}\frac{\nu_j}{\nu_0}\right)^{\beta} \delta(\mathbf{x}_i - \mathbf{x}_j), \tag{7.6}$$

where the indices i and j run over spectral channels as well as fields, so that the covariance matrix $\mathbf{C}$ is now 72×72. In (7.6) the spatial and spectral dependences of ΔT_{sky} are decoupled, equivalent to assuming that the same emission mechanism is responsible for the signal in each field. Although this is unlikely to be the case, this hypothesis can be used to quantify our rejection of a pure CMBR signal ($\beta \sim 0$). As

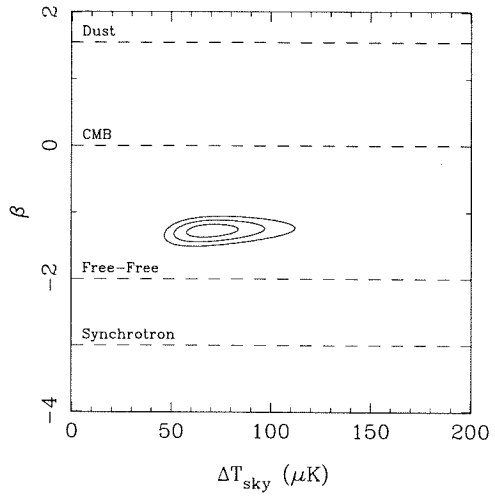

Figure 7.2 Likelihood function $\mathcal{L}(\Delta T_{sky}, \beta)$ for the Ring data, assuming CMBR + a single foreground with temperature spectral index β. Plotted are the 1, 2 and 3σ HPD intervals.

can be seen in Fig. 7.2, we find $\beta_{max} = -1.28 \pm 0.09$, so that pure CMBR emission can be ruled out with high confidence. The spectral index which maximizes the likelihood confirms what was already clear from inspection of Figures 5.13 and 5.14, that the data are consistent with a mixture of $\beta \leq -2$ and $\beta \sim 0$ signals.

7.5 Synchrotron

Recent low frequency observations with the Westerbork synthesis array (Wieringa et al. 1993) reveal diffuse polarized structure at high Galactic latitude as bright as 8 K at 325 MHz. These features, on scales of $4' - 30'$, are seen in linear polarization only; the corresponding total intensity maps are extremely smooth, and upper limits $< 0.5 - 1$ K are set on any counterparts to the polarized structures. This is intriguing, since ~ 8 K features with temperature spectral index $\beta = -2.7$ could just produce signals of the amplitude seen at Ku-Band if the receiver were sensitive to linear polarization. Both receivers, however, were designed to detect right circular polarization only, and should

be insensitive to linearly polarized structure on the sky. If a signal of the same total intensity but variable polarization angle is presented to both feeds, it can be shown (see Appendix B) that the maximum power increment produced is proportional to $\cos\beta_t$, where $\beta_t = \cot AR$ is the cotangent of the axial ratio of the polarization ellipse of a wave transmitted from the feeds. Therefore, to rule out the possibility that the observed structure in the Ku-Band data is due to polarized Galactic synchrotron emission, β_t was measured across the bandpass of the Ku-Band polarizers. Since $\beta_t = (\pi/2-\delta)/2$ for an elliptically polarized wave (see Appendix B), we can determine β_t by measuring the phase shift $\pi/2-\delta$ which the polarizer introduces in a linearly polarized transmitted wave. The average over the band was found to be $\langle\cos\beta_t\rangle = 0.06$, so that at most 6% of any linearly polarized anisotropy will be seen.

Moreover, given the smoothness of the total intensity maps, it is highly improbable that the structure in the polarized emission is due to variations in intrinsic polarization angle, and Wieringa et al. interpret the polarized structure as Faraday rotation of an intrinsically smooth, polarized synchrotron background by an intervening screen. If this interpretation is correct, any linearly polarized structure will have the ν^{-2} dependence of Faraday rotation and should be significantly reduced at 14.5 GHz.

Total intensity maps from the WENSS survey (de Bruyn 1996), covering 28 of the 36 RING5M fields, show no detectable signals in the vicinity of the NCP. If we assume that our Ka-Band data are free of steep-spectrum contamination (a reasonable assumption, since even if all of the 240 μK rms at Ku-Band is due to foreground, this would constitute less than 25% of the observed variance at Ka-Band for spectral indices as flat as -2), the difference between the variance at Ku-Band and Ka-Band is then an estimate of the variance due to foregrounds. Comparison of this residual variance with the variance of the Ring5m fields at 325 MHz places a lower limit of $\beta \geq -2.06$ on the spectral index of any steep spectrum foreground. This should be a reasonably conservative limit, since some of the Ka-Band variance is due to the

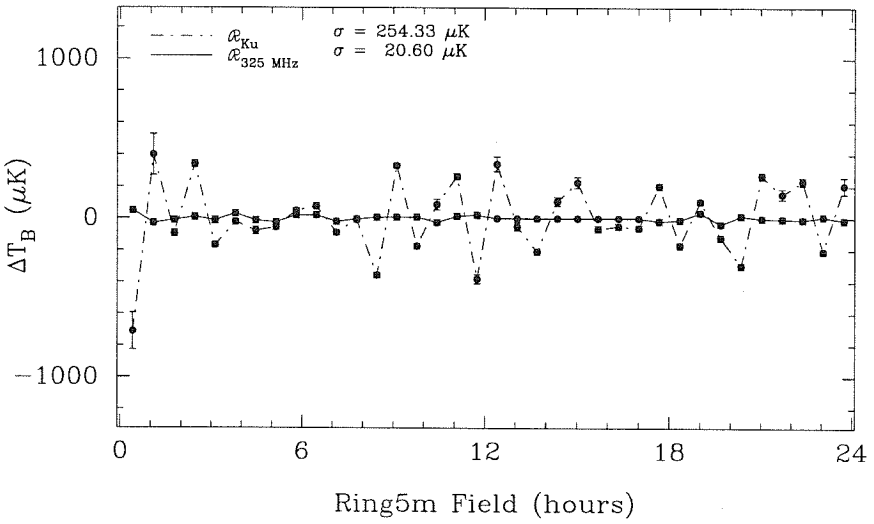

Figure 7.3 Ku-Band (dot-dashed line) and WENSS 325 MHz map of the NCP (solid line), extrapolated to 14.5 GHz assuming $\beta = -2.7$. Standard deviations are quoted for overlap region only (WENSS data are missing for fields OV5M1224 - OV5M1744). The comparison demonstrates that the structure observed at 14.5 GHz cannot be due to steep spectrum synchrotron emission.

foreground, so that the amount of signal we have to hide at 325 MHz is likely to be underestimated. Alternatively, one can ask what spectral index is required to reduce the maximum Ku-Band signal observed in the overlap region to a 3σ noise peak at 325 MHz, yielding $\beta \geq -2.21$. In either case, as can clearly be seen in Figure 7.3, whatever the foreground is, it cannot be conventional synchrotron emission.

7.6 Spectral Index of a Single Foreground

Since the measured signals represent a combination of many foregrounds — point sources, Galactic synchrotron, free-free, dust — the process of analyzing data with limited spectral coverage is one of elimination, since the data themselves provide too few constraints to disentangle these components directly. We have previously shown that point sources do not significantly contaminate the Ring data, and have independently measured and removed their contributions. On the basis of the WENSS

survey maps, we now know that the contribution of any steep-spectrum ($\beta < -2.2$) component is negligible. At the relatively low frequency of 14.5 GHz, dust emission is expected to be a negligible contaminant (discussed in more detail below), and we now restrict our investigation to a class of models in which the CMBR is observed in the presence of a single foreground.

To address what foreground spectral index is favored by the data, we follow the likelihood analysis outlined in §7.3. The data are modeled as a Gaussian CMBR component in the presence of a single foreground of variable strength from field to field but constant spectral index β. The equivalent R-J brightness temperature in each field is then given by

$$\Delta T_{iB} = \Delta T_{icmb} + \Delta T_{ifore}, \tag{7.7}$$

where $\Delta T_{ifore} \propto \nu^{\beta}$. Recall that the equivalent brightness temperature is *defined* to be

$$\Delta T_B = \frac{c^2}{2k\nu^2}\Delta I, \tag{7.8}$$

so that for a blackbody, the incremental equivalent brightness temperature in the Rayleigh-Jeans regime is related to the true incremental brightness temperature (see §4.1.3) by

$$\Delta T_{cmb} = \frac{c^2}{2k\nu^2}\Delta T\frac{\partial I}{\partial T} = \Delta T\frac{x^2e^x}{\left(e^x-1\right)^2} \equiv \Delta T\alpha(\nu), \tag{7.9}$$

where $x \equiv h\nu/kT$. Given two frequencies ν_1 and ν_2, we can eliminate the ΔT_{ifore} and solve for the CMBR component as a function of the unknown spectral index β;

$$\Delta T_{icmb} = \frac{\Delta T_{iB}(\nu_1)\nu_1^{-\beta} - \Delta T_{iB}(\nu_2)\nu_2^{-\beta}}{\alpha(\nu_1)\nu_1^{-\beta} - \alpha(\nu_2)\nu_2^{-\beta}}. \tag{7.10}$$

The covariance matrix is then constructed as before, except that now it is only a 36×36 array.

Although two frequency channels cannot provide much discrimination among the

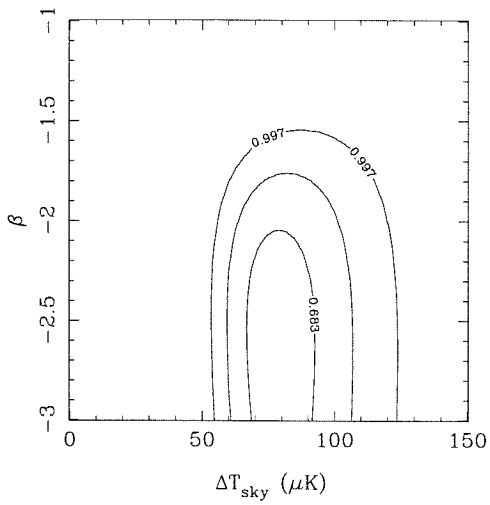

Figure 7.4 Likelihood function $\mathcal{L}(\Delta T_{sky}, \beta)$ for the Ring5m data, assuming CMBR + single foreground of temperature spectral index β. Plotted are the 1, 2 and 3σ HPD intervals.

steepest spectral indices, since the CMBR component dominates for steeper foreground spectral indices, we can reasonably truncate the prior spectral index distribution at $\beta = -3$, which is the steepest spectral index known for standard Galactic emission processes (see e.g., Reich & Reich (1988), who find that the low-frequency radio spectral index near the NCP is ~ -2.7, and Banday & Wolfendale (1991), who present evidence that the synchrotron spectral index steepens to $\beta \sim -3$ at high frequencies). The resulting likelihood is presented in Figure 7.2 and peaks at $\beta = -2.58^{+0.53}_{-0.42}$. We therefore take $\beta \simeq -2.2$ as the foreground spectral index most consistent with both our data and the low frequency maps of the NCP and conclude that the foreground is unusually flat spectrum synchrotron radiation, free-free emission, or some more exotic component of Galactic emission (see §7.10).

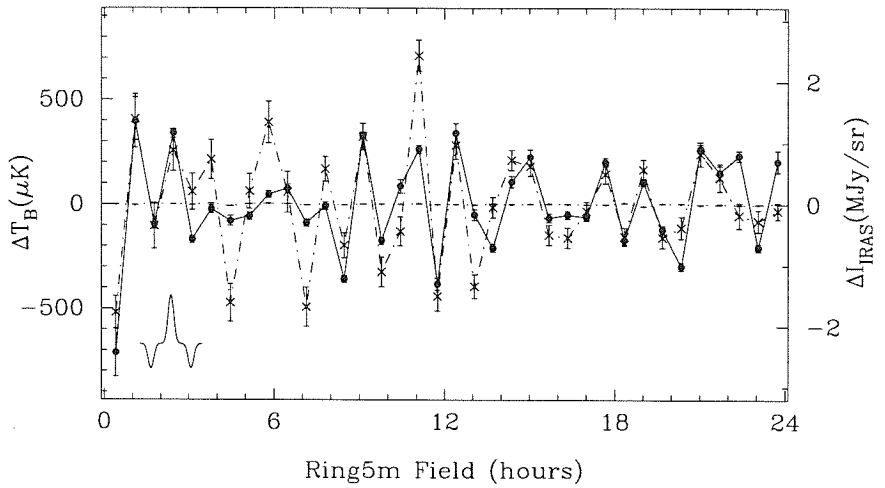

Figure 7.5 Comparison of the 14.5 GHz data (solid line) in μK, with the *IRAS* 100 μm convolution (dot-dashed line). Errors for the *IRAS* data points are the estimated standard deviations of the convolved means. The dotted line essentially coincident with the x-axis is the free-free signal, in μK, inferred from Hα images of the NCP fields, assuming $T_e = 10^4$ K. At bottom left is the "triple beam" pattern due to the double switching.

7.7 *IRAS* 100 μm Maps

In an attempt to identify this component with known Galactic foregrounds, the *IRAS* 100 μm map (*IRAS* Explanatory Supplement 1988) of the NCP was convolved with the Ku-Band beam and beam-switch. Remarkably, we find a strong correlation between the *IRAS* 100 μm maps and the 14.5 GHz data set, as can be seen in Figure 7.5.

To assess the significance of this result without prior knowledge of the distribution of *IRAS* 100 μm brightness or 14.5 GHz temperature on 7′ scales, we use the Spearman rank-order correlation coefficient r_s (Kendall 1963). Since this depends only on the data *ranks*, whose distribution is always uniform, and not on the values themselves, the significance of an observed value of r_s can be determined unambiguously. The significance of an observed value of r_s can be tested by forming the statistic $t = r_s\sqrt{\frac{N-2}{1-r_s^2}}$, which has a Student's distribution with $N-2$ degrees of freedom (Press et al. 1988, Kendall 1963). The observed correlation between the 14.5 GHz and *IRAS* 100 μm

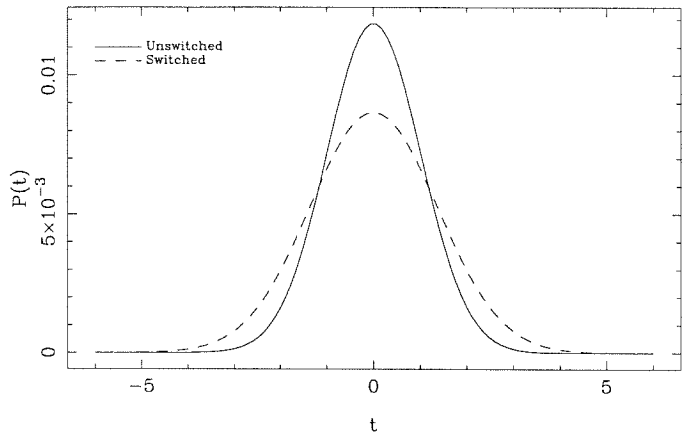

Figure 7.6 Distribution of the statistic $t = r_s\sqrt{\frac{N-2}{1-r_s^2}}$ for $N = 36$. The distribution is noticeably broadened when correlations due to the switching are taken into account (dashed line).

data is $r_s = 0.76$, and for 36 *independent* fields, the probability of observing $r_s > 0.76$ by chance is $p(r_s > 0.76) = 3.2 \times 10^{-8}$. As discussed in §7.3, our switching strategy artificially introduces correlations between neighboring fields, so that only every third field is independent, and numerical simulations show that this reduces the significance to 4.5×10^{-6} (see Figure 7.6).

Note that the region spanning 3h – 8h, where the correlation is weakest, is also the region where the strongest signals are seen at Ka-Band; the spectral indices of these fields are consistent with $\beta = 0$, indicating the presence of a significant CMBR signal.

Taking $\beta = -2.2$ as the spectral index of the foreground consistent with both the Ring5m data and the WENSS maps, we can use the 14.5 GHz and 31.7 GHz data to solve for the free-free component in the manner of Equation (7.10). A linear fit to the foreground component yields the conversion

$$T_f/I_{100\mu\mathrm{m}} = (8.4 \pm 3.6) \times 10^{-2}\ \nu_{\mathrm{GHz}}^{-2.2}\ \mathrm{K/(MJy/sr)}. \tag{7.11}$$

The separately extracted CMBR and foreground components (assuming $\beta = -2.2$)

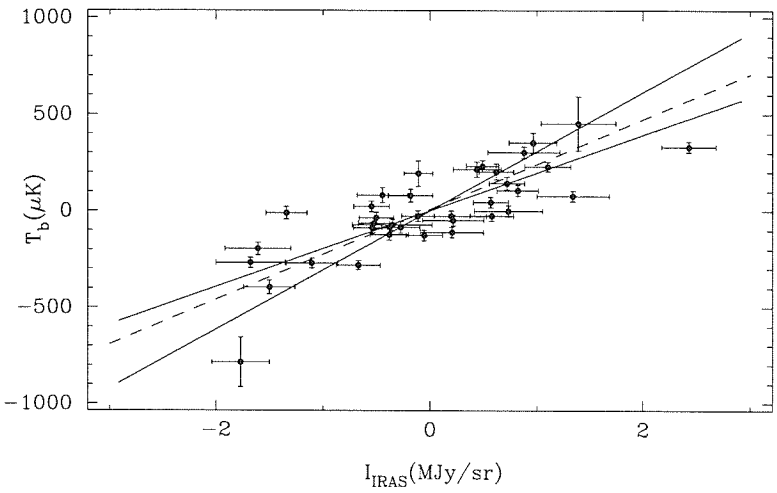

Figure 7.7 Linear regression of the Ku-Band temperatures on the *IRAS* 100 μm intensities, shown with the best-fit slope of 233 μK MJy^{-1} sr.

are displayed in Figures 7.8 and 7.9. It is found that the extracted foreground component correlates even more strongly with the *IRAS* 100 μm emission ($r_s = 0.79$); note particularly that the foreground component now shows a correlation in the regions 3h – 8h and 20h – 23h, where on spectral grounds we believe the CMBR to dominate the Ring data at both frequencies.

In Chapter 5, we concluded that the structure observed in the Ring was celestial in origin on the basis of the correlation between data acquired on independent telescopes. The detection of a correlation with a known Galactic foreground (i.e., the IR cirrus) is independent confirmation of the astronomical nature of these signals.

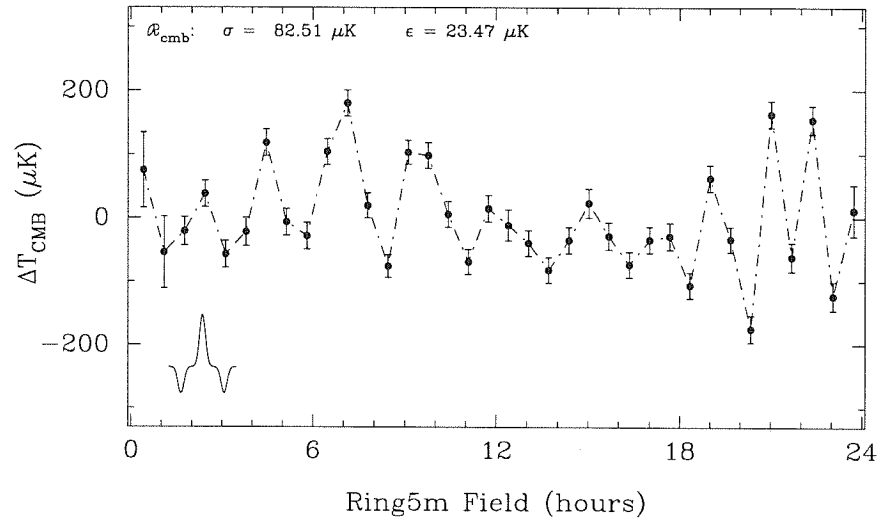

Figure 7.8 The extracted CMBR physical brightness temperatures (at Ka-Band), assuming a foreground spectral index of $\beta = -2.2$.

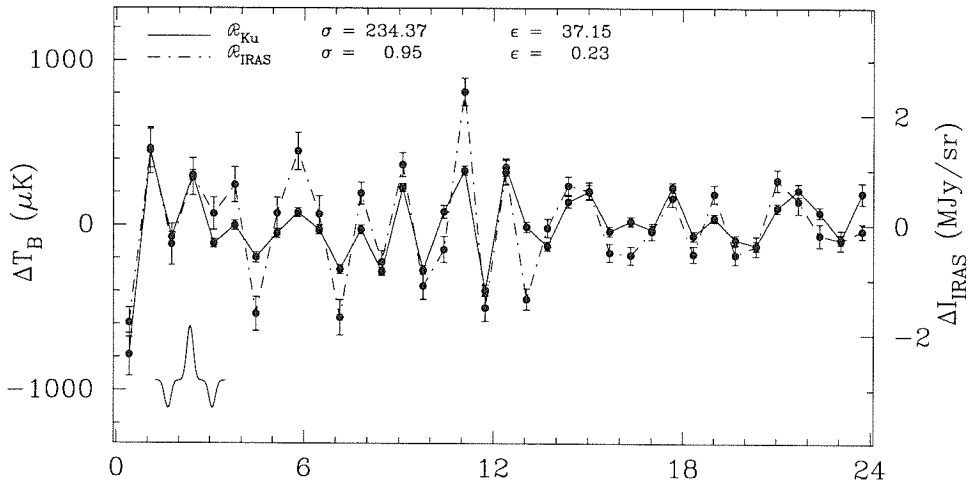

Figure 7.9 The extracted foreground equivalent brightness temperature (at Ku-Band), assuming a spectral index $\beta = -2.2$. Note that the region 3h – 8h in which the CMBR appears to dominate, now shows a noticeable correlation with the *IRAS* 100 μm intensities (cf. Figure 7.5).

7.8 Hα Observations of the NCP

Free-free emission, or thermal bremsstrahlung radiation, results from the scattering of unbound particles, typically of electrons off of protons in a $T_e \sim 10^4$ K plasma. The same gas will emit Hα recombination radiation as electrons are recaptured and cascade back to the ground state. Gaustad et al. (1996) have recently estimated the free-free contamination of small-scale anisotropy experiments through Hα observations of the NCP. For the brightness temperature of optically thin hydrogen, we expect

$$T_B(\mu\mathrm{K}) = \frac{5.43}{\nu_{10}^2 T_4^{1/2}} g_{ff}\, EM_{\mathrm{cm}^{-6}\mathrm{pc}}, \tag{7.12}$$

where

$$g_{ff} = 4.69(1 + 0.176 \ln T_4 - 0.118 \ln \nu_{10}) \tag{7.13}$$

is the free-free Gaunt factor (Spitzer 1978), the frequency is $10^{10}\nu_{10}$ GHz, the electron temperature $T_e = 10^4 T_4$ K, and $EM \equiv \int n_e^2\, dl$ is the emission measure. For $T_e \leq 2.6 \times 10^4$ K, the Hα surface brightness in rayleighs (1R $= 2.42 \times 10^{-7}$ ergs cm^{-2} s^{-1} sr^{-1} at Hα) is given by

$$I_{H\alpha}(\mathrm{R}) = 0.36\, EM_{\mathrm{cm}^{-6}\mathrm{pc}}\, T_4^{-0.9} \tag{7.14}$$

(Kulkarni & Heiles 1987).

When the observing procedure of the Ring5m experiment is simulated on the maps of Gaustad et al. (1996), we measure $\langle \Delta I \rangle_{rms} \leq 0.1$ R on 7′ scales in Hα. If we assume $T_e \simeq 10^4$ K for the temperature of the emitting gas, the inferred upper limit on the *rms* at 14.5 GHz due to free-free emission is $\langle \Delta T_{ff} \rangle_{rms} \leq 3.2$ μK, a factor of ~ 70 lower than the observed $\langle \Delta T_{ff} \rangle_{rms} = 234$ μK. Furthermore, as can be seen in Figure 7.5, the Hα maps are featureless; in the 36 RING fields, no signals are seen with $|\Delta I| > 0.2$ R. By contrast, for the ~ 300 μK signals detected at Ku-Band, (7.12)–(7.14) predict an Hα brightness $|\Delta I| \sim 9$ R.

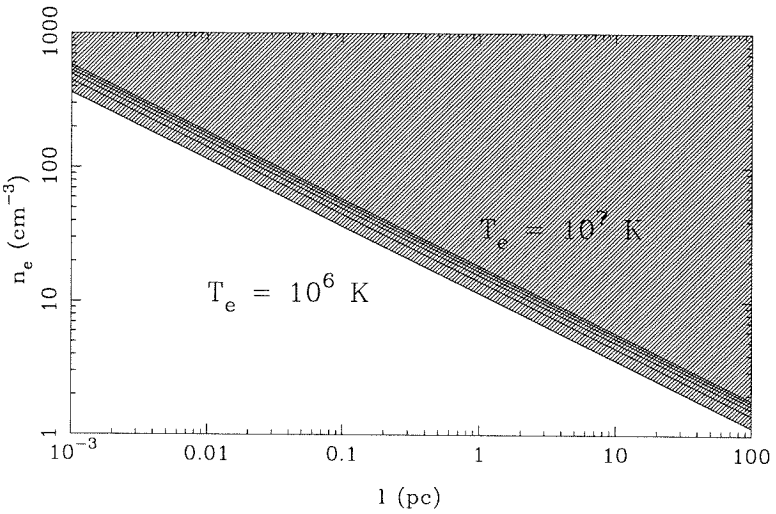

Figure 7.10 Allowed $n_e - l$ parameter space (shaded region) for $T_e \geq 10^6$ K. We can exclude $l > 100$ pc, as this requires that inhomogeneities be aligned along the line of sight to within $\sim 6 \times 10^{-3}$ rad, since we see fluctuations on the scale of the $22'$ beam throw. The solid lines correspond to $T_e = 10^6$, 2×10^6, 4×10^6, 6×10^6, 8×10^6, and 10^7 K.

If considerable dust lies along the line of sight to the NCP, extinction might account for the low levels of observed Hα emission; estimates from the *IRAS* 100 μm intensities, however, imply $\lesssim 0.6$ magnitudes of visual extinction (Simonetti et al. 1996), so that the upper limits on free-free emission can be increased by 74% at most.

As T_e is increased beyond 2.6×10^4 K, the allowed orbital space for recombination shrinks, and (7.14) is no longer valid; for $T_e > 2.6 \times 10^4$ K, a fit to the Hα recombination coefficient gives $\alpha_{H\alpha} \propto T^{-1.2}$ (Ferland 1980). The presence of 300 μK free-free emission can therefore be reconciled with the observed 3σ Hα limit if the emission is due to gas at $T_e \gtrsim 10^6$ K. For these electron temperatures, free-free brightness temperatures of 300 μK at 14.5 GHz require an $EM \gtrsim 131$. The corresponding allowed $n_e - l$ parameter space is shown in Figure 7.10.

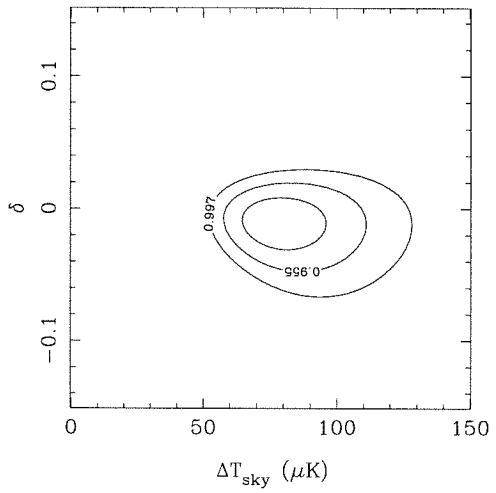

Figure 7.11 Probability contours for the amplitude of a dust component ($\Delta T \propto \nu^2$) correlated with the steep spectrum foreground detected at Ku-Band, relative to the amplitude of the steep spectrum component.

7.9 Dust

The correlation with IR cirrus in the *IRAS* maps implies that any dust emission contributing to the Ring data is likely to correlate with the steep spectrum component observed in the Ring data. Although dust is not expected to be a serious contaminant at low frequency (fits to the *COBE* FIRAS data suggest an emissivity $\epsilon \propto \nu^2$, so that the equivalent brightness temperature falls with falling frequency as ν^2; Wright et al. (1991), Reach et al. (1995)), we can exploit this fact to probe for the presence of dust emission in our data. In the presence of correlated dust emission $\Delta T_{i\,dust} = a_{i\,dust}\nu^{\beta_{dust}}$, the brightness temperature measured in each field is given by

$$\Delta T_{iB} = \Delta T_{i\,cmb} + \Delta T_{i\,fore} + \Delta T_{i\,dust} \tag{7.15}$$

$$= \Delta T_{i\,cmb} + a_{i\,fore}\nu^{\beta_{fore}}(1+\delta), \tag{7.16}$$

where

$$\delta = \frac{a_{i\,dust}}{a_{i\,fore}} \left(\frac{\nu^{\beta_{dust}}}{\nu^{\beta_{fore}}} \right) \equiv f \nu^{\beta_{dust} - \beta_{fore}}. \tag{7.17}$$

We assume a strict proportionality between the dust and steep-spectrum foreground emission in each field, quantified by f. If we take $\beta_{fore} = -2.2$ and $\beta_{dust} = +2$, we can solve for the $\Delta T_{i_{cmb}}$ as in §7.6, and construct the likelihood as before. The result is shown in Figure 7.11, restricting any dust component to be less than 1% (1σ) of the steep spectrum foreground amplitude, or a few μK *rms*.

7.10 Discussion

The observed structure in the *IRAS* 100 μm map of the NCP region is part of a large HI feature known as the NCP Loop (see Figure 7.13). This feature, which encompasses all 36 of the Ring5m fields, has been modeled by Meyerdierks et al. (1991) as the wall of an expanding cylindrical shock. While the production of a *dense* ionized component such as that implied by Figure 7.10 may pose significant difficulties — such structures will be extremely over-pressured, and must necessarily be transient phenomena — it is intriguing that the combination of large emission measure and high temperature arrived at by interpreting the structure at 14.5 GHz as free-free emission are suggestive of just such a shocked component of the ISM.

Perhaps more plausible, though no less anomalous, is the possibility that the observed structure at 14.5 GHz is due to flat-spectrum synchrotron emission. Synchrotron spectral indices as flat as $\beta = -2.0$ are typically observed only in plerions associated with the very youngest SNR (Green 1996), and we would not expect such emission from the NCP Loop, an old remnant with expansion velocity $v \simeq 20$ km/s. A notable exception to the general steepness of Galactic synchrotron radiation, however, is the filamentary structure observed toward the Galactic center. These features, consisting of long, nearly one-dimensional threads, have spectral

indices $-2.2 \leq \beta \leq -1.9$ yet show considerable linear polarization, suggesting that the dominant emission mechanism is synchrotron (Yusef-Zadeh 1989). Although such structures would suffer from a similar lifetime problem as free-free filaments and require recent injection of high-energy electrons to maintain a flat spectrum, they would obviate the high temperature and pressure required if the emission is free-free.

An alternative explanation has recently been suggested by Draine & Lazarian (1997). Ferrara & Dettmar (1994), and more recently Draine & Lazarian (1997), have demonstrated that under normal interstellar conditions, dust grains containing $N \lesssim 10^3$ atoms can produce dipole radiation in the range 10-100 GHz, when collisionally excited by ions. All models considered by Draine & Lazarian (1997) result in a grain emissivity which peaks near 30 GHz, so that various power law spectra can be reproduced by small changes in the model parameters. Their preferred model provides a good match to signal amplitudes observed in several recent anisotropy measurements, reproducing the implied 31.7 GHz temperatures from the foreground component observed in the Ring, and accounting for 30% of the emission we detect at 14.5 GHz. Although Draine and Lazarian find that the emitted spectrum can match our 14.5 GHz data only for unlikely values of the grain dipole moment, this scenario nevertheless more naturally accounts for the correlation with the *IRAS* 100 μm intensities, as does another possibility, suggested by Webster (1997), in which the 14.5 GHz emission seen in the Ring is due to molecular transitions of fullerenes in the interstellar dust.

7.11 Summary

We have detected a significant correlation between emission with temperature spectral index $\beta \sim -2$ observed at 14.5 GHz in the Ring5m experiment, and the *IRAS* 100 μm maps. If this is free-free emission, the lack of accompanying Hα emission implies

that it is from a component of the ISM with $T_e \gtrsim 10^6$ K. The large EM required to produce the observed signals at these temperatures is typical of supernova remnants, an interpretation which the morphology of the NCP Loop with which the *IRAS* emission is associated would seem to support.

Kogut et al. (1996) have recently reported a large angular scale correlation of the residual free-free component in the *COBE* DMR sky maps with far-infrared DIRBE emission. The level of this signal at 53 GHz, however, is consistent with predictions from Hα observations, implying that on 7° scales, the observed free-free emission is from a $T_e \sim 10^4$ K phase of the ISM. Moreover, if the correlation with free-free emission persists to small scales, the power spectrum of the high-latitude DIRBE 240 μm maps $P(\ell) \propto \ell^{-3}$ where $\ell \sim 60/\theta°$, implies a level of free-free emission at 0.1° scales marginally consistent with the limit inferred from Hα observations.

If the observed foreground is not unique to the NCP region, such emission could be a serious contaminant to small-scale CMBR measurements in other areas of sky. That said, it should be noted that given the level of *rms* fluctuations observed at 31.7 GHz ($\Delta T_B \simeq 100$ μK), this foreground should not seriously compromise our measurement of the microwave background signal, which is by far the dominant process there.

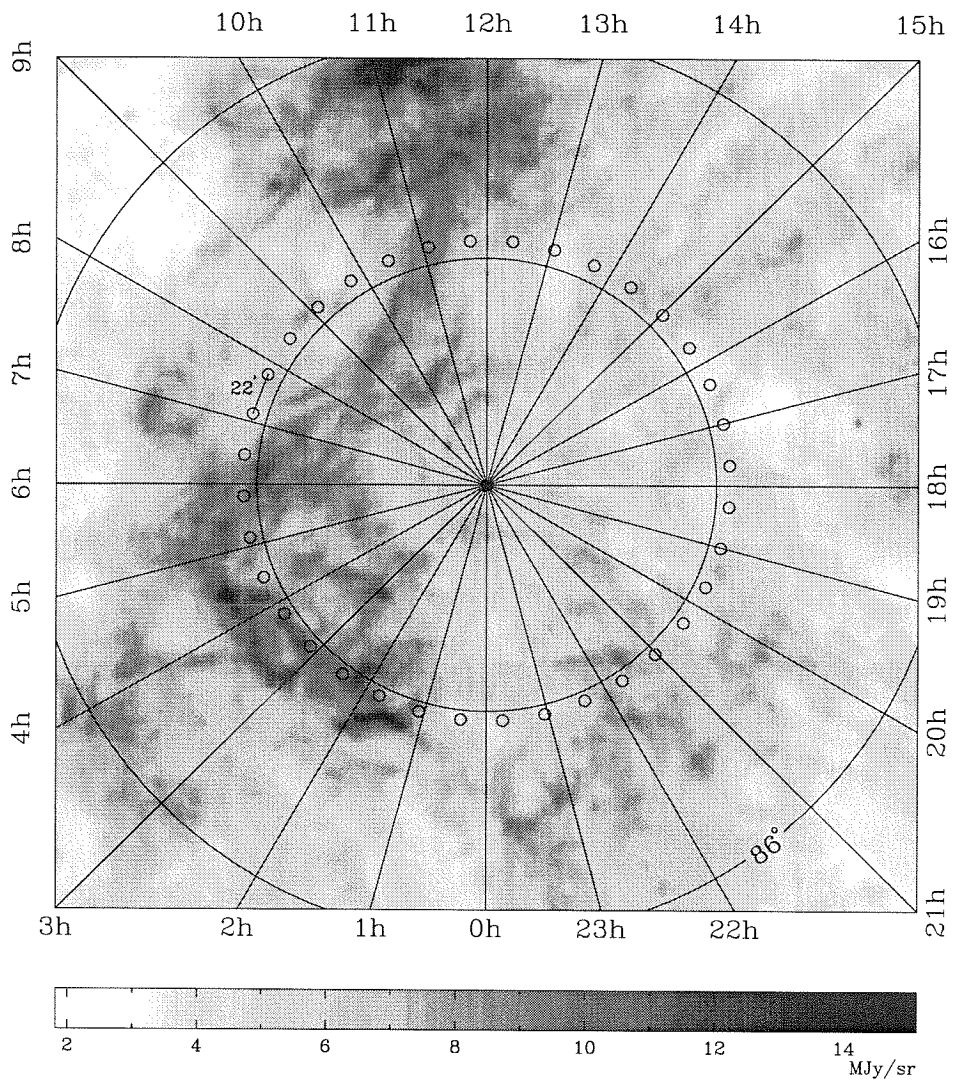

Figure 7.12 *IRAS* 100 μm map in J2000 coordinates, with RING5M fields over-plotted, ranging from $b \simeq 25°$ to $b \simeq 30°$ in Galactic latitude. The spacing of the fields is $\sim 22'$, and the FWHM of the beam is 7'.35.

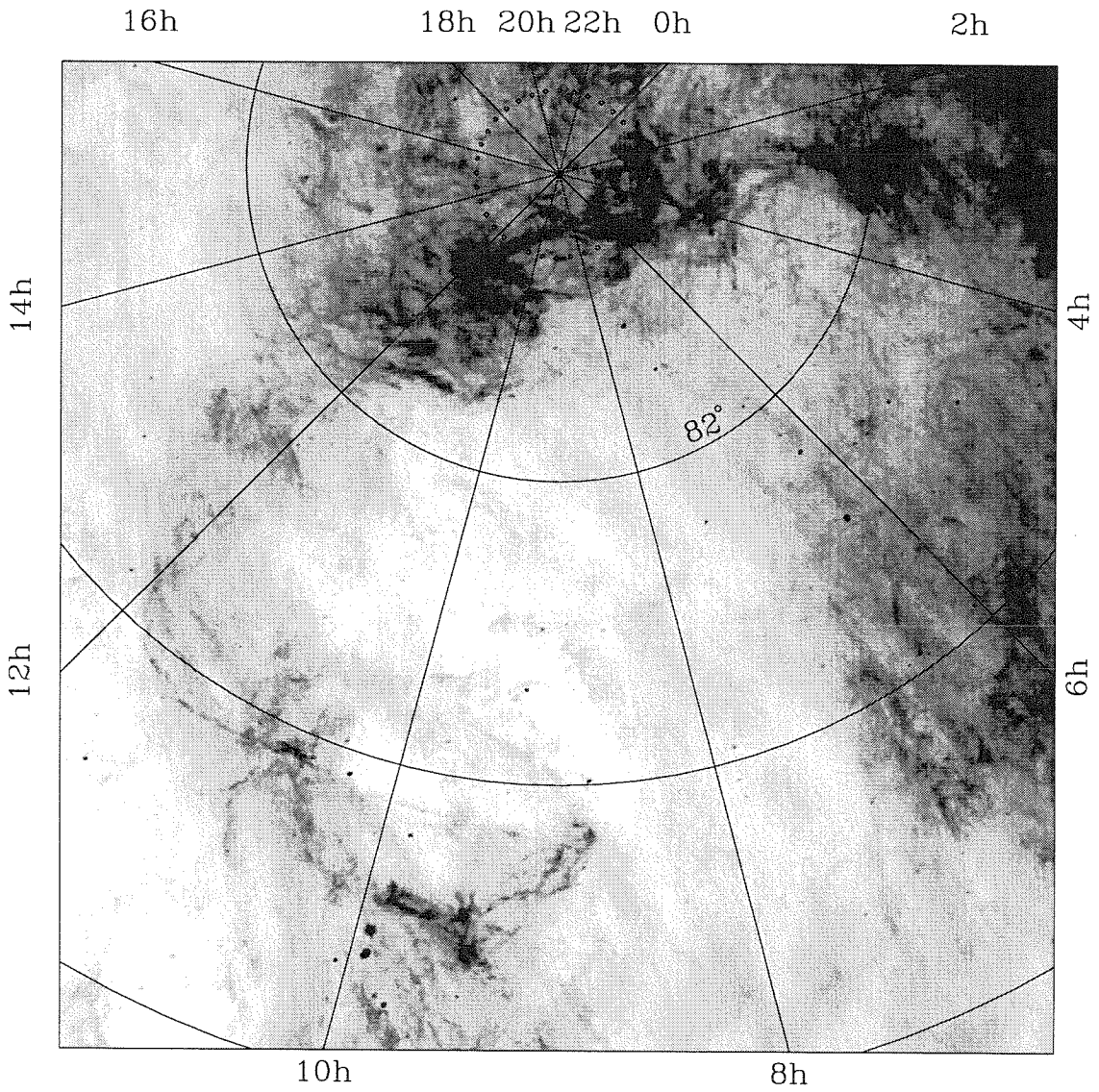

Figure 7.13 *IRAS* 100 μm map of the NCP Loop, in J2000 coordinates. Ring5m fields (shown at top) are located in the wall of a large expanding shock with $v \simeq 20$ km/s.

Chapter 8

Intrinsic Anisotropy

In previous chapters, we found that the temperature spectral index of the Ring is consistent with a mixture of steep spectrum ($\beta \sim -2$) and blackbody emission ($\beta \sim 0$), the former contributing $\sim 90\%$ of the variance at Ku-Band, the latter responsible for $\sim 90\%$ of the variance at Ka-Band. Low frequency maps of the NCP were used to rule out ($\beta < -2.2$) synchrotron emission as a possible contaminant, leaving us with a foreground which either *is* free-free, or has very nearly the same spectral dependence, in either case justifying the assumption of a single steep spectrum foreground contaminant, and allowing a reconstruction of the separate contributions of the CMBR and the Galaxy to the Ring data. Implicit in this reconstruction was the assumption of a spectral index for the foreground — in particular, we chose the index most consistent with both the low frequency maps of the NCP and the maximum likelihood spectral index estimated directly from the Ring5m data. As noted in Chapter 7, however, even if all of the signal at Ku-Band were foreground, the relative contribution to the total *rms* at Ka-Band is less than 25%, so that our estimate of the variance due to the CMBR is largely independent of the choice of spectral index and depends only on our ability to reject any flat or inverted spectrum ($\beta \geq 0$) contaminant. This can also be seen by the symmetry of the likelihood contours in Figure 7.2 about the maximum likelihood *rms* ΔT_{sky}. The unexpected correlation between the Ku-Band data

and Galactic IR cirrus provides a further constraint on the contribution of dust, so that we can proceed with confidence that the residual signal after foreground fitting is indeed the microwave background component. Note also that the steep spectrum component extracted in a two-component fit correlates strongly with the *IRAS* cirrus maps while the residual CMBR component shows no significant correlation.

8.1 Window Functions

In the previous chapter, we described the essential likelihood test which will be used here to estimate the variance from the microwave background. It was noted that the interlocked geometry of the Ring introduced spatial correlations between neighboring fields, but the computation of these elements was not explicitly described. Since model predictions are most often made in terms of the power spectrum of temperature fluctuations, what is measured in practice is the temperature autocorrelation function, since by the Wiener-Kinchin Theorem, the autocorrelation and power spectrum form a transform pair.

Consider observing the sky at position i with a telescope whose effective beam pattern (including switching) is given by $B_i(\theta, \phi)$. In the absence of switching, $B_i(\theta, \phi)$ would simply be the function $P_n(\theta, \phi)$ from §2.10 (not to be confused with the Legendre polynomials P_ℓ which appear below.) The observed sky temperature is then given by the convolution of the beam pattern with the sky temperature distribution,

$$T_i^{obs} = T_i^{sky} * B_i, \tag{8.1}$$

and the cross-correlation of the observed temperatures in fields i and j is given by

$$T_i^{obs} \otimes T_j^{obs} = (T_i^{sky} * B_i) \otimes (T_j^{sky} * B_j). \tag{8.2}$$

Denoting Fourier transform by $\mathcal{F}$, we have

$$\begin{aligned}
\mathcal{F}[T_i^{obs} \otimes T_j^{obs}] &= \mathcal{F}[T_i^{obs}] \cdot \mathcal{F}[T_j^{obs}]^* && (8.3)\\
&= \mathcal{F}[T_i^{sky} * B_i] \cdot \mathcal{F}[T_j^{sky} * B_j]^* && (8.4)\\
&= \mathcal{F}[T_i^{sky}] \cdot \mathcal{F}[B_i] \cdot \mathcal{F}[T_j^{sky}]^* \cdot \mathcal{F}[B_j]^* && (8.5)\\
&= \mathcal{F}[T_i^{sky}] \cdot \mathcal{F}[T_j^{sky}]^* \cdot \mathcal{F}[B_i] \cdot \mathcal{F}[B_j]^* && (8.6)\\
&= \mathcal{F}[T_i^{sky} \otimes T_j^{sky}] \cdot \mathcal{F}[B_i \otimes B_j], && (8.7)
\end{aligned}$$

so that

$$T_i^{obs} \otimes T_j^{obs} = (T_i^{sky} \otimes T_j^{sky}) * (B_i \otimes B_j). \quad (8.8)$$

The temperature field on the sky is most naturally expanded in spherical harmonics $T(\mathbf{x}_i) = \sum_{\ell,m} a_\ell^m Y_\ell^m(\mathbf{x}_i)$, so that assuming rotational symmetry and averaging over the whole sky, the 2-point correlation for fields separated by an angle χ_{ij} on the sky is given by

$$\langle T_i^{sky} \otimes T_j^{sky} \rangle = \frac{1}{4\pi} \sum_\ell (2\ell+1) C_\ell P_\ell(\cos\chi_{ij}), \quad (8.9)$$

where P_ℓ are the associated Legendre polynomials, and $C_\ell = \langle |a_\ell^m|^2 \rangle$ are the elements of the theoretical angular power spectrum (Peebles 1992). Defining $C_{ij_B} \equiv B_i \otimes B_j$, Equations (8.8) and (8.9) give

$$\langle T_i^{obs} \otimes T_j^{obs} \rangle = \frac{1}{4\pi} \sum_\ell (2\ell+1) C_\ell P_\ell(\cos\chi_{ij}) * C_{ij_B}, \quad (8.10)$$

so that the theoretical C_ℓ are just weighted by the *window function*

$$W_\ell^{ij} = P_\ell(\cos\chi_{ij}) * C_{ij_B}, \quad (8.11)$$

for arbitrary lag χ_{ij}. (In CMBR jargon, the spatial temperature correlation function is often spoken of in terms of *lags*, by analogy with time-series analysis. Thus, the zero-lag correlation, or (8.10) with $\chi_{ii} \equiv 0$, corresponds to the experimental variance, while the $22'$ lag is the cross-correlation of the temperatures in neighboring Ring fields.)

Equation (8.11) is a considerably more tractable form for the window function than its integral representation (obtained by inserting (8.9) into (7.4)), as the computation of W_ℓ^{ij} can be accomplished with only 2 FFTs for each ℓ, instead of a multiple integration.

8.2 Ring5m Window Functions

For computational purposes, over small areas of sky, we will switch from *az* and *za* and instead use the polar coordinates χ and ψ, the angular equivalents of r and ϕ, respectively. For the Ring5m experiment, the total beam pattern is the convolution of the switching with the beam pattern

$$B_{tot} = P_n(\chi, \psi) * S(\chi, \psi), \tag{8.12}$$

so that the zero-lag window function is given by

$$W_\ell = W_\ell^{beam} \cdot W_\ell^{switch}. \tag{8.13}$$

For a double-switched experiment, the switching is given by

$$S(\chi, \psi) = \delta(\chi, \psi) - \frac{1}{2}\delta(\chi + \chi_s, \psi) - \frac{1}{2}\delta(\chi - \chi_s, \psi), \tag{8.14}$$

where χ_s is the chopping angle, in our case $\chi_s = 22.'16$ (recall (2.8), where here the FLUX has been divided by 2). From (8.14), the autocorrelation of the switching is given by

$$C_{switch} = \frac{3}{2}\delta(\chi, \psi) - \delta(\chi+\chi_s, \psi) - \delta(\chi-\chi_s, \psi) + \frac{1}{4}\delta(\chi+2\chi_s, \psi) + \frac{1}{4}\delta(\chi-2\chi_s, \psi), \tag{8.15}$$

so that for $\chi = 0$, (8.11) gives

$$W_\ell^{switch} = \frac{3}{2} - 2P_\ell(\cos\chi_s) + \frac{1}{2}P_\ell(\cos\chi_s). \tag{8.16}$$

It can be shown (Silk & Wilson 1980, Bond & Efstathiou 1984) that for a circular Gaussian beam of width σ, W_ℓ^{beam} is given by

$$W_\ell^{beam} = \exp[-\frac{1}{2}\ell(\ell+1)\sigma^2]. \tag{8.17}$$

The full window function is then given by the product of (8.17) and (8.16).

Actual zero-lag window functions for the Ka and Ku-Band beams are compared in Figure 8.1, along with the analytic approximation given by (8.13) – (8.17). Since elements of our spatial covariance matrix in §7.3 are given by

$$C_{ij\,sky} = \frac{1}{4\pi}\sum_\ell (2\ell+1)C_\ell W_\ell^{ij}, \tag{8.18}$$

the experimental *rms*, corresponding to the diagonal elements of the theoretical covariance matrix, is given by

$$\langle \delta T \rangle_{rms} \equiv \sqrt{C_{ii\,sky}} = \sqrt{\frac{1}{4\pi}\sum_\ell (2\ell+1)C_\ell W_\ell^{ii}}. \tag{8.19}$$

Our estimate of the power spectrum is thus given by the weighted sum of the C_ℓ over the bandpass defined by the window function

$$\overline{C}_{\ell_{eff}} = \frac{\sum_\ell (2\ell+1)C_\ell W_\ell^{ij}}{\sum_\ell (2\ell+1)W_\ell^{ij}} \tag{8.20}$$

so that any difference between the Ka and Ku-Band window functions enters in only as the difference in the sum over ℓ. If we assume $C_\ell \simeq const.$ over our window, the ratio of the Ka and Ku diagonal window functions is found to be

$$C_{ii}^{Ka}/C_{ii}^{Ku} = 0.984, \tag{8.21}$$

so that we can reasonably take the window function to be the same at both frequencies. The analytic approximation (8.13) – (8.16) to the Ka-Band window function is found to be accurate to 4% ($C_{ii}^{Ka}/C_{ii}^{an} = 0.959$).

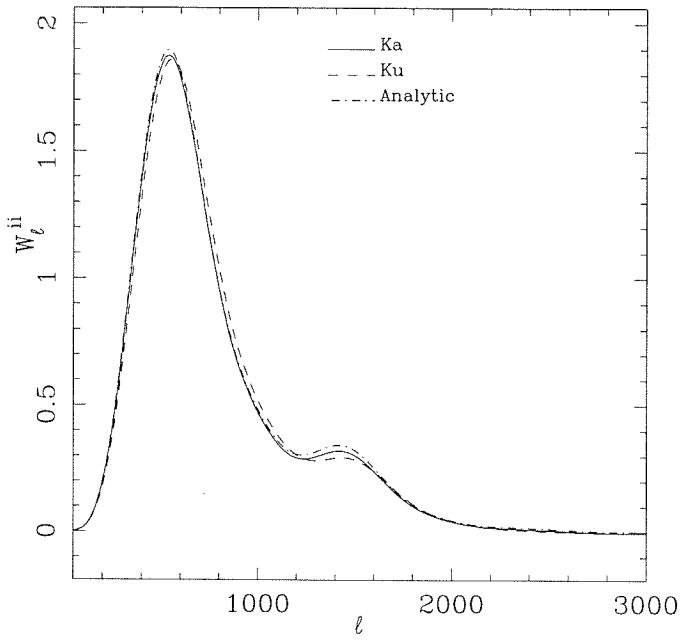

Figure 8.1 Ka, Ku-Band zero-lag window functions for the Ring5m experiment. Shown also is the analytic approximation to the Ka-Band window function given by (8.17) and (8.16).

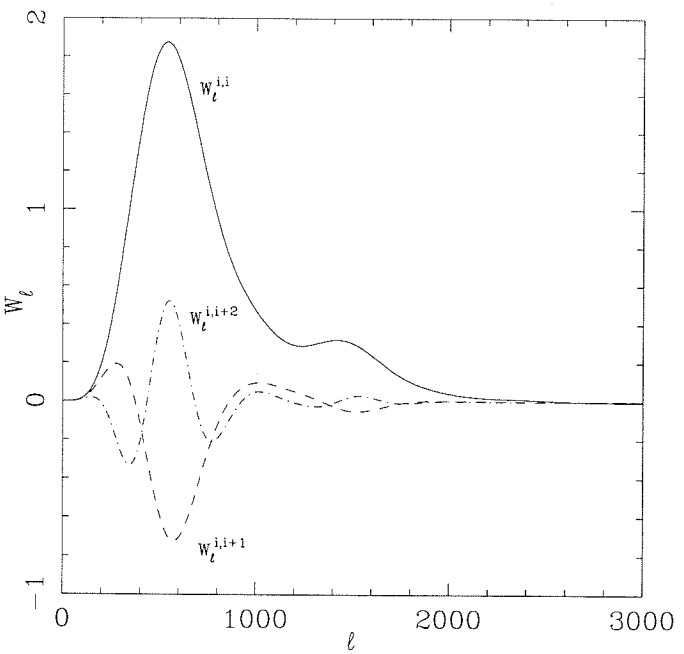

Figure 8.2 Comparison of 0 ($W_\ell^{i,i}$), 22′ ($W_\ell^{i,i+1}$) and 44′ lag ($W_\ell^{i,i+2}$) window functions for the Ring5m experiment, characterizing correlations between neighboring fields.

8.3 Noise Correlations

8.3.1 Spatial

Due to the interlocked geometry of the Ring, neighboring fields are not independent, and the spatial covariance matrix will contain non-negligible off-diagonal components given by (8.18). Since the detected signal in field i is the difference between T_i and the temperatures in the two neighboring fields, the correlated signal between neighboring fields will enter in as a negative. Window functions for the first two non-zero lags are shown in Figure 8.2. In our likelihood analyses, we include only the first two lags, as subsequent lags have a negligible effect on the estimated variance.

As noted in the previous section, given a model power spectrum, specified by the C_ℓ, and the experimental window functions W_ℓ^{ij}, the predicted *rms* is given by the diagonal elements of the theoretical covariance matrix C_{ii}. Thus, to recover the *rms* in the maximum likelihood test described in §7.3, when computing off-diagonal elements, we must normalize the spatial covariance matrix to the correlation matrix, so that for a sky *rms* with amplitude $\Delta T_{sky} = 1$, and spectral index $\beta = 0$,

$$C'_{ij\,sky} = C_{ij\,sky}/\sqrt{C_{ii\,sky}C_{jj\,sky}} = C_{ij\,sky}/C_{ii\,sky}. \tag{8.22}$$

The measured off-diagonal components for the Ring (up to $W_\ell^{i,i+2}$) give

$$C'_{i,i+1} = -0.111 \tag{8.23}$$

$$C'_{i,i+2} = +0.013 \tag{8.24}$$

for $C_\ell = const.$ over the window. As shown in Figure 8.1, neglecting these spatial correlations results in an overestimate of the sky variance by a few percent.

8.3.2 Temporal

In §6.4, we showed that the variance due to point source subtraction is given by

$$C_{ii} = \sum_k \langle b_{i,k}^2 \rangle \sigma_k^2, \tag{8.25}$$

where the $b_{i,k}$ are the beam weighting factors for the k^{th} source in the i^{th} field. In general point sources are not measured on a point-by-point basis, but are instead assumed to have a constant flux and associated error over timescales of a month (the typical time between VLA flux monitoring sessions). Since any source affects at least three fields through the double switching, subtraction of these contributions will introduce temporally correlated noise between neighboring fields, contributing

$$C_{ij} = \sum_k \langle b_{i,k} \rangle \langle b_{j,k} \rangle \sigma_k^2, \tag{8.26}$$

to the covariance matrix. When these covariances are included, even for the 1994-1995 Ring5m Ka-Band data, for which source errors are enlarged to include variability, the effect is negligible.

8.4 Likelihood Analysis

To assess the amplitude of the sky variance, we can take several approaches, the most naive being to suppose that all of the structure observed at Ka-Band is due to the microwave background. As remarked earlier, since any significant flat or inverted spectrum contamination of the Ring data can be excluded, this method gives very nearly the same result as methods which attempt to account for foregrounds, given the level of the foreground detected at Ku-Band. The likelihood is constructed as before, accounting for spatial covariances and temporal covariance introduced by point-source subtraction, yielding

$$\langle \delta T \rangle_{rms} = 83^{+12}_{-9}\ \mu\mathrm{K}, \tag{8.27}$$

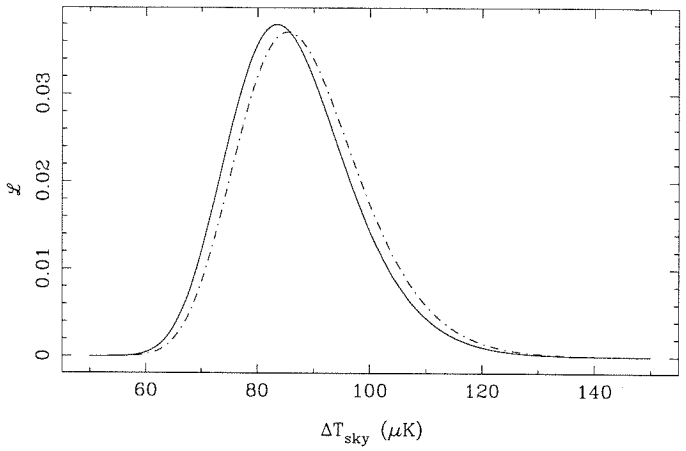

Figure 8.3 Likelihood function $\mathcal{L}(\Delta T_{sky})$ for the Ring5m source-subtracted Ka-Band data. Likelihood is shown for a diagonal covariance matrix (dot-dashed line) and for the full covariance matrix, including non zero-lag window functions and correlations introduced by point-source subtraction.

where quoted errors are the 1σ HPD confidence intervals for the likelihood shown in Figure 8.3.

Alternatively, we can assume that the structure in the Ring is a combination of CMBR and a single foreground and obtain the likelihood as a function of the (unknown) spectral index of the foreground, $\mathcal{L}(\Delta T_{sky}, \beta)$, as in §7.3. A conservative approach is to integrate out the dependence on the spectral index

$$\mathcal{L}(\Delta T_{sky}) = \int_{\beta_{min}}^{\beta_{max}} \mathcal{L}(\Delta T_{sky}, \beta) d\beta, \tag{8.28}$$

restricting the integration to bounds defined by a reasonable prior, e.g., one uniform for $-3 < \beta < 2$. The *rms* so obtained is given by

$$\langle \delta T \rangle_{rms} = 78^{+11.5}_{-8.5}\ \mu\mathrm{K}. \tag{8.29}$$

Due to the symmetry of the likelihood in Figure 7.2 about its maximum ΔT_{sky}, the limits obtained by integrating out the dependence on β are nearly identical to the limits obtained for the likelihood at β_{max}, and we take (8.29) to be definitive.

8.5 Conversion to Band Power

The mass fluctuation power spectrum is often assumed to be scale-invariant at small wave number $\mathcal{P}(k) \propto k$ (i.e., the Harrison-Zel'dovich spectrum), leading to a CMBR angular power spectrum with

$$C_\ell^{-1} \propto \ell(\ell+1) \tag{8.30}$$

on large angular scales (Peebles 1992). As a result, the *band power*

$$\delta T_\ell = \sqrt{\ell(\ell+1)C_\ell/2\pi} \tag{8.31}$$

is expected to be flat over a large part of the angular power spectrum, and is most often the quantity predicted by theory. Thus to compare the Ring5m result with theoretical predictions of the CMBR power spectrum, then, the measured *rms* must be converted to an equivalent band power. Comparing (8.19) with (8.31), we see that the band power is related to the *rms* by

$$\langle \delta T \rangle_{rms} = \sqrt{\sum_\ell \frac{(\ell+\frac{1}{2})}{\ell(\ell+1)} \delta T_\ell^2 W_\ell^{ii}}. \tag{8.32}$$

If δT_ℓ were constant over the bandpass defined by the window function, we could write

$$\langle \delta T \rangle_{rms} = \delta T_{\ell_e} \sqrt{\sum_\ell \frac{(\ell+\frac{1}{2})}{\ell(\ell+1)} W_\ell^{ii}}, \tag{8.33}$$

so that the *effective band power* defined by δT_{ℓ_e} is in general a weighted mean of the band power over the window function. Defining the discrete logarithmic integral (Bond 1995) of a function to be

$$I(f) = \sum_\ell f_\ell \frac{(\ell+\frac{1}{2})}{\ell(\ell+1)}, \tag{8.34}$$

we can write

$$\langle \delta T \rangle_{rms} = \delta T_{\ell_e} \sqrt{I(W_\ell^{ii})}. \tag{8.35}$$

In terms of the logarithmic integral, ℓ_e is given by

$$\ell_e = \frac{I(\ell W_\ell^{ii})}{I(W_\ell^{ii})}. \tag{8.36}$$

For the Ka-Band window function W_ℓ^{ii} depicted in Figure 8.1, we find

$$\ell_e = 589^{+167}_{-228}, \tag{8.37}$$

where the quoted limits are the points at which the window function has fallen by $e^{-0.5}$. The integral of the window function is

$$I(W_\ell^{ii}) = 1.96, \tag{8.38}$$

so that the equivalent band power is given by

$$\delta T_{\ell_e} = 56^{+8.2}_{-6.1}\ \mu\mathrm{K}. \tag{8.39}$$

8.6 Error Budget

Suppose N numbers t_i are drawn from a distribution with underlying variance σ^2. Add to these N numbers n_i with zero mean and variance σ_n^2. Then the variance of $x_i = t_i + n_i$ is given by

$$V(x) = V(t) + V(n) = \sigma^2 + \sigma_n^2, \tag{8.40}$$

so that the variance estimated from the samples x_i is a biased estimator of the underlying variance σ^2.

Ignoring correlations between the x_i, when we estimate the underlying variance by maximizing the likelihood, we start with

$$\mathcal{L} = \prod_i^N \frac{1}{\sqrt{2\pi(\sigma^2 + \sigma_n^2)}} \exp\left\{-\frac{(x_i^2 - \overline{x})^2}{2(\sigma^2 + \sigma_n^2)}\right\}, \tag{8.41}$$

whence

$$\ln \mathcal{L} = -\frac{1}{2}\sum_i^N \ln\left\{2\pi(\sigma^2+\sigma_n^2)\right\} - \sum_i^N \frac{(x_i^2-\overline{x})^2}{2(\sigma^2+\sigma_n^2)}. \tag{8.42}$$

Maximizing, we obtain

$$\frac{\partial \ln \mathcal{L}}{\partial \sigma^2} = 0 \Rightarrow -\sum_i^N \frac{1}{(\sigma^2+\sigma_n^2)} + \sum_i^N \frac{(x_i^2-\overline{x})^2}{(\sigma^2+\sigma_n^2)^2} = 0, \tag{8.43}$$

or

$$\sigma^2 = \frac{1}{N}\sum_i^N (x_i^2-\overline{x})^2 - \sigma_n^2, \tag{8.44}$$

which is obviously an unbiased estimator of σ^2.

What are the contributions to the error in our estimate of the variance? These come from three different sources. First, suppose each t_i represents the mean temperature in field i. Our determination of t_i has an associated variance, which, if it is the same for all fields i, we can identify with σ_n^2 above. The error which the variance in the means contributes to our estimate of $V(t)$ is given, in the Gaussian approximation, by

$$V(V(t))_{meas} = \sum_i^N \left|\frac{\partial V(t)}{\partial t_i}\right|^2 \sigma_n^2 \tag{8.45}$$

$$= \frac{4\sigma_n^2}{N^2}\sum_i^N (t_i-\overline{t})^2, \tag{8.46}$$

or

$$V(V(t))_{meas} = \frac{4\sigma_n^2}{N}V(t). \tag{8.47}$$

Next suppose we have $t_i = cf_i$, where c is a calibration factor whose mean is known to some accuracy σ_c. Then

$$V(t) = c^2 V(f), \tag{8.48}$$

and the error associated with uncertainties in c is given by

$$V(V(t))_c = 4c^2V^2(f)\sigma_c^2 \tag{8.49}$$

$$= 4V^2(t)\frac{\sigma_c^2}{c^2}. \tag{8.50}$$

The final contribution to the uncertainty is just the sampling variance of $V(t)$, that is, the uncertainty in $V(t)$ from the finite number of samples which determine it, given by (see Appendix C)

$$V(V(t)) = \frac{2}{N}V^2(t). \tag{8.51}$$

The total uncertainty in our estimate of $V(t)$ is then

$$\begin{aligned} V(V(t))_{tot} &= V(V(t))_{meas} + V(V(t))_c + V(V(t)) && (8.52) \\ &= \frac{4\sigma_n^2}{N}V(t) + 4V^2(t)\frac{\sigma_c^2}{c^2} + \frac{2}{N}V^2(t). && (8.53) \end{aligned}$$

From the maximum likelihood estimate of the variance at Ka-Band (8.29), we see that the final term dominates the uncertainties. The error in the *rms* is just 1/2 the error in the variance, so that (8.51) gives ± 10 μK for a measured *rms* of 83 μK; from (8.47), for a mean error per field of $\sim$ 17 μK, the corresponding measurement error in the *rms* is 3 μK. As is evident in (8.29), when correlations between fields, point-source subtraction, and foregrounds are taken into account, the measurement error contributes about 5% to the error in the *rms*.

In §4.1.1, we demonstrated that the calibration factor used to convert to intensity (or equivalently, to brightness temperature) is proportional to T_{cal}/η_b when measured against the noise diodes, and to S_{cal}/Ω_m when measured directly against sources (see (4.8) and (4.10)). At Ka-Band, the error in the beam efficiency is 3.5%, while the error in the diode temperature scale prior to 1996 gives 3.2% when combined in quadrature with the error in the non-linearity correction, yielding a total calibration uncertainty of 4.7%. In 1996, the data were calibrated directly against sources, with 3.3% uncertainty in the flux scale, while the beam contributes 0.6%, for a total of 3.4%. Since different calibration methods were used in different years, we cannot assume that the calibration error σ_c in (8.50) is constant. Instead, we take the mean of the calibration errors, weighted by the measurement errors in the variance from

each season, yielding a total Ka-Band calibration error of

$$\sigma_{cal}^{Ka} = 4.3\%, \tag{8.54}$$

so that 1σ errors on the band power should be increased to

$$\delta T_{\ell_e} = 56^{+8.5}_{-6.6}\ \mu\mathrm{K}. \tag{8.55}$$

Chapter 9

Post Mortem

The goal of the Ring5m experiment was to determine the CMBR anisotropy on $7' - 22'$ scales, thereby improving constraints on cosmological models on scales of direct relevance to structure formation (as opposed to large-angular scale experiments, which measure only the primordial power spectrum). The experiment was most successful, resulting in a detection of sky variance well above the noise limits of the data. With the addition of a second frequency channel and removal of point source contamination with the VLA, we are able to state with confidence that nearly all of the variance at 31.7 GHz is due to the CMBR. The final likelihood analysis yields a temperature *rms* of $\langle \delta T \rangle_{rms} = 78^{+12.9}_{-9.1}$ μK, or equivalently, a band power of $\delta T_\ell \equiv \sqrt{\ell(\ell+1)C_\ell/2\pi} = 56^{+8.5}_{-6.6}$ μK (1σ HPD confidence interval) at $\ell_e = 589^{+167}_{-228}$, for the CMBR component alone.

The addition of the low frequency channel not only enabled us to discriminate foreground contaminants, but resulted in a detection of a unique component of Galactic emission. Of intrinsic interest to astrophysics of the interstellar medium, the detection of this component is a cautionary tale for future CMBR experiments; whether the emission is due to high-temperature free-free emission correlated with Galactic dust, or to some novel type of emission from the dust itself (see §7.10), this result suggests that Galactic IR cirrus is potentially a serious contaminant of small-scale

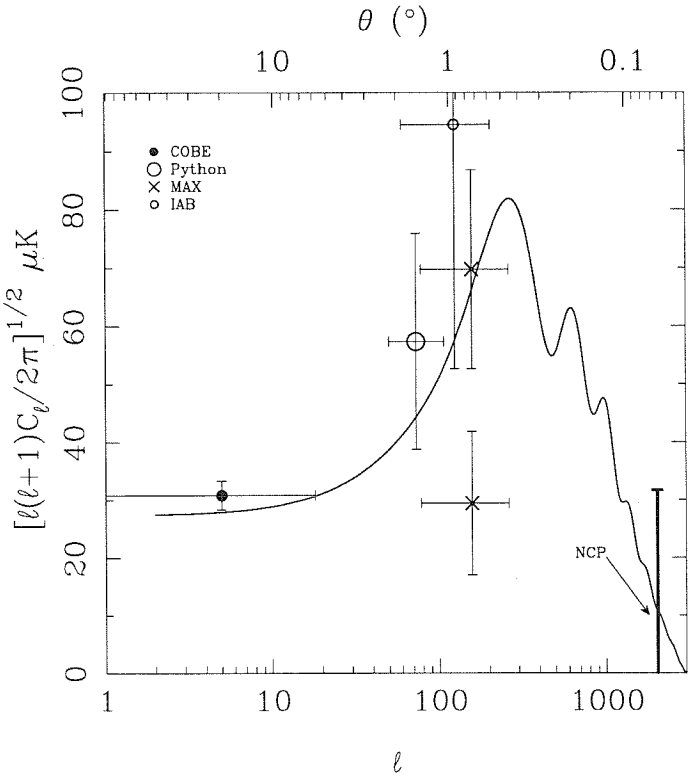

Figure 9.1 CMBR anisotropy, as of winter 1993, shown with a standard CDM model (solid line) with $H_0 = 30, \Omega_0 = 1$ and $\Omega_b = 0.05$. Data points are: COBE (Gorski et al. 1994), Python (Dragovan et al. 1993), MAX (Gunderson et al. 1993), IAB (Piccirillo & Calisse 1993), and NCP (Readhead et al. 1989).

anisotropy experiments even below 100 GHz.

When this experiment began, anisotropy in the CMBR had only recently been detected by the *COBE* DMR, with a handful of tentative detections reported at degree angular scales, as indicated in Figure 9.1. It is a testament to the rapid growth of this field that in the ensuing three years no fewer than 15 new detections of anisotropy have been reported, a sample of which are shown in Figure 9.2.

Amid the rush to detect the first "Doppler peak" (for the axiomatic $\Omega_0 = 1$ universe anyway) following the announcement of the *COBE* result in 1992

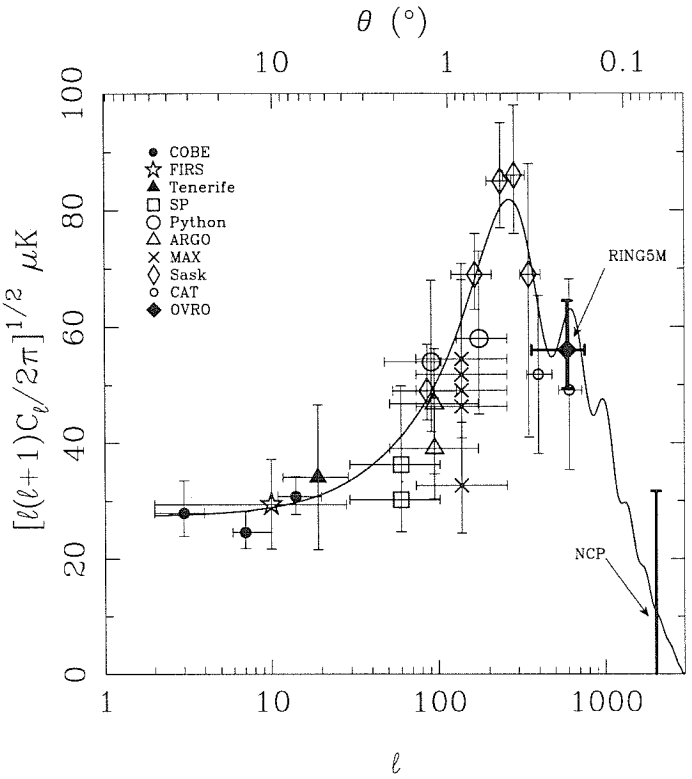

Figure 9.2 CMBR anisotropy, as of winter, 1996, shown with a standard CDM model (solid line) with $H_0 = 30, \Omega_0 = 1$ and $\Omega_b = 0.05$. Indicated in bold are the 95% confidence upper limit from the OVRO NCP experiment (Readhead et al. 1989) and the OVRO Ring5m detection of anisotropy at $\ell_e = 589$ (this thesis). The two data points near the Ring5m datum are recent results from the Cambridge Anisotropy Telescope. Data points are: COBE (Hinshaw et al. 1996), FIRS (Ganga 1994), Tenerife (Hancock et al. 1997), SP (Gunderson et al. 1995), Python (Platt et al. 1997), ARGO (de Berbardis et al. 1994), MAX (Tanaka et al. 1996), Sask (Netterfield et al. 1997), CAT (O'Sullivan et al. 1995, Scott et al. 1996).

(Smoot et al. 1992), the Ring5m experiment at its inception was in scant company in its search for evidence of secondary acoustic peaks at large ℓ. Only the White Dish experiment (Tucker et al. 1993) probed similar scales, resulting in a 95% confidence upper limit of $\Delta T/T < 2.3 \times 10^{-5}$. Recently, observations with the Cambridge Anisotropy Telescope (CAT), a 3-element interferometer designed to map the CMBR on angular scales between 10′ and 30′, have resulted in a detection of CMBR anisotropy on angular scales directly comparable to the Ring5m

(O'Sullivan et al. 1995, Scott et al. 1996). At $\ell = 590$, the CAT group measures a broadband power of $\Delta T/T = 1.8^{+0.7}_{-0.5} \times 10^{-5}$, while at $\ell = 410$, the measured power is $\Delta T/T = 1.9^{+0.5}_{-0.5} \times 10^{-5}$, with a maximum likelihood estimate for the anisotropy in a single bin in ℓ-space centered on $\ell = 500$ of $2.0^{+0.4}_{-0.4} \times 10^{-5}$, in excellent agreement with the broadband power reported in this thesis ($2.1^{+0.4}_{-0.3} \times 10^{-5}$, assuming the FIRAS result of $T_{CMBR} = 2.728$ K (Fixsen et al. 1996)).

As can be seen in Figure 9.2, the Ring5m and CAT results are forming a consensus that the CMBR power spectrum is in good agreement with predictions of *COBE*-normalized standard CDM models. Both results indicate that if the collection of data near ℓ of a few hundred can be taken as evidence for a peak in the power spectrum — and recent assessments indicate that they can (Scott et al. 1995, Lineweaver et al. 1997) — the Ring5m result is consistent with a power spectrum which is falling by $\ell \sim 600$. A χ^2 fit to the data in Figure 9.2 for a range of model power spectra (see Figure 9.3–Figure 9.6) prefers the standard CDM scenario, with $\Omega_0 = 1$, $\Omega_b = 0.05$ and $h = 0.3$, shown as the solid line in Figure 9.2. Although increasing Ω_b dramatically affects the amplitude of the first acoustic peak (recall Figure 1.1), the competing effects of damping at small scales and enhancement of compressional peaks with increasing Ω_b means that the Ring5m and CAT results cannot strongly constrain Ω_b in a closed ($\Omega_0 = 1$) universe.

On scales of 2′, the OVRO NCP 95% confidence upper limit of $\Delta T/T < 1.7 \times 10^{-5}$ has recently been confirmed by the SUZIE experiment, a 6-element bolometer array at Caltech's Submillimeter Observatory. At 142 GHz, where point source contributions are negligible, they set a 95% confidence upper limit of $\Delta T/T < 2.1 \times 10^{-5}$ on the same scale as the NCP experiment (Church et al. 1997). While these results cannot place strong constraints on standard CDM models, as anisotropies are exponentially damped at the smallest scales for all these models (see Figure 9.3), the Ring5m+CAT and NCP+SUZIE results together constitute a powerful constraint on open universe

models; models with $h = 0.3 - 0.7$ and $\Omega_b = \Omega_0 = 0.2$ overpredict small-scale power by $35\% - 50\%$ at ℓ_{Ring}, and by $10\% - 35\%$ over the NCP 95% confidence at ℓ_{NCP}. Open models with baryon density close to the lower bound allowed by Big Bang nucleosynthesis calculations, $\Omega_b h^2 \sim 0.015$ (Wagoner 1973, Dicus 1982), can reproduce the band powers observed on small angular scales (see Figure 9.6) but severely underpredict the power observed by degree-scale experiments. Thus, in combination with these experiments, our results effectively rule out open universe models.

For now, the Ring5m and NCP results, in conjunction with degree-scale anisotropy experiments, have provided tantalizing clues that standard cosmologies are not grossly wrong, but that they may nevertheless be in need of help. In the face of the growing consensus from large scale structure estimates of the total mass density, $\Omega_m \lesssim 0.3$ (Bahcall 1998), the microwave background may be presenting us with a paradox, whose unaesthetic resolution may lie with the assertion of a non-zero cosmological constant. Only the next generation of interferometric CMBR experiments (Readhead et al. 1997, White et al. 1997), and the battle at L_2, will tell.

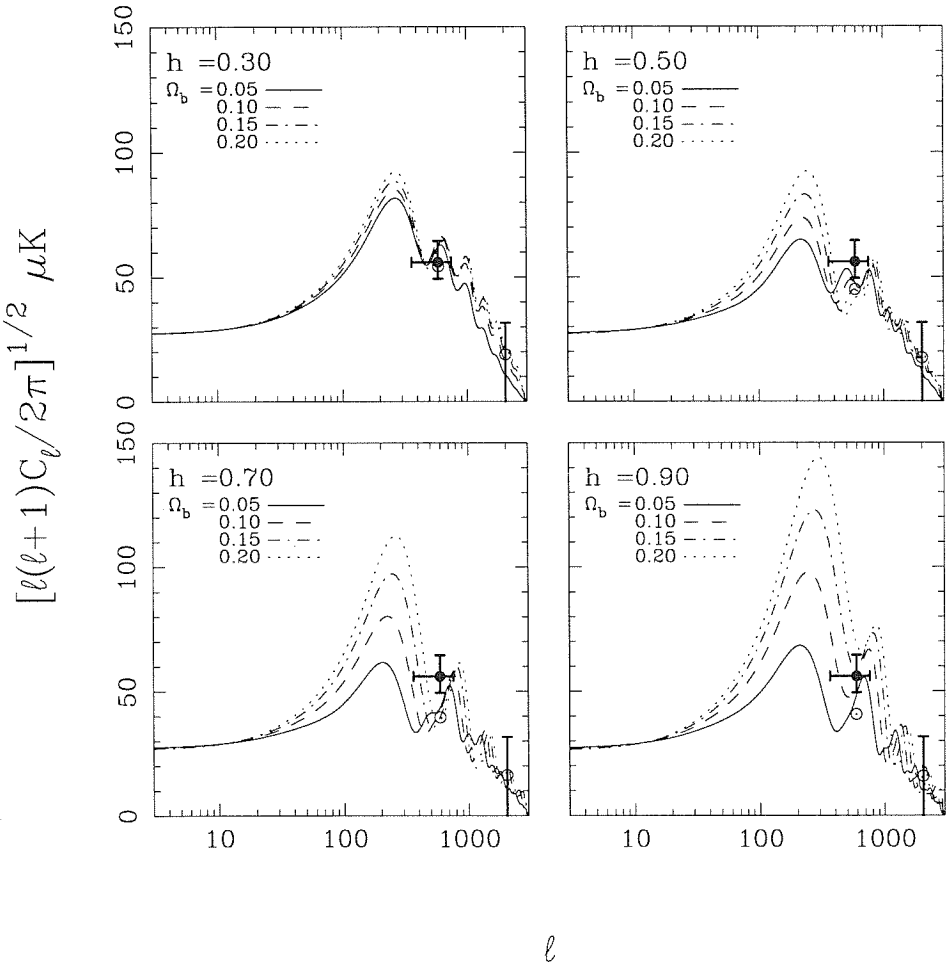

Figure 9.3 Model adiabatic power spectra, with $\Omega_0 = 1$. Open circles are the expected experimental band powers for the Ring5m and NCP experiments, for models with low baryonic content $\Omega_b = 0.05$. All models are courtesy of Seljak & Zaldarriaga (1997).

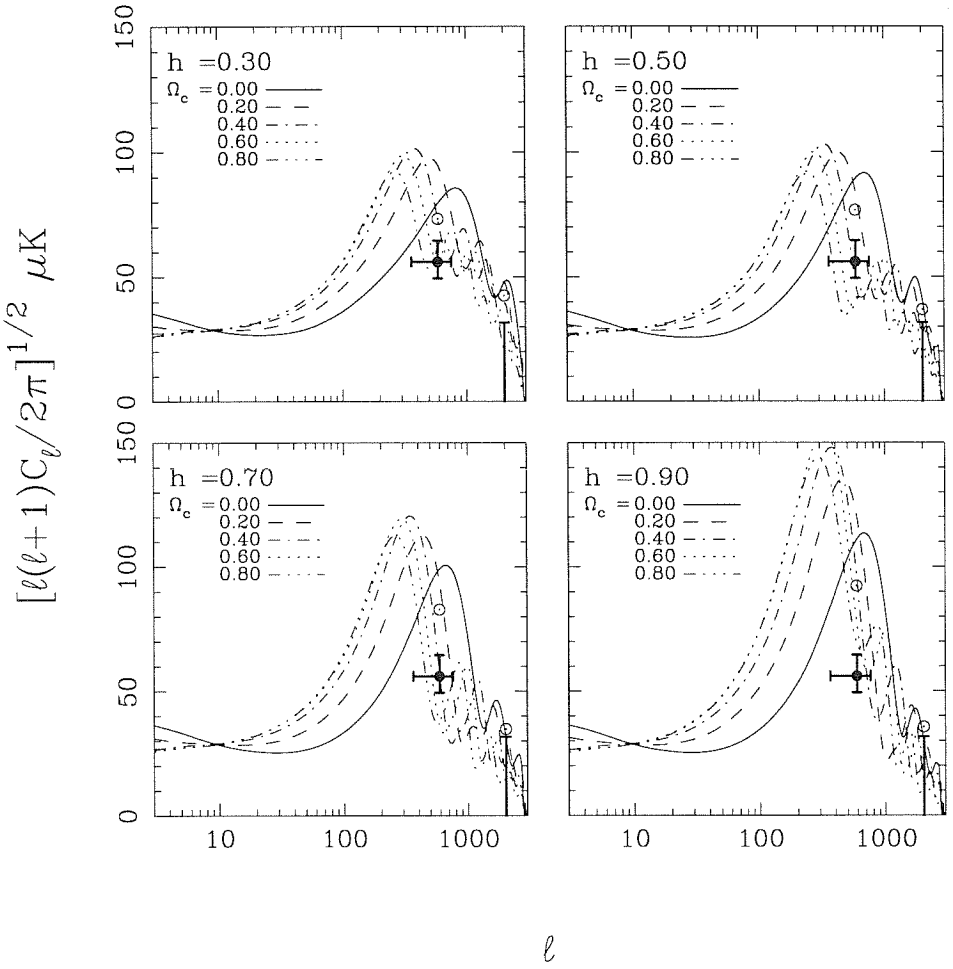

Figure 9.4 Model adiabatic power spectra, with $\Omega_b = 0.2$. Open circles are the expected experimental band powers for the Ring5m and NCP experiments, for models with no non-baryonic matter $\Omega_c = 0$.

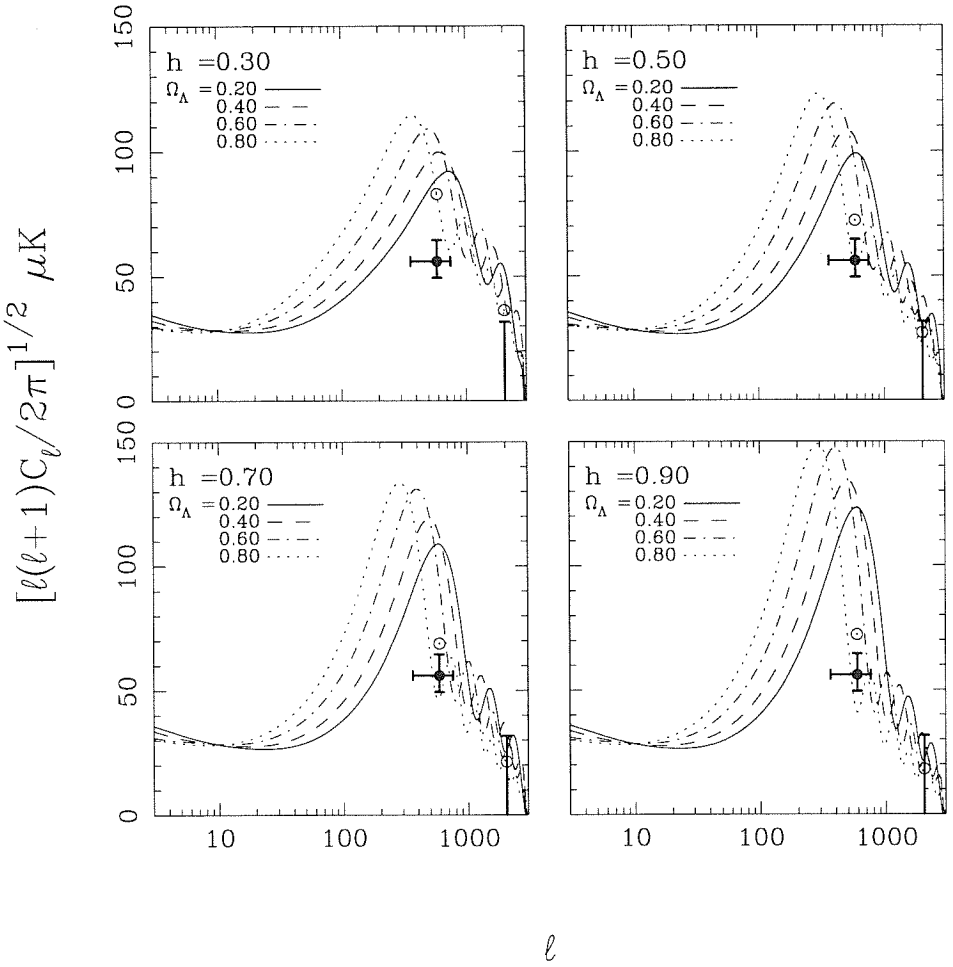

Figure 9.5 Model adiabatic power spectra, with $\Omega_b = 0.2$ and $\Omega_c = 0.0$. Open circles are the expected experimental band powers for the Ring5m and NCP experiments, for closed Λ models.

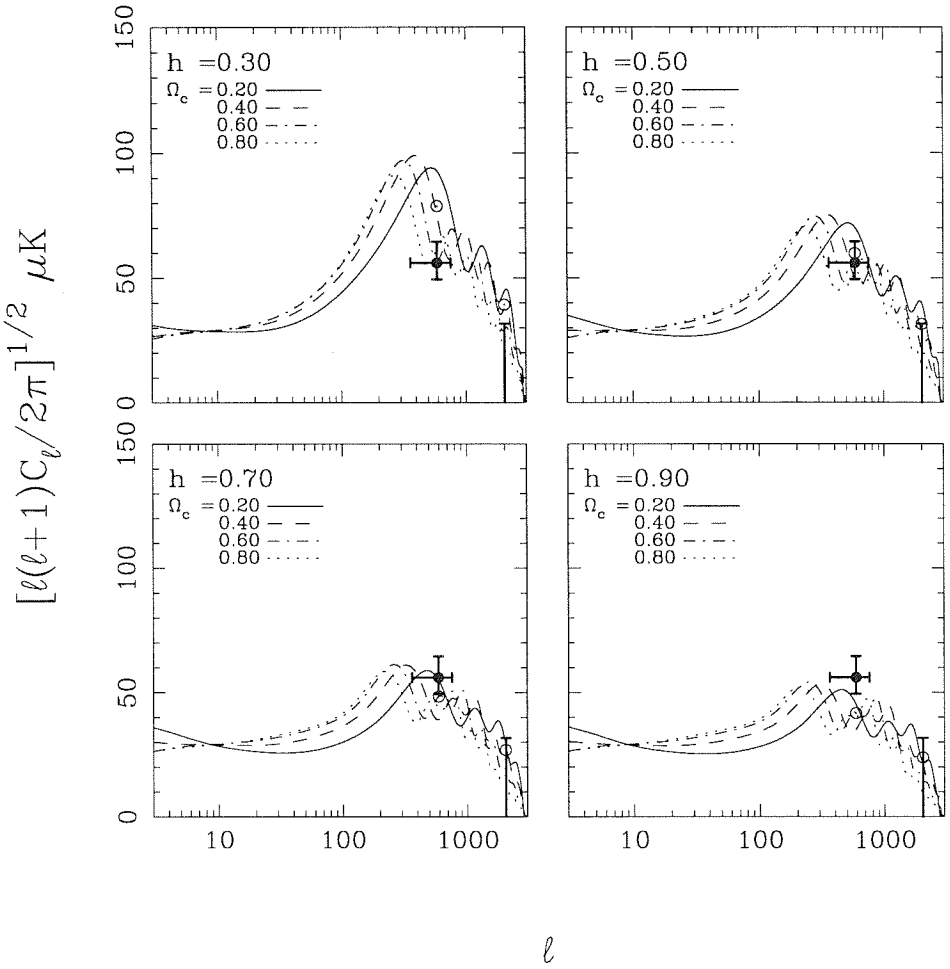

Figure 9.6 Model adiabatic power spectra for open models, with $\Omega_b h^2 = 0.015$ and $\Omega_\Lambda = 0.0$. Open circles are the expected experimental band powers for the Ring5m and NCP experiments, for $\Omega_c = 0.2$ models. For $0.5 < h < 0.7$, these band powers are consistent with the Ring5m and NCP results for $\Omega_b + \Omega_c$ consistent with current estimates from studies of galaxy clusters, but the low amplitude of these models is grossly inconsistent with degree scale anisotropy measurements.

Appendix A

Formalism for Switched Beams

A single FLUX measurement consists of four integrations, in the order off-source, on-source, on-source, off-source, or the A, B, C and D fluxes, respectively. Each segment is a time-average of the Dicke-switched power difference between two feed horns separated by $\Delta\phi$ on the sky. Let $P_A(\theta,\phi)$ and $P_R(\theta,\phi)$ be the angular power pattern of the ANT and REF feed horns on the sky, respectively, where $P(\theta,\phi) = P_n(\theta,\phi)/\iint_{4\pi} P_n(\theta,\phi)d\Omega$ and $P_n(\theta,\phi)$ is normalized such that $P_n(0,0) = 1$. Then in each on-source measurement, for a temperature field $T(\theta,\phi)$ on the sky, we measure

$$T_{on} = \iint_{\Omega_m} \{T(\theta,\phi)P_A(\theta,\phi) - T(\theta,\phi+\Delta\phi)P_R(\theta,\phi)\}d\Omega \quad \text{(A.1)}$$

$$\simeq \iint_{\Omega_m} \{T(\theta,\phi)[P_A(\theta,\phi) - P_R(\theta,\phi)] - [\Delta\phi T'(\theta,\phi) + \frac{\Delta\phi^2}{2}T'']P_R(\theta,\phi)\}d\Omega, \quad \text{(A.2)}$$

where derivatives are with respect to ϕ. In each off-source integration, we measure

$$T_{off} = \iint_{\Omega_m} \{T(\theta,\phi-\Delta\phi)P_A(\theta,\phi) - T(\theta,\phi)P_R(\theta,\phi)\}d\Omega \quad \text{(A.3)}$$

$$\simeq \iint_{\Omega_m} \{T(\theta,\phi)[P_A(\theta,\phi) - P_R(\theta,\phi)] + [\Delta\phi T'(\theta,\phi) - \frac{\Delta\phi^2}{2}T'']P_A(\theta,\phi)\}d\Omega, \quad \text{(A.4)}$$

so that

$$T_{on} - T_{off} = \iint_{\Omega_m} \{\frac{\Delta\phi^2}{2}T''(\theta,\phi)[P_A(\theta,\phi) + P_R(\theta,\phi)] +$$

$$\Delta\phi T'(\theta,\phi)[P_A(\theta,\phi) - P_R(\theta,\phi)]\}d\Omega. \tag{A.5}$$

If $P_A(\theta,\phi) \simeq P_R(\theta,\phi)$, we can discard the term linear in $\Delta\phi$. To second order, then, defining $\Delta T(\theta_0,\phi_0) = \{T_{on}(\theta_0,\phi_0) - T_{off}(\theta_0,\phi_0)\}$, and introducing $\tilde{P}(\theta_0-\theta,\phi_0-\phi) \equiv P(\theta-\theta_0,\phi_0-\phi)$, we are left with

$$\begin{aligned}\Delta T_A(\theta_0,\phi_0) &= \iint_{\Omega_m} \frac{\Delta\phi^2}{2} T''(\theta,\phi)[\tilde{P}_A(\theta_0-\theta,\phi_0-\phi) + \tilde{P}_R(\theta_0-\theta,\phi_0-\phi)]d\Omega \\ &\equiv \iint_{\Omega_m} \Delta T_B(\theta,\phi)[\tilde{P}_A(\theta_0-\theta,\phi_0-\phi) + \tilde{P}_R(\theta_0-\theta,\phi_0-\phi)]d\Omega.\end{aligned} \tag{A.6}$$

Against a source with $\Omega_s \ll \Omega_m$, we can use (A.6) to measure Ω_m. At a given offset position from the source (θ_i,ϕ_i), we measure

$$\begin{aligned}\Delta T_{A_i} &= \iint_{\Omega_m} \Delta T_B(\theta,\phi)[\tilde{P}_A(\theta_i-\theta,\phi_i-\phi) + \tilde{P}_R(\theta_i-\theta,\phi_i-\phi)]d\Omega \\ &\simeq \Delta T_B \iint_{\Omega_m} \delta(\theta,\phi)[\tilde{P}_A(\theta_i-\theta,\phi_i-\phi) + \tilde{P}_R(\theta_i-\theta,\phi_i-\phi)]d\Omega \\ &= \Delta T_B\{\tilde{P}_A(\theta_i,\phi_i) + \tilde{P}_R(\theta_i,\phi_i)\},\end{aligned} \tag{A.7}$$

so that the effective beam, which we refer to as the *mean* beam Ω_M, is just given by the average of the ANT and REF beams. Normalizing by the peak flux at the center of the beam,

$$\Delta T_{A_0} = \Delta T_B\{\tilde{P}_A(0,0) + \tilde{P}_R(0,0)\}, \tag{A.8}$$

we have

$$\frac{\Delta T_{A_i}}{\Delta T_{A_0}} = \frac{\tilde{P}_A(\theta_i,\phi_i) + \tilde{P}_R(\theta_i,\phi_i)}{\tilde{P}_A(0,0) + \tilde{P}_R(0,0)}, \tag{A.9}$$

so that

$$\Omega_M = \sum_i \frac{\Delta T_{A_i}}{\Delta T_{A_0}} \Delta\Omega. \tag{A.10}$$

Appendix B

Polarization

In this appendix, measurements of the polarization purity of the Ku-Band receiver are described. In notation and general outline, we follow the discussion of Kraus 1986.

Let $\vec{\mathbf{E}}$ be a completely polarized plane wave. In general, we can write

$$\vec{\mathbf{E}} = (E_1\hat{\mathbf{x}} + E_2\hat{\mathbf{y}})e^{-i\omega t}, \tag{B.1}$$

where E_1 and E_2 are themselves complex amplitudes

$$\begin{aligned} E_1 &= \mathcal{E}_1 e^{i\phi_1} \\ E_2 &= \mathcal{E}_2 e^{i\phi_2}. \end{aligned} \tag{B.2}$$

In general, E_1 and E_2 describe an ellipse in space. If the principal axes of the ellipse are inclined at an angle χ with respect to the coordinate axes, and the angle $\beta \equiv \cot AR$ describes the axial ratio,

$$\begin{aligned} E_x &= \mathcal{E}_0(\cos\beta\cos\chi\cos\omega t + \sin\beta\sin\chi\sin\omega t) \\ E_y &= \mathcal{E}_0(\cos\beta\sin\chi\cos\omega t - \sin\beta\cos\chi\sin\omega t). \end{aligned} \tag{B.3}$$

The Stokes parameters are then defined as

$$I \equiv \mathcal{E}_0^2 \tag{B.4}$$
$$Q \equiv \mathcal{E}_0^2\cos 2\beta\cos 2\chi \tag{B.5}$$
$$U \equiv \mathcal{E}_0^2\cos 2\beta\sin 2\chi \tag{B.6}$$
$$V \equiv \mathcal{E}_0^2\sin 2\beta. \tag{B.7}$$

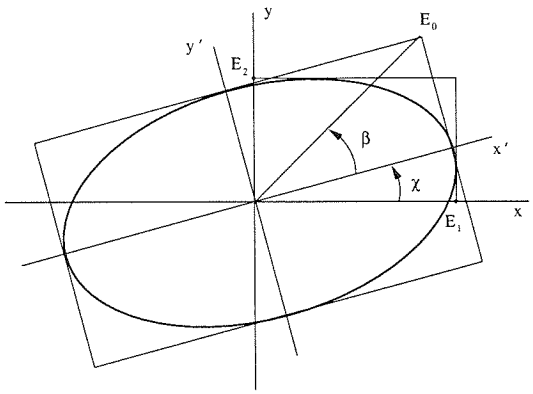

Figure B.1 Geometry of the polarization ellipse. χ describes the rotation angle, and β is the axial ratio.

Following Kraus, if we define the magnitude of the Poynting vector (flux density) to be

$$S \equiv \frac{\mathcal{E}_0^2}{Z}, \tag{B.8}$$

(in the above, we have set $Z = 1$), the Stokes parameters can be described compactly as

$$S[s_i] = S \begin{bmatrix} s_0 \\ s_1 \\ s_2 \\ s_3 \end{bmatrix} \equiv \begin{bmatrix} I \\ Q \\ U \\ V \end{bmatrix}. \tag{B.9}$$

The effective aperture of the receiving antenna is similarly given by

$$A_e[a_i] = A_e \begin{bmatrix} I_t/S_t \\ Q_t/S_t \\ U_t/S_t \\ V_t/S_t \end{bmatrix} \tag{B.10}$$

where subscripted quantities represent parameters of the transmitted wave. The response of the antenna to an incident wave of arbitrary polarization is then given by

$$W = \frac{1}{2} S A_e[\tilde{a_i}][s_i]. \tag{B.11}$$

For a completely linearly polarized wave, with $\beta = \chi = 0$,

$$S[s_i] = S \begin{bmatrix} 1 \\ 1 \\ 0 \\ 0 \end{bmatrix}. \tag{B.12}$$

The response of a right circularly polarized antenna ($\beta_t = \pi/4$) is then

$$W = \frac{1}{2} S A_e [\ 1 \quad 0 \quad 0 \quad 1\ ] \begin{bmatrix} 1 \\ 1 \\ 0 \\ 0 \end{bmatrix} = \frac{1}{2} S A_e. \tag{B.13}$$

If the antenna polarization is not completely circular, and we take $\chi_t = 0$, the effective aperture is given by

$$A_e[a_i] = A_e \begin{bmatrix} 1 \\ \cos 2\beta_t \\ 0 \\ \sin 2\beta_t \end{bmatrix}. \tag{B.14}$$

If the incident wave is linearly polarized with $\beta = 0$, the response is then given by

$$W = \frac{1}{2} S A_e [\ 1 \quad \cos 2\beta_t \quad 0 \quad \sin 2\beta_t\ ] \begin{bmatrix} 1 \\ \cos 2\chi \\ \sin 2\chi \\ 0 \end{bmatrix} = \frac{1}{2} S A_e \{1 + \cos 2\beta_t \cos 2\chi\}. \tag{B.15}$$

Thus for an intrinsically smooth polarized background, Faraday rotation will introduce anisotropies in the switched power at the level of

$$\Delta W = \frac{1}{2} S A_e \cos 2\beta_t \{\cos 2\chi_1 - \cos 2\chi_2\}. \tag{B.16}$$

Since χ_i ranges over the interval $(0, 2\pi)$, the maximum signal from a linearly polarized anisotropy will be

$$\Delta W = S A_e \cos 2\beta_t. \tag{B.17}$$

(Actually, if the χ_i are due to Faraday rotation, then $\chi_i = R_i c^2/\nu^2$, where R_i is the rotation measure, and (B.16) should be integrated over the bandpass.)

From (B.1)–(B.3), with $\chi = 0$, we can show that $\phi_1 - \phi_2 = 2\beta_t$. If $\phi_1 - \phi_2 = m\pi$, then $\beta_t = 0$ or $\pm\pi/2$, and the wave is linearly polarized. If $\phi_1 - \phi_2 = m\pi/2$, with m odd, then $\beta_t = \pm\pi/4$ and the wave is circularly polarized. If $\phi_1 - \phi_2 = m\pi/2 - \delta$, the wave is elliptical, and $\beta_t = (\pi/2 - \delta)/2$. Thus β_t was measured across the band by measuring the phase shift $90 - \delta$ which the polarizer introduced in a linearly polarized transmitted wave. The average over the band was found to be $\langle \cos 2\beta_t \rangle = 0.06$, implying that *at most* 6% of a linearly polarized anisotropy will be seen.

TABLE B.1
KU-BAND AXIAL RATIOS

ν	δ
12	2.0
12.5	7.0
13	1.0
13.5	3.5
14	0.5
14.5	0.9
15	2.0
15.5	6.5
16	5.0
16.5	7.0

$\beta = \frac{90-\delta}{2}$.

Appendix C

Cosmic Variance

For experiments which sample a small area of sky, the estimate of the underlying variance is limited by the sampling variance, i.e., by the number of independent samples of the temperature distribution which determine the variance on a given angular scale. (In CMBR circles, the sampling variance is widely referred to as "cosmic variance.") This appendix outlines a simple method for estimating the magnitude of the sample variance, after Sivia (1996).

If we expand the natural logarithm of the Likelihood function $L(X)$ about the point $X = X_0$, we obtain

$$\ln L(X_0 + X) \simeq \ln L(X_0) + \left.\frac{d \ln L}{dX}\right|_{X_0} (X - X_0) + \frac{1}{2} \left.\frac{d^2 \ln L}{dX^2}\right|_{X_0} (X - X_0)^2 + \ldots \quad \text{(C.1)}$$

With the best estimate of X given by the condition

$$\left.\frac{d \ln L}{dX}\right|_{X_0} = 0, \quad \text{(C.2)}$$

the first three terms in the expansion yield

$$L \propto \exp\left(\frac{1}{2} \left.\frac{d^2 \ln L}{dX^2}\right|_{X_0} (X - X_0)^2\right), \quad \text{(C.3)}$$

which is just a Gaussian of width

$$\sigma = \left(-\left.\frac{d^2 \ln L}{dX^2}\right|_{X_0}\right)^{-1/2}. \quad \text{(C.4)}$$

The best estimate of the parameter of interest X is then given by (C.2), with associated error given by (C.4).

If the likelihood is given by a Gaussian with variance X

$$L(X) = \prod_i^N \frac{1}{\sqrt{2\pi X}} \exp\left(\frac{-(x_i-\mu)^2}{2X}\right), \tag{C.5}$$

then the logarithm of the likelihood is

$$\ln L = \sum_i^N \ln\left(\frac{1}{\sqrt{2\pi X}}\right) - \sum_i^N \frac{(x_i-\mu)^2}{2X}, \tag{C.6}$$

and (C.2) yields

$$\left.\frac{d\ln L}{dX}\right|_{X_0} = -\frac{1}{2}\sum_i^N \frac{1}{X_0} + \sum_i^N \frac{(x_i-\mu)^2}{2X_0^2} = 0 \tag{C.7}$$

or

$$X_0 = \frac{1}{N}\sum_i^N (x_i-\mu)^2, \tag{C.8}$$

with associated error

$$\begin{aligned}\left.\frac{d^2\ln L}{dX^2}\right|_{X_0} &= \frac{1}{2}\sum_i^N \frac{1}{X_0^2} - \sum_i^N \frac{(x_i-\mu)^2}{X_0^3} \\ &= \frac{1}{2X_0^2}\left(N - 2\sum_i^N \frac{(x_i-\mu)^2}{X_0}\right) \\ &= -\frac{N}{2X_0^2},\end{aligned} \tag{C.9}$$

so that the variance is

$$X_0 = \left(\frac{1}{N}\sum_i^N (x_i-\mu)^2\right)\left(1 \pm \sqrt{\frac{2}{N}}\right). \tag{C.10}$$

Appendix D

CMBPROG

CMBPROG is a C software package originally intended as a tool for the calibration, monitoring and reduction of data from the filled-aperture telescopes at the OVRO. When I first began work at the Owens Valley Observatory, no software existed for accessing data from the OVRO 40-meter and 5.5-meter telescopes, what software there was consisting of a heterogeneous collection of specialized routines. The original intent was to create an environment for the rapid inspection of data relating to the operation of the telescopes, including the monitoring data routinely accumulated in the digital backend in addition to the science data itself. In experiments such as the Ring5m, requiring extraordinary stability over many years of observations with complex radiometers, the ability rapidly to detect and identify sources of systematic error, instrumental or otherwise, is the only safeguard against an imperfect world, and time and again experience has proven the old adage that a picture is worth a thousand words; on this philosophy, CMBPROG was built around a series of PGPLOT (Pearson 1995) graphical interfaces, including facilities for histogramming, linear, grayscale, contour and 2D projection plotting, with a variety of editing, fitting, and statistical filtering capabilities accessible directly from the graphics cursor, or alternatively from the user interface, for which it employs the DIFMAP interface developed by Martin Shepherd (Shepherd et al. 1995). All the analysis presented in

this thesis, from reduction of the raw Ka-Band and Ku-Band data, to analysis of *IRAS* 100 μm maps and computation of the Ring5m window functions, was done in CMBPROG. In addition to the CMBPROG-specific graphics routines, in combination with the DIFMAP interface, CMBPROG provides interface-level access to nearly all PGPLOT subroutines, so that CMBPROG can also be used as a general plotting package; all the plots in this thesis were produced within CMBPROG. In addition, random number generators in CMBPROG and the DIFMAP interface make it a flexible environment (if not the fastest) for Monte Carlo simulations.

Over the years, CMBPROG has rapidly outgrown its original charter, now comprising more than 100,000 lines of code, not including the DIFMAP front end. Although the internal memory structure of CMBPROG is oriented toward data types produced by the OVRO telescopes, it allows for the inspection of data not only from the telescopes, an on-site weather station and a local water vapor radiometry system, but has built-in capabilities for handling FITS images (NASA FITS User's Guide 1997), and in conjunction with the user interface, can operate on data in virtually any format. At the interface level, CMBPROG includes a complement of routines for interpolation, fitting, statistics and data editing, including generalized sliding-buffer edits (a few specific applications of which are described in §5.3) which can be customized to virtually any application. A suite of more task-oriented routines exists for calibration, including gain calibration and corrections for planetary ephemerides, beam mapping, focus-curve fitting, and many others. CMBPROG also provides a series of routines for 1D and 2D convolution, correlation, power spectral analysis and digital filtering.

As CMBPROG is now in use by several different groups, this appendix is intended as a brief introduction to its use; a listing of all functions available in CMBPROG and detailed help on using each of them can be obtained from within the CMBPROG environment itself. One of the most powerful aspects of CMBPROG is the scripting

capability of the DIFMAP interface. The combination of customizable routines with the ability automatically and reproducibly to repeat analysis sessions has proven invaluable to this thesis, allowing efficient exploration of large data parameter spaces whether tracking down telescope problems or investigating the effects of different editing schemes on the Ring results. Since the scripting capabilities of the DIFMAP interface have never been documented, this appendix concludes with a brief description of the interface environment, which users of DIFMAP and CMBPROG alike may find of use.

D.1 An Introduction to CMBPROG

D.1.1 General

In what follows, examples of text typed at the CMBPROG prompt appear in `typewriter font`. The prompt itself is the symbol `0>`, not to be confused with commands entered by the user.

The general format for entering commands in cmbprog is

```
command arg1, arg2, arg3, etc.
```

To see a list of user commands available in cmbprog, type '`help cmbprog`.' To search the list of command descriptions for matching strings, use the '`apropos`' facility. For help on individual commands, typing '`help command`' will provide a listing and explanation of the arguments that '`command`' expects.

Minimum matching is performed on all commands.

Scripts are also provided for in the interface; command files are invoked by using the '`@`' symbol, followed by the name of the file:

```
0>@reduce_my_data
```

Commands in files are typed exactly as at the prompt, and can be separated by newlines or semi-colons.

D.1.2 Data Input

CMBPROG is designed to operate on data which is in 5.5-meter of 40-meter log file or monitor file format (see Pearson 1992). You can read and write data using the commands '`rlog`,' and '`wlog`,' respectively:

```
0>rlog jun94, 01jun94.log
```

CMBPROG also supports a cmb data format, which is a binary representation of log or monitor file data and is considerably more compact. Cmb files can be read with '`rcmb`,' and written with the appropriate format argument to '`wlog`.'

Other functions related to reading data:

`glog` — Read logfiles directly from the archive.
`rmon` — Read one or more monitor files into a given season.
`gmon` — Read monitor files directly from the archive.

Files and archives can also be accessed on remote machines, and in compressed (gzip) format. See help on '`rlog`' or '`glog`' for more information.

When read into memory, data are organized into structures called *seasons.* In the above example, the log file `01jun94.log` has been read into a season called "jun94." Multiple files can be read into the same season, or separate seasons can be created for each logfile read in:

```
0>rlog jun94, 01jun94.log
Reading log file(s) into season jun94
0>rlog jun94, 02jun94.log
Reading log file(s) into season jun94
```

Inside a season, data is organized by telescope *procedures* — for instance AVERAGE, FLUX, and CAL (see §2.4) — each of which has a set of data *members* which CMBPROG recognizes. To see a complete listing of procedures and their members, type '`help procedures`.' To specify a procedure member to any CMBPROG function, the usual format is '`proc.member`.' For instance, to see all the SDs from FLUX procedures in the current season as a function of time, type (case-insensitive):

```
0>plot flux.time, flux.sd
```

D.1.3 Data Selection

When manipulating data inside CMBPROG, subsets of data are extracted from the main memory tree into structures called *ferrets*. Subsets are specified by selection criteria set by the user. CMBPROG routines which operate on data will by default operate only on data matching the current set of selection criteria (by default, all appropriate data). Thus in the example

```
0>plot flux.time, flux.sd
```

CMBPROG would create a ferret containing all FLUX procedures so far read in. To see a list of all ferrets created so far, type '`list`.'

Data can be selected by season, source, tag, or any combination thereof. To see the list of seasons you've created using '`rlog`,' type '`sealist`.' To select data from a particular season, use the command '`season`':

```
0>sealist
jun94
0>season jun94
The currently selected season is: jun94
0>
```

To select data from multiple seasons, you can give '`season`' a list of arguments:

```
0>sealist
01jun94
02jun94
03jun94
0>season 01jun94, 02jun94
The currently selected seasons are:
01jun94
02jun94
0>
```

Within each season, subsets of the data can be selected by source name and/or tags. The command '`slist`' displays a list of all recognized sources and the command '`source`' is used to restrict operations to data associated with specific sources. Similarly, the command '`tlist`' displays the recognized tags, and '`tag`' selects data by tag name:

```
0>slist
OBS:       SRC=3C345 RA=16:42:58.80 DEC=39:48:37.0 EQ=J2000
OBS:       SRC=3C286 RA=13:31:08.29 DEC=30:30:33.0 EQ=J2000
OBS:       SRC=3C273 RA=12:29:06.70 DEC=02:03:09.0 EQ=J2000
OBS:       SRC=3C84  RA=03:19:48.20 DEC=41:30:42.0 EQ=J2000
0>source 3C84, 3C286
The currently selected sources are:
OBS:       SRC=3C345 RA=16:42:58.80 DEC=39:48:37.0 EQ=J2000
OBS:       SRC=3C286 RA=13:31:08.29 DEC=30:30:33.0 EQ=J2000
0>
```

Additionally, you can select ranges of a particular procedure member using '`clip`' or '`cut`.' These will flag all data inside/outside the specified range of the selected member. To flag all fluxes outside the pa range (40, 100):

```
0>clip flux.pa, 40, 100, exc
```

In addition, certain procedure-specific tags are also provided:

```
0>target LOAD
The currently selected target is: LOAD
0>caltag ANT
The currently selected caltag is: ANT
0>diode NOISE
The currently selected diode is: NOISE
0>
```

will select only ANT NOISE cals done against a LOAD.

A new ferret will be created by any data-manipulating routine whenever the selection criteria are changed, thus which ferret '`flux.time`' refers to depends on the current set of selection criteria. To associate a non-variable name with a particular ferret, use '`name`.' Thus,

```
0>name flux,myferret
0>plot myferret.time,myferret.flux
```

is identical to the command

```
0>plot flux.time,flux.flux
```

D.1.4 Calibration

Once you have selected the relevant season, sources and tags, you can calibrate data using the command '`calibrate`.' Calibrate operates on all relevant members of the specified procedure. For instance

```
0>calib flux
```

calibrates the A, B, C, D, FLUX, and SD members of the FLUX procedures in the selected season by referencing appropriate CAL procedures. Type '`help procedures`' for a listing of valid procedures and associated members.

Calibrate also provides for telescope gain calibration, i.e.,

```
0>calib flux, gain
```

will perform gain calibration of all relevant members of the FLUX procedures.

Calibrate uses default telescope parameters for each season which can be changed or entered by the user by invoking the command '`telpar`':

```
0>season jun94
The currently selected season is: jun94
0>telpar "ncurve", 6
0>telpar "gx", 2.500, 12.500, 17.500, 27.500, 32.500, 42.500
0>telpar "gy", 0.604,  0.784,  0.921,  1.002,  1.000,  0.947
```

reads a gain curve into the telescope descriptor for the season "jun94."

'`calib`' also allows atmospheric calibration, and the application of simple scale factors to data:

```
0>telpar "tau", 0.03
0>calib flux,atm
```

calibrates flux data by applying a 3% atmospheric correction.

D.1.5 Filtering

Once your data is calibrated, you can use '`filter`' to apply various rejection criteria to your data set:

```
0>filt flux, thermal, 2
```

will flag all fluxes whose sds are greater than 2× the expected thermal sd for the procedure.

`outlier` — Provides iterative outlier rejection.

`clip` — Allows the exclusion of 1D ranges of data.

`cut` — Allows the exclusion of 2D ranges of data.

`gfilt` — Allows the user to design completely general sliding buffer edits.

In addition to non-interactive filtering methods, the graphical interface provides for outlier rejection and other convenient (albeit subjective) ways of flagging data. Type '`help plotfn`.'

D.1.6 Referencing

Members of one procedure can be associated with members of another procedure using the command '`reference`':

```
0>ref flux.time, setfocus.cz, focus
```

associates with each FLUX measurement the focus position nearest in time, storing the referenced values as a new FLUX procedure member which can be accessed as '`flux.focus`.'

To specify the type of referencing to perform, and associated limiting parameters, a set of three functions '`setintt`,' '`setintd`,' and '`setintb`' are provided. To read about their use, type '`help`,' followed by any of the above.

Reference also provides for linear interpolation and boxcar smoothing of the member to be referenced.

D.1.7 Plotting

To look at data, use the command '`plot`,' which takes as its arguments an x-axis, plus any number of y-axes:

```
0>plot flux.time,flux.flux,flux.sd,flux.za
```

will produce plots of flux-procedure FLUXs, SDs and ZAs vs. time.

Plot provides an extensive graphical interface which you can read about by typing '`H`' ('`h`') in the plot window, or '`help plotfn`' at the prompt.

In addition to simple plotting tasks, the following commands are provided:

`project` — Produce 2D projections of 3D data.

`cont` — Make a contour plot of 3D data.

`plgrey` — Make a grayscale plot of 3D.

`hplot` — Histogram a member.

Type '`help`,' followed by any of the above to read about a specific command.

D.1.8 Arithmetic Operations

For numerical manipulation of procedure members, use the functions '`arith`' and '`trans`.' '`arith`' allows for simple operations between a procedure member and another member of the same procedure, or a referenced member from another procedure, while '`trans`' allows more complicated transformations of procedure members.

```
0>arith flux.flux, flux.sd, div, /
0>
```

divides the FLUX fluxes by the corresponding sds, storing the result in a new member called '`flux.div`,' while

```
0>trans flux.sd, weight, pow, -2
0>
```

creates a new member called '`flux.weight`' which consists of the inverse squares of the sds.

D.1.9 Special Manipulations

In addition to the basic operations above, there exist a number of task-specific routines for specialized data reduction:

`focus` — Fit Gaussians/polynomials to a series of focus scans.

`cbeam` — Reduce beam cuts in azimuth or zenith angle.

`gain` — Compute a gain curve by polynomial fitting.

`etc...`

D.2 The DIFMAP Interface Environment

In this section, I describe some aspects of the DIFMAP interface environment not documented elsewhere, but which greatly increase the power of scripts in CMBPROG. This introduction is intended as a quick reference guide only, and makes no pretense at being comprehensive. Although for concision, I couch examples in terms of CMBPROG alone, the discussion is equally valid for users of DIFMAP.

D.2.1 General

As described in §D.1.1, the DIFMAP interface allows non-interactive input through the use of scripts. Commands in files are typed exactly as at the prompt, and must be separated by newlines or semi-colons. Command files are invoked at the DIFMAP prompt by prefacing the file name with the `@` symbol.

Every session of DIFMAP or CMBPROG is recorded in a logfile in the current directory. Lines typed by the user appear as commands, while messages returned by functions appear as comments. Sessions can be replayed by invoking these logfiles as scripts.

D.2.2 Variables

The DIFMAP environment allows the user to declare variables which can be used to store and manipulate return values from CMBPROG routines, data read in from a file, or simply auxiliary data entered by the user.

The following variable types are supported:

`float` — Floating point number.

`integer` — Integer.

`string` — Character string.

`logical` — Boolean variable, with values "`true`" or "`false`."

Variables of any type can be declared as scalars or as arrays with up to three dimensions. Array elements are delineated by `()`.

The following are examples of valid variable declarations:

```
integer i, iarray1d(2), iarray2d(2,2)
float   f, farray1d(2), farray2d(2,2)
string  s, sarray1d(2), sarray2d(2,2)
logical l, larray1d(2), larray2d(2,2)
```

Arrays can be resized, but once a variable has been declared, it cannot be deleted or that variable name associated with another variable type.

The DIFMAP interface supports the following array indexing operators:

`array(a)`	This returns the value of element `a` of the specified 1-dimensional array. Array indices start at 1.
`array(a,b)`	This yields a single element of the specified 2-dimensional array. Arrays can have up to 3 dimensions. The following sub-array operators are illustrated with 1-dimensional arrays, but they can also be used with multi-dimensional arrays.
`array(a:b)`	This yields a sub-array of the specified array, formed from the elements with indices between `a` and `b`.
`array(a:b:c)`	This yields a sub-array of the specified array, formed from every c^{th} element between elements `a` and `b`.

Variables can be assigned values straightforwardly, and manipulated with the usual rules of mathematical precedence. The value of a variable can be accessed using the function '`print`' or '`type`,' as illustrated by the following example:

```
0>farray1d = 1.0,2.0
0>s = "Mean ="
0>f = (farray1d(1) + farray1d(2))/2
0>print s,f
Mean = 1.5
0>
```

To see a listing of declared variables, use 'var':

```
0>var f*
rwd  float f
rwd  float farray1d(2)
rwd  float farray2d(2,2)
0>
```

The DIFMAP interface will perform vector operations on arrays of the same dimension. Thus

```
0>float arr1(10), arr2(10), result(10)
0>result = arr1 + arr2
```

is the same as

```
0>float arr1(10), arr2(10), result(10)
0>do i=1,10
0>result(i) = arr1(i) + arr2(i)
0>end do
```

(see §D.2.4 below for more on looping in DIFMAP).

When used as arguments to CMBPROG routines, vector expressions are evaluated before being passed to the called function, so that if `xs1(100)` and `xs2(100)` are two float arrays,

```
0>float result(100)
0>result = x1 + x2
0>hist result
```

is equivalent to

```
0>hist x1+x2
```

(where 'hist' is a CMBPROG routine to histogram arrays).

Variables can be used to store return values from CMBPROG routines (to see if a routine returns a value to the interface, type "help commandname" at the 0> prompt):

```
0>f = mean(farray1d)
0>print f
1.5
0>
```

Some routines are functions which return values to the interface, but can also be invoked as simple commands; others cannot. (Type "help commandname" to see how to call a particular routine.) Thus to see a printout of statistics on a set of fluxes, you would type

```
0>fstat flux.flux
```

but to store the return values in an array, the invocation

```
0>float array(1)
0>array=fstat(flux.flux)
```

must be used. When return values are stored in an array, as in the above example, the array is automatically resized by the returning function, so that the number of elements in the original variable declaration is irrelevant.

D.2.3 Operations

The following arithmetic operators are supported in DIFMAP:

- `+` — Add two numbers.
- `-` — Subtract two numbers.
- `*` — Multiply two numbers.
- `/` — Divide two numbers.
- `^` — Raise a number to a given power.

Arithmetic expressions may be grouped by using `()`. The interface also provides the standard complement of mathematical functions, including trigonometric functions, logarithms, exponentials, modulus, etc. Their names are intuitive and will not be listed here. Use the '`help`' command to see an alphabetic listing of available functions.

The following relational operators are supported:

These operators can be applied either to numbers or strings:

`a > b` True if `a` is greater than `b`.

`a >= b` True if `a` is greater than or equal to `b` (numbers or strings).

`a < b` True if `a` is less than `b`.

`a <= b` True if `a` is less than or equal to `b`.

`a == b` True if `a` is identical to `b`.

`a != b` True if `a` and `b` are different.

The following operators can only be applied to strings:

`a ~ b` True if string `a` is matched by the simple regular expression in b.

`a !~ b` True if string `a` is not matched by the simple regular expression in `b`.

DIFMAP also supports the usual Boolean operators, which can only be applied to operands of type `logical`:

`! a` True if `a` is false. False if `a` is true.

`a & b` True if both `a` and `b` are true. Otherwise false.

`a | b` True if either or both of `a` and `b` is true.

Strings can be concatenated with the command

`a // b` The result is a string that contains the concatenation of strings `a` and `b`.

D.2.4 Looping and Conditional Structures

The DIFMAP interface provides "`do...end do`", "`while(true)...end while`", "`if...else if...else...end if`" and "`repeat...until(true)`" commands. These can be executed in a script or directly from the prompt, for instance:

```
0>float array(2)
0>array = 1,2
0>do i=1,2
1>print array(i)
1>end do
1
2
0>
```

Note that the prompt symbol changes to indicate the current level of nesting, i.e., the statement "`print array(i)`" occurs inside the first nested loop in the example above.

As described in §D.2.3, logical AND, OR, EQUALS and NOT EQUALS are represented by `&`, `|`, `==` and `!=`, respectively. Logical negation is accomplished by the usual `!` operator. The following fragment script illustrates some aspects of conditional statements

```
test.scr:
        k = 1
        while(k < 2)
          do i=1,3
             do j=1,3
                if(i != 3 & j != 3)
                  print i,j
                end if
             end do
          end do
```

```
    k = k + 1
  end while
```

which when executed, produces the following output:

```
0>@test.scr
1 1
1 2
2 1
2 2
0>
```

D.2.5 Reading Files

The DIFMAP interface provides functions for reading and writing files. Files are associated with integer descriptors ("logical units") and are opened using the '`infile`' and '`outfile`' functions. The logical unit '0' by default refers to standard out (and to standard in). Files are closed by using the function '`close`.' Data can be read or written using the functions '`fread`' and '`fprintf`,' with grammar similar to the C functions '`fprintf`' and '`fscanf`.' To read three pairs of floats from a file called '`mydata`'

```
0>float xarr(3),yarr(3)
0>integer lun
0>lun = infile(mydata)
0>do i=1,3
0>fread lun,"ff",xarr(i),yarr(i)
0>end do
0>close(lun)
```

To write formatted output to a file, use the function '`fprintf`.'

```
0>xarr = 1,2,3; yarr = 2,3,4
0>lun = outfile(newdata)
0>do i=1,3
0>fprintf lun,"%s = %.2f, %s =  %.2f\n","x",xarr(i),"y",yarr(i)
0>end do
0>close(lun)
0>
```

would cause the following to be written to the file 'newdata':

```
x = 1.00, y = 2.00
x = 2.00, y = 3.00
x = 3.00, y = 4.00
```

Format arguments and special characters follow the conventions of Kernigan & Ritchie (1988).

D.2.6 Macros

Macros can be defined by typing '#+macroname definition', where 'definition' is any series of valid commands:

```
0>#+mymacro print "This is a macro"
0>mymacro
This is a macro
0>
```

Macros with arguments can be defined by using the % character:

```
0>#+myothermacro print %1
0>myothermacro "This is another macro"
This is another macro
0>
```

Multiple commands can be included by using a semicolon, but multiple lines must also be continued by using the \ character. The interface will return a ? prompt until the macro definition is complete:

```
0>#+yetanothermacro integer i;do i=1,3;\
?print i\
?end do
0>yetanothermacro
1
2
3
0>
```

To see a list of macros defined, type #? at the prompt. Macros can be deleted by typing '#-macroname.'

D.2.7 Script Arguments

Like macros, scripts can also take arguments. A file called '`myscript`' consisting of the command '`print %1,%2`' would be invoked by typing

```
0>@myscript "This is a passed argument","and this is another."
This is a passed argument and this is another.
0>
```

The variable type is implicitly cast by the interface to a float, a string or a literal string (a string without "" marks around it). The string value of a literal string is accessed inside the script by typing "`%%1`". Compare the following two examples:

```
pstring:
        if(%1=="test")
          print %1
        end if

0>@pstring "test"
test
0>
```

and the literal string version:

```
pliteral:
         if("%%1"=="test")
           print %1
         end if

0>@pliteral test
test
0>
```

Numeric arguments passed as literal strings can be used in arithmetic expressions in a straightforward manner:

```
pnum:
     if("%%1"=="3")
       print %1
       print %1+2
     end if

0>@pnum 3
3
5
0>
```

D.2.8 Escapes

The interface environment provides escape sequences which allow the user to interact with the shell environment:

Any command preceded by an exclamation mark ! is ignored by the interface, allowing the inclusion of comments in a script file.

Any command preceded by a $ is passed directly to the parent shell.

Complicated shell commands can be written into a string and passed to the parent shell by using the 'system()' command.

Thus

```
0>$ls -l
```

and

```
0>system("ls -l")
```

will both cause the current directory to be listed under a UNIX environment.

D.3 Examples

The scripts on the following two pages demonstrate some aspects of data analysis (§D.3.1) and plotting (§D.3.2) in the CMBPROG environment.

D.3.1 Using CMBPROG to Reduce Data

```
!=========================================================================
! Set up to read compressed data from the archive on sable
!=========================================================================

rdef /sable,/scr/mbr/,true

!-------------------------------------------------------------------------
! Read in data from the 40-meter from Jan 1 1998 to Jan 10
!-------------------------------------------------------------------------

glog myseason, 40m, 01jan98,10jan98

!-------------------------------------------------------------------------
! Select data on the Ring fields (named like OV5M0024, OV5M0104, etc.)
!-------------------------------------------------------------------------

source OV5M*

!-------------------------------------------------------------------------
! Linearly interpolate CAL measurements onto the FLUXes, flagging any
! FLUX procedures for which no bracketing CALs were found with 1 hour
!-------------------------------------------------------------------------

setcalt linear
setcald 0,7200
calib flux,flux

!-------------------------------------------------------------------------
! Calibrate for atmosphere, assuming an opacity of 0.045
!-------------------------------------------------------------------------

telpar "tau", 0.045
calib flux,atm

!-------------------------------------------------------------------------
! And write a plot of the calibrated FLUX data to the file "fluxplot.ps"
!-------------------------------------------------------------------------

dev fluxplot.ps/ps
plot flux.time, flux.flux
pgend

!-------------------------------------------------------------------------
! Write the calibrated data out as a CMB format file called "jan98.cmb"
!-------------------------------------------------------------------------

wlog myseason, jan98.cmb, true, true
```

D.3.2 Using CMBPROG as a PGPLOT Interface

In the following, `ka_cmb.fld` is a file containing three columns of 36 numbers, assumed to be the x-axis, y-axis and errors, respectively. The output of this script is shown on the following page.

```
!======================================================================
! Define a macro to read in the data
!======================================================================

#+readfld lun=infile(%1);\
   float %2(36),%3(36),%4(36);\
   do i=1,36;\
    fread lun,"fff",%2(i),%3(i),%4(i);\
   end do;\
   close lun

!----------------------------------------------------------------------
! Read in the data
!----------------------------------------------------------------------

readfld ka_cmb.fld, xfld, yfld, sfld

!----------------------------------------------------------------------
! Draw the plot
!----------------------------------------------------------------------

pgsvp 0.2,0.9,0.2,0.8
pgwindow 1,23,-300,300
pgscf 2; pgsch 1.5
pgbox BCNST, 6, 6, BCNSTV, 0, 5
pgpt xfld,yfld,17
pgerry xfld,yfld-sfld,yfld+sfld
pgsls(3)
pglin xfld,yfld

!----------------------------------------------------------------------
! And label
!----------------------------------------------------------------------

string text
label "Ring5m Field (hours)","",""
pgmtext L,3.5,0.5,0.5,"\\gDT\\dCMB\\u (\\gmK)"

pgsch 1
pgtext 0.5,285,"\\(0568)\\dcmb\\u:"
text = "\\gs = "//ftoa("%6.2f",rms(yfld))//" \\gmK"
pgtext 3,285,text
text = "\\ge = "//ftoa("%.2f",mean(sfld))//" \\gmK"
pgtext 15,285,text
```

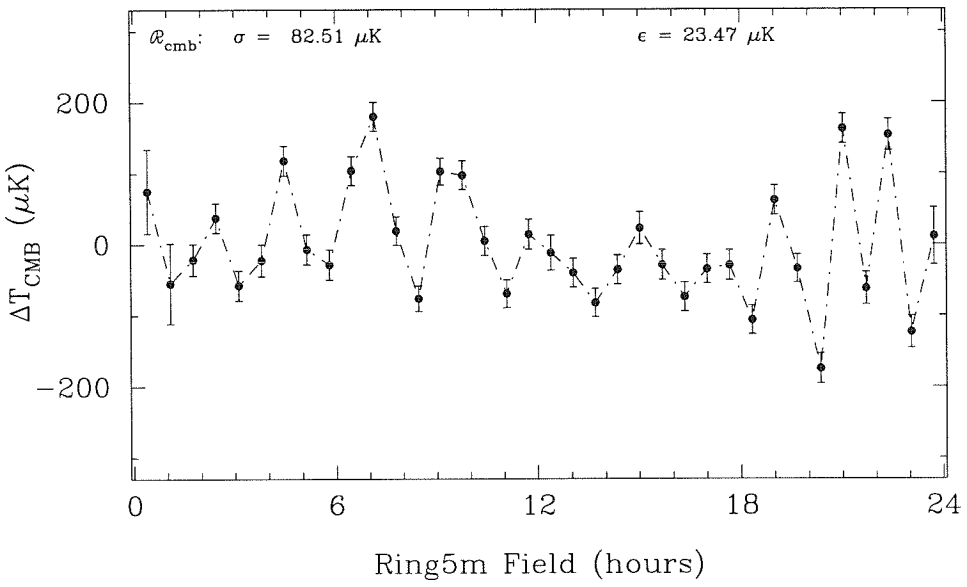

Figure D.1 The output of the example script on the previous page, showing the use of CMBPROG as an interface to the PGPLOT subroutine library.

REFERENCES

Baars, J. W. M., Genzel, R., Pauliny-Toth, I. I. K. & Witzel, A. 1977, *Astron. Astrophys.*, **61**, 99-106.

Bahcall, N. A. 1998, 12^{th} *Potsdam Cosmology Workshop* (Large Scale Structure: Tracks and Traces).

Banday, A. J. & Wolfendale, A. W. 1991, *MNRAS*, **248**, 705-714.

Berge G. L. & Gulkis, S. 1976, in *Jupiter*, T. Gehrels, Ed. (Univ. of Arizona Press, Tucson), 621-692.

Bond, J. R. & Efstathiou, G. 1984, *Ap. J.*, **285**, L45.

Bond, J. R. 1995, *Astrophys. Lett. and Comm.*, **32**, 63.

Church, S. E., Ganga, K. M. et al. 1997, *Ap. J.*, **484**, 523-537.

de Bernardis, P. et al. 1991, *Ap. J.*, **382**, 515.

de Bernardis, P. et al. 1994, *Ap. J.*, **422**, L33.

de Bruyn, A. G. 1996, IAU Symp. 175 (Extragalactic Radio Sources, ed. R. Ekers et al.), 495.

Dent, W. A. 1972, *Ap. J.*, **177**, 93.

Dicus, D. A., et al. 1982, *Phys. Rev. D*, **26**, 2694.

Emerson & Cuming, Canton. Mass. *Technical Bulletin*, 8-2-4.

Emerson & Cuming, Canton. Mass. *Technical Bulletin*, 8-2-14.

Ferland, G. J. 1980, *PASP*, **92**, 596.

Ferrara, A., Dettmar, R. J. 1994, *Ap. J.*, **427**, 155-159.

Downes, D. & Rinehart, R. 1966, *Ap. J.*, **144**, 568.

Dragovan, M. et al. 1993, *Ap. J.*, **427**, L67-L70.

Draine, B. & Lazarian, A. 1997, astro-ph/9710152.

Fixsen, D. J., Cheng, E. S. & Gales, J. M. 1996, *Ap. J.*, **473**, 576-587.

Ganga, K., Page, L., Cheng, E. S., Meyer, S. 1994, *Ap. J.*, **432**, L15.

Gary, B. 1974, *Astron. J.*, **79**, 318-320.

Gaustad, J. E., McCullough, P. R., & Van Buren, D. 1996, *PASP*, **108**, 823.

Gorski, K. M. et al. 1994, *Ap. J.*, **430**, L89.

Green, D. A. 1996, *A Catalogue of Galactic Supernova Remnants* (1996 August version), (Cambridge, UK: Mullard Radio Astronomy Observatory) (available on the World-Wide-Web at `http://www.mrao.cam.ac.uk/surveys/snrs/`).

Gulkis, S. 1997, private communication.

Gunderson, J. O. et al. 1993, *Ap. J.*, **413**, L1.

Gunderson, J. O. et al. 1995, *Ap. J.*, **443**, L57.

Hancock, S., Gutierrez, C. M., Davies, R. D., Lasenby, A. N., Rocha, G. et al. 1997, *MNRAS*, **289**, 505-514.

Herbig, T.H. 1994, Ph.D. thesis, Caltech.

Herbig, T., Lawrence, C. R., Readhead, A. C. S. & Gulkis, S. 1995, *Ap. J.*, **449**, L5.

Hinshaw, et al. 1996, *Ap. J.*, **464**, L17.

Hu, W., Sugiyama, N. & Silk, J. 1997, *Nature*, **386**, 37-43.

IRAS Catalogs and Atlases: Explanatory Supplement (1988, ed. C.A. Beichman, G. Neugebauer, H.J. Habing, P.E. Clegg and T.J. Chester, Washington, DC: GPO).

Kendall, M.G. 1955, *Rank Correlation Methods* (London: Charles Griffin & Co. Ltd.).

Kendall, M. G. & Stuart, A. 1963, *The Advanced Theory of Statistics* (New York: Hafner Pub. Co.).

Kernigan, B. W. & Ritchie, D. M. 1988, *The C Programming Language* (Englewood Cliffs: Prentice Hall).

Kogut, A., et al. 1996, *Ap. J.*, **460**, 1.

Kraus, J. D. 1986, *Radio Astronomy* (Ohio: Cygnus-Quasar Books).

Kulkarni, S. R., & Heiles, C. 1987, in *Interstellar Processes*, ed. D.J. Hollenbach & H.A. Thronson, Jr. (Reidel: Dordrecht), 87.

Lai, R., Bautista, J. J., Fujiwara, B., et al. 1994, *IEEE Microwave and Guided Wave Letters*, **4**, 329-331.

Lawrence, C. R., Herbig, T. & Readhead, A. C. S. 1994, *Proc. of the IEEE*, **82**, 763-767.

Lawson, K. D., *et al.* 1987, *MNRAS*, **225**, 307.

Leitch, E. M., Myers, S. T., Readhead, A. C. S. & Pearson, T. J. 1997, *Ap. J.*, **486**, L23.

Lineweaver, C. H., Barbosa, D., Blanchard, A. & Bartlett, J. G. 1997, *A& AS*, **322**, 365-374.

Meyerdierks, H., Heithausen, A. & Reif, K. 1991, *A&A*, **245**, 247.

Mezger, P. G. & Henderson, A. P. 1967, *Ap. J.*, **147**, 471.

Morsi, H. W. 1997, private communication.

Myers, S. T., 1990, PhD thesis, Caltech.

Myers, S. T., Baker, J. E., Readhead, A. C. S., Leitch, E. M. & Herbig, T. 1997, *Ap. J.*, **485**, 1-21.

NASA/GSFC 1997, *A User's Guide for the Flexible Image Transport System (FITS)* (available on the World-Wide-Web at `http://www.cv.nrao.edu/fits/documents/documents.html`).

Netterfield, C. B, Devlin, M. J., Jarosik, N., Page, L. & Wollack, E. 1997, *A.J.*, **474**, 47-66.

Osterbrock, D. E. 1989, *Astrophysics of Gaseous Nebulae and Active Galactic Nuclei* (Mill Valley: University Science Books).

O'Sullivan, C. et al. 1995, *MNRAS*, **274**, 861-868.

Pearson, T. J. 1992, *OVRO 40-m and 5.5-m Antennas Control System* (Owens Valley Radio Observatory).

Pearson, T. J. 1995, *PGPLOT Graphics Subroutine Library* (available on the World-Wide-Web at `http://astro.caltech.edu/~tjp/pgplot/`).

Peebles, P. J. E. 1992, *Principles of Physical Cosmology* (Princeton: Princeton Univ. Press, 517).

Perley, R. A., Scwab, F. R. & Bridle, A. H. 1988, *Synthesis Imaging in Radio Astronomy* (San Francisco: Astronomical Society of the Pacific).

Picirillo, L. & Calisse, P. 1993, *Ap. J.*, **411**, 529.

Platt, S. R., Kovac, J., Dragovan, M., Peterson, J. B. & Ruhl, J. E. 1997, *Ap. J.*, **475**, L1.

Press, W. H., Flannery, B. P., Teukolsky, S. A. & Vetterling, W. T. 1988, *Numerical Recipes in C* (Cambridge: Cambridge Univ. Press).

Reach, W. T., et al. 1995, *Ap. J.*, **451**, 188.

Readhead, A. C. S., Lawrence, C. R., Myers, S. T., Sargent, W. L. W., Hardebeck, H. E. & Moffet, A. T. 1989, *Ap. J.*, **346**, 566.

Readhead, et al. 1998, in preparation (`http://astro.caltech.edu/~tjp/CBI/`).

Reich, P. & Reich, W. 1988, *A&A Suppl.*, **74**, 7-23.

Rohlfs, K. & Wilson, T. L. 1996, *Tools of Radio Astronomy* (Berlin: Springer-Verlag, 48-63).

Rybicki, G. B. & Lightman, A. P. 1979, *Radiative Processes in Astrophysics* (New York: Wiley).

Sachs, R. K. & Wolfe, A. M. 1967, *Ap. J.*, **147**, 73.

Scott, D., Silk, J. & White, M. 1995, *Science*, **268**, 829-835.

Scott, D. & White, M. 1995, *General Relativity and Gravitation*, **27**, 1023-1030.

Scott, P. F., Saunders, R., Pooley, G. et al. 1996, *Ap. J.*, **461**, L1.

Seljak, U. & Zaldarriaga, M. 1997, *CMBFAST* (available on the World-Wide-Web at `http://arcturus.mit.edu:80/~matiasz/CMBFAST/cmbfast.html`).

Shepherd, M. C., Pearson, T. J. & Taylor, G. B. 1995, *Bull. Amer. Astr. Soc.*, **27**, 903.

Silk, J. & Wilson, M. L. 1980, *Phys. Scripta*, **21**, 708.

Simonetti *et al.*, 1996, *Ap. J.*, **458**, L1-L3.

Sivia, D. S. 1996, *Data Analysis: A Bayesian Tutorial* (Oxford: Clarenton Press).

Smoot, G. F. et al. 1992, *Ap. J.*, **396**, L1.

Spitzer, L. 1978, *Physical Processes in The Interstellar Medium* (New York: John Wiley & Sons, Inc.).

Tanaka, S. et al. 1996, *Ap. J.*, **468**, L81.

Thompson, A. R., Moran, J. M. & Swenson, G. W. 1991, *Synthesis Imaging in Radio Astronomy* (Malabar: John Wiley & Sons, Inc.).

Tucker, G. S., Griffin, G. S., Nguyen, H. T. & Peterson, J. B. 1993, *Ap. J.*, **419**, L45-L48.

Wagoner, R. V. 1973, *Ap. J.*, **179**, 343.

Webster, A. 1997, private communication.

White, M., Carlstrom, J. E., & Dragovan, M. 1997, astro-ph/9712195.

White, M., Scott, D. & Silk, J. 1994, *ARAA*, **32**, 319-370.

Wieringa, M. H., de Bruyn, A. G., Jansen, D., Brouw, W. N. & Katgert, P. 1993, *A&AS*, **268**, 215.

Wright E. L., Mather J. C. & Bennett, C. L. 1991, *Ap. J.*, **381**, 200-209.

Yusef-Zadeh, F. 1989, in *The Center of the Galaxy*, ed. M. Morris (Kluwer Academic: Dordrecht), 243.